CIRCULAR ARRAY TECHNIQUES FOR SONAR APPLICATIONS

BY

RON EIGES

A thesis submitted to the University of London for the Degree of
Doctor of Philosophy in Electronic Engineering

Department of Electronic and Electrical Engineering
University College London

APRIL 1993

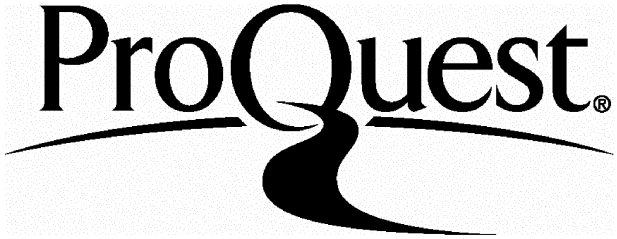

Abstract

This research has been conducted at University College London in collaboration with Loughborough University of Technology. It is aimed at studying the theoretical and practical aspects of circular radiating arrays under conventional and high-resolution processing for sonar applications.

The thesis opens with a short introductory review on circular arrays, quoting relevant past and recent publications and pointing to the significance of the sonar context. Some of the basic concepts involved in the conventional analysis of discrete circular arrays are then recalled, in particular that of phase-mode excitation and the derived techniques of mode-space beamforming, null steering and phase-comparison (multimodal) direction finding.

From a multimodal direction finding scheme that requires no mode alignment the study leads on to the introduction of the novel notion of sectoral phase modes and their possible application in directional multimodal direction finding with enhanced immunity to out-of-sector interference, and in sectorally-controlled multibeam nulling. One aspect pertaining to the benefit of sectoral phase modes as well as to the usefulness of most modal techniques is that of bandwidth. Options and limitations relating to digitally-implemented broadband mode alignment are examined and shown to depend on the directional properties of the element patterns. The effect of random homoscedastic aperture errors on the performance of modally-formed beams are analysed next followed by the introduction of a calibration-based least-squares correction scheme which is designed to compensate for deterministic or random variations in element radiation pattern behaviour and in array channel responses. The proposed two-stage multimode correction scheme, which is shown to be equivalent to a least-squares correction of a multiple set of mode-space beams, is extended to the wideband case, with some simulated results demonstrating the expected performance of filtered phase modes, sectoral phase modes and mode-space beams.

Finally, the application of spatial superresolution estimators to circular arrays is considered, where, after an overview of various relevant approaches and specific algorithms, a covariance-matrix structural equivalence is shown between narrowband element-space linear-array methods and the corresponding mode-space circular-array formulation. It is shown that spatial estimators for the latter case are better modelled under an ambient noise field that varies in elevation, and it is demonstrated that

established linear-array algorithms such as the Minimum Norm estimator and the decorrelating technique of spatial smoothing may be reformulated to apply to circular arrays in mode space. Furthermore it is noted that, under wideband processing, mode-space estimators are particularly suited for handling a multipath environment by virtue of an inherent frequency-domain smoothing effect.

TO RONIT, HADAS AND NITZAN

לרונית, הדס וניצן

WITH LOVE

באהבה

Acknowledgement

The research described in this thesis has been sponsored during its first year by the Admiralty Research Establishment in Portland and during the second and third years by the UK Science and Engineering Research Council. During the second year it has also received the support of the ORS Award Scheme.

I wish to thank Dr Hugh Griffiths for his superb supervision and inspiring guidance, and for having made my stay at UCL a real pleasure. I am likewise very grateful to our visiting professors Dr Ken Milne and Dr Ralph Benjamin for their whole-hearted assistance, constructive advice and useful comments that had helped keep me on the right tracks. Special thanks are due to Professor Roy Griffiths and Professor Colin Cowan of Loughborough University and to Professor Tom Curtis of DRA Portland for having shared with me some of their immense knowledge, experience and insight, as well as to Dr Tahseen Rafik for the very close cooperation and helpful discussions. I am also very much indebted to my employer RAFAEL for having provided me with the opportunity to undertake this research and for their continuous support.

Finally, I would like to express my gratitude to all my fellow postgraduates for the warm and welcoming atmosphere, and in particular to Dr Wolfram Titze whose constructive ideas and suggestions have contributed a lot to the presentability of this work.

Contents

E. Appendices for chapter 5

F. Beamforming Simulation program

List of figures

List of tables

Section **Page no.**

1. INTRODUCTION

1.1 GENERAL

The circular symmetry of ring and cylindrical arrays has attracted the attention of antenna and sonar researchers over the past sixty years. Potentially, these arrays offer 360° azimuth coverage for communications, direction-finding, radar and sonar applications, and may be installed on or conveniently wrapped round land, naval or airborne platforms. However, the rapid theoretical and technological growth in the related field of linear and planar arrays as well as the more complex and lossy feeding schemes devised for the earlier circular arrays, have inevitably limited the interest in their implementation and have held back their development. The past three decades have seen significant progress in the analysis of circular arrays, based on the concept of phase mode excitation, which has led to the development of 'multi-modal' direction-finding systems and to new techniques for the synthesis and steering of directional beams and nulls.

Sonar transducer arrays of various shapes have likewise been under research and development for many years [HAY 20], [HOL 47], [AND 63], [QUE 70]. Experimental as well as operational arrays of (receiving) hydrophones and (transmitting) projectors in linear, planar, circular, cylindrical, and spherical arrangement have been built and used for passive or active source detection and localisation, for minesweeping, fish finding, communication and telemetry [URI 83], [BUR 91]. The low (acoustic) speed of propagation in water has led to the development of multiple-beam sonar array systems with the emphasis being placed (in the case of passive sonar) on true time-delay beamformers which could handle the wide bandwidths involved. Aided by the low frequencies of the useful 'sonar spectrum', fully-digital beamformers have, to a large extent, replaced the earlier analogue networks of receiving sonar arrays, thus opening the way to more elaborate signal processing algorithms [AND 60], [CUR 80].

Over the last three decades there has also been tremendous interest directed at surpassing the Rayleigh resolution limit of spatial spectral estimation. Known collectively as spatial superresolution techniques, these are non-linear signal

processing methods that use the information available in the received (and sampled) incoming wavefront, subject to some assumptions, to (statistically) enhance the system performance in detecting and separating between closely-spaced sources. They are generally relevant in the context of digitally processed receiving arrays of arbitrary shape, but a number of important high-resolution schemes have been either restricted to, or better modelled, when applied to equi-spaced linear arrays. The inherent symmetry and full peripheral coverage that characterise sensor arrays with circular geometry have, rather surprisingly, attracted only limited interest of authors in the field [ZEY 91], [ROC 88], [MES 90].

Papers on circular arrays started to appear in the 1930s dealing mainly with the azimuth and elevation patterns as well as the directivity of co-phased, equi-phased and periodically-phased arrays [STE 29], [CHI 36], [HAN 38], [HAN 39]. The basic radiation properties of ring and cylindrical arrays, their radiation impedance and directivity continued to feature in later works [CAR 43], [PAG 48a], [PAG 48b], [LEP 50], [KUN 51], [KUN 53], [TIL 55], [KUN 56], [KIN 56], [WAI 58], [CHU 59], [MIT 59], [HIC 60], [HIC 61], [HIC 63], [MAC 63], [ROY 64], [ROY 66], [CHE 67], [KIN 68], some of which included an analysis of concentric ring arrays proposed for improving pattern control [STE 29], [HAN 38], [HAN 39], [PAG 48b], [LEP 50], [STE 65], [MAW 68], [GOT 70]. The synthesis of directional beams based on co-phased (or close to co-phased) excitation has likewise provided a popular subject of research [DUH 52], [TAY 52], [ZIE 64], [FEN 65a], [FEN 65b], [JAM 65], [MOT 68], [TSE 68], [RED 70], [COL 70], [GOT 77], [NAG 78], [WAT 80], although the development of the phase mode excitation concept [COL 69], [PRO 72], [DAV 81a], [DAV 83] in the 1960s has led to a simple transformation from the then well-established linear array synthesis techniques to circular arrays [DAV 65b], [LON 67], [RAH 80], [RAH 81], [RAH 82], [JON 89], [JON 90]. Beam scanning and multi-beam forming which had previously required the commutation of excited array sectors, the switching of a feed lens ports or a phase-modulating network (for continuous beam rotation) [NEF 50], [NEF 60], [TAN 62], [MCC 63], [DAV 65a], [FEN 68], [LON 68], [BOY 68], [STA 69], [BOY 70], [BOG 74] could now be achieved by feeding the array with a Butler matrix and applying a linear progressive phase taper to its output ports [BUT 61], [CHA 62], [CHO 66], [CHO 67], [SHE 68], [DAV 69], [WIT 69], [SHE 70], although practical aspects of realising large Butler matrices have led some authors to consider alternative hybrid beam switching schemes in which a small phased Butler matrix is used for fine phase-centre deflection of the excited aperture or beamforming lens sector [HOL 74], [SKA 75]. One application for a Butler-matrix-fed circular array as a transmit-receive antenna on a communication-antenna site is proposed in [GUY 83b] where use is made of the isolation between different phase modes excited by the matrix. An interesting application for an electronically rotating circular-array beam

(however implemented) relates to obtaining a non-rotating directional radiation pattern from an antenna mounted on a spinning spacecraft [GRE 74]. Null forming and null steering techniques have similarly benefited from the novel phase-mode approach making it possible to synthesise omnidirectional 'modes' as well as directional beams with a specified number of steerable pattern nulls [LIM 75], [LIM 77], [DAV 77], [RIZ 77], [DAV 78a], [DAV 78b], [DAV 81b], [GRI 86], [KAR 86], [CVE 88a], [CVE 88b].

Early applications considered for circular arrays included direction finders [CRA 47], [EAR 47], [RIN 56], [BAI 60], [GET 66], [WUN 66], [GET 78], [KUM 83a] of which the Wullenwever array is perhaps the most well known, naval and air navigational aids [HAN 53], [CHR 74], [SHE 74] and HF communications antennas [STA 69]. The classic 4-element Adcock array patented in 1919 and more so the 8-element (interleaved) Adcock are in fact examples of a circular array implementation of a direction finding system [CRA 47], [ADC 19], [GUY 83a]. More recent circular-array DF techniques are based on multi-beam amplitude comparison, multi-modal phase comparison, a nulling scheme or any combination of the above [CVE 88a], [CVE 88b], [REH 80]. The formation of nulls to suppress interference may also be achieved through the use of adaptive hardware and software, applicable at either element level or at mode level [GUY 81].

Closely related with the idea of adaptive array processing are superresolution techniques for the spatial resolution of incident plane waves emanating from a number of far-field sources [JOH 86], [NIC 87]. A variety of algorithms have been developed and analysed in the literature, among them scalar-search (one-dimensional parameter-search) methods such as Capon's MVDR, Burg's Max-Entropy, MUSIC, and Min-Norm [CAP 69], [BUR 67], [BUR 68], [BUR 75], [SCH 79], [SCH 81], [BIE 80], [RED 79], [KUM 83b], [KUM 83c], [NIC 88], [LIV 90] search-free (translational invariance) methods such as ESPRIT and TAM [PAU 85], [PAU 86], [ROY 86a], [ROY 86b], [ROY 87], [OTT 88], [ROY 89], [OTT 90], [OTT 91], [VIB 91a], [LIC 91], [KUN 86], [RAO 88], [RAO 89], [LIV 91] and vector-search (multidimensional) schemes such as IMP, Stochastic Max-Likelihood, Deterministic Max-Likelihood and WSF [TUF 82], [MAT 89], [KAV 91], [CLA 88], [CLA 91], [SCH 68], [VAN 68], [BAN 71], [LIG 73], [OWS 81], [WAX 83], [WAX 85], [BOH 84], [BOH 85], [BOH 86], [JAF 88], [ZIS 87], [ZIS 88], [SAN 87], [STO 89], [STO 90a], [STO 90b], [STO 91], [OTT 89], [OTT 92], [VIB 91a], [VIB 91b].

Superresolution estimators may be directly applied to the signals received by the array elements, but it often proves beneficial to pre-process the array outputs, transforming the superresolution scheme from 'element space' onto 'beam space' [BIE 84], [GRA 84], [XUB 89], [XUB 90], [LEE 92]. The particularly useful transformation from element space to circular-array mode space which is to play a major role in our

study, has, however, excited but fleeting consideration in the literature [Moo 80], [Mil 81].

1.2 OBJECTIVES AND LAYOUT OF THESIS

Despite the dearth of published material in the field of circular arrays for sonar applications, most antenna array techniques for HF, VHF, UHF and microwave frequencies are basically applicable to sonar arrays. In fact adapting these techniques to sonar array systems means that traditional beamforming matrices whose imperfect analogue components have often limited their performance at microwave frequencies, may now be implemented digitally in hardware or in software, thereby allowing complex processing configurations and making the systems more amenable to corrective calibration and alignment schemes. Indeed, it may well be argued that the context of our study, which had initially been targeted at circular sonar arrays, has somewhat shifted to address circular digitally-processed receiving arrays of either antenna elements or sonar hydrophones; in the latter case, though, one has the double benefit of both low frequency and manageable array size.

Our research study thus aims at exploring theoretical and practical aspects of conventional as well as high-resolution circular-array processing schemes for sonar applications, adapting some of the established circular-array techniques, as well as applying a number of new ideas to circular sonar arrays fed by digital beamformers. The material contained in this thesis is organised as follows:

CHAPTER 2 reviews some of the basic concepts involved in the analysis of discrete circular arrays and considers some transient aspects of the array radiation patterns.

CHAPTER 3 deals with conventional beamforming and nulling techniques based on phase-mode analysis, introduces the idea of directional multimodal direction finding based on the new notion of *sectoral phase modes*, and studies the options and limitations of wideband mode alignment which directly affect the usefulness of the above techniques.

CHAPTER 4 examines the effect of random aperture errors on the performance of a modally formed beam and introduces a correction scheme which is designed to compensate for deterministic or random variations in element radiation pattern behaviour and in array channel responses.

CHAPTER 5 is devoted to the application of superresolution techniques to circular arrays. From a brief review of this dynamic field it leads on to the viability of mode-space circular-array spatial estimators in terms of signal and noise

covariances, and to the possible implementation of spatial and frequency-domain smoothing.

CHAPTER 6 concludes the main part of the thesis with a summary of the main results and recommendations for further study.

CHAPTER 7 holds the bibliographical references quoted in the thesis and is divided into five sections, each containing the references for the respective chapter and its appendices. Publications are quoted in the text using a bracketed 'key' comprising the first three letters of the (first) author's surname and the last two digits of the year of publication. Whenever two or more publications share the same key, they are distinguished by appending a, b, etc. to their respective keys. Thus [DAV 78a] and [DAV 78b] refer to two different articles both of which had D. E. N. Davies as principal author, and both of which were published in 1978.

The remainder of the thesis is divided into six parts. Part A contains an extensive list of the abbreviations and symbols that appear in the thesis. Although an effort has been made to maintain a reasonable globality of definitions, some symbol re-designation has proved to be unavoidable. Parts B to E hold the appendices to chapters 2 to 6 respectively, each part corresponding to a single chapter, while part F describes the latest version of a computer simulation program for the conventional analysis of circular arrays, including an overview of the program with structural details of its code as well as a layout of all user-interface menus in the form of a concise manual.

2. BASIC CONCEPTS

2.1 GENERAL

The idea of stacking discrete aperture elements of an antenna or sonar system in a regularly-shaped array fed by a power combining/dividing network saw its first (antenna) implementation in the late 1920s. Such an arrangement allows the synthesis of prescribed radiation beams through the control of the aperture distribution, enhances the single-element signal-to-noise ratio (SNR) in reception[1], enables the delivery of high ERP[2] in transmission through the use of the active array[3] concept and provides the basis for electronic scanning[4] and multiple beamforming[5]. Although the radiation fields produced by an excited array (and likewise, the signals picked up by an array from outside sources) are governed by the solution to the wave equation[6] under the appropriate boundary conditions imposed by the array structure and loading, the underlying approach behind array theory is the principle of superposition. Accordingly, the radiation pattern of the array at a given observation angle[7] is obtained by a linear combination of the element-pattern fields

1 The single-element SNR is improved under the assumption of low aperture correlation of the received noise and low loss of the feeding network.

2 ERP stands for the Effective Radiated Power of the array, denoting the power per unit solid angle transmitted by the array in a given direction, divided by 4π.

3 An active array uses a set of power amplifiers whose outputs are combined in space. The amplifiers are attached to the array elements or distributed within the branches of the feeding network, replacing the traditional approach of a single power amplifier at the input.

4 Electronic scanning refers to the electronically-controlled inertialess movement of an array radiation beam via the controlled switching of element channel phases or delays.

5 A multiple beamformer is an array feed network that can simultaneously generate a set of radiation beams, ordinarily at different directions.

6 The wave equation is derived in a source-free region from either Maxwell's equations for the electric and magnetic fields (e.g. [Har 61], [Col 91]) or from the hydrodynamic equations for the acoustic pressure and particle velocity fields [Bre 80].

7 The term radiation pattern of a transmitting system denotes the frequency-domain (far-) field strength, measured on a constant radius with the excited antenna or sonar system at its centre, as a function of angle. By virtue of reciprocity, the same concept equally applies to the signal picked up by a receiving system from a far-field point source, as a function of its angular position.

in that direction. Note though that each element-pattern contribution refers to the radiation pattern of a single array element in the presence of all other elements, but such that the superimposed parameter (say, incident feedline mode) does not excite any other element. In the inevitable presence of inter-element coupling, superposition of incident-modes is therefore only applicable in a matched-terminated environment of the surrounding feedlines. The shape of each element pattern is theoretically obtainable from the exact solution of the prevailing boundary-value problem, and in the case of periodic (infinite) linear or planar arrays of closely-spaced radiators, it is also fully expressible in terms of inter-element coupling coefficients. Practically, though, the required patterns may be measured on the antenna or sonar range, and we shall therefore assume their availability in the pursuing analysis.

Superimposing the radiation patterns of identical array elements, all facing in the same direction[8], results in a separable spatial array pattern that is the product of the element pattern with the *array factor*. The latter pattern which is controllable via the (complex) weight excitation of the element signals at the array aperture, is the main contributor to the shape of the array radiation pattern, its beamwidth, sidelobe level and peak direction of its maximum lobe (i.e. scan angle). The element pattern, being typically characterised by a relatively broader main radiation beam, affects these pattern parameters to a much lesser extent, and has its main influence on the potential angular coverage of the array, and in the electromagnetic case, also on the polarisation of the radiated fields. Naturally, the array pattern is also affected by geometry. Under a large inter-element spacing, the effective spatial sampling involved in the formation of the array factor may, in the case of a regularly-shaped array, give rise to visible *Floquet modes* commonly referred to as *grating lobes* [AMI 72], a phenomenon that is the spatial manifestation of the time-domain under-sampling occurrence of aliasing[9]. Grating lobes may be somewhat suppressed by the directional properties of the element pattern, and are diffused on departure from regular linear or planar geometry.

The work contained in this thesis is devoted to circular arrays of radially-symmetric elements, also known as ring arrays. Unlike linear or planar arrays the radiation pattern of a circular array is not separable and spatial-aliasing contributions

8 Strictly speaking, for all element radiation patterns to be identical, all elements must 'sense' the same array environment. This imposes a periodic structural constraint of an infinitely-long linear or planar array of uniformly spaced radiators.

9 Strictly speaking, Floquet modes are relevant to a periodic (and therefore infinite) array structure under uniform excitation, representing the radiated field by a series of few ('main beam' + 'grating lobes') propagating plane waves and an infinite number of evanescent plane-wave terms. In the case of a finite (linear or planar) array, grating lobes are spatially aliased contributions of the array factor.

are not represented by distinct grating lobes. In this chapter we review two fundamental feeding concepts on which much of the analyses and implementations of discrete circular arrays have been based, namely the *beam-cophased* and *phase-mode* excitation schemes.

Beam-cophased (or 'phase-compensated') excitation involves the phase equalisation of the contributions from all the array element, when the array receives a signal from (or transmits to) a specified angular direction. In the case of a linear or planar phased array the elements are co-phased by the (controlled) application of a linear phase taper across the array, whose gradient determines the scan angle of the array radiation beam. Although the pattern's characteristics such as directivity[10], beamwidth and sidelobes are separately controlled by the (usually constant) amplitude weighting taper (shading), the gain, beamwidth and sidelobe level typically deteriorate with scan, limiting the angular coverage of such arrays to (depending on bandwidth) 90°-120°. The beam-cophased excitation for circular arrays is a direct extension of the linear array phasing concept and has consequently received considerable attention as a directional beam forming technique. Associated with this concept is the idea of co-delayed excitation whereby true time-delay equalisation of the element signals ensures the wideband operation of the array [LON 68], [STA 69]. Unfortunately, in the case of a circular array, the required phase (or delay) taper is not linear (leading, in the case of analogue beamforming architecture, to more complex digitally-controlled phase or delay shifters); a reasonable sidelobe performance requires the application of both amplitude and phase taper to the co-phased (or co-delayed) array, and scanning a beam (beyond a limited 'within sector' deflection) requires the commutation of the excited array sector. The beamwidth of the 'wideband' co-delayed circular array beam is frequency-dependent[11] just as in the case of a linear array, but it does offer the advantage of 360° coverage with virtually no attendant beam deformation.

The concept of circular-array phase modes refers to the excitation of the array elements with equal amplitude and a linear-periodic phase taper. The excitation of each 'phase mode' has been shown to form a far-field pattern which, on any conical surface around the array axis, approaches omni-directionality in amplitude with linear

10 The directivity of a radiation pattern is defined as the power per unit solid angle directed at a given direction (ordinarily that of the pattern peak), normalised to $(1/4\pi)$ of the total integrated power. Directivity is commonly expressed in dBi units ('dB above isotropic'), denoting 10 times the logarithm to the base 10 of the above power ratio.

11 This dependence may be reduced by exciting the array through a lens feed or a multiple-beam network, and feeding the outputs to a 'conversion matrix' that linearly combines the interlaced feed outputs.

phase-versus-angle characteristics, whose average gradient depends on the number of excited phase cycles around the array. A phase moding network may be implemented as an analogue Butler matrix or as a digital Discrete Fourier Transform (DFT) unit, and as described in chapter 3, it provides (at least in theory) a convenient basis for multiple-beamforming, direction finding and null steering. The outputs of a phase moding network fed by a circular array share one common property with the outputs of a uniformly-weighted multibeam network connected to a (strictly speaking infinitely long) linear array. Each of the outputs represents an excitation condition under which the electrical (or acoustic) environment of all array elements is identical. This means that although they are all subjected to mutual coupling, their active radiation impedance[12] is the same and can in theory be compensated for by applying the appropriate filters to the network's outputs.

In section 2.2 the far-field radiation pattern for a discrete circular array of co-phased or co-delayed directional elements is formulated and represented as an infinite Fourier series with Bessel function coefficients. The transient effects associated with the reception of short or frequency-coded pulses by a co-delayed circular array are then considered in section 2.3. Finally, the far-field representation for each phase mode pattern as another infinite Fourier series with Bessel coefficients is developed in section 2.4. The result is classic although previous analyses have either treated non-directional elements or have simulated a discrete array by sampling a continuously excited array.

---

12 The active radiation impedance at an input port of an array is the port impedance measured while the array is operational. In terms of coupling coefficients (of a non-operating match-terminated array) it is given by the complex sum of the reflection coefficient at that port and the coupling coefficients to all other ports, each multiplied by the complex weight to be applied to the corresponding array element when operational. In an infinitely-long equi-spaced linear or planar array of identical elements under uniform amplitude and linear phase excitation, as well as in a (finite) equi-spaced circular array of identical radially-symmetric elements under phase-mode excitation, all elements share the same active impedance.

2.2 BEAM-COPHASED EXCITATION

Consider an array of M elements (antenna radiators in an antenna array or acoustic transducers in a sonar array) uniformly arranged on a circle of radius R with radial symmetry, as depicted in *Fig. 2.2.1* which also serves to define the relevant coordinate system. Let the radiation pattern of the m'th array element as functions of direction and frequency be given by $M^{-1/2}\, e^{j(\omega R/c)\sin\theta\cos(\varphi-2\pi m/M)} g_m(\theta, \varphi, \omega)$, where c is the velocity of propagation and ω is the temporal (angular) frequency. In the above expression, the phase term $e^{j(\omega R/c)\sin\theta\cos(\varphi-2\pi m/M)}$ corresponds to the propagation delay from a far-field source to the m'th array element, with the reference point (of zero delay) chosen at the array centre; the remaining functional

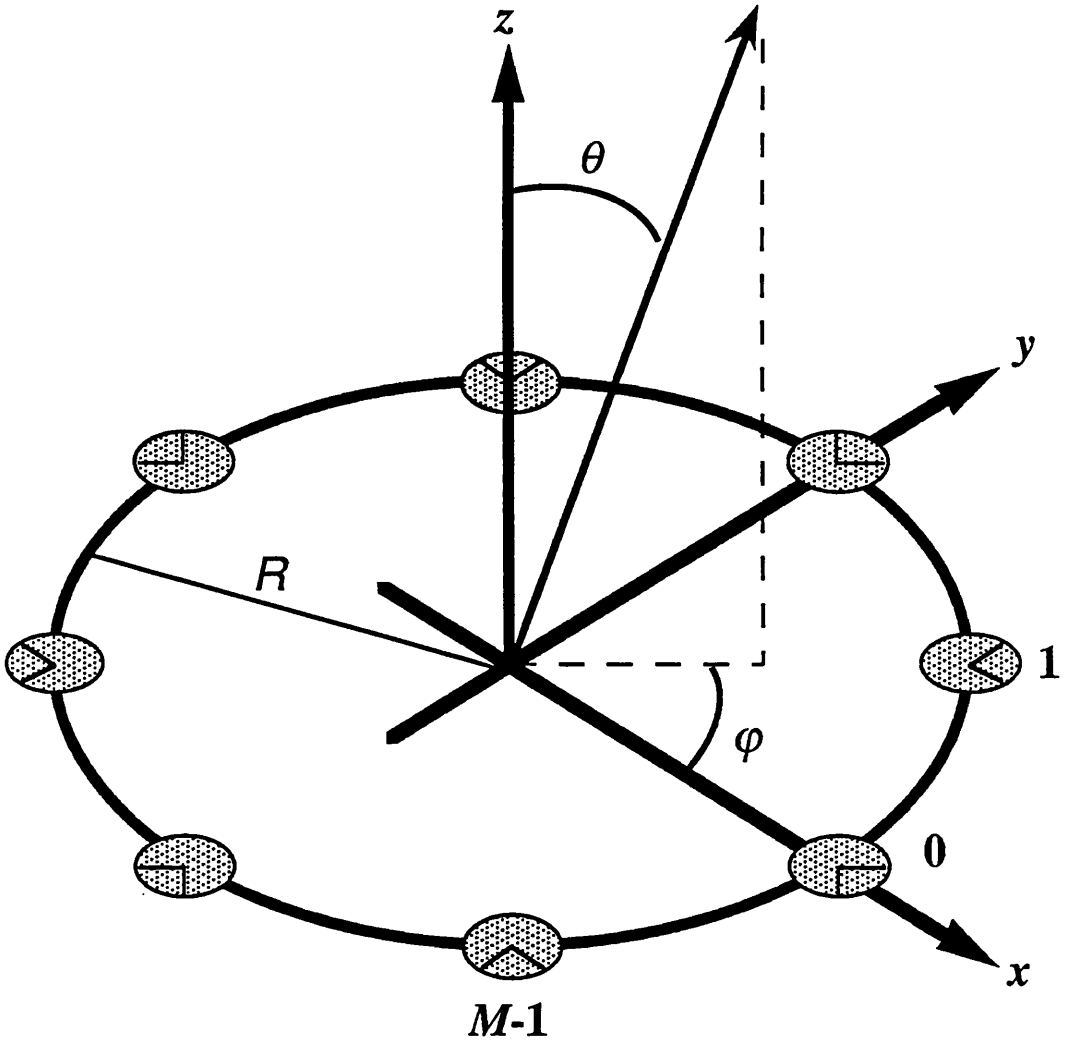

Fig. 2.2.1 Circular array geometry

dependence of the element pattern on direction and frequency is contained in $g_m(\theta, \varphi, \omega)$ with $M^{-1/2}$ serving as a convenient normalising constant. We generally allow $g_m(\theta, \varphi, \omega)$ to become complex, in which case the array elements either have no phase centres, or else these are not stationary with respect to direction and frequency[13]. Assuming that over the relevant frequency band all element patterns are symmetrically identical and frequency-independent, we have:

$$g_m(\theta, \varphi, \omega) = g(\theta, \varphi - 2\pi m/M) \quad , \quad m = 0, 1, \cdots, M-1 \qquad \cdots (2.2.1)$$

and the far-field radiation pattern of the array is given by:

$$F(\theta, \varphi, \omega) = \frac{1}{M} \sum_{m=0}^{M-1} a_m g(\theta, \varphi - 2\pi m/M) e^{j(\omega R/c) \sin\theta \cos(\varphi - 2\pi m/M)} \qquad \cdots (2.2.2)$$

where $\{a_m\}$ is a complex weighting taper applied to the array channels. A directional pattern may be formed by constructively summing the contributions of some or all of the array elements in a given direction. In other words, at the specified frequency, channel phases are set (to within a constant delay) to:

$$\{a_m\} = \{|a_m| e^{-j(\omega R/c) \sin\tilde{\theta} \cos(\tilde{\varphi} - 2\pi m/M)}\} \qquad \cdots (2.2.3)$$

where $(\tilde{\theta}, \tilde{\varphi})$ define the desired beam pointing angle on the (θ, φ) coordinate system of *Fig. 2.2.1*. Such phase setting is known as beam-cophased excitation. If all the array elements are co-phased and uniformly weighted in amplitude, the resulting radiation pattern may be given an alternative representation in terms of Bessel functions of the first kind. Let us first assume that $g(\theta, \varphi)$ is a directional element pattern expressible as the following Fourier series:

$$g(\theta, \varphi) = \sum_{i=-\infty}^{\infty} h_i(\theta) e^{ji\varphi} \qquad \cdots (2.2.4)$$

The expression for the far-field array pattern is then given by,

---

13 A phase centre of an antenna or sonar element is the centre of a coordinate system with respect to which the (unwrapped) far-field phase pattern is either globally constant or has an extremum in a given direction. In the latter case one speaks of a non-stationary or apparent phase centre [Dys 67]. If stationary phase centres do exist, then R is taken as the *electrical* rather than the physical radius of the array, i.e. the radius of the circle on which all phase centres lie.

$$F(\theta, \varphi, \omega) =$$

$$= \frac{1}{M} \sum_{m=0}^{M-1} g(\theta, \varphi - \frac{2\pi}{M} m) e^{j(\omega R/c)[\sin\theta \cos(\varphi - 2\pi m/M) - \sin\tilde{\theta} \cos(\tilde{\varphi} - 2\pi m/M)]}$$

$$= \frac{1}{M} \sum_{i=-\infty}^{\infty} h_i(\theta) e^{ji\varphi} \sum_{m=0}^{M-1} e^{-j(2\pi/M)im} e^{j(\omega R/c)\cos(\vartheta - 2\pi m/M)} \quad \cdots (2.2.5)$$

where:

$$\mathcal{R}(\theta, \varphi, \tilde{\theta}, \tilde{\varphi}) = R[(\sin\theta\cos\varphi - \sin\tilde{\theta}\cos\tilde{\varphi})^2 + (\sin\theta\sin\varphi - \sin\tilde{\theta}\sin\tilde{\varphi})^2]^{1/2}$$

$$= R[\sin^2\theta + \sin^2\tilde{\theta} - 2\sin\theta\sin\tilde{\theta}\cos(\varphi - \tilde{\varphi})]^{1/2} \quad \cdots (2.2.6)$$

$$\mathcal{R}\cos\vartheta = R(\sin\theta\cos\varphi - \sin\tilde{\theta}\cos\tilde{\varphi}) \quad \cdots (2.2.7)$$

$$\mathcal{R}\sin\vartheta = R(\sin\theta\sin\varphi - \sin\tilde{\theta}\sin\tilde{\varphi}) \quad \cdots (2.2.8)$$

But the term $e^{j(\omega\mathcal{R}/c)\cos(\vartheta - 2\pi m/M)}$ on the right hand side of *(2.2.5)* may be represented by the following infinite Bessel series:

$$e^{j(\omega\mathcal{R}/c)\cos(\vartheta - 2\pi m/M)} = \sum_{\nu=-\infty}^{\infty} j^{\nu} J_{\nu}(\omega\mathcal{R}/c) e^{-j\nu(\vartheta - 2\pi m/M)} \quad \cdots (2.2.9)$$

where $J_{\nu}(x)$ denotes a Bessel function of the first kind of order ν and argument x. Substituting in *(2.2.5)* and changing the order of summations we then have:

$$F(\theta, \varphi, \omega) = \frac{1}{M} \sum_{i=-I}^{I} h_i(\theta) e^{ji\varphi} \sum_{\nu=-\infty}^{\infty} j^{\nu} J_{\nu}(\omega\mathcal{R}/c) e^{-j\nu\vartheta} [\sum_{m=0}^{M-1} e^{-j(2\pi/M)(i-\nu)m}]$$

$$\cdots (2.2.10)$$

with I denoting the order of the highest non-vanishing element-pattern Fourier coefficient. Noting that the bracketed term in *(2.2.10)* is equal to:

$$\sum_{m=0}^{M-1} e^{-j(2\pi/M)(i-\nu)m} = M \sum_{q=-\infty}^{\infty} \delta(i - \nu + qM) \quad \cdots (2.2.11)$$

where $\delta(n)$ is the Kronecker delta function,

$$\delta(n) = \begin{cases} 1 & , \quad n=0 \\ 0 & \quad n \neq 0 \end{cases} \qquad \cdots (2.2.12)$$

the expression for $F(\theta, \varphi, \omega)$ takes the form:

$$F(\theta, \varphi, \omega) = \sum_{i=-I}^{I} h_i(\theta)\, e^{j i(\varphi - \vartheta)} \sum_{q=-\infty}^{\infty} j^{i+qM} J_{i+qM}(\omega \mathcal{R}/c) e^{-j qM \vartheta}$$

$$= \sum_{q=-\infty}^{\infty} [\sum_{i=-I}^{I} j^{i+qM} h_i(\theta) J_{i+qM}(\omega \mathcal{R}/c) e^{j i(\phi - \vartheta)}]\, e^{-j qM \vartheta}$$

$$= \sum_{q=-\infty}^{\infty} K_q(\omega, \theta, \varphi) e^{-j qM \vartheta} \qquad \cdots (2.2.13)$$

where:

$$K_q(\omega, \theta, \varphi) = \sum_{i=-I}^{I} j^{i+qM} h_i(\theta) J_{i+qM}(\omega \mathcal{R}/c) e^{j i(\phi - \vartheta)} \qquad \cdots (2.2.14)$$

and use has also been made of the identity:

$$j^{-\nu} J_{-\nu}(\alpha) = j^{\nu} J_{\nu}(\alpha) \qquad \cdots (2.2.15)$$

For the special case of element patterns that are omnidirectional in φ, the expression for the far-field pattern simplifies to:

$$F(\theta, \varphi, \omega) = h_0(\theta) \sum_{q=-\infty}^{\infty} j^{qM} J_{qM}(\omega \mathcal{R}/c) e^{-j qM \vartheta}$$

$$= h_0(\theta)[J_0(\omega \mathcal{R}/c) + 2 \sum_{q=1}^{\infty} j^{qM} J_{qM}(\omega \mathcal{R}/c) \cos(qM\vartheta)] \qquad \cdots (2.2.16)$$

which, save for the $h_0(\theta)$ element pattern variation in elevation, comprises simply the zero-order Bessel function $J_0(\omega \mathcal{R}(\theta, \phi, \tilde{\theta}, \tilde{\varphi})/c)$, distorted by an infinite series of higher order terms.

Assuming that the desired beam peak is set to lie on the azimuth ($\theta=\pi/2$) plane[14], the array azimuth pattern is approximately given by:

$$\theta=\tilde{\theta}=\pi/2 \;\Rightarrow\; \begin{aligned}\mathcal{R}/R &= [(\cos\varphi-\cos\tilde{\varphi})^2 + (\sin\varphi-\sin\tilde{\varphi})^2]^{1/2} \\ &= 2\sin[(\varphi-\tilde{\varphi})/2]\end{aligned}$$

$$F(\varphi,\omega) \approx J_0[2(\omega R/c)\sin\frac{\varphi-\tilde{\varphi}}{2}]$$

whereas in the main elevation plane,

$$\tilde{\theta}=\pi/2\ ,\ \varphi=\tilde{\varphi} \;\Rightarrow\; \begin{aligned}\mathcal{R}/R &= [(\sin\theta\cos\varphi-\cos\varphi)^2 + (\sin\theta-\sin\varphi-\sin\varphi)^2]^{1/2} \\ &= 1-\sin\theta\end{aligned}$$

and the elevation pattern is thus approximated by the expression:

$$F(\theta,\omega) \approx h_0(\theta)\, J_0[(\omega R/c)(1-\sin\theta)]$$

Note that strictly speaking expression *(2.2.3)* defines a 'co-delayed' rather than a 'co-phased' excitation taper, by which we mean that the array remains properly compensated regardless of the operating frequency. In the case of narrowband co-phased excitation at frequency ω_0, $\mathcal{R}$ and ϑ must be redefined as follows:

$$\mathcal{R} = R[\sin^2\theta + (\omega_0/\omega)^2\sin^2\tilde{\theta} - 2\frac{\omega_0}{\omega}\sin\theta\sin\tilde{\theta}\cos(\varphi-\tilde{\varphi})]^{1/2} \quad \cdots (2.2.17)$$

$$\mathcal{R}\cos\vartheta = R(\sin\theta\cos\varphi - \frac{\omega_0}{\omega}\sin\tilde{\theta}\cos\tilde{\varphi}) \quad \cdots (2.2.18)$$

$$\mathcal{R}\sin\vartheta = R(\sin\theta\sin\varphi - \frac{\omega_0}{\omega}\sin\tilde{\theta}\sin\tilde{\varphi}) \quad \cdots (2.2.19)$$

and the two special cases considered above are respectively modified to:

$$F(\varphi,\omega) \approx J_0\{(\omega_0 R/c)[(\frac{\omega}{\omega_0}-1)^2+4(\omega/\omega_0)\sin^2(\frac{\varphi-\tilde{\varphi}}{2})]^{1/2}\}$$

and

$$F(\theta,\omega) \approx h_0(\theta)J_0\{(\omega_0 R/c)\,|(\omega/\omega_0)\sin\theta - 1|\}$$

---

14 Any other setting of $\tilde{\theta}$ would by symmetry also apply to $(\pi-\tilde{\theta})$ leading to a wider or even partly-split beam in elevation

In practice not all the elements of a circular array are excited for the formation of a co-phased or co-delayed beam in a given direction. Since element patterns in an array environment are in general outward-directional, it is often wiser to generate the required beam using a typical aperture sector of 90° to 120° facing the specified beam pointing direction so that backward radiation in the form of sidelobes is reduced. A further reduction in sidelobe level may be achieved by the symmetric application of amplitude weighting, phase weighting or both[15], although mode-space beamforming described in chapter 3, presents a more systematic approach to pattern synthesis. A major drawback in the beam cophased architecture lies in the interlaced sector feeding and switching needed for multiple beamforming[16] and beam scanning respectively. The latter arrangement is exemplified by *Fig. 2.2.2* which schematically describes a 120° switched feeding configuration for a 24-element circular phased array.

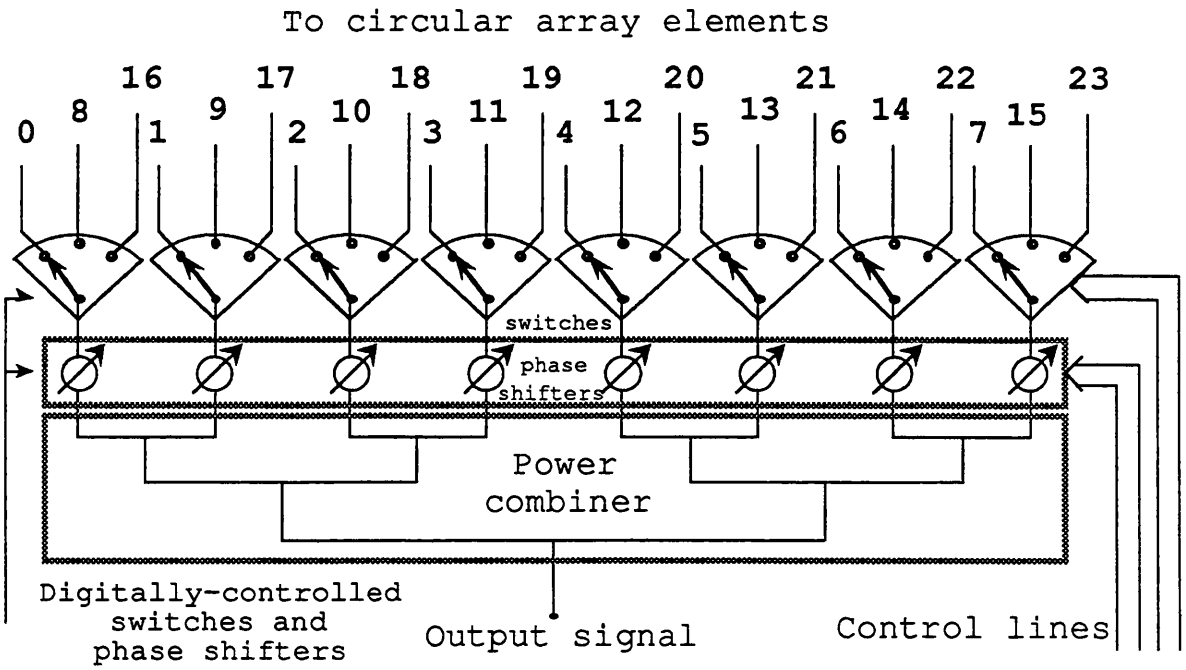

Fig. 2.2.2 Feeding matrix for a 24-element circular phased array

15 A number of papers dealing with co-phased pattern synthesis and sidelobe reduction have appeared in the 1960s and '70s – see for example [FEN 65].

16 At microwave frequencies multiple cophased beams for circular antenna arrays are conveniently generated via two-dimensional spatial feed in the form of an electromagnetic R2R or RKR lens. Full 360° coverage by the same array, however, requires the combination of 2 identical lenses through a set of hybrid coupler devices.

2.3 TRANSIENT EFFECTS

When the bandwidth of the received signals is of the same order of, or greater than the reciprocal of the propagation delay across the array (as may be the case in the reception of frequency-coded or short CW pulses), the radiation performance of the array cannot be satisfactorily represented by its steady-state array pattern at a single frequency. The true time-varying response of the array depends on the characteristics of the received pulse as well as on the frequency dependence of the array radiation pattern.

Qualitatively, the transient effects associated with the reception of a short CW pulse are fairly simple to visualise. Pulsed signals incident at the different elements of the array are in general temporally displaced depending on the array geometry and on the relative direction of the radiation source. Unless these delays are negligible compared with the duration of the pulses, they may not all overlap in time – this is depicted in *Fig. 2.3.1* for the case of a 4-element semi-circular array. Without appropriate compensation, the radiation pattern of the array will consequently be distorted by the fact that contributions from the array elements do not occur simultaneously, or equivalently by the frequency-dependent phase differences between the summed signals which make up the array response over the whole bandwidth of the pulse.

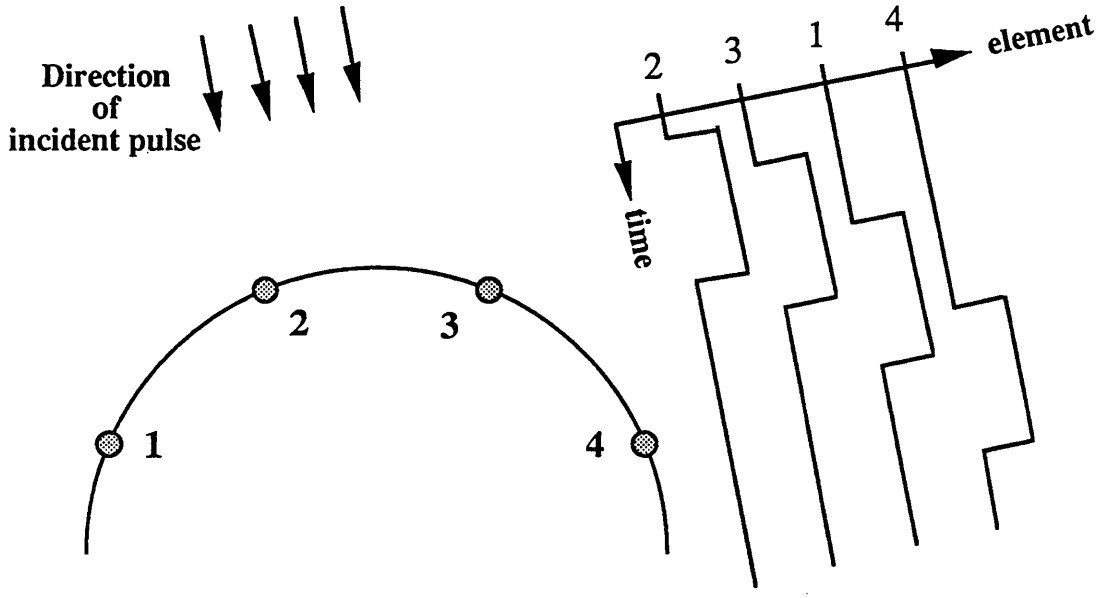

Fig. 2.3.1 Reception of a CW pulse whose duration is not much greater than the propagation delay across the array

A common method for the wideband compensation of either a linear array or a circular beam-cophased array is by the implementation of true time delays at the array channels. In the case of an M-element circular array of radius R the required delays (to within a constant delay) are:

$$\tilde{\tau}_m = (R/c)\sin\tilde{\theta}\cos(\tilde{\varphi}-\frac{2\pi}{M}m) \qquad 0\leq m\leq M-1 \qquad \cdots (2.3.1)$$

where $(\tilde{\theta}, \tilde{\varphi})$ define the direction for which the array is to be delay-matched and c is the velocity of propagation. These delays may be realised by using physical transmission line sections or, when digital beamforming architecture is employed, by utilising previously stored data samples in conjunction with interpolation filters for the reduction of delay quantisation errors. If the array is delay-matched to the direction of arrival of the signal, then at the beam peak direction all contributions are coherent and occur simultaneously. However, if a signal pulse hits the array from any other direction, especially well away from the main beam, channel contributions will once more depart from proper temporal alignment and will no longer be simultaneously processed. Depending on the shape and duration of the received pulse this delay mis-match may degrade the sidelobe performance of the array.

For a more quantitative examination of a circular array response to a short CW pulse, let us consider the following signal travelling towards the array of *Fig. 2.2.1* from direction (θ, φ):

$$p(t) = \Pi(t)e^{j\omega_0 t} \qquad \cdots (2.3.2)$$

where $\Pi(t)$ denotes the waveform envelope (a rectangular pulse, a shaped pulse etc.) and ω_0 is the carrier (angular) frequency. At the m'th array element the received signal is given in the frequency domain by $g_m(\theta, \varphi, \omega)\int_{-\infty}^{\infty} dt' p(t'-t_c-t_m)e^{-j\omega t'}$ where $g_m(\theta, \varphi, \omega)$ is the radiation pattern of that element, t_c denotes the time of pulse arrival at the array centre and t_m is given by:

$$t_m = \tilde{\tau}_m - (R/c)\sin\theta\cos(\varphi-2\pi m/M) \qquad \cdots (2.3.3)$$

The summed response of the whole array is given by:

$$\hat{P}(\theta, \varphi, \omega) = e^{-j\omega t_c}\hat{\Pi}(\omega-\omega_0)F(\theta, \varphi, \omega) \qquad \cdots (2.3.4)$$

where $\hat{\Pi}(\omega)$ is the Fourier transform of the waveform $\Pi(t)$ and for a given set $\{a_m\}$ of applied shading coefficients, $F(\theta, \varphi, \omega)$ is the steady-state array pattern given by

$$F(\theta, \varphi, \omega) = \frac{1}{M}\sum_{m=0}^{M-1} a_m g_m(\theta, \varphi, \omega) e^{-j\omega t_m} \qquad \cdots (2.3.5)$$

The time-domain array response is therefore given by,

$$P(\theta, \varphi, t) = \frac{e^{j\omega_0(t-t_c)}}{2\pi}\int_{-\infty}^{\infty} d\omega e^{j\omega(t-t_c)} F(\theta, \varphi, \omega+\omega_0)\hat{\Pi}(\omega) \qquad \cdots (2.3.6)$$

From *(2.3.6)* it is clear that if to within some delay response $e^{-j\omega t_d}$, $F(\theta, \varphi, \omega+\omega_0)$ can be made approximately frequency invariant over the bandwidth of $\hat{\Pi}(\omega)$,

$$F(\theta, \varphi, \omega+\omega_0) \approx e^{-j\omega t_d} F(\theta, \varphi) \qquad \cdots (2.3.7)$$

then:

$$P(\theta, \varphi, t) \approx F(\theta, \varphi) p(t-t_c-t_d) e^{j\omega_0 t_d} \qquad \cdots (2.3.8)$$

and the steady-state array radiation pattern applies. An inspection of *(2.3.5)* reveals (as expected) that this indeed is what beam co-delayed excitation sets out to achieve. By requiring that in the direction of the main beam:

$$t_m = 0 \quad , \quad 0 \le m \le M-1$$

$F(\tilde{\theta}, \tilde{\varphi}, \omega+\omega_0)$ is made dependent only on the frequency response of the element patterns, which is assumed to be fairly flat over the relevant band. Away from the main beam direction $F(\theta, \varphi, \omega+\omega_0)$ *is* frequency dependent and should be characterised by low sidelobes over the whole bandwidth of $\hat{\Pi}(\omega)$ for the sidelobe level of $P(\theta, \varphi, t)$ to remain low. Omnidirectional delay matching is possible, but as we show in chapter 3, it requires each array beam to be synthesised from wideband aligned phase modes. Phase modes are reviewed and discussed in section 2.4 of this chapter; their broadband alignment is treated in section 3.5 of chapter 3.

Transient phenomena may also (and are more likely to) result from the (equalised) reception of frequency-coded pulses. For an examination a circular-array response to a linear FM pulse, refer to appendix B.1.

2.4 PHASE-MODE EXCITATION

Phase mode excitation refers to the excitation of circular-array elements with uniform amplitude but with a linear phase sequence which obeys the periodicity condition, allowing only an integer number of 360° phase cycles around the array – see *Fig. 2.4.1*. For a radially-symmetric ring array of M elements whose frequency-independent patterns are symmetrically identical and denoted by *(2.2.1)*, the μ'th far-field phase mode pattern $\Phi_\mu(\theta, \varphi, \omega)$ is expressible as the following sum:

$$\Phi_\mu(\theta, \varphi, \omega) = \frac{1}{M}\sum_{m=0}^{M-1} g\,(\theta, \varphi - 2\pi m/M)\, e^{-j[(2\pi/M)\mu m - (\omega R/c)\sin\theta\cos(\varphi - 2\pi m/M)]} \qquad \cdots (2.4.1)$$

which, under the Fourier series representation *(2.2.4)* for the element patterns, may be rewritten as:

$$\begin{aligned}\Phi_\mu(\theta, \varphi, \omega) &= \frac{1}{M}\sum_{m=0}^{M-1}\Big[\sum_{i=-I}^{I} h_i(\theta) e^{j(\varphi - 2\pi m/M)i}\Big] e^{-j[(2\pi/M)\mu m - (\omega R/c)\sin\theta\cos(\varphi - 2\pi m/M)]} \\ &= \frac{1}{M}\sum_{i=-I}^{I} h_i(\theta) e^{j i \varphi} \sum_{m=0}^{M-1} e^{-j(2\pi/M)(\mu+i)m} e^{j(\omega R/c)\sin\theta\cos(\varphi - 2\pi m/M)}\end{aligned} \qquad \cdots (2.4.2)$$

with I denoting the maximum non-vanishing element-pattern coefficient in *(2.2.4)*. A simpler though quite useful representation for the element pattern is the following:

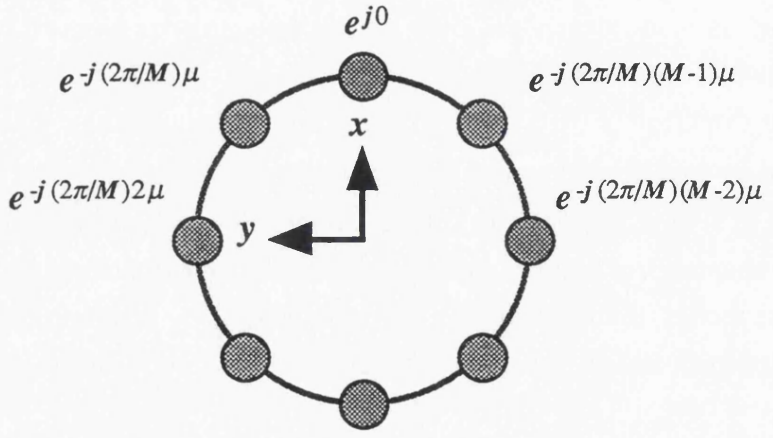

Fig. 2.4.1 Phase mode excitation of mode no. μ

$$g(\theta, \varphi) = h_0(\theta)\rho^{(1-\sin\theta\cos\varphi)} \quad , \quad \rho > 0 \qquad \cdots (2.4.3)$$

with $h_0(\theta)$ denoting an arbitrary elevation dependence, for which the corresponding array pattern is –

$$\Phi_\mu(\theta, \varphi, \omega) = \frac{\rho h_0(\theta)}{M} \sum_{m=0}^{M-1} e^{-j(2\pi/M)\mu m} e^{j[(\omega R/c)+j\ln\rho]\sin\theta\cos(\varphi-2\pi m/M)} \qquad \cdots (2.4.4)$$

The term $e^{j(\omega R/c)\sin\theta\cos(\varphi-2\pi m/M)}$ which appears in *(2.4.2)* is expressible as the following infinite Bessel series:

$$e^{j(\omega R/c)\sin\theta\cos(\varphi-2\pi m/M)} = \sum_{\nu=-\infty}^{\infty} j^\nu J_\nu\left(\frac{\omega R}{c}\sin\theta\right) e^{-j\nu(\varphi-2\pi m/M)} \qquad \cdots (2.4.5)$$

Substituting in *(2.4.2)* and changing the order of summations we have:

$$\Phi_\mu(\theta, \varphi, \omega) =$$

$$\sum_{i=-I}^{I} h_i(\theta) \sum_{\nu=-\infty}^{\infty} j^\nu J_\nu\left(\frac{\omega R}{c}\sin\theta\right) e^{j(i-\nu)\varphi} \left[\frac{1}{M}\sum_{m=0}^{M-1} e^{-j(2\pi/M)(\mu+i-\nu)m}\right] \qquad \cdots (2.4.6)$$

The bracketed term in *(2.4.6)* is equal to zero or to 1 according to the values of m, i and ν:

$$\frac{1}{M}\sum_{m=0}^{M-1} e^{-j(2\pi/M)(\mu+i-\nu)m} = \sum_{q=-\infty}^{\infty} \delta(\mu+i-\nu+qM) \qquad \cdots (2.4.7)$$

The expression for $\Phi_\mu(\theta, \varphi, \omega)$ therefore takes the form:

$$\Phi_\mu(\theta, \varphi, \omega) = \sum_{i=-I}^{I} h_i(\theta) \sum_{q=-\infty}^{\infty} j^{\mu+i+qM} J_{\mu+i+qM}\left(\frac{\omega R}{c}\sin\theta\right) e^{-j(\mu+qM)\varphi}$$

$$= \sum_{q=-\infty}^{\infty} \left[\sum_{i=-I}^{I} j^{\mu+i+qM} h_i(\theta) J_{\mu+i+qM}\left(\frac{\omega R}{c}\sin\theta\right)\right] e^{-j(\mu+qM)\varphi}$$

$$= \sum_{q=-\infty}^{\infty} C_{\mu q}(\omega, \theta) e^{-j(\mu+qM)\varphi} \qquad \cdots (2.4.8)$$

where $C_{\mu q}(\omega, \theta)$ is the frequency-dependent phase mode coefficient of order q for the μ'th phase mode, and is given by:

$$C_{\mu q}(\omega, \theta) = \sum_{i=-I}^{I} j^{\mu+i+qM} h_i(\theta) J_{\mu+i+qM}[(\omega R/c)\sin\theta] \qquad \cdots (2.4.9)$$

The far-field pattern of a phase mode is thus expressible as a sum of the form

$$\Phi_\mu(\theta, \varphi, \omega) = \sum_{q=-\infty}^{\infty} C_{\mu q}(\omega, \theta) e^{-j(\mu+qM)\varphi} \qquad \cdots (2.4.10)$$

which may be viewed as the azimuthally-omnidirectional linear-phase pattern $C_{\mu 0}(\omega, \theta)e^{-j\mu\varphi}$, distorted by an infinite series of higher order terms[17]. Note that *(2.4.10)* still applies when element patterns of the form *(2.4.3)* are assumed, only each phase mode coefficient is given by (see appendix B.2 for details):

$$C_{\mu q}(\omega, \theta) = \rho h_0(\theta) j^{(\mu+qM)} J_{\mu+qM}[(\frac{\omega R}{c} + j\ln\rho)\sin\theta] \qquad \cdots (2.4.11)$$

For array elements that are omnidirectional in azimuth, we have $h_i = 0$, $i \neq 0$ in *(2.2.4)*, or equivalently $\rho = 1$ in *(2.4.3)*, both of which lead to:

$$C_{\mu q}(\omega, \theta) = j^{\mu+qM} h_0(\theta) J_{\mu+qM}(\frac{\omega R}{c}\sin\theta) \qquad \cdots (2.4.12)$$

Since *(2.4.12)* also applies to the dominant $q = 0$ mode, whenever the frequency and the array radius are such that $J_\mu(\frac{\omega R}{c})$ hits one of its zeros, there will effectively be a 'hole' in the far-field circumferential coverage of that mode around elevation zero ($\theta = \pi/2$). In the vicinity of the zero, the far-field azimuth pattern is not completely cut out, but ripple from higher order terms (especially those characterised by $q = \pm 1$) will dominate, and thus limit the practical usefulness of that mode. If on the other hand the element patterns are of the form:

---

17 The original motivation for considering the zero-order term as dominant stems from the corresponding analysis of a continuously-distributed circular-array source under linear-phase excitation [Dav 83], [Jon 90] where the far-field pattern for the μ'th mode is seen to be given by $j^\mu J_\mu[(\omega R/c)\sin\theta]e^{-j\mu\varphi}$. In the case of a circular array of discrete but closely spaced elements (an inter-element spacing of less than half a wavelength), higher order modes (though not necessarily the first one) will indeed die out by virtue of the asymptotic properties of a Bessel function whose order is much greater than its argument.

$$g(\theta, \varphi) = g_\theta(\theta)\cos^2\frac{\varphi}{2} = g_\theta(\theta)[\frac{1}{2}+\frac{1}{2}\cos\varphi]$$

then,

$$C_{\mu q}(\omega, \theta) =$$

$$\frac{j^{\mu+qM}}{2} g_\theta(\theta)\{J_{\mu+qM}(\frac{\omega R}{c}\sin\theta) + \frac{j}{2}[J_{\mu+qM+1}(\frac{\omega R}{c}\sin\theta) - J_{\mu+qM-1}(\frac{\omega R}{c}\sin\theta)]\}$$

$$= \frac{j^{\mu+qM}}{2} g_\theta(\theta)[J_{\mu+qM}(\frac{\omega R}{c}\sin\theta) - jJ'_{\mu+qM}(\frac{\omega R}{c}\sin\theta)] \qquad \cdots (2.4.13)$$

where $J_\nu'(\cdot)$ signifies the derivative of the Bessel function of the first kind with respect to its argument. Since the zeros of $J_\nu(\cdot)$ and of $J_\nu'(\cdot)$ do not coincide for any ν, it follows that for this type of element pattern the phase mode coefficients never fall to zero. In fact noting that the zeros of a Bessel function of integer order are always real it follows that any element pattern of the form *(2.4.3)* which is either outward-directional ($\rho < 1$) or even inward-directional ($\rho > 1$) leads to phase mode coefficients *(2.4.11)* that never fall to zero.

One last result relates to symmetric element patterns given either by *(2.4.3)* or by *(2.2.4)* with:

$$h_i(\theta) = h_{-i}(\theta) \quad , \quad i > 0$$

The phase mode coefficients of symmetric modes are then related by:

$$C_{(-\mu)(-q)} = \sum_{i=-I}^{I} j^{-\mu-i-qM} h_i(\theta)\, J_{-\mu-i-qM}[(\omega R/c)\sin\theta] = C_{\mu q} \qquad \cdots (2.4.13)$$

as can also be directly deduced from *(2.4.11)*, where use has been made of the Bessel identity *(2.2.15)*. Consequently if $\Phi_\mu(\theta, \varphi, \omega)$ is given by *(2.4.10)* then the corresponding expression for $\Phi_{-\mu}(\theta, \varphi, \omega)$ is:

$$\Phi_{-\mu}(\theta, \varphi, \omega) = \sum_{q=-\infty}^{\infty} C_{\mu q}(\omega, \theta) e^{j(\mu+qM)\varphi} \qquad \cdots (2.4.14)$$

In the next chapter we shall show how the above symmetry may be used in phase-comparison direction finding without resorting to mode alignment. Another important point to note is that by symmetry, the phase-mode coefficients for modes $\mu = M/2$ and

$\mu = -M/2$ (when M is even) are the same, and both mode terms are 'available' in $\Phi_{\pm M/2}(\theta, \varphi, \omega)$, constituting a far-field pattern that is very different in both amplitude and phase from the desired linear-phase omnidirectional pattern[18]:

$$\Phi_{\pm M/2}(\theta, \varphi, \omega) \approx C_{(M/2)\,0}(\omega, \theta)[e^{j(M/2)\,\varphi} + e^{-j(M/2)\,\varphi}] = 2C_{(M/2)\,0}(\omega, \theta)\cos(M\varphi/2)$$

2.5 CONCLUDING REMARKS

In this chapter we have reviewed the beam-cophased and phase-mode excitation methods for circular arrays. The first approach, although a direct extension of linear-array beamforming, does not lend itself to systematic pattern synthesis techniques and is quite awkward to incorporate in a scanning array system. We have seen that even when delay-matched, transient effects may alter the designed sidelobe performance of the array. A beam-cophased array of reciprocal transducers is also susceptible to aperture excitation errors due to the combined effect of inter-element coupling and feed network back coupling.

The alternative approach of transforming from 'element space' onto 'phase-mode space' provides us with a set of (possibly rippled) omnidirectional patterns, each characterised by a linear far-field phase. Although we have hitherto considered the synthesis of a single phase-mode pattern from an M-element circular array, it is simple in principle to simultaneously generate up to M independent phase modes with the aid of an analogue Butler-type matrix, or through a spatial Discrete Fourier Transform (DFT) operation on the digitised outputs of the array sensors. Phase modes are affected by mutual coupling, but since they each place all the array elements under identical periodic boundary conditions, the outcome is that each phase mode simply 'acquires' a new complex coefficient which is correctable through re-calibration. Properly aligned phase modes may be weighted and linearly combined according to well established linear-array synthesis techniques, to form directional beams. This well known technique together with other existing schemes and some new related ideas, such as directional phase mode beams and omnidirectional delay matching, are discussed next in chapter 3.

---

18 The summed pair of oppositely-numbered phase modes is sometimes called *an amplitude mode.* The case of $\mu = M/2$ is unique in that both phase modes appear at the same output port already in amplitude-mode form.

3. CONVENTIONAL MODE-SPACE TECHNIQUES AND APPLICATIONS

3.1 GENERAL

Circular array phase modes provide a convenient basis for a number of interesting antenna and sonar array applications. Their most common use is in multimodal direction finding where the phases of several pairs of excited modes are detected and compared, achieving the angular accuracy of larger amplitude-comparison (multibeam) DF systems[1]. Other conventional techniques[2] include the phased addition of adjacent modes to form patterns with phase-controlled steerable nulls, as a way of suppressing co-channel interference, and directional beamforming where phase modes are weighted, phased and combined by essentially linear-array feeders. Sections 3.2, 3.3 and 3.4 of this chapter are devoted to a short review of these schemes. The usefulness of the latter two depends on the broadband alignment of the phase modes, which calls for the separate deconvolution of their dominant coefficients. It is worth noting that once such wideband alignment is successfully implemented, the array becomes circumferentially delay-matched for incident pulses of lower bandwidth.

In mode-space beamforming a set of excited phase modes is treated, after some angular transformation, as omnidirectional elements of a fictitious linear array, where all phase modes are assumed to be aligned and distortions due to higher order modes are neglected. The modes are linearly combined using linear-array synthesis

1 In the traditional circular-array amplitude-comparison DF system the array is fed by a multiple beam-cophased network (normally an RKR electromagnetic lens in the case of microwave antennas), in conjunction with a beamwidth-stabilising sidelobe-reducing interlaced conversion matrix. The attained angular resolution of the system is a function of beamwidth which in turn depends on the array dimensions. In contrast, the angular resolution obtainable from a multimodal array may actually improve (due to reduced ripple) when the array radius is decreased (up to a limit below which radiation efficiency drastically drops)

2 The term *conventional* is used here to distinguish from high-resolution methods which are discussed in chapter 5.

techniques (for, say, sidelobe suppression), and under broadband mode alignment, the generated beams remain unchanged with frequency. The essence of this well known concept and a convenient technique for exciting a multiple set of directional beams are briefly recalled, together with a number of examples, in section 3.2.

Multimodal direction finders detect and compare the phases of pairs of phase modes, utilising the approximate linear-phase characteristics of their far-field patterns to provide an output voltage that is linearly proportional to the angular location of a single far-field source. It is commonly accepted that to within an angular ambiguity of 180°, no mode alignment or look-up calibration tables are theoretically required. In section 3.3 we show that under some reasonable and easily verifiable assumptions, the above angular ambiguity may in fact be eliminated.

Mode-space null-steering is based, as described in section 3.4, on a tree arrangement that starts by the phased subtraction of adjacent phase modes and continues, if desired, by a similar subtraction of adjacent output beams[3]. Provided the subtracted modes are properly aligned, this scheme yields far-field patterns with one independently-steered null per stage. The incorporation of a null-forming network in a DF system may provide an iterative (though non-adaptive) direction finder that can handle a multiple source environment [CVE 88a], [CVE 88b].

In section 3.5 we introduce a new type of beams which we name *sectoral phase modes*. A sectoral phase mode is a directional beam with phase-mode-like phase behaviour, which may be synthesised by a linear combination of omnidirectional phase modes that have been equalised over the relevant frequency band. Sectoral phase modes allow the phase-mode concept to be confined to a single or multiple angular sectors instead of the usual omnidirectional phase-mode coverage. A single-sector implementation may be used to limit the spatial sensitivity of a circular array to a given (possibly large) angular zone, whereas multiple-sector applications include phase-comparison direction-finding with enhanced immunity to interference and sectorally-controlled multibeam null-steering.

The question of bandwidth is finally dealt with in section 3.6, which includes a somewhat academic search for the 'optimal' element pattern, but also a discussion on the viability and design considerations for a set of stable phase mode filters. The chapter concludes with a summary of the main techniques, their advantages and possible limitations.

---

3 The outputs of stage 1 are wide mode-space beams, each formed by two phase modes, those of stage 3 are a linear combination of three phase modes, etc.

3.2 DIRECTIONAL MULTIBEAM EXCITATION

Approximating a set of phase mode patterns $\{\Phi_\mu(\theta, \varphi, \omega)\}_{\mu=-\Lambda}^{\Lambda}$ by:

$$\Phi_\mu(\theta, \varphi, \omega) \approx C_{\mu 0}(\omega, \theta) e^{-j\mu\varphi} \quad , \quad -\Lambda \leq \mu \leq \Lambda \qquad \cdots (3.2.1)$$

where the coefficients $\{C_{\mu 0}\}_\mu$ are all non-zero, enables one to use linear array techniques to synthesise a low-sidelobe $(2\Lambda+1)$-"element" directional beam in any direction [DAV 65]. The application of a linear array aperture taper to form the weighted sum of distortionless phase modes, each normalised to its zero-order coefficient $C_{\mu 0}$, results in a radiation pattern that is identical to the array factor of the corresponding linear array but with the following coordinate transformation:[4]

$$2\pi(d/\lambda)\sin\varphi \text{ [linear array]} \rightarrow \varphi \text{ [circular array]} \qquad \cdots (3.2.2)$$

where d is the inter-element spacing for the linear array. This means that as long as *(3.2.1)* holds, the resulting array pattern is independent of frequency, provided a way is found to flatten out the frequency responses of all the zero-order mode coefficients. As previously noted, a multiple set of $(2\Lambda+1)$ phase modes may be generated from an M-element circular array with the aid of an $M\times(2\Lambda+1)$ analogue Butler matrix, or its digital equivalent of a spatial DFT unit. Cascading the modeforming unit with an array of deconvolving filters, a set of weights $\{\alpha_\mu\}$[5] and an inverse DFT unit (assuming digital implementation), as schematically illustrated in *Fig. 3.2.1*, results in the simultaneous excitation of M (possibly broadband) radiation patterns[6]

$$F_m(\varphi) \approx \frac{1}{M^{1/2}} \sum_{\mu=-\Lambda}^{\Lambda} \alpha_\mu e^{-j\mu(\varphi - 2\pi m/M)} \quad , \quad 0 \leq m \leq M-1 \qquad \cdots (3.2.3)$$

with respective beam pointing directions $\{\varphi_m = 2\pi m/M\}$. One possible implementation for each of the digital filters in *Fig. 3.2.1* is illustrated in *Fig. 3.2.2*, where two temporal DFT units are used to divide the frequency band into N_ω separately aligned bins with complex weights $\{\mathcal{H}_{\mu n}\}$ which are given by:

---

4 We refer here to the radiation pattern on the xy-plane from a circular array lying on the same plane and from a linear array lying parallel to the y-axis.

5 Each weighting unit may in fact be incorporated with the corresponding mode filter.

6 We assume a constant elevation cut (say, $\theta = 90°$) for both the deconvolution of the phase mode coefficients and for the radiation patterns.

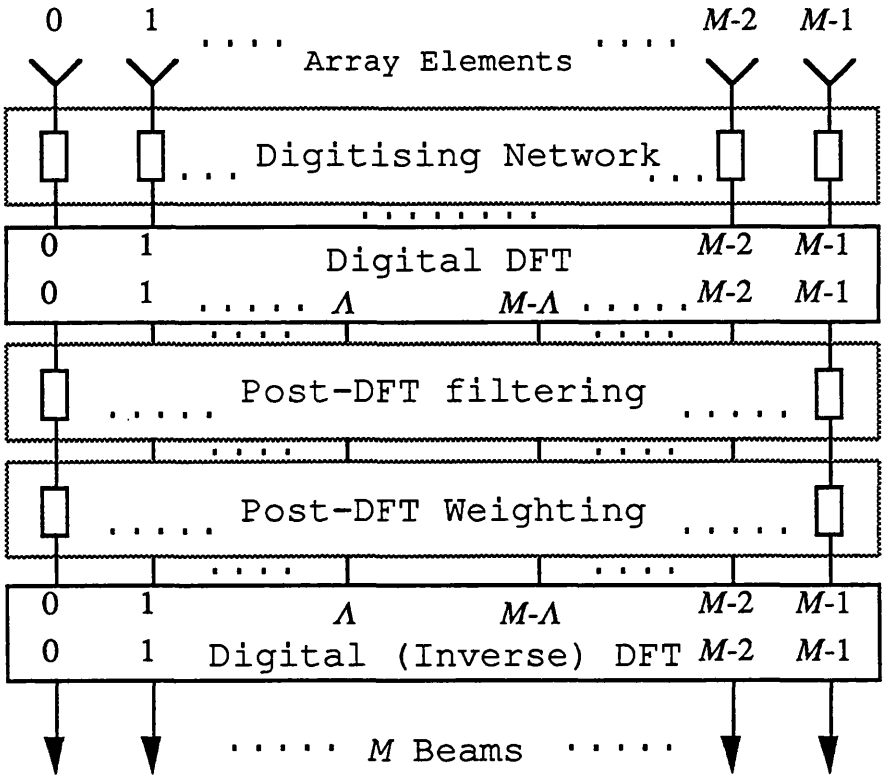

Fig. 3.2.1 Digital multibeam network

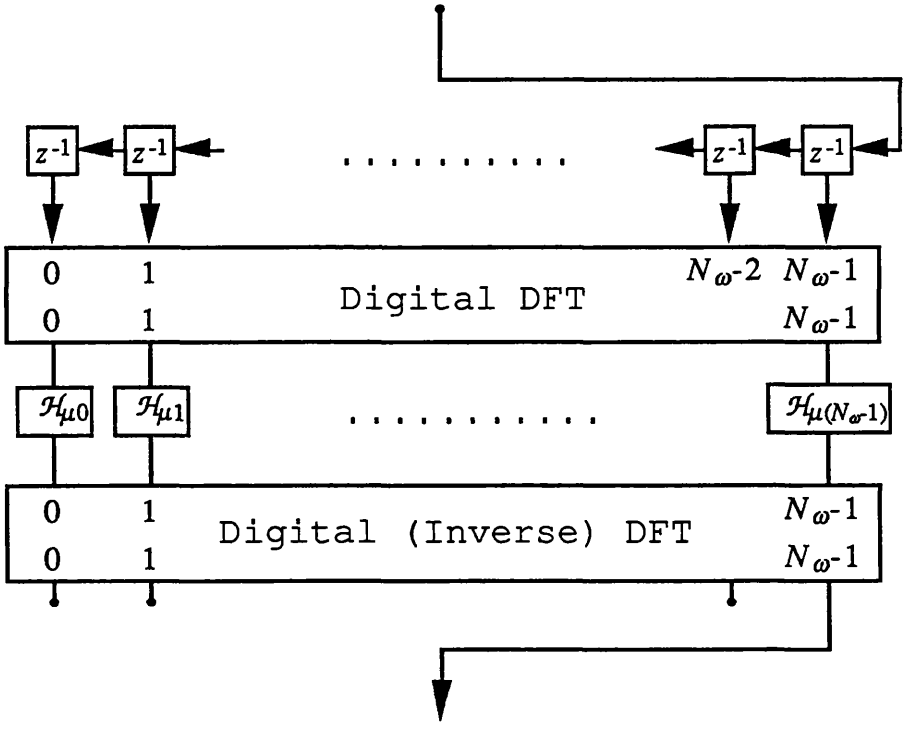

Fig. 3.2.2 FIR filtering unit for the μ'th phase mode

$$\mathcal{H}_{\mu n} = 1/C_{\mu 0}(\omega = n\omega_s/N_\omega,\ \theta = \pi/2) \quad , \quad 0 \le n \le N_w\text{-}1 \qquad \cdots (3.2.4)$$

where ω_s is the (angular) sampling frequency. However the Fourier transform of $1/C_{\mu 0}(\omega\,,\ \theta = \pi/2)$ is not necessarily finite in its extent, and consequently the required order N_ω for this finite impulse response (FIR) approach (as well as other FIR filter realisations) may become excessively large (see for example [OPP 76]).[7] Alternatively, the order of an IIR (infinite impulse response) filter realisation is shown in section 3.6 to depend on the Fourier transform of $C_{\mu 0}(\omega\,,\ \theta = \pi/2)$ whose extent is indeed finite.

Let us now return to expression *(3.2.3)* for the approximate far-field pattern of mode-space radiation beams. Such a multiple set of beams with a reduced sidelobe level is displayed in *Fig. 3.2.3* for the case of an array of 7 directional elements at 0.456-wavelengths spacing[8], using a set of 5 aligned phase modes ($\mu = -2$ to 2), pre-weighted as follows:

Mode	-2	-1	0	1	2
Weights	-10.5 dB	-2.3 dB	0 dB	-2.3 dB	-10.5 dB

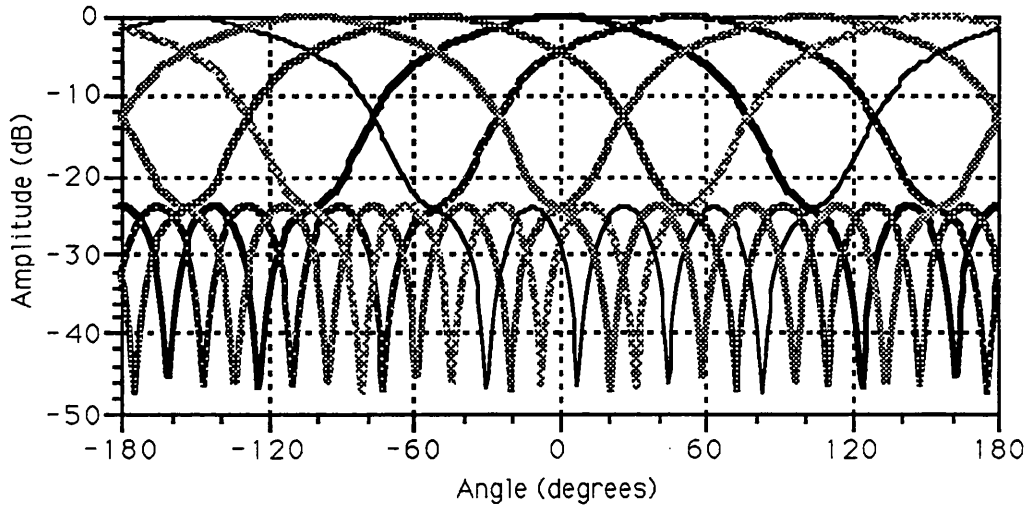

Fig. 3.2.3 Multibeam pattern formed by 5 weighted modes from a 7-element array ($R = 0.508\lambda$, $g_\varphi(\varphi) = 0.612 + 0.384\cos\varphi + 0.004\cos 2\varphi$)

7 This really depends on the smoothness of each of the phase mode coefficients, which in turn is a function of the element pattern.

8 A sonar array of these dimensions was built at Loughborough University of Technology in 1992, and a parametrised version of its measured element patterns is used here.

In the case of a uniform amplitude weighting, *(3.2.3)* may be put in the following closed form:

$$F_m(\varphi) = \frac{(1+2\Lambda)}{M^{1/2}} \frac{\sin[(1+2\Lambda)(\varphi-2\pi m/M)/2]}{(1+2\Lambda)\sin[(\varphi-2\pi m/M)/2]} \quad , \quad 0 \le m \le M-1 \quad \cdots (3.2.5)$$

which is the familiar sampling function pattern whose directivity increases with the number $(1+2\Lambda)$ of combined phase modes. Table 3.2.1 compares the beamwidths and peak sidelobe levels of uniformly excited modal beams formed by different numbers of normalised phase modes for a circular array of 8 omnidirectional radiators at half-wavelength spacings. The 9-mode case refers to the excitation of all 8 phase modes with mode $\mu = \pm 4$ weighted 6dB above all other modes. This accounts for the fact that modes $\mu = +4$ and $\mu = -4$ are both 'available' at the same port. Equivalently, the 9 modes $\mu = -4$ to $+4$ are uniformly excited. Note also that although modes +4 and -4 are not independent, they require the same phasing for a 9-mode beam to be scanned to (or simultaneously formed at) the following 8 directions:

$$\varphi_\ell = (\pi/4)\ell \quad , \quad 0 \le \ell \le 7$$

and in general for an M-element array, an undistorted $(M+1)$-mode beam may be formed at M directions given by:

Number of modes	True pattern			Expression *(3.2.3)*		
	Beamwidth		Peak sidelobe level	Beamwidth		Peak sidelobe level
	-3 dB	null to null		-3 dB	null to null	
3	49.6°	236°	-7.8 dB	111.8°	240°	-9.5 dB
4	43.1°	186°	-10.4 dB	82.0°	180°	-11.3 dB
5	39.3°	140°	-12.6 dB	64.9°	144°	-12.0 dB
6	42.4°	124°	-10.4 dB	53.8°	120°	-12.4 dB
7	41.0°	112°	-8.7 dB	46.0°	103°	-12.6 dB
9	32.9°	86°	-12.4 dB	35.6°	80°	-12.9 dB

Table 3.2.1: Uniformly excited mode-space beams from an 8-element array [omnidirectional radiators, 0.5λ inter-element spacing]

$$\varphi_\ell = (2\pi/M)\ell \quad , \quad 0 \le \ell \le M\text{-}1$$

Table 3.2.1 shows that (at least the null-to-null) beamwidth of the main beam is indeed reduced when the number of phase modes used for its synthesis is increased. The apparent deviation from the 'ideal' beam pattern expressed by *(3.2.3)*, and in particular the irregular shapes of the broader beams (leading to the misleadingly small half-power beamwidths) is a consequence of the pronounced presence of higher-order terms attendant to phase modes ±1, ±2 and ±3. These phase modes carry a peak-to-peak amplitude ripple of 3.8 dB, 2.4 dB and 5.5 dB respectively. Note though that although mode 4 is characterised by an even larger ripple, this is due to the combination of modes +4 and -4 and in fact it follows very closely a pattern of $\frac{1}{2}[e^{-j4\varphi}+e^{+j4\varphi}] = \cos 4\varphi$.

The phase and amplitude ripples of modes ±1 to ±3 may be reduced and the modal beam patterns be made to more closely follow *(3.2.3)* by reducing the array radius so that the inter-element spacing is well below half a wavelength. The performance of the same 8-element array but with 0.4 wavelengths spacing between radiators is summarised in Table 3.2.2, where one may note the closer resemblance, though not identity, to the 'ideal' $\sin(N\varphi/2)/N\sin(\varphi/2)$ patterns.

Number of modes	True pattern			Expression *(3.2.3)*		
	Beamwidth		Peak sidelobe level	Beamwidth		Peak sidelobe level
	-3 dB	null to null		-3 dB	null to null	
3	111.5°	242°	-9.6 dB	111.8°	240°	-9.5 dB
4	81.3°	178°	-11.2 dB	82.0°	180°	-11.3 dB
5	63.2°	146°	-11.8 dB	64.9°	144°	-12.0 dB
6	57.2°	118°	-12.4 dB	53.8°	120°	-12.4 dB
7	50.6°	104°	-11.0 dB	46.0°	103°	-12.6 dB
9	37.3°	82°	-12.5 dB	35.6°	80°	-12.9 dB

Table 3.2.2: Uniformly excited mode-space beams from an 8-element array [omnidirectional radiators, 0.4λ inter-element spacing]

3.3 MULTIMODAL DIRECTION FINDING

A direction finder is a sub-system designed to indicate the direction of arrival of signals. Simple single-source scenarios have classically been handled by one of several conventional approaches:

i amplitude comparison
ii phase comparison
iii monopulse

Modern amplitude-comparison systems process the (pre-calibrated) outputs of a multibeam array network to find the one with the highest power level as a rough indication of source direction, with the relative power at the neighbouring ports serving to fine-tune the initial bearing estimation. In element-space phase-comparison DF, the angle of arrival is obtained from the (relative) detected phases of signals received by pairs of array elements. Phase detection is also part of the monopulse approach, but this time it is between the *difference* and *sum*[9] outputs of a (mechanically or electronically) scanning beamformer. In the context of mode-space circular array beamforming, one can think of a DF system employing amplitude comparison between a multiple set of frequency-independent directional beams, or even of the incorporation of a mode-space monopulse unit.

The mode-space equivalent of the phase-comparison approach, and perhaps also the most common use for phase modes, is the so called multimodal DF [REH 80]. In its usual application the phases of several pairs of symmetrically numbered phase modes are detected and compared providing a high-resolution angle-versus-phase function:

$$\arg[\Phi_{-\mu}(\theta, \varphi, \omega)/\Phi_{\mu}(\theta, \varphi, \omega)] \approx 2\mu\varphi \qquad \cdots (3.3.1)$$

where symmetric element patterns have been assumed, so that, as we presently show, the corresponding phase mode coefficients effectively cancel out. Angular ambiguity is resolved by comparing the phases of two adjacent modes, say modes no. -1 and 0:

$$\arg[\Phi_{-1}(\theta, \varphi, \omega)/\Phi_{0}(\theta, \varphi, \omega)] \approx \varphi + \arg[C_{(-1)0}(\omega, \theta)/C_{00}(\omega, \theta)] \qquad \cdots (3.3.2)$$

but that entails, as is evident from *(3.3.2)*, the alignment or at least the calibration of the corresponding two (zero-order) phase mode coefficients.

---

9 Sum and difference beams are produced by respectively adding and subtracting the summed outputs from two symmetric halves of an array. In its simple implementation the same weighting taper is used for both beams, but this is not always so. In any case, the sum beam is typically characterised by a pattern maximum, whereas the difference beam has a null in that direction.

Actually, there is a neat way to avoid (at least in theory) mode calibration by relying on the assumed symmetry of the element patterns. Specifically, we assume element patterns to be given either by an expression of the form *(2.4.3)*, or by the Fourier series *(2.2.4)* with:

$$h_{-i}(\theta)=h_i(\theta) \quad , \quad i>0 \qquad \cdots (3.3.3)$$

which, as can be inferred from *(2.4.14)* in section 2.4 of chapter 2, leads to the following expression for the radiation pattern of phase mode $-\mu$, relative to that of phase mode $+\mu$:

$$\Phi_{-\mu}(\theta, \varphi, \omega)/\Phi_{\mu}(\theta, \varphi, \omega) =$$

$$\frac{\sum_{q=-\infty}^{\infty} C_{\mu q}(\omega, \theta) e^{j(\mu+qM)\varphi}}{\sum_{q=-\infty}^{\infty} C_{\mu q}(\omega, \theta) e^{-j(\mu+qM)\varphi}} = \frac{\alpha_{\mu}(\omega, \theta, \varphi)+j\beta_{\mu}(\omega, \theta, \varphi)}{\alpha_{\mu}(\omega, \theta, \varphi)-j\beta_{\mu}(\omega, \theta, \varphi)} e^{j2\mu\varphi} \qquad \cdots (3.3.4)$$

where,

$$\alpha_{\mu}(\omega, \theta, \varphi) = 1 + \sum_{q=1}^{\infty} \frac{C_{\mu q}(\omega, \theta) + C_{\mu(-q)}(\omega, \theta)}{C_{\mu 0}(\omega, \theta)} \cos qM\varphi \qquad \cdots (3.3.5)$$

$$\beta_{\mu}(\omega, \theta, \varphi) = \sum_{q=1}^{\infty} \frac{C_{\mu q}(\omega, \theta) - C_{\mu(-q)}(\omega, \theta)}{C_{\mu 0}(\omega, \theta)} \sin qM\varphi \qquad \cdots (3.3.6)$$

and clearly, for the $2M$ directions given by:

$$\varphi_{\ell} = 2\pi(\ell/2M) \quad , \quad 0 \le \ell \le 2M-1 \qquad \cdots (3.3.7)$$

we have

$$\frac{\Phi_{-\mu}(\theta, \varphi_{\ell}, \omega)}{\Phi_{\mu}(\theta, \varphi_{\ell}, \omega)} = e^{j2\mu\varphi_{\ell}} \qquad \cdots (3.3.8)$$

which is the basis for the approximation *(3.3.1)*. In other words, the comparative phase response between the two phase modes is characterised by symmetric and equi-ripple phase fluctuation of $\pm 2\tan^{-1}[\beta_\mu(\omega,\theta,\varphi)/\alpha_\mu(\omega,\theta,\varphi)]$ about the value of $2\mu\varphi$ and is thus usable for DF purposes without the need for mode alignment.

The angular ambiguity inherent in *(3.3.8)* (in comparing the phases of non-adjacent phase modes) may be resolved by detecting and comparing the phases of both mode Φ_{-1} and Φ_1 to that of mode Φ_0:

$$\frac{\Phi_{\pm 1}(\theta,\varphi,\omega)}{\Phi_0(\theta,\varphi,\omega)} = \frac{C_{10}(\omega,\theta)}{C_{00}(\omega,\theta)} \frac{\alpha_1(\omega,\theta,\varphi) \mp j\beta_1(\omega,\theta,\varphi)}{\alpha_0(\omega,\theta,\varphi)} e^{\mp j\varphi} \qquad \cdots (3.3.9)$$

$$\frac{\Phi_{\pm 1}(\theta,\varphi_\ell,\omega)}{\Phi_0(\theta,\varphi_\ell,\omega)} = \frac{C_{10}(\omega,\theta)}{C_{00}(\omega,\theta)} \frac{\alpha_1(\omega,\theta,\varphi_\ell)}{\alpha_0(\omega,\theta,\varphi_\ell)} e^{\mp j\varphi_\ell} \quad , \quad 0 \le \ell \le 2M-1 \qquad \cdots (3.3.10)$$

where the angles $\{\varphi_\ell\}$ are given by *(3.3.7)*. Now, we often find that the phase bias $\arg[C_{10}(\omega,\theta)\alpha_1(\omega,\theta,\varphi_\ell)/[C_{00}(\omega,\theta)\alpha_0(\omega,\theta,\varphi_\ell)]$ is less in absolute value than $\pi/2$. In fact, for an array of omnidirectional elements, $[\arg C_{10}(\omega,\theta) - \arg C_{00}(\omega,\theta)]$ (which is normally dominant in the above phase-bias expression) is clearly equal to $\pm\pi/2$ (see *(2.4.12)*), and as we show at the beginning of section 3.6 of this chapter, it is asymptotically (for large $(\omega R/c)$) equal to zero in the case of directional elements of the form $(1+\cos\varphi)$, and is always zero for impulsively-directional array elements. Having the phase bias bounded by $\pm 90°$ allows its straightforward elimination via:

$$\arg[C_{10}(\omega,\theta)\alpha_1(\omega,\theta,\varphi_\ell)/[C_{00}(\omega,\theta)\alpha_0(\omega,\theta,\varphi_\ell)] =$$

$$-\pi + \frac{1}{2}[\pi + \arg\frac{\Phi_{-1}(\theta,\varphi_\ell,\omega)}{\Phi_0(\theta,\varphi_\ell,\omega)} + \arg\frac{\Phi_1(\theta,\varphi_\ell,\omega)}{\Phi_0(\theta,\varphi_\ell,\omega)}]_{\text{mod } 2\pi} \quad , \quad 0 \le \ell \le 2M-1 \qquad \cdots (3.3.11)$$

where $[x]_{\text{mod } 2\pi}$ denotes the modulo-2π value of x.

Associated with the omnidirectional nature of the compared phase mode patterns is the obvious advantage of 360° coverage, but also the attendant drawback of high vulnerability to co-channel interference. In section 3.5 we propose an alternative phase-comparison DF scheme in which the compared phase modes become directional in amplitude while retaining their linear phase characteristics, and therefore less susceptible to interference.

3.4 NULL STEERING

The need for generating radiation pattern nulls arises in communication as well as in direction-finding applications, where the receiving array has to reject unwanted interference or jamming signals. The synthesis of static or steerable nulls in the far-field pattern of an antenna array has been described in the past by a number of authors in the context of non-adaptive linear [DAV 67], [CLA 68], [MEL 70] and later also circular arrays [LIM 75], [LIM 77], [DAV 77], [RIZ 77], [DAV 78a], [DAV 78b], [DAV 81], [GRI 85], [KAR 86], [CVE 88a], [CVE 88b]. A variety of adaptive and semi-adaptive signal processing techniques have also been suggested for the closed-loop generation of pattern nulls in the directions of the interfering signals. Interference may, of course, refer to a multi-source or multipath environment which often degrades the performance of a conventional direction finder. In that event a nulling scheme might be devised that sequentially nulls out sources whose bearings have already been determined, and is then iterated in order to reduce bias errors in the estimated locations of the sources and nulls.

One method for forming a steerable cardioid-shaped single-null circular-array pattern is by the phase-controlled combination of two adjacent phase modes of equalised amplitudes. Thus, if the far-field patterns of phase modes Φ_μ and $\Phi_{\mu+1}$ are respectively given by:

$$\Phi_\mu(\theta, \varphi, \omega) \approx C_{\mu 0}(\omega, \theta) e^{-j\mu\varphi}$$

and

$$\Phi_{\mu+1}(\theta, \varphi, \omega) \approx C_{\mu 0}(\omega, \theta) e^{-j(\mu+1)\varphi}$$

then a null in direction β is produced by subtracting the normalised and phased $\Phi_{\mu+1}$ output from the normalised output Φ_μ:

$$\frac{\Phi_\mu(\theta, \varphi, \omega)}{C_{\mu 0}(\omega, \theta)} - \frac{\Phi_{\mu+1}(\theta, \varphi, \omega)}{C_{(\mu+1)\,0}(\omega, \theta)} e^{j\beta} = j2e^{-j\mu\varphi} e^{-j(\varphi-\beta)/2} \sin\frac{\varphi-\beta}{2} \qquad \cdots (3.4.1)$$

The new pattern is characterised by a new phase slope of $-(\mu+1/2)$, a phase offset of $\beta/2$ and a $\sin(\varphi/2)$-type null in direction β which introduces a phase jump of $\pm\pi/2$. The null may be steered by controlling the inter-mode phase-shift β, but note that the $\beta/2$ phase offset changes also. Additional phase modes may be used to either reduce

the null width [LM 77] or to introduce additional pattern nulls. The latter option, suggested in [DAV 77] is illustrated in *Fig. 3.4.1*. Here, each output beam is formed by linearly combining three adjacent phase modes, with two sets of phase shifts β_1 and β_2 independently controlling the respective directions of two $\sin(\varphi/2)$-type pattern nulls. Except for two $\pm\pi/2$ phase jumps at $\varphi=\beta_1$ and $\varphi=\beta_2$, the resulting phase patterns remain linear, following as before the average phase slopes of the generating phase modes. A double-null output beam with phase slope $-\mu$ is thus obtained from phase modes $\Phi_{\mu-1}$, Φ_μ and $\Phi_{\mu+1}$:

$$[\frac{\Phi_{\mu-1}(\theta,\varphi,\omega)}{C_{(\mu-1)0}} - \frac{\Phi_\mu(\theta,\varphi,\omega)}{C_{\mu 0}} e^{j\beta_1}] - [\frac{\Phi_\mu(\theta,\varphi,\omega)}{C_{\mu 0}} - \frac{\Phi_{\mu+1}(\theta,\varphi,\omega)}{C_{(\mu+1)0}} e^{j\beta_1}] e^{j\beta_2} \approx$$

$$-4e^{-j\mu\varphi}\, e^{j(\beta_1+\beta_2)/2} \sin\frac{\varphi-\beta_1}{2} \sin\frac{\varphi-\beta_2}{2} \qquad \cdots (3.4.2)$$

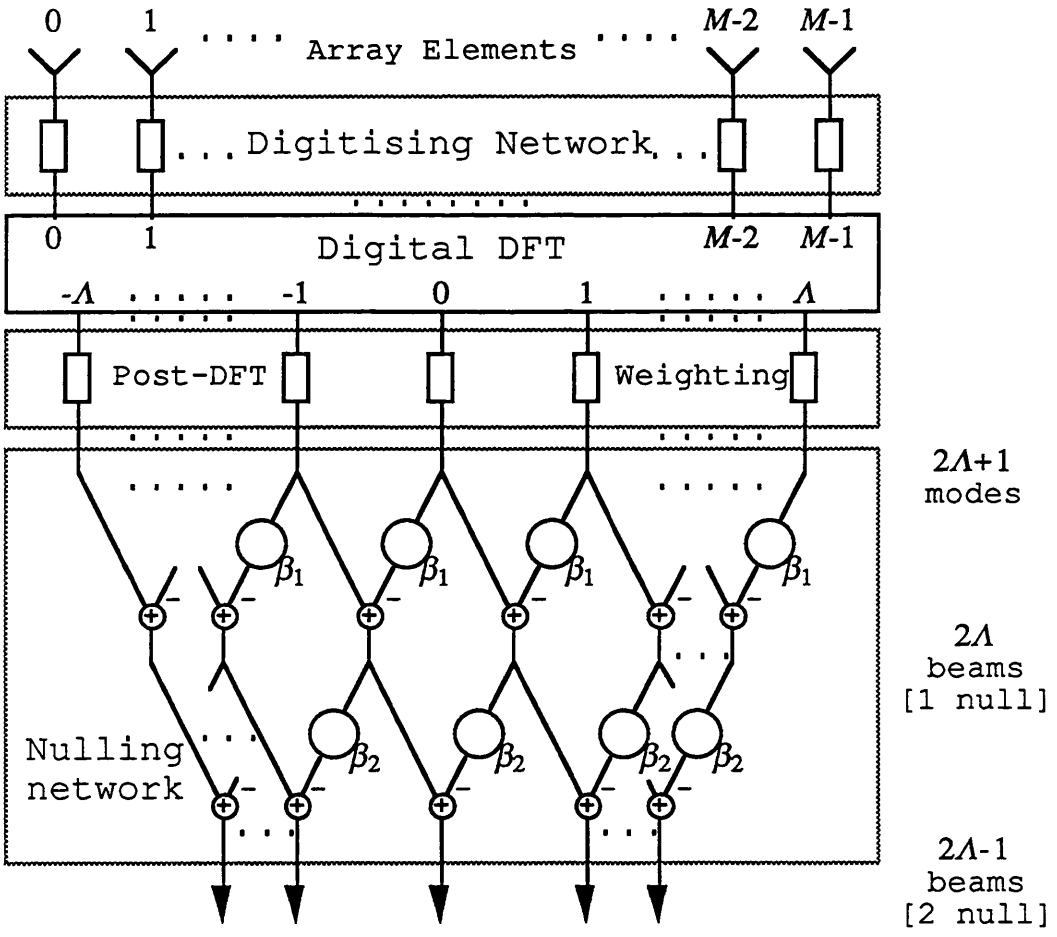

Fig. 3.4.1 Independent angular steering of multiple nulls

Three or more nulls may be similarly generated by extending the nulling network of *Fig. 3.4.1*, with the number of beam outputs decreasing at each stage. Eventually, a single beam with 2Λ independently steerable nulls will be produced.

Pattern nulls sharper than $\sin[(\varphi-\beta)/2]$ may be synthesised at each stage at the expense of fewer beams (or equivalently fewer nulls) and increased complexity. Instead of forming each nulled beam from a pair of adjacent phase modes as illustrated in *Fig. 3.4.1*, each sharply-nulled beam is generated by linearly combining an interlaced set of $N>2$ modes – see *Fig. 3.4.2* for the case of $N=3$. Each set of phase modes is linearly phased (with phase shifts β, 2β, 3β etc.) as well as multiplied by a set of weights $\{w_n\}$, where $\beta\pm\pi$ is the desired direction of the null and the weights are yet to be determined. A pattern synthesised by a set of N symmetrically numbered phase modes (with N odd) may be expressed as:

$$\mathcal{N}(\varphi) = e^{j(N-1)\beta/2} \sum_{n=0}^{N-1} w_n e^{-j[n-(N-1)/2](\varphi-\beta)} \qquad \ldots (3.4.3)$$

and, following the lines suggested in [LIM 77], the single-null target pattern we seek is given by:

$$\mathcal{T}(\varphi) = e^{j(N-1)\beta/2}\, e^{-j(\varphi-\beta)/2} \qquad \ldots (3.4.4)$$

One may therefore use standard Fourier analysis to solve:

$$\sum_{n=0}^{N-1} w_n e^{-j[n-(N-1)/2](\varphi-\beta)} = e^{-j(\varphi-\beta)/2} \qquad \ldots (3.4.5)$$

which yields:

$$w_n = \frac{\sin[(n-N/2)\pi]}{(n-N/2)\pi} = \frac{(-1)^{n-(N-1)/2}}{(-n+N/2)\pi} \quad , \quad 0 \le n \le N-1 \qquad \ldots (3.4.6)$$

For example, if $N = 3$ we have:

$$w_0 = -2/3\pi$$
$$w_2 = w_3 = 2/\pi$$

Note that whichever type of radiation pattern nulls are produced, the same null factors are shared by all the (typically wide) output beams, the latter being also characterised, as we remember, by linear phase. This makes the above null-steering schemes readily adaptable for the generation of directional beams with steerable nulls.

A multibeam network that achieves this is schematically illustrated in *Fig. 3.4.3*. Here a weighted set of double-null beams are operated on by an inverse DFT unit to form a multiple set of M directional beams with pattern nulls at $\varphi = \beta_1$ and $\varphi = \beta_2$. Assuming wide $\sin(\varphi/2)$-type nulls, each of these directional beams is approximately given by:

$$F_m(\varphi) = \frac{-4e^{j(\beta_1+\beta_2)/2}}{M^{1/2}} \sin\frac{\varphi-\beta_1}{2} \sin\frac{\varphi-\beta_2}{2} \sum_{\mu=-\Lambda+1}^{\Lambda-1} \alpha_\mu e^{-j\mu(\varphi-2\pi m/M)}$$

$$0 \le m \le M-1 \qquad \cdots (3.4.7)$$

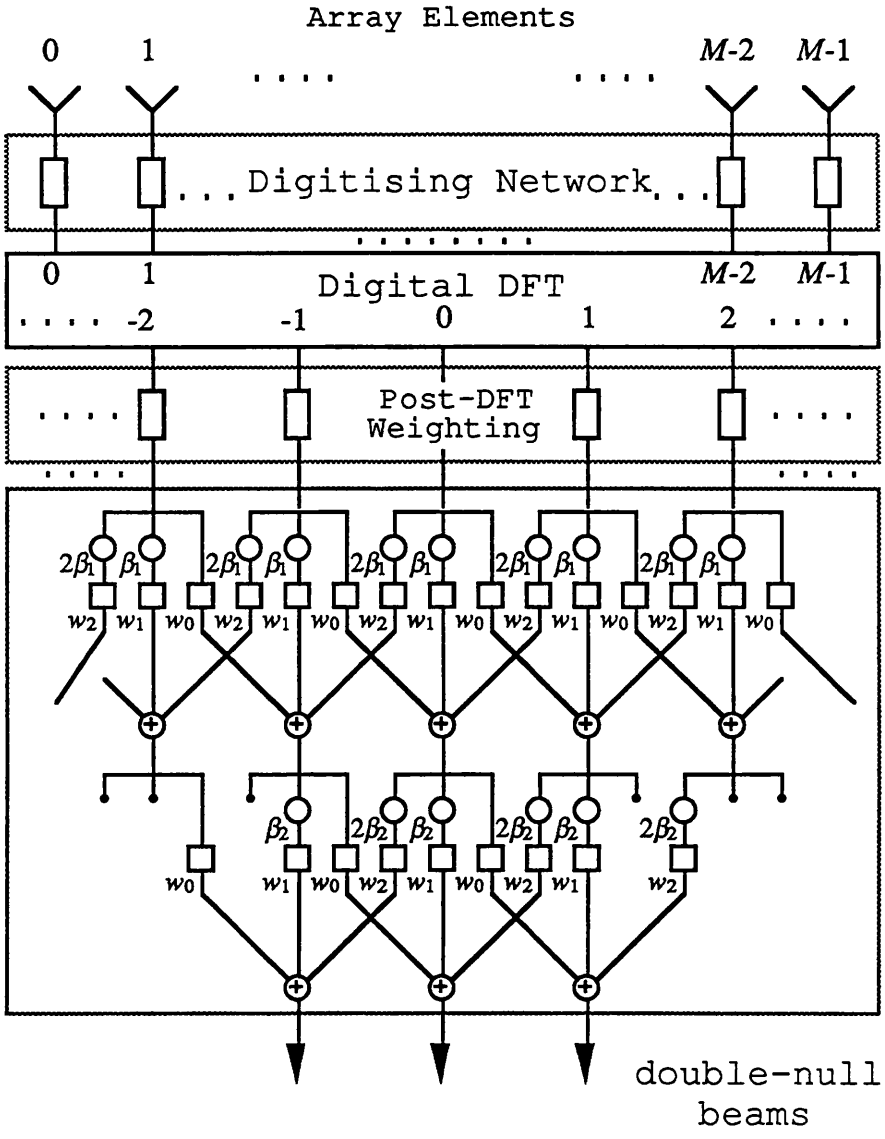

Fig. 3.4.2 Independent angular steering of sharp nulls

where $\{\alpha_\mu\}$ is the set of weights applied by the post-nulling weighting unit. If uniform amplitude weighting is used, then *(3.4.7)* takes the form:

$$F_m(\varphi) = -4\frac{(2\Lambda-1)}{M^{1/2}} e^{j(\beta_1+\beta_2)/2} \sin\frac{\varphi-\beta_1}{2} \sin\frac{\varphi-\beta_2}{2}$$

$$\frac{\sin[(\varphi-2\pi m/M)(2\Lambda-1)/2]}{(2\Lambda-1)\sin[(\varphi-2\pi m/M)/2]} \quad , \quad 0 \le m \le M-1 \qquad \cdots (3.4.8)$$

In section 3.5 we introduce the new concept of *sectoral phase modes*, which one may describe as phase modes with directional properties, and propose a more agile multibeam nulling architecture where the order of operations (null forming followed by multiple beamforming) is effectively reversed.

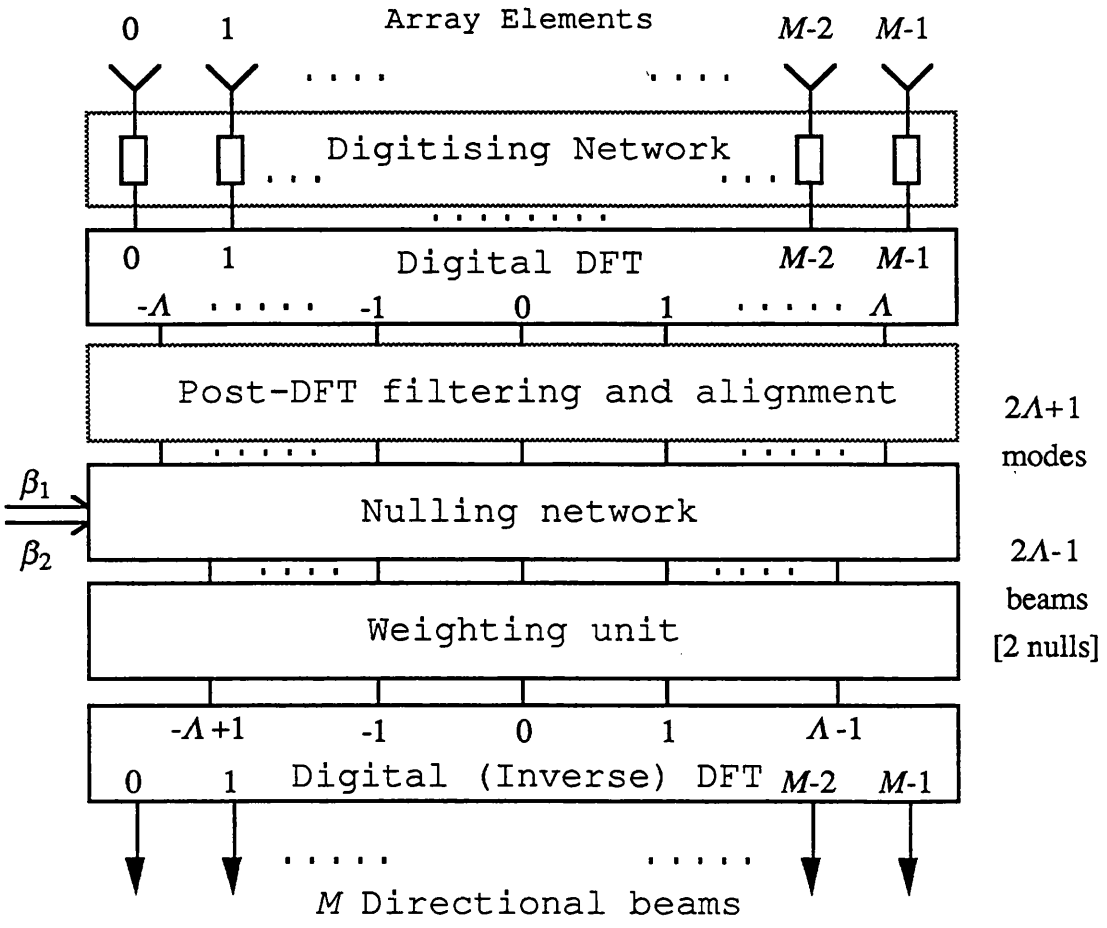

Fig. 3.4.3 A multibeam network with 2 steerable nulls

3.5 SECTORAL PHASE MODES

The multimodal direction finder described in section 3.3 combines the advantage of full circumferential coverage with the benefit of small size and (theoretically) automatic calibration by symmetry. One of its main drawbacks though is its high susceptibility to co-channel interference. In fact applying *(3.3.2)* to evaluate the direction of arrival of a signal, when a second signal at the same frequency is also received by the array, will result (see appendix C.1 for details) in angular errors which, at a worst-case scenario, may reach the values tabulated in Table 3.5.1.

Improved immunity to interference may be attained, at the expense of some reduction in angular resolution and of having to align the modes, by transforming the compared phase modes into directional beams while retaining their linear-phase property. The idea is to divide the azimuth observation plane into a number of angular sectors, and form two sets of multibeam patterns so that each angular sector is covered by a pair of low-sidelobe directional beams with linear and opposite phase slopes. Inter-sector amplitude comparison may then be used to unambiguously determine the angular sector facing each incident signal, while a more accurate bearing is obtained by detecting and comparing the phases of the two directional beams covering that sector, just as with ordinary phase modes, but with a much reduced susceptibility to out-of-sector interference. Since the phase behaviour of these beams in their respective angular sectors is similar to that of omnidirectional phase modes, we have chosen to name them *sectoral phase modes* or equivalently *SPM beams.*

Relative strength of second signal	Minimum angular error	Maximum angular error
-30 dB	0°	3.6°
-25 dB		6.4°
-20 dB		11.5°
-15 dB		20.5°
-10 dB		36.9°

Table 3.5.1 Angular errors in multimodal DF due to the presence of a second signal

A set of M pairs of sectoral phase modes pointing in directions:

$$\varphi_m=(2\pi/M)m \quad , \quad 0\le m\le M\text{-}1$$

may be approximately synthesised by applying a spatial (inverse) DFT operation to two aligned sets of asymmetrically-numbered omnidirectional phase modes, say modes no. $\{-\Lambda \text{ to } \Lambda\text{-}\Lambda_0\}$ and $\{-\Lambda+\Lambda_0 \text{ to } \Lambda\}$, under the same symmetric weighting taper. The radiation patterns for the m'th pair of beams are then given by:

$$F^{m\,\Lambda_0}_{-\Lambda_0/2}(\varphi) = \sum_{\mu=-\Lambda}^{\Lambda-\Lambda_0} \alpha_{k_{\mu+\Lambda_0/2}} e^{j(2\pi/M)m\mu} \frac{\Phi_\mu(\pi/2,\varphi,\omega)}{C_{\mu 0}(\omega,\pi/2)}$$

$$\approx A(\varphi\text{-}2\pi m/M)\, e^{j(\Lambda_0/2)(\varphi-2\pi m/M)} \qquad \cdots (3.5.1)$$

$$F^{m\,\Lambda_0}_{\Lambda_0/2}(\varphi) = \sum_{\mu=-\Lambda+\Lambda_0}^{\Lambda} \alpha_{k_{\mu-\Lambda_0/2}} e^{j(2\pi/M)m\mu} \frac{\Phi_\mu(\pi/2,\varphi,\omega)}{C_{\mu 0}(\omega,\pi/2)}$$

$$\approx A(\varphi\text{-}2\pi m/M)\, e^{-j(\Lambda_0/2)(\varphi-2\pi m/M)} \qquad \cdots (3.5.2)$$

where $\Lambda<M/2$, $0<\Lambda_0<2\Lambda$,

$$k_x=\mathrm{Int}(\,|\,x\,|+1/2\,) \qquad \cdots (3.5.3)$$

$$A(\varphi) = \alpha_0 + 2\sum_{k=1}^{\Lambda-\mathrm{Int}(\Lambda_0/2)} \alpha_k \cos k\varphi \qquad \cdots (3.5.4)$$

and for an odd Λ_0: $\alpha_0=0$. The superscripts m and Λ_0 on the left hand side of *(3.5.1)* and *(3.5.2)* indicate respectively the direction φ_m of the two beams and the number of unused phase modes (out of the set $\{-\Lambda \text{ to } \Lambda\}$) in the synthesis of each beam. We refer to the subscripts $\pm\Lambda_0/2$ as the *effective mode numbers*, denoting, in analogy with mode numbers of omnidirectional phase modes, the local phase slope of the corresponding far-field sectoral phase mode pattern. A schematic block diagram for a digital SPM beamformer is given in *Fig. 3.5.1.* Under uniform weighting, the common far-field amplitude pattern of the beams becomes:

$$A(\varphi) = \sin[(2\Lambda\text{-}\Lambda_0)\,\varphi/2]/\sin(\varphi/2) \qquad \cdots (3.5.5)$$

with a null-to-null beamwidth of $\Delta\varphi = 4\pi/(2\Lambda\text{-}\Lambda_0) > 4\pi/M$. The full coverage of each

of the M angular sectors $|\varphi-(2\pi/M)m|\leq\pi/M$, $0\leq m\leq M-1$ is thus ensured with some main-lobe illumination of the neighbouring sectors and a peak sidelobe level of approximately -13.5 dB. This sidelobe performance may be improved at the expense

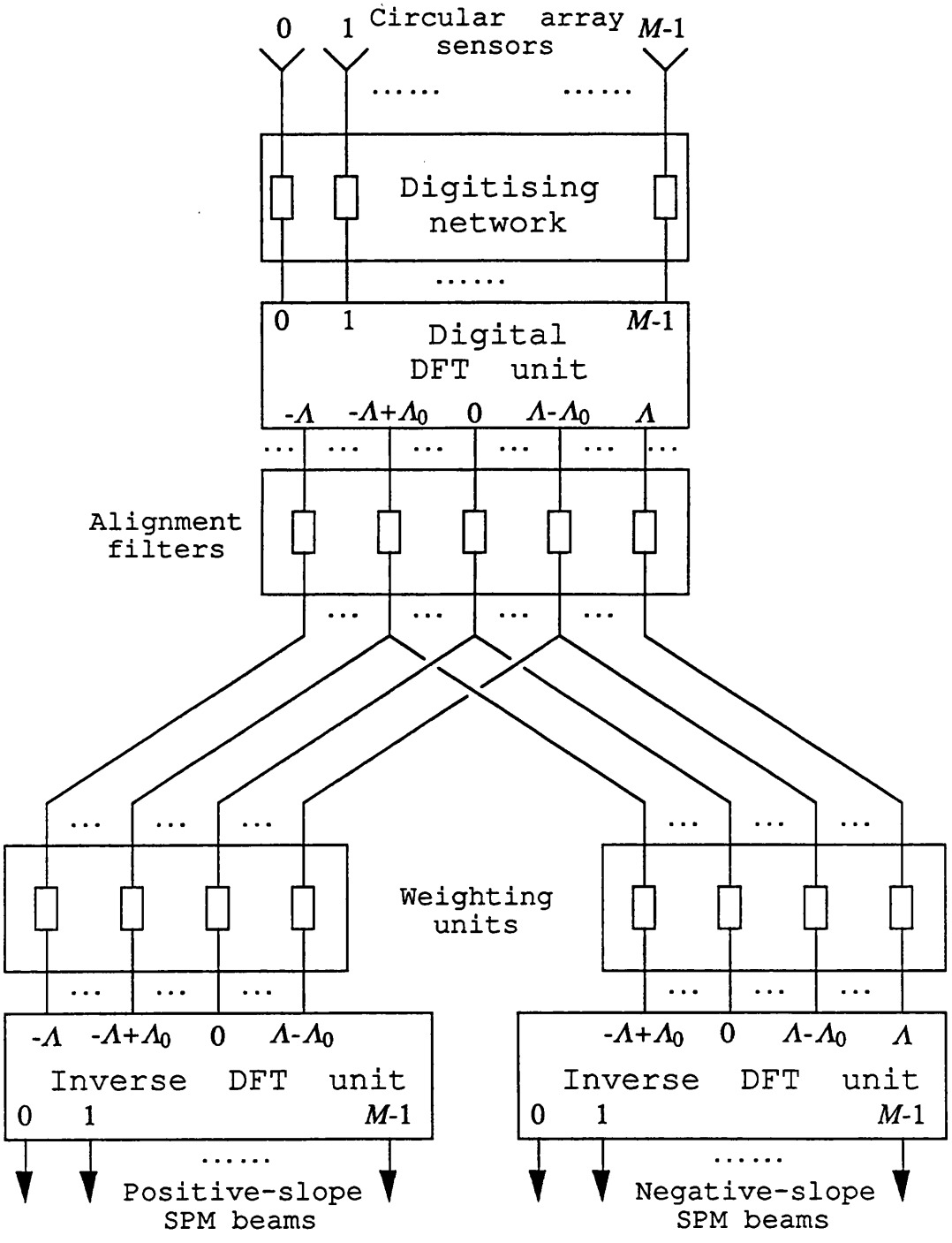

Fig. 3.5.1 Digital beamformer generating 2 sets of sectoral phase modes

of an increased beamwidth by applying a weighting taper such as a sampled linear Taylor distribution to the combined phase modes. *Fig. 3.5.2* displays the amplitude and phase patterns for a pair of sectoral phase modes with effective mode numbers ±1/2. The beams are formed from a 16-element circular array by the linear combination of two overlapping sets of 14 phase modes. Note the almost identical low-sidelobe amplitude patterns and the comparative linear phase slope of approximately 1 over an azimuth angular sector larger than 360°/14 = 25.7°.

The choice of Λ_0 affects both the amplitude pattern and the phase slopes of the SPM beams. As previously noted, the effective mode numbers of the two SPM beams $F^{m\Lambda_0}_{-\Lambda_0/2}(\varphi)$ and $F^{m\Lambda_0}_{\Lambda_0/2}(\varphi)$ defined by *(3.5.1)* and *(3.5.2)* are given by $-\Lambda_0/2$ and $\Lambda_0/2$ respectively. The larger Λ_0, the higher are these effective mode numbers, indicating steeper phase slopes but the wider are the beams. Thus whereas the highest DF accuracy but poorest immunity to out-of-sector interference are achieved by comparing the phases of the highest-order omnidirectional phase modes $\Phi_{-\Lambda}$ and Φ_{Λ}, best immunity but least accuracy result from the comparison of two sectoral phase modes with $\Lambda_0=1$. In the latter case the effective mode numbers of the two compared SPM beams are -1/2 and 1/2 respectively, and

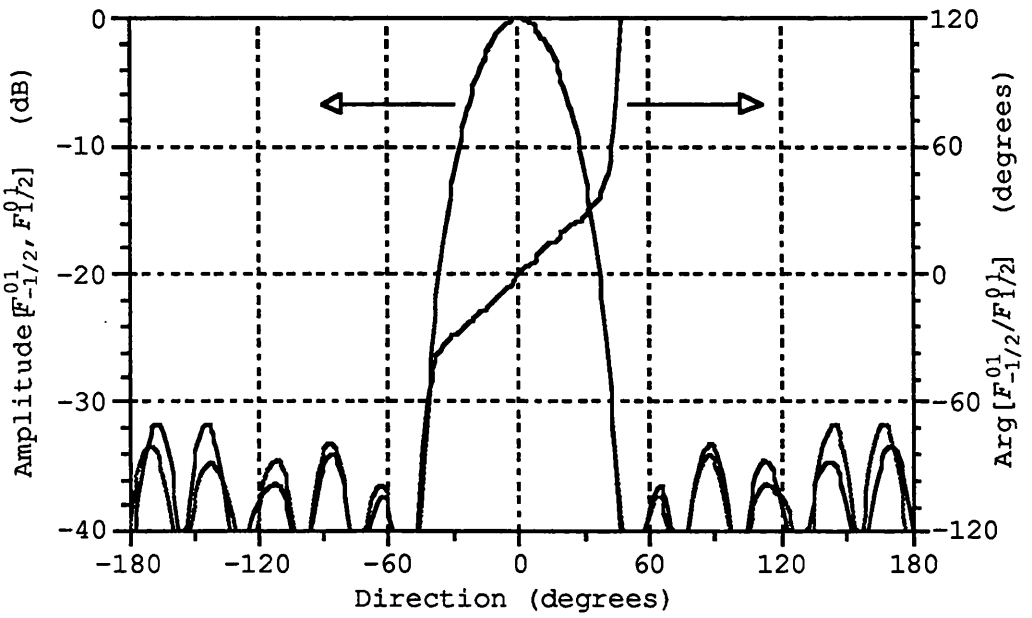

Fig. 3.5.2 Comparative phase plot and amplitude patterns for a pair of sectoral phase modes. (M = 16, Λ = 7, Λ_0 = 1, $g(\pi/2, \varphi)=\cos\varphi/2$, $2\pi R/M = 0.4\lambda$)
Mode weighting [in dB]:
{-15.5 -12.8 -8.3 -4.7 -2.3 -0.7 0 -0.7 -2.3 -4.7 -8.3 -12.8 -15.5}

$$\arg F_{-1/2}^{m\,1}(\phi) - \arg F_{1/2}^{m\,1}(\phi) = \phi - 2\pi m/M \qquad \cdots (3.5.6)$$

Note also that when $\Lambda_0 > 1$, more than two SPM beams may be synthesised to serve each angular sector. In fact one may generate $\Lambda_0 + 1$ such beams:

$$F_\nu^{m\,\Lambda_0}(\varphi) =$$

$$\sum_{\mu=-\Lambda+\Lambda_0/2+\nu}^{\Lambda-\Lambda_0/2+\nu} \alpha_{k_{\mu\nu}} e^{j(2\pi/M)m\mu} \Phi_\mu(\pi/2, \varphi, \omega)/C_{\mu 0}(\omega, \pi/2)$$

$$\approx A(\varphi - 2\pi m/M) e^{-j\nu(\varphi - 2\pi m/M)} \quad , \quad \nu = -\Lambda_0/2, -\Lambda_0/2+1, \cdots, \Lambda_0/2 \qquad \cdots (3.5.7)$$

with effective mode numbers:

$$\nu = -\Lambda_0/2, -\Lambda_0/2+1, \cdots\cdots, \Lambda_0/2$$

respectively. This set of beams may then be used to add a sectoral null-steering capability to the beamformer, an application which we consider next.

In section 3.4 we saw how a set of $2\Lambda+1$ phase modes $\Phi_{-\Lambda}, \Phi_{-\Lambda+1}, \cdots, \Phi_\Lambda$ is used to form a set of 2Λ 'modified' phase-mode beams

$$\Psi_{-\Lambda+1/2}^{\beta}, \Psi_{-\Lambda+3/2}^{\beta}, \cdots, \Psi_{\Lambda-1/2}^{\beta} \qquad \cdots (3.5.8)$$

all sharing the same $\sin(\varphi/2)$-type null at $\varphi = \beta$:

$$\Psi_{\mu+1/2}^{\beta} = \Phi_\mu/C_{\mu 0} - e^{j\beta}\Phi_{\mu+1}/C_{(\mu+1)0}$$
$$\approx j2e^{j\beta/2} e^{-j(\mu+1/2)\varphi} \sin(\varphi - \beta)/2 \qquad \cdots (3.5.9)$$

The superscript and subscript on the left hand side of *(3.5.8)* signify the direction of the null and the effective mode number (i.e., the phase slope in reverse sign) of the modified mode beam $\Psi_{\mu+1/2}^{\beta}$, respectively. When the elements of the set *(3.5.8)* are linearly combined by an inverse DFT operator, the result is a multiple pattern of M directional beams all sharing the same pattern null (or nulls for a multistage nulling network). If each angular sector $|\varphi - (2\pi/M)m| \le \pi/M \quad , \quad 0 \le m \le M-1$ is served by a set of two or more SPM beams $F_{-\Lambda_0/2}^{m\,\Lambda_0}, F_{-\Lambda_0/2+1}^{m\,\Lambda_0}, \cdots\cdots, F_{\Lambda_0/2}^{m\,\Lambda_0}$ then one may consider an alternative multibeam nulling scheme that will allow each directional beam to steer its

own nulls. Instead of combining and phasing adjacent phase modes, the same nulling concept is applied here to adjacent *sectoral* phase modes, as illustrated in *Fig. 3.5.3* for the case of $\Lambda_0 = 2$ and three sectoral phase modes per sector. Under this last configuration, the m'th directional beam will be given by:

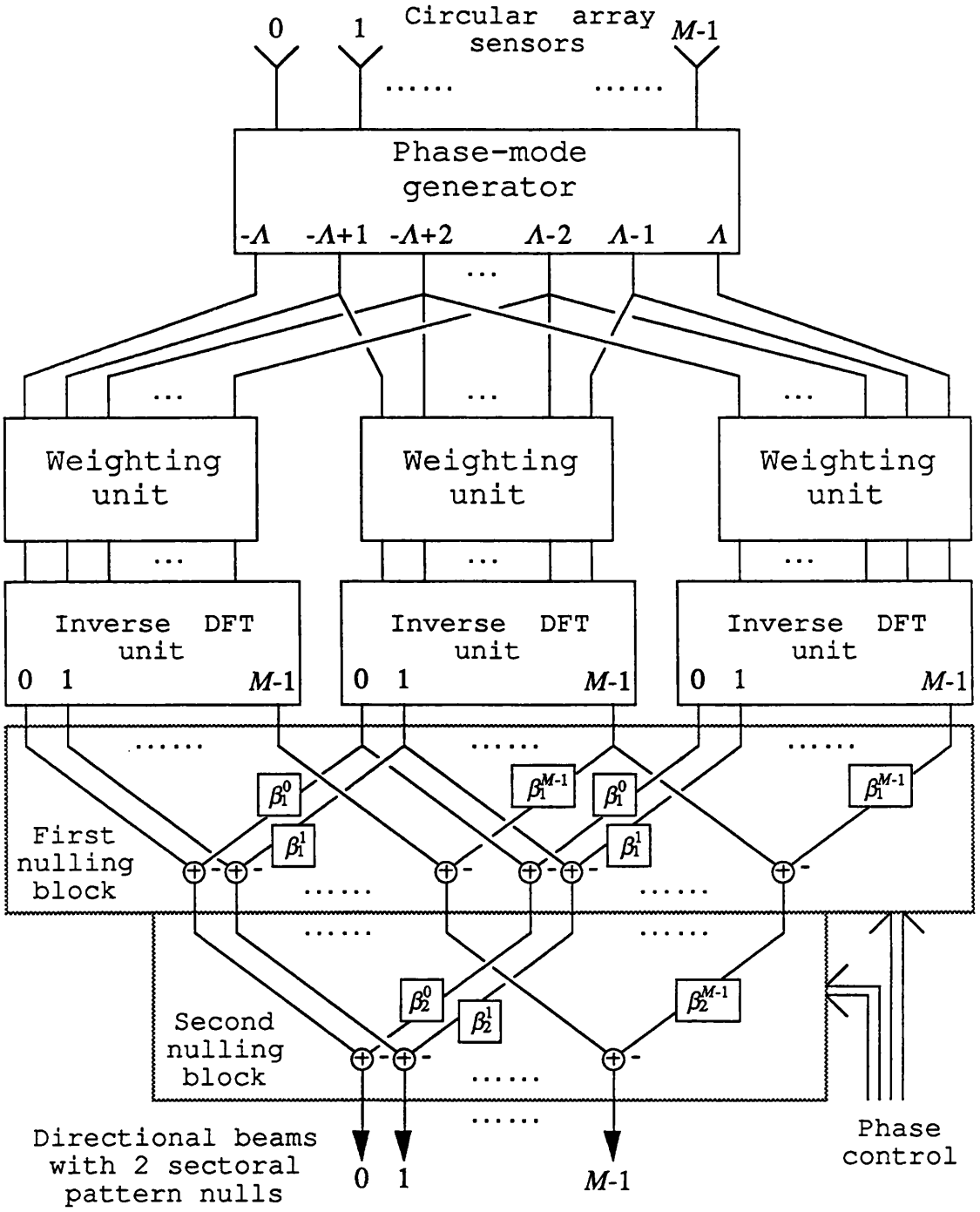

Fig. 3.5.3 Multibeam null-steering scheme incorporating sectoral phase modes

$$[F_{-1}^{m2}(\varphi)-e^{j\beta_1^m}F_0^{m2}(\varphi)]-e^{j\beta_2^m}[F_0^{m2}(\varphi)-e^{j\beta_1^m}F_1^{m2}(\varphi)]\approx$$

$$(j2)^2 e^{j(\beta_1^m+\beta_2^m)/2} A(\varphi-2\pi m/M)$$

$$\sin(\varphi-\beta_1^m-2\pi m/M)/2 \sin(\varphi-\beta_2^m-2\pi m/M)/2 \quad \cdots (3.5.10)$$

where $A(\varphi)$ and $\{F_v^{m2}(\varphi)\ ,\ v=-1,0,1\}$ are given by *(3.5.4)* and *(3.5.7)* respectively, with Λ_0 set equal to 2. In contrast with the two control phases β_1 and β_2 in the multibeam network of *Fig. 3.4.3* which employs a standard two-stage nulling scheme, there are now M pairs of phase shifts $\{\beta_0^m, \beta_1^m\}_{m=0}^{M-1}$ available in *Fig. 3.5.3*, allowing each sectoral beam to independently control two pattern nulls. A similar scheme for synthesising sectorally-controlled sharp nulls is described in appendix C.2. A directional beam with a sectoral pattern null is depicted in *Fig. 3.5.4*. The nulled pattern is synthesised by applying a 30° phase shift to one of two sectoral phase modes and subtracting one from the other. The sectoral phase modes themselves are formed from a 16-element circular array by combining two sets of 14 phase modes each with the same low-sidelobe taper. The result is a $\sin(\varphi/2)$-type null at $\varphi = 32.3°$.

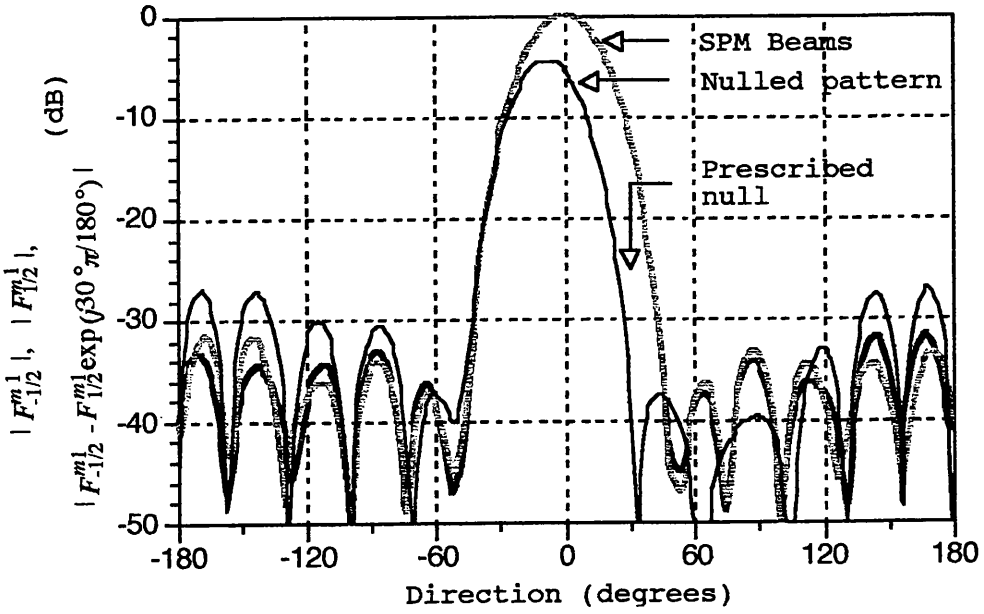

Fig. 3.5.4 A directional beam with a designed pattern null formed close to 30° by the phased subtraction of two SPM beams $F_{-1/2}^{01}$ and $F_{1/2}^{01}$.
($M = 16$, $\Lambda = 7$, $g(\pi/2, \varphi)=\cos(\varphi/2)$, $2\pi R/M = 0.4\,\lambda$, mode weighting [in dB]: {-15.5 -12.8 -8.3 -4.7 -2.3 -0.7 0 -0.7 -2.3 -4.7 -8.3 -12.8 -15.5})

3.6 BANDWIDTH CONSIDERATIONS

The practical usefulness of the non-adaptive mode-space beamforming, null steering and sectorally-confined direction finding schemes that have been discussed in this chapter, depends, to a large extent, on our ability to equalise the intrinsic frequency response variations between the excited phase modes which constitute the building blocks in the implementation of the above techniques. One possible solution to the problem is that of narrowband mode alignment, which refers to the calibration of each phase mode over the relevant frequency band, so that a look-up table may be set up and used (in conjunction with possible interpolation) for its alignment at each frequency. This method is instantaneously narrowband in the sense that it is limited to the reception of narrowband signals that must all have the same carrier frequency, which is either known or pre-detected.

Of course if element patterns were controllable (alas, they rarely are) one could try and achieve wideband mode alignment by searching for an ideal element pattern that will flatten, or at least linearise the frequency responses of all phase mode coefficients. A hint to the solution for this somewhat academic pattern control problem has been provided in section 2.4 of chapter 2, where an azimuth element pattern of $(1+\cos\varphi)$ was shown to lead to phase mode coefficients that cannot fall to zero. In fact by examining the asymptotic expression for the relevant Bessel functions of large arguments[10], expression *(2.4.13)* for the μ'th phase mode coefficient takes the form:

$$C_{\mu 0}(\omega,\theta) \sim g_\theta(\theta) e^{-j\pi/4} (2c/\pi\omega R\sin\theta)^{1/2} e^{j(\omega R/c)\sin\theta} \qquad \cdots (3.6.1)$$

which is indeed linear in its phase response, but requires amplitude equalisation for broadband operation. A little thought will reveal the 'optimal' solution for which all phase mode coefficients become linear in phase and invariant in amplitude, only it turns out to be impulsive in φ:

$$g(\theta,\varphi) = g_\theta(\theta) \sum_{i=-\infty}^{\infty} e^{ji\varphi} \qquad \cdots (3.6.2)$$

Under *(3.6.2)* all phase mode coefficients become (see *(2.4.9)*):

---

[10] When the order and argument of $J_{\mu+i}[(\omega R/c)\sin\theta]$ are such that: $|\mu+i| \ll (\omega R/c)\sin\theta$, or equivalently $|\mu+i| \ll M/2$ (for an inter-element spacing smaller than $\lambda/2$ and $\theta = \pi/2$) then:

$$J_{\mu+i}[(\omega R/c)\sin\theta] \sim (2c/\pi\omega R\sin\theta)^{1/2}\cos[(\omega R/c)\sin\theta - \pi/4 - (\mu+i)\pi/2]$$

$$C_{\mu q}(\omega,\theta) \rightarrow \sum_{i=-\infty}^{\infty} j^{\mu+qM} J_{\mu+qM}[(\omega R/c)\sin\theta] = e^{j(\omega R/c)\sin\theta} \qquad \cdots (3.6.3)$$

but this affects all coefficients regardless of order, with the result that each phase mode pattern is given by a series of M impulses at angles $\varphi = 2\pi m/M$, $0 \le m \le M\text{-}1$, which, after all, is to be expected from M impulsive element patterns. The pursuit after the ideal element pattern is further discussed in appendix C.3.

A more pragmatic approach for the broadband alignment of circular-array phase modes to which we devote the rest of this section, involves the separate deconvolution of their dominant coefficients $\{C_{\mu 0}(\omega,\theta_0)\}_\mu$ for a given azimuth cut $\theta=\theta_0$. The required analogue transfer function for the μ'th phase mode filter is accordingly given by:[11]

$$H_\mu(s)|_{s=j\omega} = e^{-j\omega\tau}/C_{\mu 0}(\omega,\pi/2) \quad , \quad \omega_{LO} \le \omega \le \omega_{HI}$$

where the (assumed finite) time delay τ is needed to make the impulse response of $H_\mu(j\omega)$ causal, and ω_{LO} and ω_{HI} are, respectively, the lower and upper frequency in the operating band. The stability of such a filter would depend on the radiation properties of the element patterns. Assuming the latter to be of the form *(2.4.3)* then from *(2.4.11)* we have:

$$C_{\mu 0}(\omega,\pi/2) = \rho j^\mu J_\mu(\frac{\omega R}{c} + j\ln\rho) \qquad \cdots (3.6.4)$$

and the filter's Laplace-domain transfer function is

$$H_\mu(s) = e^{-s\tau}/\rho j^\mu J_\mu[-j(sR/c)+j\ln\rho] \qquad \cdots (3.6.5)$$

Noting that the zeros of a Bessel function of integer order are always real, it follows that for outward directional element patterns characterised by $0<\rho<1$, the poles of $H_\mu(s)$ are located on the left half of the complex s-plane, rendering it stable. In contrast, omnidirectional elements ($\rho = 1$) as well as inward-directional elements ($\rho > 1$) both lead to unstable filter designs.

In the context of discrete time-sampled signals, a corresponding causal digital filter will be stable if and only if the poles of its transfer function $\mathcal{H}_\mu(z)$ all lie inside the unit circle on the complex z-plane. A stable realisation of $\mathcal{H}_\mu(z)$ as $1/\mathcal{D}_\mu(z)$, where $\mathcal{D}_\mu(z)$ is the digital implementation of *(3.6.4)*, therefore depends on $\mathcal{D}_\mu(z)$ having all

11 We henceforth assume: $\theta = \pi/2$ and $h_0(\pi/2) = 1$.

its zeros confined to within the unit circle, which in turn, as we shall shortly see, is again a function of the shape of the element patterns. For the implementation of a causal digital filtering unit $\mathcal{D}_\mu(z)$ having a finite impulse response of length N, and a non-aliased frequency response which, over the bandwidth $0 \le \omega \le \omega_{HI}$, is equal (to within a constant group delay) to $C_{\mu 0}(\omega, \pi/2)$, we must have:

$$\mathcal{D}_\mu(e^{j\omega\Delta t}) = \sum_{p=-\infty}^{\infty} C_{\mu 0}(\omega - 2\pi p/\Delta t, \pi/2) S(\omega\Delta t - 2\pi p) e^{-j(\omega - 2\pi p/\Delta t)(N-1)\Delta t/2} \quad \cdots (3.6.6)$$

where $S(\Omega)$ is a sampling window function which is zero for values of Ω outside the interval $[-2\pi + \omega_{HI}\Delta t, 2\pi - \omega_{HI}\Delta t]$ and Δt is the temporal sampling interval (with $\omega_s = 2\pi/\Delta t$ denoting the sampling frequency)[12] – see *Fig. 3.6.1*. The corresponding transfer function for this filter is then given by:

$$\mathcal{D}_\mu(z) = \mathcal{D}_\mu(|z| e^{j\Omega}) =$$

$$\rho j^\mu z^{-(N-1)/2} \sum_{p=-\infty}^{\infty} S(\Omega - 2\pi p) e^{j\pi p(N-1)} J_\mu[(R/c\Delta t)(\Omega - 2\pi p) + j \ln \frac{\rho}{|z|^{R/c\Delta t}}]$$

$$= \rho j^\mu z^{-(N-1)/2} S(\Omega) J_\mu[\frac{\Omega R}{c\Delta t} + j \ln \frac{\rho}{|z|^{R/c\Delta t}}] \quad , \quad -\omega_{HI}\Delta t \le \Omega \le \omega_{HI}\Delta t \qquad \cdots (3.6.7)$$

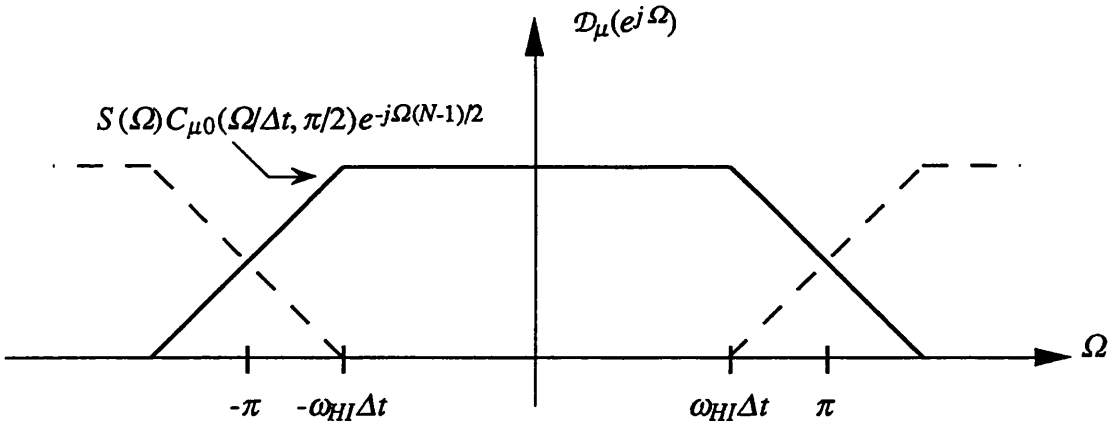

Fig. 3.6.1 Digital implementation of phase mode coefficient response

12 Under the finite-impulse-response assumption (which is later proven), the addition of the delay term $e^{-j\omega\tau}$ to $C_{\mu 0}(\omega, \pi/2)$ with $\tau = (N-1)\Delta t/2$, renders the filter causal.

and it is evident from *(3.6.7)* that the zeros of $\mathcal{D}_\mu(z)$ (and therefore the poles of $\mathcal{H}_\mu(z)$) lie on a circle of radius $\rho^{c\Delta t/R}$ in the complex z-plane. A stable design once more depends on the array elements being outward directional with $\rho < 1$ – see *Fig. 3.6.2.*

In order to adequately describe a single Bessel function $J_\mu(\omega R/c)$ multiplied by a window $S(\omega\Delta t)$ of approximate temporal duration[13] $8\pi/\omega_s$ from its frequency samples, the frequency-sampling period $\Delta\omega = 2\pi/\tau_s$ must be such that:

$$\tau_{HI} < \pi/\Delta\omega \qquad \cdots (3.6.8)$$

where τ_{HI} is the maximum effective extent in the time domain of the convolved expression $\hat{J}_\nu(t)*\hat{S}(t)$, where:

$$\hat{J}_\nu(t) = \frac{1}{2\pi}\int_{-\infty}^{\infty} d\omega e^{j\omega t} J_\nu(\omega R/c) = \begin{cases} \dfrac{(j)^\nu T_\nu(ct/R)}{\pi[(R/c)^2 - t^2]^{1/2}} & |t| < R/c \\ 0 & |t| > R/c \end{cases} \qquad \cdots (3.6.9)$$

$\hat{S}(t)$ is the Fourier transform of $S(\omega\Delta t)$ and $T_\nu(x)$ is the Chebyshev polynomial of the first kind of order ν. Since $\hat{J}_\nu(t)$ and $\hat{S}(t)$ are bounded in the time domain by $|t| < R/c$ and $|t| < 4\pi/\omega_s$ respectively, it follows that:

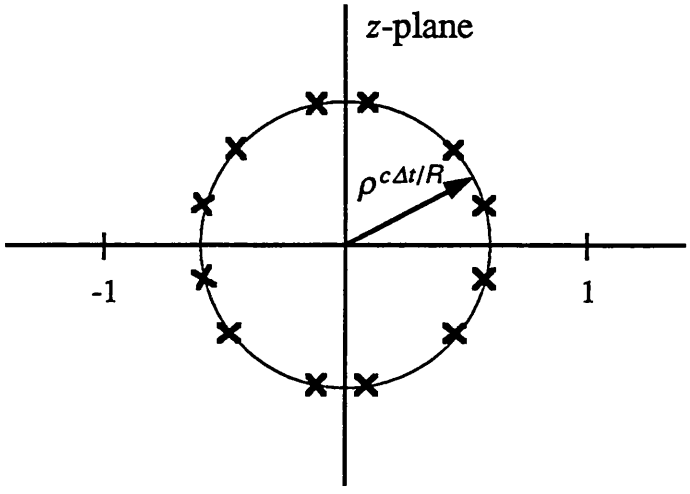

Fig. 3.6.2 Poles of $1/\mathcal{D}_\mu(z)$ on the complex z-plane

[13] This is the null-to-null width of mainlobe + first sidelobes in the Fourier transform of a rectangular window whose cutoff frequencies are at $\omega\Delta t = \pm\pi$

$$t_{HI} = (R/c) + 4\pi/\omega_s \qquad \cdots (3.6.10)$$

which in view of *(3.6.8)* also means that:

$$\tau_s > 2R/c + 8\pi/\omega_s \qquad \cdots (3.6.11)$$

Now, exactly the same argument holds for a Bessel function $J_\mu(\omega R/c)$ of any order. Since each phase mode coefficient is expressible as a sum of such Bessel functions[14], It follows that $\Delta\omega$ is also the frequency sampling period required for the digital representation of $C_{\mu 0}(\omega, \pi/2)S(\omega\Delta t)$, and the fact that it is effectively bounded both in frequency and in time justifies our attempts to implement it as a finite impulse response (FIR) filter. The number of required frequency samples N which defines the order of the filter $\mathcal{D}_\mu(z)$ is given by the inequality:

$$N = \tau_s/\Delta t > 2(2 + R/c\Delta t) \qquad \cdots (3.6.12)$$

whereas the frequency sampling period must not exceed:

$$\Delta\omega = 2\pi/t_s = \frac{\omega_s}{N} < \frac{\omega_s}{4 + \omega_s R/\pi c} \qquad \cdots (3.6.13)$$

Denoting

$$\begin{aligned} \kappa_\tau &= \omega_s/2\omega_{HI} > 1 \\ \kappa_\omega &= \tau_s/2\tau_{HI} > 1 \end{aligned} \qquad \cdots (3.6.14)$$

we can write:

$$N = \lceil 2\kappa_\omega(2 + \kappa_\tau\omega_{HI}R/\pi c) \rceil \qquad \cdots (3.6.15)$$

where $\lceil x \rceil$ the ceiling of x is defined as-

$$\lceil x \rceil = 1 + \mathrm{Int}(x) - \mathrm{Int}[\mathrm{Int}(x+1) - x] \qquad \cdots (3.6.16)$$

Noting that the arcwise inter-element spacing must be kept smaller than 0.5 or even

---

14 This clearly follows from *(2.4.9)* when element patterns are represented by *(2.2.4)*, but it is also the case under the representation *(2.4.3)* by virtue of the identity:

$$J_\mu(\frac{\omega R}{c} + j\ln\rho) = \sum_{i=-\infty}^{\infty} j^i I_i(-\ln\rho) J_{\mu+i}(\frac{\omega R}{c})$$

where $I_\nu(x) = j^{-\nu}J_\nu(jx)$ is the modified Bessel function of the first kind of order ν and argument x

0.4 of a wavelength at the highest operating frequency, we define a third constant κ with a value of about 1.25:

$$\omega_{HI}R/c = \frac{1}{\kappa}(M/2)$$

which allows us to rewrite *(3.6.15)* as:

$$N = \lceil 2\kappa_\omega(2+\frac{\kappa_\tau}{\kappa}M/2\pi) \rceil \qquad \cdots (3.6.17)$$

Assuming: $\kappa = 1.25$, $\kappa_\tau = \kappa_\omega = 1.5$ we thus conclude that an 8-element array would require at least 11 frequency samples, a 16-element array would need no less than 16 samples and 25 frequency samples are the minimum requirement for a 32-element array.[15]

The FIR filter block $\mathcal{D}_\mu(z)$ may be realised in a variety of ways [OPP 76] such as one of the designs based on a frequency sampling structure:

$$\mathcal{D}_\mu(z) = \frac{1 - z^{-N}}{N} \sum_{n=0}^{N-1} \frac{\mathcal{D}_\mu(e^{j\omega_n \Delta t})}{1 - z^{-1} e^{j\omega_n \Delta t}} \qquad \cdots (3.6.18)$$

or in a direct-form implementation, the coefficients for which are obtained via an N-point (inverse) DFT operation on the set of samples $\{\mathcal{D}_\mu(e^{j\omega_n \Delta t})\}_{n=0}^{N-1}$, where:

$$\omega_n \Delta t = \begin{cases} 2\pi n/N & N \text{ odd} \\ 2\pi(n+1/2)/N & N \text{ even} \end{cases} \qquad 0 \le n \le N-1 \qquad \cdots (3.6.19)$$

Explicit expressions for the frequency samples $\{\mathcal{D}_\mu(e^{j\omega_n \Delta t})\}_{n=0}^{N-1}$ are given in appendix C.4, in terms of the μ'th phase mode coefficient as well as in terms of element pattern measurement data.

Two of several possible schemes for realising the μ'th deconvolution filter $\mathcal{H}_\mu(z) = 1/\mathcal{D}_\mu(z)$ are suggested in *Fig. 3.6.3* and *Fig. 3.6.4*. In the first scheme the inverse of the frequency sampling expression *(3.6.18)* is implemented with a minor correction in the form of a parameter $\zeta < 1$ which is close to unity. This parameter is introduced in order to relocate the N common poles and zeros of *(3.6.18)* from the unit circle onto a circle of radius ζ on the complex z-plane [OPP 76], [GOL 69]:

15 The actual number of frequency samples needed may be somewhat higher depending on the exact window function used.

$$\mathcal{H}_\mu(z) = \frac{N}{1-\zeta^N z^{-N}} \left[\sum_{n=0}^{N-1} \frac{\mathcal{D}_\mu(e^{j(2\pi/N)n})}{1-\zeta z^{-1} e^{j(2\pi/N)n}}\right]^{-1}$$

$$= \frac{N}{1-\zeta^N z^{-N}} \left[\sum_{n=0}^{N-1} \frac{\mathcal{D}_\mu(e^{j(2\pi/N)(n+1/2)})}{1-\zeta z^{-1} e^{j(2\pi/N)(n+1/2)}}\right]^{-1} \quad \cdots (3.6.20)$$

and in view of:

$$\mathcal{D}_\mu(e^{j(2\pi/N)(N-n)}) = \mathcal{D}_\mu^*(e^{j(2\pi/N)n}) \qquad 1 \le n \le \lceil N/2 \rceil - 1$$

$$\mathcal{D}_\mu(e^{j(2\pi/N)(N-1-n+1/2)}) = \mathcal{D}_\mu^*(e^{j(2\pi/N)(n+1/2)}) \qquad 0 \le n \le \lceil N/2 \rceil - 1$$

the above structure may be reduced to a network with real weights by implementing the complex poles in second-order sections [Opp 76].

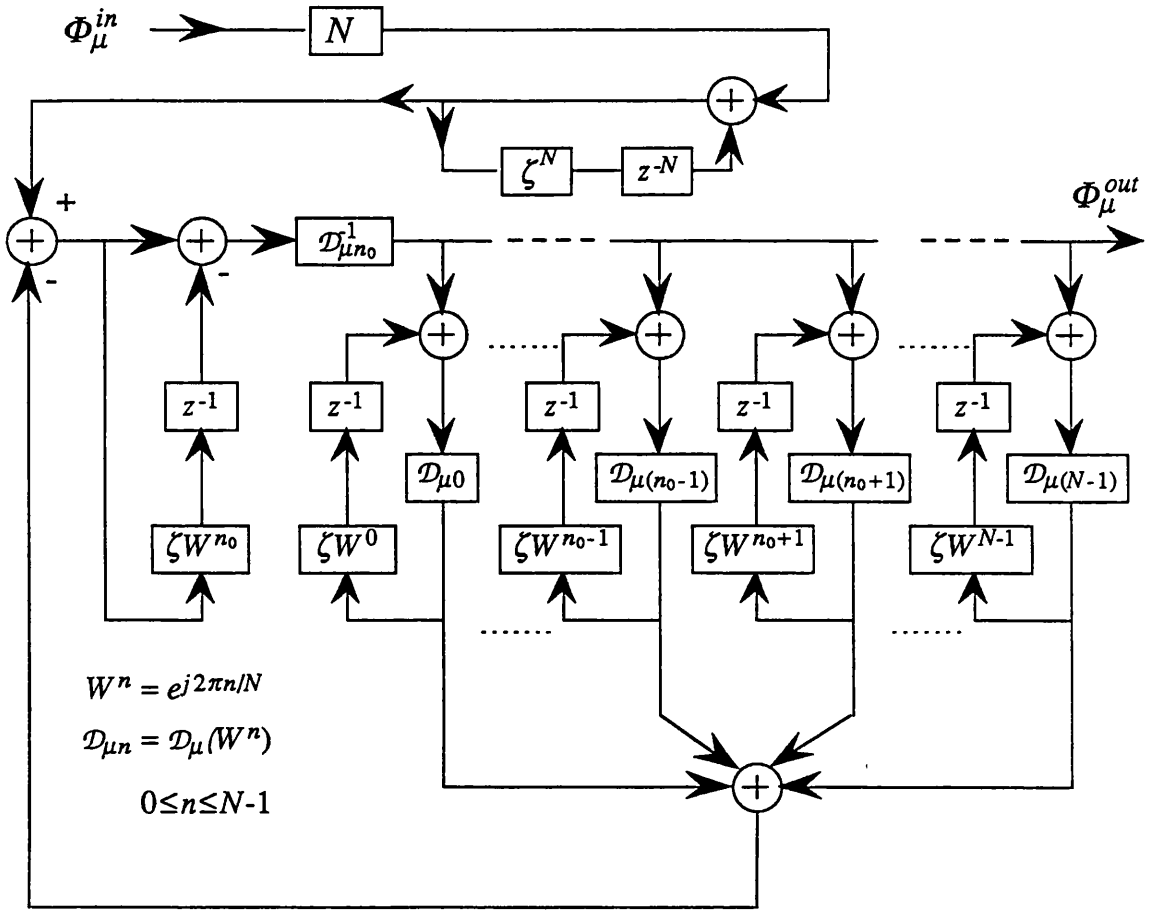

Fig. 3.6.3 IIR frequency-sampling phase mode filter

The second filter shown is a direct-form IIR realisation for which the real impulse-response sequence of the block $\mathcal{D}_\mu(z)$ has to be evaluated:

$$d_{\mu k} = \frac{1}{N}\sum_{n=0}^{N-1} e^{j(2\pi/N)nk}\, \mathcal{D}_\mu(e^{j(2\pi/N)n}) \qquad \cdots (3.6.21)$$

$$= \frac{1}{N}\sum_{n=0}^{N-1} e^{j(2\pi/N)(n+1/2)k}\, \mathcal{D}_\mu(e^{j(2\pi/N)(n+1/2)}) \quad , \quad 0 \le k \le N-1$$

The availability of this sequence also allows us to apply Jury's stability criterion [JUR 64], [ANT 79] in order to ensure the stability of the designed $1/\mathcal{D}_\mu(z)$ filter.

As noted in section 3.2 of this chapter, there is also the option of approximating $\mathcal{H}_\mu(z)$ by a non-recursive (FIR) filter. Since the extent of the Fourier transform of $1/C_{\mu 0}(\omega, \pi/2)$ in the time domain does not equal R/c but rather depends on the exact nature of the array element patterns, the length of the filter's impulse response may have to be determined by simulations. The impulse response sequence itself may be obtained by truncating the infinite series:

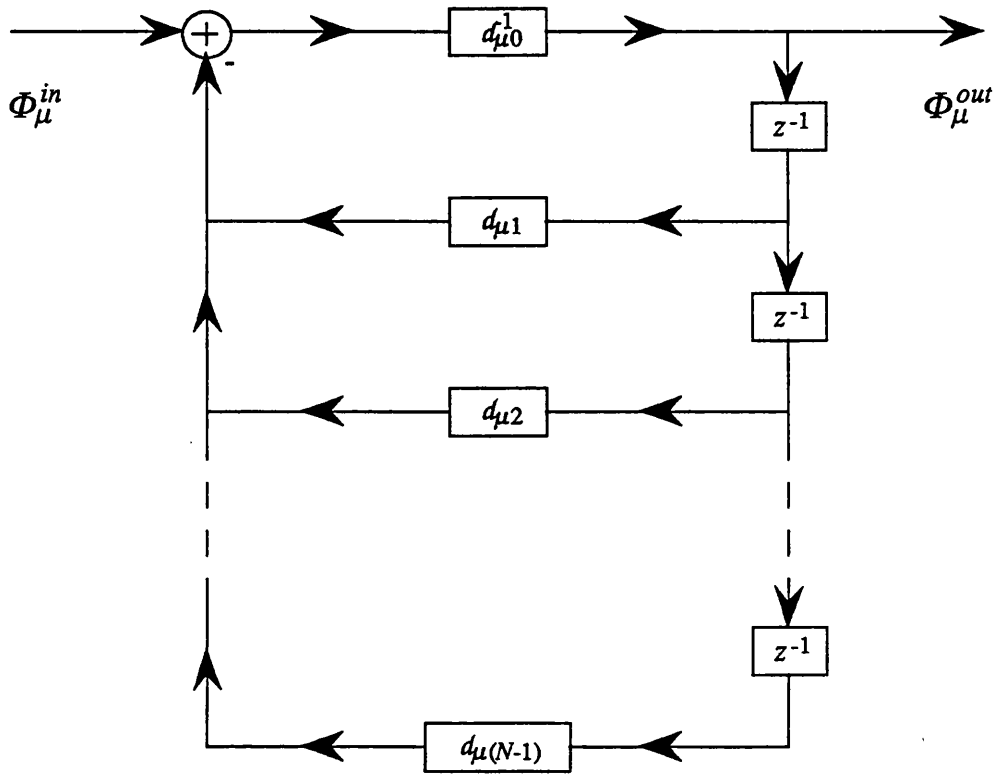

Fig. 3.6.4 IIR phase mode filter: direct-form implementation

$$1/\mathcal{D}_\mu(z) = \sum_{\nu=0}^{\infty} [1-\mathcal{D}_\mu(z)]^\nu$$

at some power $(N_\omega - 1)$ of z^{-1}, where $\mathcal{D}_\mu(z)$ is given by *(3.6.18)*, or the implementation of $\mathcal{H}_\mu(z)$ may be based on the set $\{1/\mathcal{D}_\mu(e^{j\omega_n \Delta t})\}_{n=0}^{N_\omega - 1}$ which are taken as the frequency samples of $\mathcal{H}_\mu(e^{j\omega\Delta t})$. The FIR filter may then be designed in various forms such as a frequency-sampling realisation of

$$\mathcal{H}_\mu(z) = \frac{1 - \zeta^N z^{-N}}{N} \sum_{n=0}^{N-1} \frac{\mathcal{H}_\mu(e^{j\omega_n \Delta t})}{1 - \zeta z^{-1} e^{j\omega_n \Delta t}}$$

with ζ serving the same purpose as in *(3.6.20)*, a direct-form realisation of which the schematic diagram shown in *Fig 3.6.5* below is an example, or a DFT-based realisation as was suggested in *Fig. 3.2.2.*

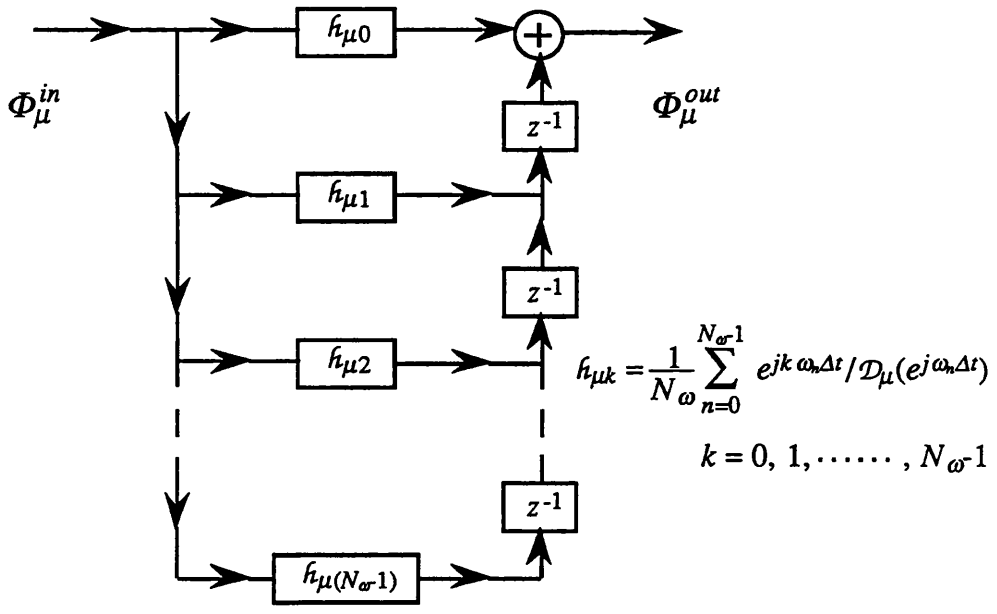

Fig. 3.6.5 FIR phase mode filter: direct-form implementation

3.7 SUMMARY

In this chapter we have been looking into spatial processing techniques for circular arrays based on phase mode analysis, which appear to have practical aspects in the context of digital beamforming. Previously studied beamforming, null-steering and direction finding methods were reviewed and new ideas pertaining to their digital implementation and to their performance over wide bandwidths were examined.

We began with the classic linear-array to circular-array synthesis transformation which, in principle, allows one to produce frequency-independent directional beams. It was however noted that a temporal filtering unit would be needed at the output of each phase mode in order to equalise the frequency characteristics of all zero-order phase mode coefficients. The principles of the multimodal phase-comparison direction finder were subsequently recalled, where it was shown that relying on element pattern symmetry and assuming the phase mode coefficients for modes 0 and 1 to have their arguments differ by less than $\pm\pi/2$, one may obtain unambiguous angular information without the need for mode alignment. Also reviewed were mode-space null forming and null steering methods, leading up to the implementation of a digital multibeam network with one or more steerable nulls

Next, we introduced the idea of transforming the essentially omnidirectional phase modes into a new set of beams which are still linear in phase but directional in their far-field amplitude patterns. It was shown that two multiple sets of such beams, which we named sectoral phase modes, may be used to enhance the immunity of multimodal DF to co-channel interference while retaining its 360° azimuth coverage, and add sectorally-controlled null steering capability to a multibeam system. With the latter application, being based on the linear combination of adjacent sectoral phase modes whose linear-phase characteristics are confined to approximately a $360°/M$ angular sector, the synthesised nulls should be steered within their own sectors.

The viability of broadband mode alignment as the basis for wideband mode-space techniques was finally considered. Following an initial discussion on the quest for the 'ideal' element pattern, a recursive digital scheme was suggested for the de-convolution of zero-order phase mode coefficients, its stability depending on the directional properties of the array elements. The resultant broadband phase modes, as well as beams derived by their linear combination, provide the array with omnidirectional delay matching to incident pulses.

4. PATTERN CORRECTION

4.1 GENERAL

The ability of an array system to meet its design goals largely depends on the sensitivity of its specified performance to variations in the effective illumination of the array aperture. The nominally weighted aperture distribution of amplitudes and phases, which shape and steer the radiated or received beams, is inevitably perturbed by a number of contributing factors both stationary and time varying in nature. Amplitude and phase fluctuations due to internal reflections and to non-ideal transfer characteristics of electronic components, phase-centre displacement and variations in element patterns (such as pattern rolls) due to production tolerances, inter-coupling and site effects, as well as quantisation and thermal noise all effectively modify the weighted aperture excitation, whereas non-linear channel operation and imperfect in-phase/quadrature mixing[1] may introduce spurious responses in both the frequency domain and in beam space. Another important cause for errors which is especially relevant in the sonar context, is ambient noise. As noted in chapter 5, section 5.3, an isotropic or semi-isotropic spatial distribution of independent noise sources will deliver uncorrelated noise[2] to the half-wavelength spaced elements of a linear array. There (and in appendix E.3) we show that although the noise received by circular-array elements will not be uncorrelated, mode-space noise will be uncorrelated when the ambient noise field is azimuthally isotropic and impulsive in elevation.

The effects of random amplitude and phase excitation errors at the aperture of a linear or planar array have been studied in the past [RUZ 52], [RON 59], [SKO 80] where it has been shown that for small uncorrelated errors, the expected value of the array power pattern differs from that of the error-free power pattern by effectively a constant term. That term, which is directly proportional to the sum of the aperture error variances and inversely proportional to the number of array elements, is known

1 This is relevant to arrays employing digital beamforming

2 Two random variables x and y with corresponding expected values $\mathcal{E}x = \bar{x}$ and $\mathcal{E}y = \bar{y}$ are said to be uncorrelated if $\mathcal{E}(x-\bar{x})(y-\bar{y})^* = 0$. By uncorrelated noise at the array elements we mean that for any two elements, the received noise is pairwise uncorrelated.

(with respect to the pattern's peak) as the rms sidelobe level due to errors. In the context of circular arrays of closely spaced sensors, we show in section 4.2 that uncorrelated equi-variance contributions from ambient noise fields to the phase-mode signals will affect the rms sidelobe level of mode-space beams in a very similar manner. Uncorrelated equi-variance aperture errors, on the other hand, generally lead to an angle-dependent rms sidelobe pattern, unless the array elements are omnidirectional. This is shown for amplitude, phase, element displacement and pattern rotation errors in sections 4.3 and 4.4.

Various schemes for monitoring, correcting and maintaining the accuracy of antenna and sonar arrays, have appeared in the calibration literature. Those relevant to arrays with digital beamforming, ordinarily comprise initial pre-deployment calibration measurements and a re-alignment procedure based on a near-field source or on internally injected test signals [BAR 80], [WAR 89], [LON 85a]. The latter procedure is executed prior to, or interlaced with the normal operational deployment of the array, using test equipment attached to or built into the system. Sections 4.5 and 4.6 of this chapter examine ways of re-aligning a digitally-beamformed circular array of a known geometry with given element patterns and channel responses. The idea behind these calibrating algorithms has been inspired by [LON 85b] which deals with the correction of site effects on a phased array radiation pattern. We start by introducing the concept of 'least squares' pattern correction for a single co-phased beam at a single frequency, where a set of correction weights is applied to the array channels. A narrowband correction algorithm for the special case of a single phase mode pattern is then considered, and later extended to include a multimode scheme which involving two sets of correction weights. A similar formulation for a multibeam excitation is then followed, and is shown to be equivalently implementable as a two-stage multimode correction algorithm. Sections 4.7, 4.8 and 4.9 conclude this chapter with wideband versions of the foregoing correction algorithms, a set of simulation plots and a summary of the main results.

4.2 MODE-SPACE EXCITATION ERRORS

Let us consider an M-element circular array excited to form a nominal (i.e. error-free) mode-space beam pattern $F_m(\varphi)$ whose peak is 'scanned' to direction $\varphi_m = (2\pi/M)m$. The beam is synthesised by the linear combination of $(2\Lambda+1)$ of the circular array phase modes $\Phi_{-\Lambda}, \Phi_{-\Lambda+1}, \cdots, \Phi_{\Lambda}$, $\Lambda \leq M/2$. Each of the processed phase modes is assumed to have undergone appropriate alignment, in addition to which it is linearly phased and weighted, as represented (for the μ'th phase mode) by the phasing operator $e^{j(2\pi/M)m\mu}$ and the (possibly complex) weight α_μ. If (for an even M) $\Lambda = M/2$, we assume the alignment of phase mode $\mu = \pm M/2$ to be such that:

$$\frac{\Phi_{M/2}}{C_{(M/2)0}} = \frac{\Phi_{-M/2}}{C_{(M/2)0}} = \cos(M\varphi/2) \; + \; \text{distortion terms}$$

The sensitivity of the array to uncorrelated mode-space errors pertains, as mentioned in section 4.1, to the effect of a circumferentially-isotropic and elevationwise-impulsive ambient noise field. Its analysis, being similar to that relating to linear arrays, is based on the inclusion of a zero-mean phase error ε_μ and a fractional amplitude error κ_μ with each of the summed phase modes in the expression *(3.2.3)* for $F_m(\varphi)$, where the errors are uncorrelated and their variances independent of μ. The perturbed far-field mode-space beam pattern, denoted here by $\mathcal{F}_m(\varphi)$, is given by:

$$\mathcal{F}_m(\varphi) \approx \frac{1}{M^{1/2}} \sum_{\mu=-\Lambda}^{\Lambda} \alpha_\mu (1+\kappa_\mu) e^{j\varepsilon_\mu} e^{-j\mu(\varphi - 2\pi m/M)} \qquad \cdots (4.2.1)$$

and the expected value of $|\mathcal{F}_m(\varphi)|^2$ is clearly given by

$$\mathcal{E}|\mathcal{F}_m(\varphi)|^2 \approx \frac{1}{M} \sum_{\mu'=-\Lambda}^{\Lambda} \sum_{\mu''=-\Lambda}^{\Lambda} \alpha_{\mu'} \alpha_{\mu''}^{*} (1+\kappa_{\mu'})(1+\kappa_{\mu''}) e^{j(\varepsilon_{\mu'} - \varepsilon_{\mu''})} e^{-j(\mu' - \mu'')(\varphi - 2\pi m/M)}$$

$$\cdots (4.2.2)$$

Now, for small errors one can approximately write:

$$\mathcal{E}[(1+\kappa_{\mu'})(1+\kappa_{\mu''}) e^{j(\varepsilon_{\mu'} - \varepsilon_{\mu''})}] \approx (1-\sigma_\varepsilon^2)[1+\sigma^2 \delta(\mu' - \mu'')] \qquad \cdots (4.2.3)$$

where σ_κ^2, σ_ε^2 and σ^2 denote the error variances

$$\begin{matrix}\sigma_\kappa^2 = \mathcal{E}\,\kappa_\mu^2 \\ \sigma_\varepsilon^2 = \mathcal{E}\,\varepsilon_\mu^2\end{matrix} \quad , \quad -\Lambda \le \mu \le \Lambda \qquad \cdots (4.2.4)$$

$$\sigma^2 = (\sigma_\kappa^2 + \sigma_\varepsilon^2)/(1-\sigma_\varepsilon^2) \qquad \cdots (4.2.5)$$

and $\delta(n)$ is the Kronecker delta function. Expression *(4.2.2)* may consequently be rewritten as:

$$\mathcal{E}|\mathcal{F}_m(\varphi)|^2 \approx (1-\sigma_\varepsilon^2)(|F_m(\varphi)|^2 + |\Delta F|^2) \qquad \cdots (4.2.6)$$

where the nominal power pattern $|F_m(\varphi)|^2$ has been augmented by an additional constant term $|\Delta F|^2$ which is given by:

$$|\Delta F|^2 = (\sigma^2/M)\sum_{\mu=-\Lambda}^{\Lambda} |\alpha_\mu|^2 = \frac{\sigma^2}{(2\Lambda+1)\,\mathcal{G}}\,|F_m(2\pi m/M)|^2 \qquad \cdots (4.2.7)$$

with[3]

$$\mathcal{G} = |\sum_{\mu=-\Lambda}^{\Lambda} \alpha_\mu|^2/(2\Lambda+1)\sum_{\mu=-\Lambda}^{\Lambda} |\alpha_\mu|^2 \qquad \cdots (4.2.8)$$

The constant factor $\sigma^2/(2\Lambda+1)\,\mathcal{G}$ multiplying $|F_m(2\pi m/M)|^2$ on the right hand side of *(4.2.7)*, constitutes the *rms sidelobe level* of the mode-space beam, and is seen to be directly proportional to the sum of the error variances, and inversely proportional to the number of phase modes and to the gain factor of the tapered array. A very similar result has been obtained for an M-element linear array under uncorrelated zero-mean amplitude and phase aperture errors, with M substituted for $(2\Lambda+1)$ in the expressions *(4.2.7)* and *(4.2.8)* above.

In the next two sections we shall be examining the effect of uncorrelated equi-variance amplitude and phase errors at the circular array elements, as well as element displacement and pattern rotation errors, on the sidelobe level of mode-space beams.

---

3 $\mathcal{G}$ is commonly referred to in the array literature as the *gain factor*, denoting the relative power per unit solid angle directed, under the given weighting taper, by the array in the direction of its main lobe peak, as compared to the power per unit solid angle directed in that direction by the same array under a uniform taper.

4.3 APERTURE EXCITATION ERRORS

In order to analyse the effect of aperture errors on mode-space beams, we assume as before the presence of uncorrelated zero-mean equi-variance phase and fractional amplitude errors, but this time at the element channels. The receive channel connected to the m'th array element thus includes a random error signal whose phase and fractional amplitude are given by ε_m and κ_m respectively. The expression for the μ'th perturbed phase mode on the azimuth ($\theta = \pi/2$) plane becomes:

$$\Phi_\mu = \frac{1}{M}\sum_{i=-I}^{I} h_i e^{ji\varphi} \sum_{m'=0}^{M-1} (1+\kappa_{m'}) e^{j\varepsilon_{m'}} e^{-j(2\pi/M)(\mu+i)m'} e^{j(\omega R/c)\cos(\varphi - 2\pi m'/M)} \qquad \ldots (4.3.1)$$

and the m'th mode-space beam generated from a set of $(2\Lambda+1)$ modes, is given by:

$$\begin{aligned} \mathcal{F}_m(\varphi) &= \frac{1}{M^{1/2}} \sum_{\mu=-\Lambda}^{\Lambda} [\alpha_\mu / C_{\mu 0}(\omega, \pi/2)] e^{j(2\pi/M)m\mu} \Phi_\mu(\pi/2, \varphi, \omega) \\ &= \frac{1}{M^{3/2}} \sum_{i=-I}^{I} h_i e^{ji\varphi} \sum_{\mu=-\Lambda}^{\Lambda} \frac{\alpha_\mu}{C_{\mu 0}(\omega, \pi/2)} e^{j(2\pi/M)m\mu} \\ &\quad \sum_{m'=0}^{M-1} (1+\kappa_{m'}) e^{j\varepsilon_{m'}} e^{-j(2\pi/M)(\mu+i)m'} e^{j(\omega R/c)\cos(\varphi - 2\pi m'/M)} \qquad \ldots (4.3.2) \end{aligned}$$

where the (finite) Fourier series representation *(2.2.4)* for the element patterns has been used. The expected value of $|\mathcal{F}_m(\varphi)|^2$ is given for small errors by the expression:

$$\begin{aligned} &\mathcal{E}|\mathcal{F}_m(\varphi)|^2 = \\ &\frac{1}{M^3} \sum_{i'=-I}^{I} \sum_{i''=-I}^{I} h_{i'} h_{i''}^* e^{j(i'-i'')\varphi} \sum_{\mu'=-\Lambda}^{\Lambda} \sum_{\mu''=-\Lambda}^{\Lambda} \frac{\alpha_{\mu'} \alpha_{\mu''}^*}{C_{\mu' 0}(\omega, \pi/2) C_{\mu'' 0}^*(\omega, \pi/2)} e^{j(2\pi/M)m(\mu'-\mu'')} \\ &\sum_{m'=0}^{M-1} \sum_{m''=0}^{M-1} \mathcal{E}[(1+\kappa_{m'})(1+\kappa_{m''}) e^{j(\varepsilon_{m'} - \varepsilon_{m''})}] e^{-j(2\pi/M)[(\mu'+i')m' - (\mu''+i'')m'']} e^{j(\chi_{m'} - \chi_{m''})} \\ &\approx (1-\sigma_\varepsilon^2)(|F_m(\varphi)|^2 + |\Delta F_m(\varphi)|^2) \qquad \ldots (4.3.4) \end{aligned}$$

with

$$\chi_m = (\omega R/c)\cos(\varphi - 2\pi m/M) \quad , \quad 0 \le m \le M-1 \qquad \ldots (4.3.5)$$

where use has again been made of *(4.2.3)*. $|F_m(\varphi)|^2$ is the nominal far-field power pattern and $|\Delta F_m(\varphi)|^2$ is an error power pattern which is given by:

$$|\Delta F_m|^2 = \frac{\sigma^2}{M^3}\sum_{i'=-I}^{I}\sum_{i''=-I}^{I} h_{i'}h_{i''}^{*}e^{j(i'-i'')\varphi}\sum_{\mu'=-\Lambda}^{\Lambda}\sum_{\mu''=-\Lambda}^{\Lambda}\frac{\alpha_{\mu'}\alpha_{\mu''}^{*}}{C_{\mu'0}C_{\mu''0}^{*}}e^{j(2\pi/M)m(\mu'-\mu'')}$$

$$\sum_{m'=0}^{M-1} e^{-j(2\pi/M)(\mu'-\mu''+i'-i'')m'}$$

$$= \frac{\sigma^2}{M^2}\sum_{k=-2I}^{2I}\sum_{i=-\min(I,I-k)}^{\min(I,I+k)} h_i h_{i-k}^{*}e^{jk\varphi}\sum_{\nu=-2\Lambda}^{2\Lambda}\sum_{\mu=-\min(\Lambda,\Lambda-\nu)}^{\min(\Lambda,\Lambda+\nu)}\frac{\alpha_\mu\alpha_{\mu-\nu}^{*}}{C_{\mu0}C_{(\mu-\nu)0}^{*}}e^{j(2\pi/M)m\nu}$$

$$\sum_{q=-\infty}^{\infty}\delta(k+\nu+qM) \qquad \cdots (4.3.6)$$

and may also be written as:

$$|\Delta F_m|^2 = \frac{\sigma^2}{M^2}\sum_{q=-\mathrm{Int}[2(I+\Lambda)/M]}^{\mathrm{Int}[2(I+\Lambda)/M]}\sum_{k=-\min(2I,\,2\Lambda+qM)}^{\min(2I,\,2\Lambda-qM)} e^{jk(\varphi-2\pi m/M)}$$

$$\sum_{i=-\min(I,I-k)}^{\min(I,I+k)} h_i h_{i-k}^{*}\sum_{\mu=-\min(\Lambda,\Lambda+k+qM)}^{\min(\Lambda,\Lambda-k-qM)}\frac{\alpha_\mu\alpha_{\mu+k+qM}^{*}}{C_{\mu0}C_{(\mu+k+qM)0}^{*}} \qquad \cdots (4.3.7)$$

As is evident from *(4.3.7)*, random aperture errors lead, in general, to a φ-dependent rms sidelobe pattern, so that different rms levels of spurious sidelobes are expected at different directions. However in the case of omnidirectional elements, $I = 0$ and we are once more left with a constant rms error level, though this time it is given by:

$$|\Delta F_m|^2 \xrightarrow[I=0]{} |\Delta F|^2 = \frac{\sigma^2}{M^2}|h_0|^2\sum_{\mu=-\Lambda}^{\Lambda}|\alpha_\mu|^2/|C_{\mu0}|^2$$

$$\approx \frac{\sigma^2}{(2\Lambda+1)\mathcal{G}}\left[\sum_{\mu=-\Lambda}^{\Lambda}|\alpha_\mu/J_{\mu0}(\omega R/c)|^2/M\sum_{\mu=-\Lambda}^{\Lambda}|\alpha_\mu|^2\right]|F_m(2\pi m/M)|^2 \qquad \cdots (4.3.8)$$

where $\mathcal{G}$ is given by *(4.2.8)*.

The effects of element displacement and pattern rotation errors on the rms sidelobe level of mode-space beams are treated next in section 4.4.

4.4 ELEMENT DISPLACEMENT AND PATTERN ROTATION ERRORS

Displacement and rotational errors respectively refer to the random radial and/or angular deviation of each element from its nominal equi-spaced position in the array, and to the random angular roll of element patterns from their nominal orientation. In order to assess the effect of such errors let us re-examine the mode-space beam pattern of section 4.3 under an error model in which the phase centre of the m'th radiating element is displaced radially by Rr_m, and angularly by β_m and the radiation pattern of that element is rotated about the array centre through a random angle of ψ_m. The μ'th phase mode is then expressible as:

$$\Phi_\mu = \frac{1}{M}\sum_{i=-I}^{I} h_i e^{ji\varphi} \sum_{m'=0}^{M-1} e^{j\psi_{m'}} e^{-j(2\pi/M)(\mu+i)m'} e^{j(\omega R/c)(1+r_{m'})\cos(\varphi-\beta_{m'}-2\pi m'/M)} \quad \ldots (4.4.1)$$

and the m'th mode-space generated beam is given by:

$$\begin{aligned}\mathcal{F}_m(\varphi) &= \frac{1}{M^{1/2}}\sum_{\mu=-\Lambda}^{\Lambda} [\alpha_\mu / C_{\mu 0}(\omega, \pi/2)] e^{j(2\pi/M)m\mu} \Phi_\mu(\pi/2, \varphi, \omega) \\ &= \frac{1}{M^{3/2}}\sum_{i=-I}^{I} h_i e^{ji\varphi} \sum_{\mu=-\Lambda}^{\Lambda} \frac{\alpha_\mu}{C_{\mu 0}(\omega, \pi/2)} e^{j(2\pi/M)m\mu} \\ &\quad \sum_{m'=0}^{M-1} e^{j\psi_{m'}} e^{-j(2\pi/M)(\mu+i)m'} e^{j(\omega R/c)(1+r_{m'})\cos(\varphi-\beta_{m'}-2\pi m'/M)} \quad \ldots (4.4.2)\end{aligned}$$

Taking the expected value of $|\mathcal{F}_m(\varphi)|^2$ for small errors as before we obtain

$$\begin{aligned}&\mathcal{E}|\mathcal{F}_m(\varphi)|^2 = \\ &\frac{1}{M^3}\sum_{i'=-I}^{I}\sum_{i''=-I}^{I} h_{i'} h_{i''}^* e^{j(i'-i'')\varphi} \sum_{\mu'=-\Lambda}^{\Lambda}\sum_{\mu''=-\Lambda}^{\Lambda} \frac{\alpha_{\mu'}\alpha_{\mu''}^*}{C_{\mu' 0}(\omega, \pi/2) C_{\mu'' 0}^*(\omega, \pi/2)} e^{j(2\pi/M)m(\mu'-\mu'')} \\ &\sum_{m'=0}^{M-1}\sum_{m''=0}^{M-1} e^{-j(2\pi/M)[(\mu'+i')m'-(\mu''+i'')m'']} \mathcal{E}[e^{j(\psi_{m'}-\psi_{m''})} \\ &e^{j[\chi_{m'}(1+r_{m'})\cos\beta_{m'}-\chi_{m''}(1+r_{m''})\cos\beta_{m''}]} e^{j[\xi_{m'}(1+r_{m'})\sin\beta_{m'}-\xi_{m''}(1+r_{m''})\sin\beta_{m''}]} \\ &\qquad \ldots (4.4.3)\end{aligned}$$

where,

$$\xi_m = (\omega R/c)\sin(\varphi - 2\pi m/M) \quad , \quad 0 \le m \le M-1 \qquad \cdots (4.4.4)$$

It is not hard to see that rotational errors in *(4.4.3)* play the same role as the phase errors in *(4.3.4)*. Consequently, when only amplitude, phase and rotational errors are present we have, for small zero-mean equi-variance uncorrelated errors:

$$\mathcal{E}|F_m(\varphi)|^2 \approx (1-\sigma_\varepsilon^2-\sigma_\psi^2)(|F_m(\varphi)|^2+|\Delta F_m(\varphi)|^2) \qquad \cdots (4.4.5)$$

where,

$$\mathcal{E}\psi_m^2 = \sigma_\psi^2 \quad , \quad 0 \le m \le M-1 \qquad \cdots (4.4.6)$$

$|F_m(\varphi)|^2$ is the nominal m'th modal pattern and the error power pattern $|\Delta F_m(\varphi)|^2$ is given by *(4.3.7)* with σ^2 defined as:

$$\sigma^2 = (\sigma_\kappa^2+\sigma_\varepsilon^2+\sigma_\psi^2)/(1-\sigma_\varepsilon^2-\sigma_\psi^2) \qquad \cdots (4.4.7)$$

Finally, we account for displacement errors by making the usual assumption of small zero-mean equi-variance uncorrelated random errors, while also letting:

$$\mathcal{E}r_m^2 = \mathcal{E}\beta_m^2 = \sigma_r^2 \quad , \quad 0 \le m \le M-1 \qquad \cdots (4.4.8)$$

We may then approximate,

$$\mathcal{E}e^{j[\chi_{m'}(1+r_{m'})\cos\beta_{m'}-\chi_{m''}(1+r_{m''})\cos\beta_{m''}]}e^{j[\xi_{m'}(1+r_{m'})\sin\beta_{m'}-\xi_{m''}(1+r_{m''})\sin\beta_{m''}]} \approx$$

$$e^{j(1-\sigma_r^2/2)(\chi_{m'}-\chi_{m''})}[1-\sigma_r^2+\sigma_r^2\,\delta(m'-m'')] \qquad \cdots (4.4.9)$$

and therefore, when all errors are included, $\mathcal{E}|\mathcal{F}_m(\varphi)|^2$ takes the form:

$$\mathcal{E}|\mathcal{F}_m(\varphi)|^2 \approx (1-\sigma_\varepsilon^2-\sigma_\psi^2-\sigma_r^2)(|\tilde{F}_m(\varphi)|^2+|\Delta F_m(\varphi)|^2) \qquad \cdots (4.4.10)$$

where $\tilde{F}_m(\varphi)$ is the nominal m'th mode-space pattern of the array at a modified radius of $(1-\sigma_r^2/2)^{1/2}R$ and $|\Delta F_m(\varphi)|^2$ is given by *(4.3.7)* with σ^2 defined as:

$$\sigma^2 = (\sigma_\kappa^2+\sigma_\varepsilon^2+\sigma_\psi^2+\sigma_r^2)/(1-\sigma_\varepsilon^2-\sigma_\psi^2-\sigma_r^2) \qquad \cdots (4.4.11)$$

4.5 SINGLE-PATTERN CORRECTION

The effect of aperture errors on the array performance may be alleviated by incorporating one or more correction units in the design of the system. Each correction unit comprises a set of complex weights, so selected as to align one or more of the array patterns, in the least squares sense, with its desired spatial responses.[4] In its simplest form schematically illustrated in *Fig. 4.5.1*, such an error compensation scheme may be used to correct a single beam-cophased pattern. Here M complex weights $\{v_0, v_1, \cdots, v_{M-1}\}$ modify the corresponding M element channel signals, which are then phased, weighted and summed to form a single output beam.[5] Sampling the desired far-field radiation pattern $F(\varphi)$ at L equally-spaced observation angles[6]

$$\varphi_\ell = (2\pi/L)\ell \quad , \quad \ell = 0, 1, \cdots, L\text{-}1 \qquad \cdots (4.5.1)$$

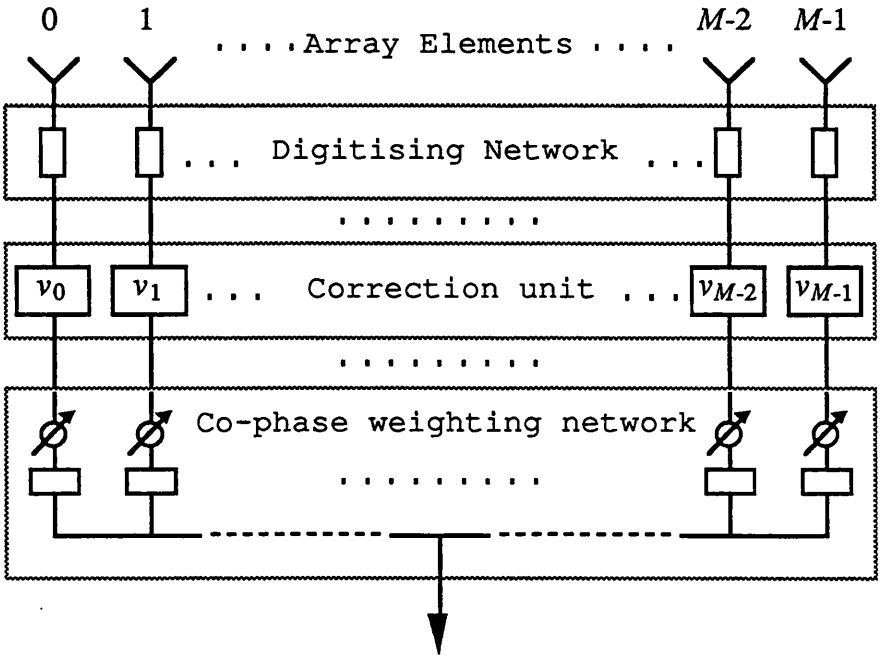

Fig. 4.5.1 Single beam co-phased correction

4 We restrict our discussion to azimuth-plane pattern correction, with the elevation angle being kept constant at $\theta = \pi/2$.

5 The functions of the correction unit and of the co-phase weighting unit may of course be combined in a single complex weighting unit.

6 A different range of angles and different angular spacings (say, uniform in $\sin\varphi$ space) may be chosen, especially in the case of a linear array.

where in general $L > M$, the required set of weights is found by solving, in the least squares sense, the following matrix equation:

$$\mathbf{G}\mathbf{K}\boldsymbol{v} = \boldsymbol{F} \qquad \cdots (4.5.2)$$

where:

$$\boldsymbol{v} = [v_0\ v_1 \cdots v_m \cdots v_{M-1}]^T \qquad \cdots (4.5.3)$$

$$\boldsymbol{F} = [F(\varphi_0)\ F(\varphi_1) \cdots F(\varphi_\ell) \cdots F(\varphi_{L-1})]^T \qquad \cdots (4.5.4)$$

$\mathbf{K}$ is a diagonal $M \times M$ co-phase weighting matrix whose mm'th element is given in the case of a circular array (for $\tilde{\theta} = \pi/2$) by *(2.2.3)*, and $\mathbf{G}$ is an $L \times M$ element pattern matrix available from calibration measurements, whose ℓm'th element is given by:

$$[G]_{\ell m} = M^{-1/2}\, e^{j(\omega R/c)\cos[2\pi(\ell/L - m/M)]}\, g[\pi/2, 2\pi(\ell/L - m/M), \omega]$$
$$0 \le \ell \le L-1 \quad , \quad 0 \le m \le M-1 \qquad \cdots (4.5.5)$$

The optimal vector $\boldsymbol{v}$ is obtained from *(4.5.2)* by minimising the following cost function expression:

$$\mathcal{E} = [\boldsymbol{v}^H\mathbf{K}^H\mathbf{G}^H - \boldsymbol{F}^H]\mathbf{W}[\mathbf{G}\mathbf{K}\boldsymbol{v} - \boldsymbol{F}] \qquad \cdots (4.5.6)$$

where $\mathbf{W}$ is an $L \times L$ real diagonal weighting matrix whose elements may be chosen, for satisfactory sidelobe performance down to a level of η dB below the peak of the main lobe, as:

$$[W]_{\ell\ell} = 1/\max[10^{-\eta/10}, |F(\varphi_\ell)/F(\varphi_{\ell_0})|^2] \quad , \quad 0 \le \ell \le L-1 \qquad \cdots (4.5.7)$$

$$|F(\varphi_{\ell_0})|^2 = \max[|F(\varphi_0)|^2, |F(\varphi_1)|^2, \cdots, |F(\varphi_{L-1})|^2] \qquad \cdots (4.5.8)$$

Taking the 'complex gradient' with respect to $\boldsymbol{v}^H$ and equating to zero[7] we obtain the standard least-squares solution to the above problem:

$$\boldsymbol{v} = [\mathbf{K}^H\mathbf{G}^H\mathbf{W}\mathbf{G}\mathbf{K}]^{-1}\mathbf{K}^H\mathbf{G}^H\mathbf{W}\boldsymbol{F} \qquad \cdots (4.5.9)$$

Note that the evaluated weight vector $\boldsymbol{v}$ is only optimal with respect to the target pattern $\boldsymbol{F}$. In section 4.6 we shall be looking at ways of handling the simultaneous

7 The concept of complex gradient is defined and explained in [Bra 83].

correction of a number of beams. But before we do that, let us first apply the same concept for the correction of a single circular-array phase mode. The μ'th uncorrected phase mode $\Phi_\mu(\pi/2, \varphi, \omega)$ and the target mode pattern $\Psi_\mu(\varphi)$ will be represented by the $L\times 1$ vectors:

$$\boldsymbol{\Phi}_\mu = [\Phi_\mu(\pi/2, 0, \omega) \cdots \Phi_\mu(\pi/2, \tfrac{2\pi}{L}\ell, \omega) \cdots \Phi_\mu(\pi/2, \tfrac{2\pi}{L}(L\text{-}1), \omega)]^T \qquad \cdots (4.5.10)$$

$$\boldsymbol{\Psi}_\mu = [\Psi_\mu(0) \cdots\cdots \Psi_\mu(\tfrac{2\pi}{L}\ell) \cdots\cdots \Psi_\mu(\tfrac{2\pi}{L}(L\text{-}1))]^T$$
$$= [1 \cdots\cdots e^{-j(2\pi/L)\mu\ell} \cdots\cdots e^{-j(2\pi/L)\mu(L-1)}]^T \qquad \cdots (4.5.11)$$

and our aim is to find a 'pre-DFT' correction vector $\boldsymbol{v}$ of complex weights, which we shall apply, as illustrated in *Fig. 4.5.2*, to the outputs of the array channels prior to the formation of modes such that the expression

$$\mathcal{E} = |\mathbf{G}\mathbf{E}_\mu^H \boldsymbol{v} - \boldsymbol{\Psi}_\mu|^2 = [\boldsymbol{v}^H \mathbf{E}_\mu \mathbf{G}^H - \boldsymbol{\Psi}_\mu^H][\mathbf{G}\mathbf{E}_\mu^H \boldsymbol{v} - \boldsymbol{\Psi}_\mu] \qquad \cdots (4.5.12)$$

is minimised. In *(4.5.12)* above, $\mathbf{E}_\mu$ is an $M\times M$ diagonal mode forming matrix for the μ'th phase mode, whose mm'th element is given by:

$$[E_\mu]_{mm} = e^{j(2\pi/M)\mu m} \quad , \quad 0 \le m \le M\text{-}1 \qquad \cdots (4.5.13)$$

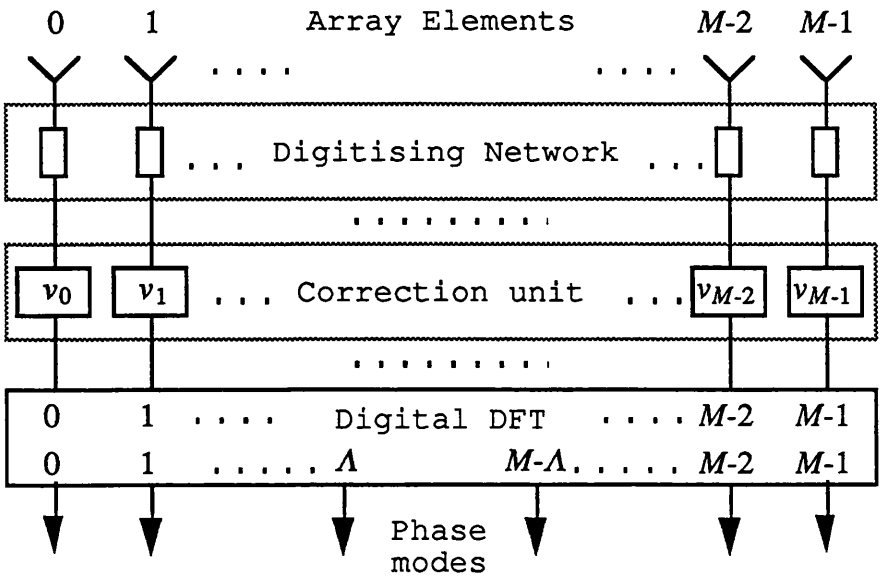

Fig. 4.5.2 Single mode correction

Note that since the target pattern is omnidirectional in amplitude, there is no need for a weighting matrix. $\boldsymbol{v}$ is obtained as before by differentiating $\mathcal{E}$ with respect to $\boldsymbol{v}^H$ and equating to zero. The mode-dependent result is:

$$\boldsymbol{v} = \mathbf{E}_\mu[\mathbf{G}^H\mathbf{G}]^{-1}\mathbf{G}^H\boldsymbol{\Psi}_\mu \qquad \cdots (4.5.14)$$

and the single corrected phase mode $\hat{\boldsymbol{\Phi}}_\mu$ is given by:

$$\hat{\boldsymbol{\Phi}}_\mu = \mathbf{G}\mathbf{E}_\mu^H\boldsymbol{v} = \mathbf{G}[\mathbf{G}^H\mathbf{G}]^{-1}\mathbf{G}^H\boldsymbol{\Psi}_\mu \qquad \cdots (4.5.15)$$

One rather complex scheme for the simultaneous correction of more than one phase mode is suggested in *Fig 4.5.3*. It is based on *(4.5.15)*, rewritten as

$$\hat{\Phi}_\mu(\pi/2, \varphi_\ell, \omega) = \sum_{k=0}^{L-1}\{\sum_{m=0}^{M-1}[G]_{\ell m}[\Gamma]_{mk}\}e^{-j(2\pi/L)\mu k} \quad , \quad 0\le\ell\le L\text{-}1 \cdots (4.5.16)$$

with $[\Gamma]_{mk}$ denoting the mk'th element of $\Gamma = [\mathbf{G}^H\mathbf{G}]^{-1}\mathbf{G}^H$. The above expression indeed constitutes an L-point DFT as implemented in *Fig. 4.5.3*. A more elegant multimode scheme based on a two-stage correction is the subject of section 4.6.

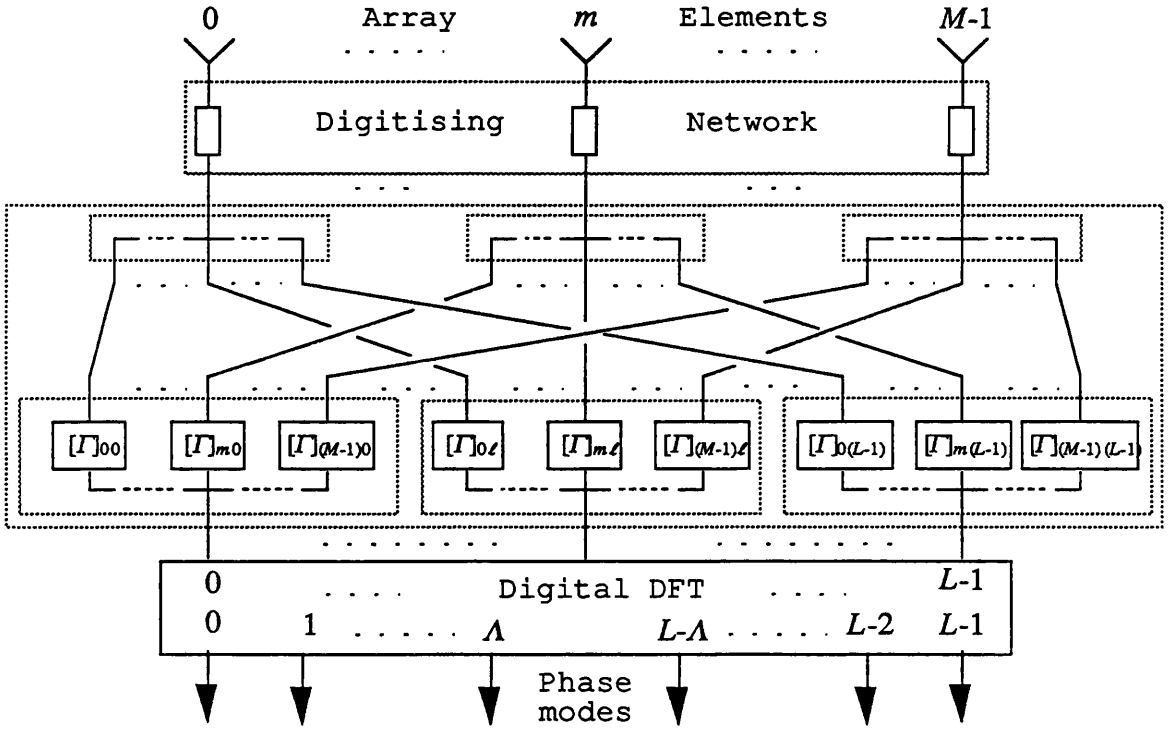

Fig. 4.5.3 Multimode correction using a pre-DFT matrix

4.6 MULTI-PATTERN CORRECTION

Although the pre-DFT weight vector $\boldsymbol{v}$ as given by *(4.5.14)* is phase-mode dependent and may not provide simultaneous correction for more than one phase mode, we may try and find another 'global' weight vector that will minimise the deviation of a prescribed set of phase modes from their respective ideal patterns. Noting that for an error-free circular array:

$$\mathbf{G}\mathbf{E}_\mu\,[1\,1\cdots 1]^T \approx \Psi_\mu M^{1/2} C_{\mu 0}(\omega, \pi/2) \quad , \quad -\Lambda \le \mu \le \Lambda$$

it appears reasonable to add a second set

$$\boldsymbol{u} = [u_{-\Lambda}\, u_{-\Lambda+1} \cdots u_\mu \cdots u_\Lambda]^T \qquad \cdots (4.6.1)$$

of complex weights at the output of the DFT unit of *Fig. 4.5.2*, which we shall refer to as post-DFT correction weights. This scheme, which is illustrated in *Fig. 4.6.1*, is more easily implemented that the one suggested in *Fig. 4.5.3*, and moreover a post-DFT weighting unit would in any case be needed for the purpose of mode alignment and for the possible application of an additional (amplitude) taper in the implementation of low-sidelobe mode-space radiation beams.

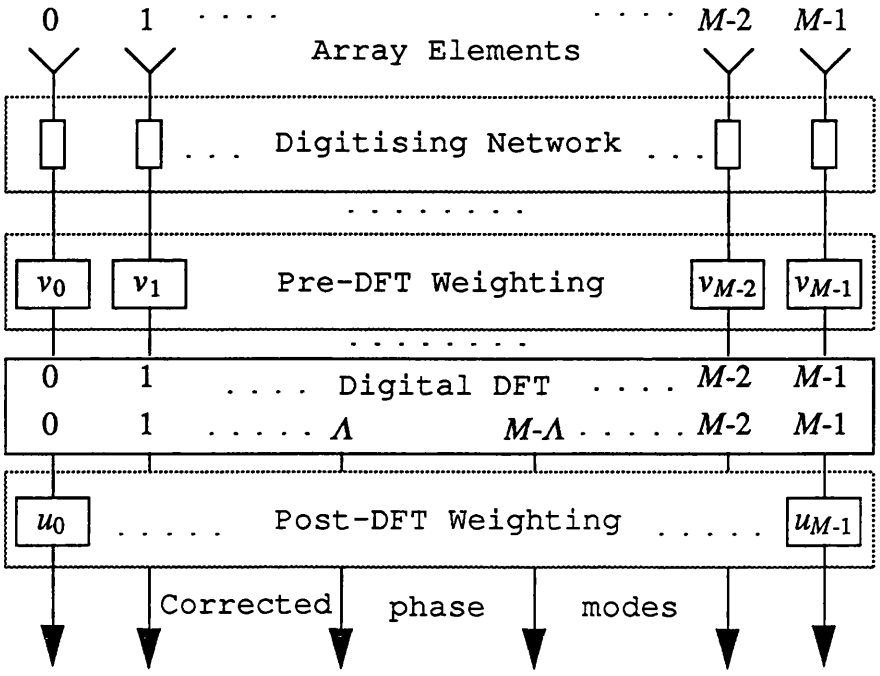

Fig. 4.6.1 Two-stage multimode correction

We thus seek a new pre-DFT weight vector $\boldsymbol{v}$ which minimises the expression:

$$\mathcal{E} = \sum_{\mu=-\Lambda}^{\Lambda} [\boldsymbol{v}^H \mathbf{E}_\mu \mathbf{G}^H - \gamma_\mu^* \boldsymbol{\Psi}_\mu^H][\mathbf{G}\mathbf{E}_\mu^H \boldsymbol{v} - \boldsymbol{\Psi}_\mu \gamma_\mu] \qquad \cdots (4.6.2)$$

where

$$\gamma_0 = 1 \qquad \cdots (4.6.3)$$

and $\{\gamma_\mu\}_{\mu=-\Lambda}^{\Lambda} = \{1/u_\mu\}_{\mu=-\Lambda}^{\Lambda}$ is the second set of minimisation parameters. Differentiating with respect to $\boldsymbol{v}^H$ and $\{\gamma_\mu^*\}_{\mu\neq 0}$ and equating to zero leads to the following result (refer to appendix D.1 for details):

$$\boldsymbol{v} = [\mathbf{G}^H\mathbf{G} + \sum_{\substack{\mu=-\Lambda \\ \mu\neq 0}}^{\Lambda} \mathbf{E}_\mu(\mathbf{G}^H\mathbf{G} - L^{-1}\mathbf{G}^H\boldsymbol{\Psi}_\mu\boldsymbol{\Psi}_\mu^H\mathbf{G})\mathbf{E}_\mu^H]^{-1}\,\mathbf{G}^H\boldsymbol{\Psi}_0 \qquad \cdots (4.6.4)$$

and the corrected (but as yet mis-aligned) phase mode patterns $\{\hat{\boldsymbol{\Phi}}_\mu\}_{\mu=-\Lambda}^{\Lambda}$ are given by:

$$\hat{\boldsymbol{\Phi}}_\mu = \mathbf{G}\mathbf{E}_\mu^H\boldsymbol{v}$$

$$= \mathbf{G}\mathbf{E}_\mu^H[\mathbf{G}^H\mathbf{G} + \sum_{\substack{\mu=-\Lambda \\ \mu\neq 0}}^{\Lambda} \mathbf{E}_\mu(\mathbf{G}^H\mathbf{G} - L^{-1}\mathbf{G}^H\boldsymbol{\Psi}_\mu\boldsymbol{\Psi}_\mu^H\mathbf{G})\mathbf{E}_\mu^H]^{-1}\,\mathbf{G}^H\boldsymbol{\Psi}_0 \qquad \cdots (4.6.5)$$

The set of post-DFT alignment will now be evaluated in two slightly different ways:

i As part of the minimisation process of expression *(4.6.2)* which in addition to *(4.6.4)* (see equation *(D.1.2)* in appendix D.1) also yields:

$$u_\mu = \frac{1}{\gamma_\mu} = \frac{L}{\boldsymbol{\Psi}_\mu^H\hat{\boldsymbol{\Phi}}_\mu} = [\frac{1}{L}\sum_{\ell=0}^{L-1} \hat{\Phi}_\mu(\pi/2, 2\pi\ell/L, \omega)\, e^{j(2\pi/L)\mu\ell}]^{-1}$$

$$\mu = 0, \pm 1, \cdots\cdots, \pm\Lambda \qquad \cdots (4.6.6)$$

ii By the application of the following 'least squares' minimisation process to each mode:

$$|\hat{\boldsymbol{\Phi}}_\mu u_\mu - \boldsymbol{\Psi}_\mu|^2 \rightarrow \min \quad , \quad -\Lambda \leq \mu \leq \Lambda \qquad \cdots (4.6.7)$$

which leads to:

$$u_\mu = \frac{\hat{\Phi}_\mu^H \Psi_\mu}{|\hat{\Phi}_\mu|^2} = \frac{\sum_{\ell=0}^{L-1} \Phi_\mu^*(\pi/2, 2\pi\ell/L, \omega) e^{-j(2\pi/L)\mu\ell}}{\sum_{\ell=0}^{L-1} |\Phi_\mu(\pi/2, 2\pi\ell/L, \omega)|^2}$$

$$\mu = 0, \pm 1, \cdots, \pm\Lambda \qquad \cdots (4.6.8)$$

This last option, as we now show, is also optimal for the correction of a multiple set of mode-space beams. Such an arrangement is schematically illustrated in *Fig. 4.6.2*, with the post-DFT alignment unit being also used for controlling the mode-space 'aperture' illumination. Consider the following set of target beams:

$$F_m = \sum_{\mu=-\Lambda}^{\Lambda} \Psi_\mu \alpha_\mu e^{j(2\pi/M)m\mu} = \Psi \Xi_m \alpha \quad , \quad 0 \le m \le M-1 \qquad \cdots (4.6.9)$$

where

$$\Psi = [\Psi_{-\Lambda} \cdots\cdots \Psi_0 \cdots\cdots \Psi_\Lambda] \qquad \cdots (4.6.10)$$

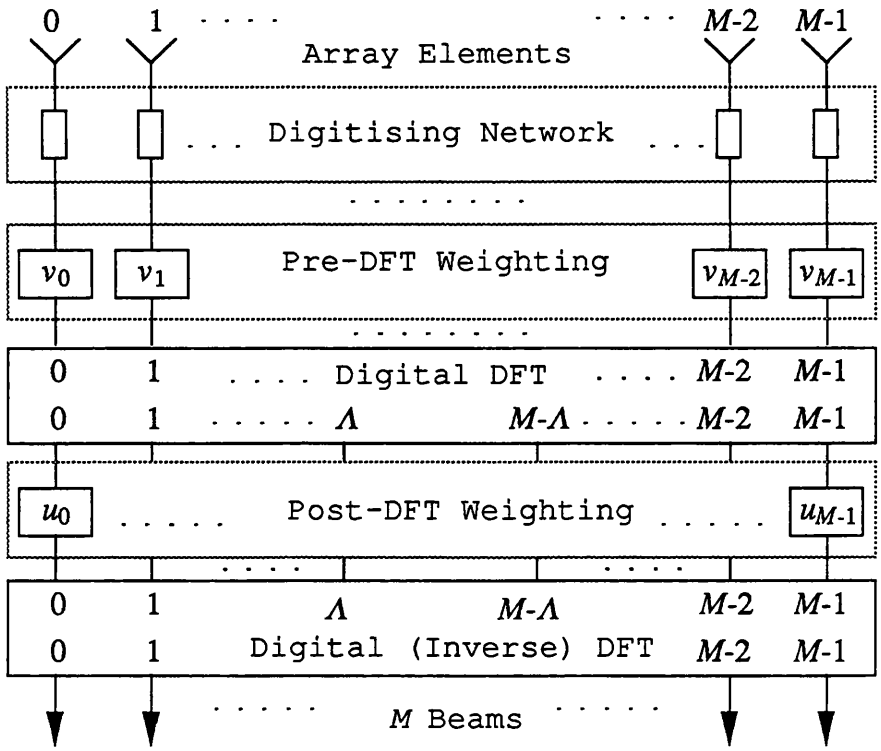

Fig. 4.6.2 Two-stage mode-space multibeam correction

and each Ξ_m is a diagonal $(2\Lambda+1)\times(2\Lambda+1)$ matrix whose elements are given by:

$$[\Xi_m]_{\mu\mu} = e^{j(2\pi/M)m\mu} \quad , \quad -\Lambda \le \mu \le \Lambda \qquad \cdots (4.6.11)$$

Assuming that the availability of the pre-DFT correction weights, and consequently also of the corrected (but mis-aligned) phase modes via *(4.3.14)* and *(4.3.15)* respectively, we seek a vector $\boldsymbol{u}$ of post-DFT weights which will minimise the following cost function:

$$\mathcal{E} = \sum_{m=0}^{M-1} [\boldsymbol{u}^H \Xi_m^H \hat{\boldsymbol{\Phi}}^H - \boldsymbol{\alpha}^H \Xi_m^H \boldsymbol{\Psi}^H] \mathbf{W} [\hat{\boldsymbol{\Phi}} \Xi_m \boldsymbol{u} - \boldsymbol{\Psi} \Xi_m \boldsymbol{\alpha}] \qquad \cdots (4.6.12)$$

where,

$$\hat{\boldsymbol{\Phi}} = [\hat{\boldsymbol{\Phi}}_{-\Lambda} \cdots\cdots \hat{\boldsymbol{\Phi}}_0 \cdots\cdots \hat{\boldsymbol{\Phi}}_{\Lambda}] \qquad \cdots (4.6.13)$$

$$\boldsymbol{\alpha} = [\alpha_{-\Lambda} \cdots\cdots \alpha_0 \cdots\cdots \alpha_{\Lambda}]^T \qquad \cdots (4.6.14)$$

and $\mathbf{W}$ is a real diagonal weighting matrix. Minimisation of $\mathcal{E}$ with respect to $\boldsymbol{u}$ yields:

$$[\sum_{m=0}^{M-1} \Xi_m^H \hat{\boldsymbol{\Phi}}^H \mathbf{W} \hat{\boldsymbol{\Phi}} \Xi_m] \boldsymbol{u} = [\sum_{m=0}^{M-1} \Xi_m^H \hat{\boldsymbol{\Phi}}^H \mathbf{W} \boldsymbol{\Psi} \Xi_m] \boldsymbol{\alpha} \qquad \cdots (4.6.15)$$

and since for every $(2\Lambda+1)\times(2\Lambda+1)$ matrix $\mathbf{A}$, the following is true when $\Lambda < M/2$:

$$\frac{1}{M} \sum_{m=0}^{M-1} \Xi_m \mathbf{A} \Xi_m^H = \mathrm{diag}(\mathbf{A}) \qquad \cdots (4.6.16)$$

Expression *(4.6.15)* leads to:

$$\mathrm{diag}(\hat{\boldsymbol{\Phi}}^H \mathbf{W} \hat{\boldsymbol{\Phi}}) \boldsymbol{u} = \mathrm{diag}(\hat{\boldsymbol{\Phi}}^H \mathbf{W} \boldsymbol{\Psi}) \boldsymbol{\alpha} \qquad \cdots (4.6.17)$$

which may also be written as:

$$u_\mu = (\hat{\boldsymbol{\Phi}}_\mu^H \boldsymbol{\Psi}_\mu / |\hat{\boldsymbol{\Phi}}_\mu|^2) \alpha_\mu \quad , \quad -\Lambda \le \mu \le \Lambda \qquad \cdots (4.6.18)$$

which is exactly *(4.6.8)* cascaded with the corresponding mode-space weighting taper.

4.7 WIDEBAND CORRECTION

In the pattern correction algorithms outlined so far, narrowband operation of the array over a constant elevation cone has been assumed. The element pattern matrix was defined in *(4.5.5)* for a single frequency ω and a constant elevation angle $\theta = \pi/2$ at which the performance of the compensated array was subsequently optimised. This approach may suffice for narrowband operation over a limited elevation range, or in applications where the elevation bearing of the received signal is known and its frequency is either known (e.g. hops in a known sequence) or pre-detected. The correction scheme may then be independently performed at a number of frequencies at the prescribed elevation angle (at which element pattern measurement data must be available) and a corresponding set of look-up weight vectors constructed. In most other instances a single weight vector must cater for the whole frequency band and over some finite range of elevation angles.

The simplest approach for correcting a broadband array is by averaging over both frequency and elevation range. This option is reasonable when the frequency band and range of elevation over which the correction algorithm must be applied are small. Referring to the two-stage multimode corrections scheme discussed in the previous section, we now look for a weight vector v which will minimise the following expression:

$$\mathcal{E} = \frac{1}{\Delta\omega}\int_{\omega_{LO}}^{\omega_{HI}} d\omega \frac{1}{2\Theta}\int_{\pi/2-\Theta}^{\pi/2+\Theta} d\theta \sum_{\mu=-\Lambda}^{\Lambda} [v^H \mathbf{E}_\mu \mathbf{G}^H(\omega,\theta) - \gamma_\mu^* \boldsymbol{\Psi}_\mu^H][\mathbf{G}(\omega,\theta)\mathbf{E}_\mu^H v - \boldsymbol{\Psi}_\mu \gamma_\mu] \qquad \cdots (4.7.1)$$

where $\gamma_0 = 1$, $\{\gamma_\mu\}_{\mu=-\Lambda}^{\Lambda} = \{1/u_\mu\}_{\mu=-\Lambda}^{\Lambda}$ is a second set of minimisation parameters and $\mathbf{G}(\omega,\theta)$ is a frequency and elevation angle dependent element pattern matrix. Minimising $\mathcal{E}$ with respect to v and $\{\gamma_\mu\}_{\mu\neq 0}$ we obtain (see appendix D.2):

$$v = [\overline{\mathbf{G}^H\mathbf{G}} + \sum_{\substack{\mu=-\Lambda \\ \mu\neq 0}}^{\Lambda} \mathbf{E}_\mu(\overline{\mathbf{G}^H\mathbf{G}} - L^{-1}\bar{\mathbf{G}}^H\boldsymbol{\Psi}_\mu\boldsymbol{\Psi}_\mu^H\bar{\mathbf{G}})\mathbf{E}_\mu^H]^{-1}\bar{\mathbf{G}}^H\boldsymbol{\Psi}_0 \qquad \cdots (4.7.2)$$

where,

$$\bar{\mathbf{G}} = \frac{1}{\Delta w}\int_{\omega_{LO}}^{\omega_{HI}} d\omega \frac{1}{2\Theta}\int_{\pi/2-\Theta}^{\pi/2+\Theta} d\theta \mathbf{G}(\omega,\theta) \qquad \cdots (4.7.3)$$

$$\bar{\mathbf{G}}^H = \frac{1}{\Delta\omega}\int_{\omega_{LO}}^{\omega_{HI}} d\omega \frac{1}{2\Theta}\int_{\pi/2-\Theta}^{\pi/2+\Theta} d\theta \mathbf{G}^H(\omega,\theta) \qquad \cdots (4.7.4)$$

$$\overline{\mathbf{G}^H\mathbf{G}} = \frac{1}{\Delta\omega}\int_{\omega_{LO}}^{\omega_{HI}} d\omega \frac{1}{2\Theta}\int_{\pi/2-\Theta}^{\pi/2+\Theta} d\theta \mathbf{G}^H(\omega,\theta)\mathbf{G}(\omega,\theta) \qquad \cdots (4.7.5)$$

$[\omega_{LO}, \omega_{HI}]$ – range of frequencies

$[\pi/2-\Theta, \pi/2+\Theta]$ – range of elevation angles

and where matrix integration is understood to mean integration of each of its elements. The corrected (but still mis-aligned) phase modes are now given by:

$$\boldsymbol{\Phi}_\mu(\theta,\omega) = \mathbf{G}(\omega,\theta)\mathbf{E}_\mu^H \boldsymbol{v}$$

$$= \mathbf{G}(\omega,\theta)\mathbf{E}_\mu^H[\overline{\mathbf{G}^H\mathbf{G}} + \sum_{\substack{\mu=-\Lambda \\ \mu\neq 0}}^{\Lambda} \mathbf{E}_\mu(\overline{\mathbf{G}^H\mathbf{G}} - L^{-1}\bar{\mathbf{G}}^H\boldsymbol{\Psi}_\mu\boldsymbol{\Psi}_\mu^H\bar{\mathbf{G}})\mathbf{E}_\mu^H]^{-1}\bar{\mathbf{G}}^H\boldsymbol{\Psi}_0$$

$$\cdots (4.7.6)$$

The post-DFT alignment weight vector $\boldsymbol{u}$ may be evaluated along the same lines. Option 2 of of section 4.6 is accordingly modified by seeking a set of weights that will minimise the cost functions:

$$\mathcal{E}_\mu = \frac{1}{\Delta\omega}\int_{\omega_{LO}}^{\omega_{HI}} d\omega \frac{1}{2\Theta}\int_{\pi/2-\Theta}^{\pi/2+\Theta} d\theta |\hat{\boldsymbol{\Phi}}_\mu(\theta,\omega)u_\mu - \boldsymbol{\Psi}_\mu|^2 \quad , \quad -\Lambda\leq\mu\leq\Lambda \qquad \cdots (4.7.7)$$

resulting in:

$$u_\mu = \overline{\hat{\boldsymbol{\Phi}}_\mu^H}\boldsymbol{\Psi}_\mu / \overline{|\hat{\boldsymbol{\Phi}}_\mu|^2} \quad , \quad -\Lambda\leq\mu\leq\Lambda \qquad \cdots (4.7.8)$$

where

$$\overline{\hat{\boldsymbol{\Phi}}_\mu^H} = \frac{1}{\Delta\omega}\int_{\omega_{LO}}^{\omega_{HI}} d\omega \frac{1}{2\Theta}\int_{\pi/2-\Theta}^{\pi/2+\Theta} d\theta \hat{\boldsymbol{\Phi}}_\mu^H(\theta,\omega) \quad , \quad -\Lambda\leq\mu\leq\Lambda \qquad \cdots (4.7.9)$$

$$\overline{|\hat{\Phi}_\mu|^2} = \frac{1}{\Delta\omega}\int_{\omega_{LO}}^{\omega_{HI}} d\omega \frac{1}{2\Theta}\int_{\pi/2-\Theta}^{\pi/2+\Theta} d\theta\, |\hat{\Phi}_\mu(\theta,\omega)|^2 \quad , \quad -\Lambda \le \mu \le \Lambda \qquad \cdots (4.7.10)$$

Frequency and elevation averaging as described above is only applicable to very small bandwidths and elevation ranges. The degradation in array performance attendant to broadband frequency averaging may be reduced by utilising post-DFT filters, pre-DFT filters or both. For post-DFT filtering, the frequency domain is sampled in accordance with the results of chapter 3, section 3.6, and a set of frequency-dependent post-DFT weight vectors $\{\boldsymbol{u}(\omega_n)\}_n$ are independently evaluated by the minimisation of,

$$\mathcal{E}_\mu(\omega_n) = \frac{1}{2\Theta}\int_{\pi/2-\Theta}^{\pi/2+\Theta} d\theta\, |\hat{\boldsymbol{\Phi}}_\mu(\theta,\omega_n)\boldsymbol{u}_\mu(\omega_n) - \boldsymbol{\Psi}_\mu|^2 \quad , \quad -\Lambda \le \mu \le \Lambda \qquad \cdots (4.7.11)$$

which results in:

$$\boldsymbol{u}_\mu(\omega_n) = \overline{\hat{\boldsymbol{\Phi}}^H_\mu(\omega_n)}\,\boldsymbol{\Psi}_\mu / \overline{|\hat{\boldsymbol{\Phi}}_\mu(\omega_n)|^2} \quad , \quad -\Lambda \le \mu \le \Lambda \qquad \cdots (4.7.12)$$

where

$$\overline{\hat{\boldsymbol{\Phi}}^H_\mu(\omega_n)} = \frac{1}{2\Theta}\int_{\pi/2-\Theta}^{\pi/2+\Theta} d\theta\, \hat{\boldsymbol{\Phi}}^H_\mu(\theta,\omega_n) \quad , \quad -\Lambda \le \mu \le \Lambda \qquad \cdots (4.7.13)$$

$$\overline{|\hat{\boldsymbol{\Phi}}_\mu(\omega_n)|^2} = \frac{1}{2\Theta}\int_{\pi/2-\Theta}^{\pi/2+\Theta} d\theta\, |\hat{\boldsymbol{\Phi}}_\mu(\theta,\omega_n)|^2 \quad , \quad -\Lambda \le \mu \le \Lambda \qquad \cdots (4.7.14)$$

A digital filter is then implemented at the output of each mode using one of the configurations suggested in chapter 3, section 3.6 (as illustrated in *Fig. 3.6.3* and in *Fig. 3.6.4*), with the set of weights $\{u_\mu^{-1}(\omega_n)\}$ substituted for the values $\{\mathcal{D}_{\mu n}\}$ appearing in *Fig. 3.6.3*.

4.8 SIMULATION RESULTS

The narrowband and wideband correction algorithms discussed in sections 4.5 to 4.7 have been included in a computer simulation program for conventionally processed circular arrays, the details of which are given in appendix F. In this section we have collected some results pertaining to the post-DFT filtering of a circular array operating in the frequency range 12 to 24 kHz. These include amplitude and phase plots of phase mode patterns in *Fig. 4.8.1* and *Fig. 4.8.2* respectively, as well as a

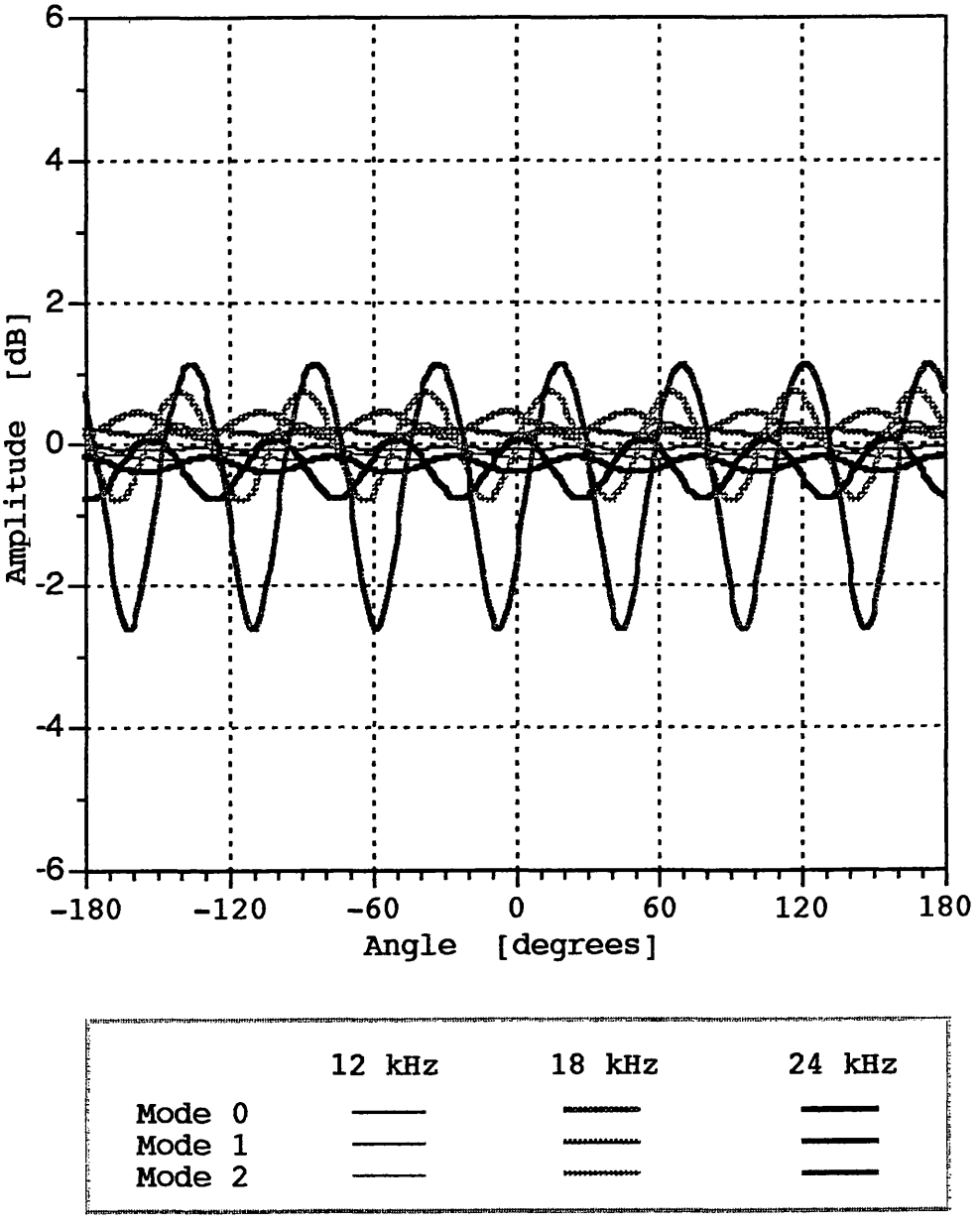

Fig. 4.8.1 Simulated amplitude plots of digitally filtered phase modes no. 0, 1 and 2 from a 7-element circular array at frequencies: 12, 18 and 24 kHz.

mode-space directional beam and a sectoral phase mode in *Fig. 4.8.3* and *Fig. 4.8.4*. The array in question was a 7-sensor sonar ring of radius 28.8 mm, whose measured element patterns[8] were parametrised as:

$$g_{\varphi}(\varphi, \omega) = 0.43 + 0.68\cos\varphi - 0.11\cos 2\varphi + [0.03 - 0.12\cos\varphi + 0.09\cos 2\varphi][(\omega/\omega_0) - 1]$$

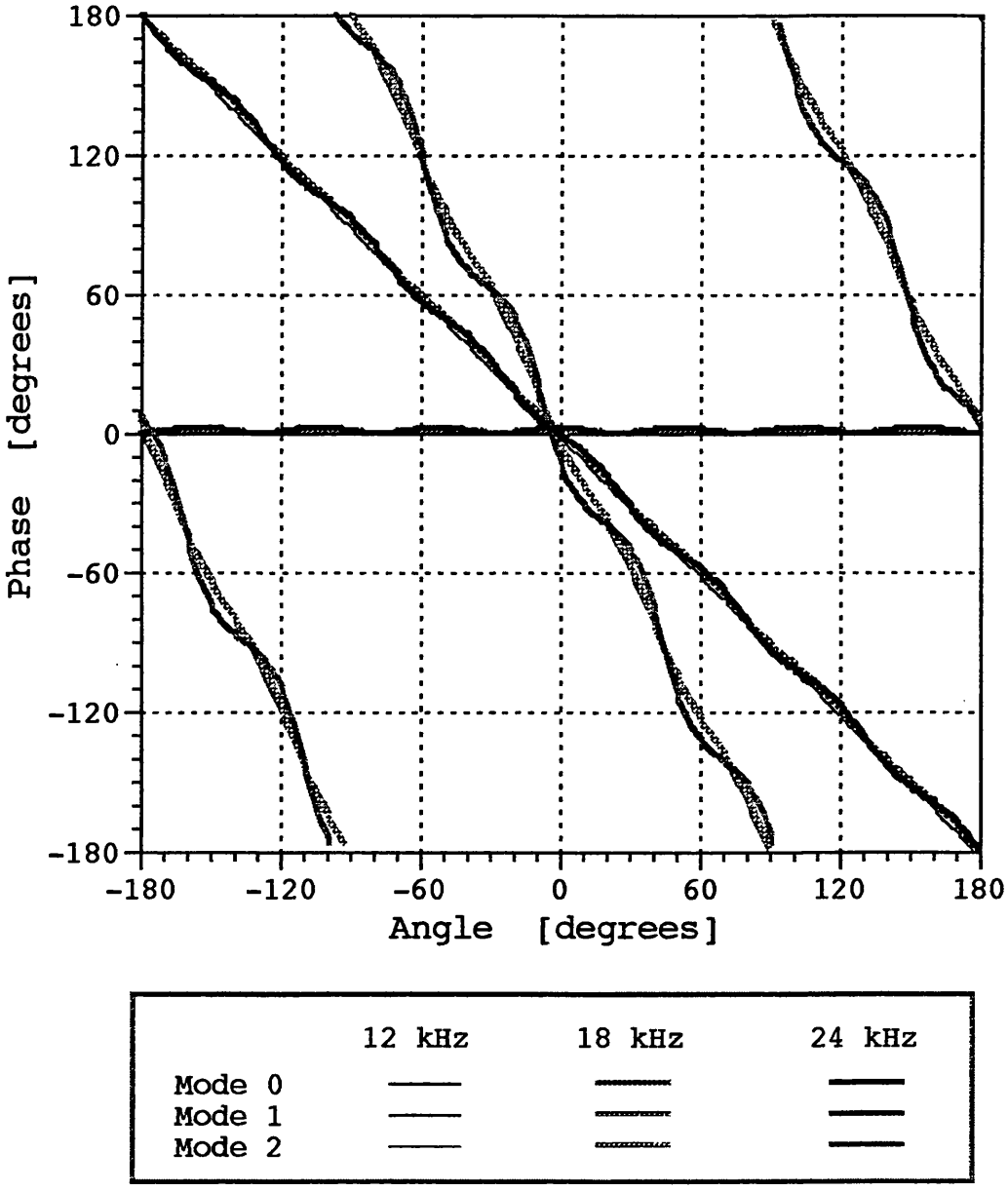

Fig. 4.8.2 Simulated phase plots of digitally filtered phase modes no. 0, 1 and 2 from a 7-element circular array at frequencies: 12, 18 and 24 kHz

8 The array was developed and measured at Loughborough University of Technology in 1992.

where ω_0 refers to a frequency of 18 kHz. Assuming the acoustic propagation speed to be given by $c = 1500\ \text{ms}^{-1}$, the simulated array radius was taken as 0.4608 wavelengths at 24 kHz. Equivalently, the (arcwise) inter-element spacing at that frequency was entered as 0.4136 wavelengths. IIR filtering was simulated with the sampling frequency and the order of the filters being given by:

$$\omega_s/2\pi = 72\text{kHz}$$

$$N = 12$$

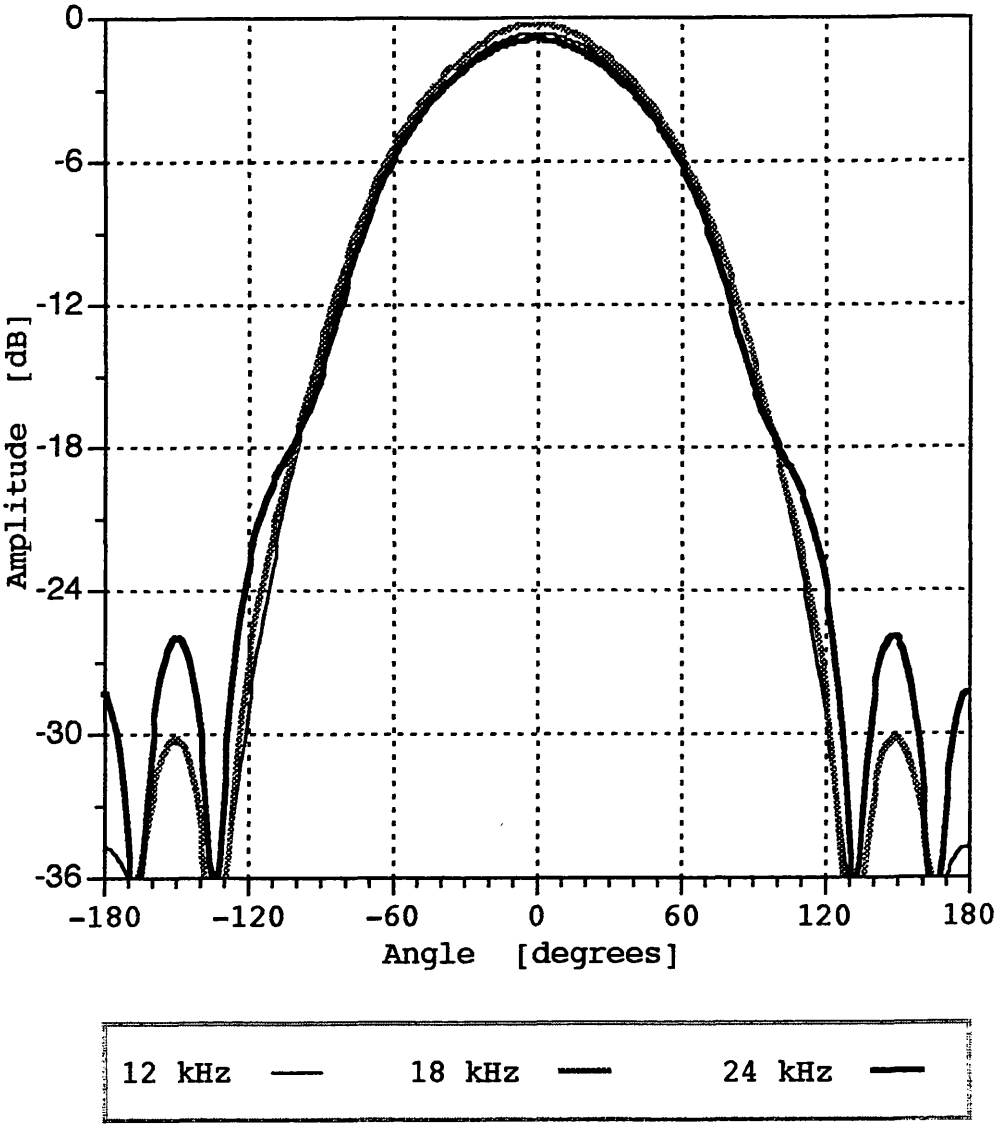

Fig. 4.8.3 Simulated mode-space beam from digitally filtered phase modes -2 to 2 excited in a 7-element circular array at frequencies: 12, 18 and 24 kHz Mode weighting = {-14 dB -3 dB 0 dB -3 dB -14 dB}

In *Fig. 4.8.1* and *Fig. 4.8.2*, the presence of higher-order mode ripple is particularly noticeable in phase mode number 2 at the upper frequency. Nevertheless, the synthesised directional beam of *Fig. 4.8.3* as well as the pair of oppositely-numbered sectoral phase modes[9] are almost independent of frequency, at least in their main-lobe sector.

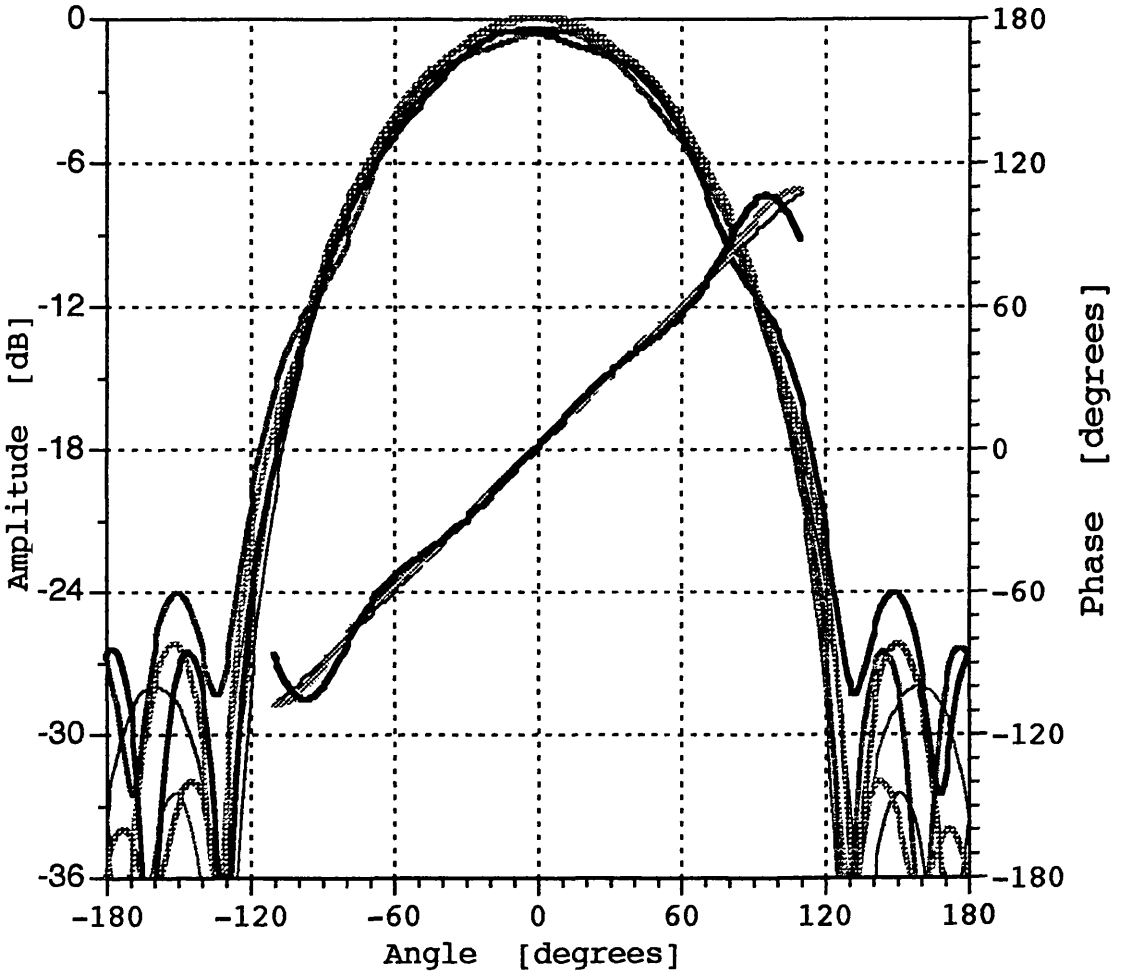

	12 kHz	18 kHz	24 kHz
Beam 1 (ampl)	—	—	—
Beam 2 (ampl)	—	—	—
Compared phase	—	—	—

Fig. 4.8.4 Simulated sectoral phase modes from digitally filtered phase modes {-2 to 1} and {-1 to 2} excited in a 7-element circular array at 12, 18 and 24 kHz. Mode weighting = {-7.5 dB 0 dB 0 dB -7.5 dB}

9 The effective mode numbers of the two sectoral phase modes are 1/2 and -1/2 respectively.

4.9 SUMMARY

In this chapter we have examined the effect that amplitude and phase fluctuations as well as position and roll errors of circular array elements, may have on the power pattern of a mode-space directional beam, and have suggested a least-squares correction approach for calibrating and re-aligning the array. An expression was derived for the expected value of the far-field power pattern in the presence of small unbiased and mutually uncorrelated random errors of specified variances. This pattern was shown to be expressible as the nominal pattern multiplied by a gain reduction coefficient, plus an additional (generally direction-dependent) error term, and in the case of position errors a reduction in the effective array radius was also noted. That additional error term when referred to the (gain reduced) peak of the nominal pattern constitutes the rms sidelobe pattern due to aperture errors. It is directly proportional to the (approximate) sum of all the error variances, becoming a constant function of direction in the case of equi-variance mode-space errors, as well as under equi-variance aperture errors when the array elements are omnidirectional.

The above error analysis was followed with a proposed calibration-based procedure for the least-squares pattern optimisation of a multiple set of beams. The algorithm was shown to be equivalently realisable as a two-stage correction scheme, comprising a set of complex correction weights applied to the element channels, plus a second set of complex weights at the phase mode outputs. For broadband operation, these weights may be replaced by appropriate 'pre-DFT' and 'post-DFT' filters, the latter being implemented in accordance with the results of chapter 3.

5. APPLICATION OF SUPERRESOLUTION TECHNIQUES

5.1 INTRODUCTION

Superresolution schemes for enhanced spatial estimation are considered whenever conventional beamforming fails to deliver the required bearing accuracy of a sensor array under a constrained aperture size. These are spectral estimation algorithms which adaptively use information provided by the received signals, usually through second-order statistics of their temporal Fourier transforms, with the aim of surpassing the Rayleigh resolution limit of Fourier-based direction-finding methods. According to the classical Rayleigh resolution criterion, two uncorrelated equi-power far-field sources are just resolvable when their angular separation equals half the null-to-null delay-and-sum beamwidth of the receiving array.[1] If the angular separation of the two sources is decreased below this limit, the two (mainlobe) pattern peaks in the spectral response of a conventional beamformer will merge into a single maximum representing the two sources. In practice the beamforming receiver may also be adversely affected by the presence of additional noise which can mask the received signals altogether, let alone allow their resolution. High-resolution estimation of directions of arrival (DOA) from noisy data has therefore attracted intensive research interest for over 30 years and a variety of different spatial spectral estimation algorithms have been developed or adapted from the closely related context of time-frequency signal analysis.

In the simplest scenario often investigated, spatial and temporal samples of the received signals are assumed to originate from a number of narrowband sources all having the same centre frequency. A somewhat more realistic model consists of narrowband sources centred at known but different frequencies. In both cases, as well as in the more general case of wideband sources of known spectral densities, the problem is effectively that of a one-dimensional spectral estimation in the spatial domain.[2]

---

1 For a uniformly illuminated line source or linear array of length D/λ wavelengths, this angular separation is approximately equal to λ/D radians.

The spatial distribution of the array sensors may or may not be restricted by the specific algorithm used while the sensors themselves may take a variety of forms such as antenna elements or acoustic hydrophones in radar and sonar systems respectively. In any event, the digitised array outputs are assumed to be available, together with a precise knowledge of the array geometry (in some cases, the arrangement of the array sensors need only be partially known, subject to some structural constraint) and (for most estimators) a calibrated record of the array element patterns over the relevant frequency band and angular sector.

Two different types of data models are generally used to map the observation space of received signals onto the parameter space of estimated directions of arrivals [STO 90b]. Under the *stochastic* (or *unconditional*) model the signals emanating from the distant sources are regarded as random processes, and are ordinarily assumed to be stationary zero-mean jointly complex Gaussian, uncorrelated with the additive noises. The *deterministic* (*conditional*) model, on the other hand, assumes the received signals to be non-random. In both cases the additive noises received or generated at the array channels are considered to be random, and commonly taken as stationary zero-mean uncorrelated ("spatially white") complex Gaussian processes.

In section 5.2 we review and compare several superresolution schemes pertinent to arbitrarily shaped arrays, as well as methods apposite to arrays of some constrained geometry. The algorithms considered may involve a scalar ('one-dimensional') search in which the DOA parameters are sought one at a time, a vector parameter search for the simultaneous ('multi-dimensional') estimation of all directions of arrivals, or they may employ no parameter search at all. Section 5.3 then considers the application of such techniques to circular arrays and in particular to their phase-mode outputs. It is shown that this particular kind of 'beam-space' formulation allows superresolution algorithms which are specific to linear arrays to be also applicable to circular arrays. The (pre-processing) transformation from 'element space' to 'mode space' also allows the decorrelation of coherent sources or multipathed signals received by a circular array, through spatial and omni-directional frequency smoothing; these two techniques, which have hitherto been restricted to linear arrays, are discussed in the context of circular arrays in section 5.4. Section 5.5 concludes this chapter with a simulated study of DOA estimation procedures under various multiple-source scenarios, in which the performances of a representative superresolution algorithm using linear and circular arrays are examined and compared.

---

2 Strictly speaking a spatial spectra estimator is *one-dimensional* only when the estimated (DOA) parameters are evaluated one by one.

5.2 GENERAL OVERVIEW

5.2.1 CRAMÉR-RAO LOWER BOUND

The effectiveness of any method for the estimation of a $K\times1$ vector $\boldsymbol{\phi}$ of K DOA parameters from a random observation vector $\boldsymbol{u}$, is ordinarily evaluated in accordance with the following quality criteria:

i. Resolvability - its ability to reveal the presence of two equal-power sources of nearly equal bearings
ii. Bias - the average error in estimating the location of a source. An estimate is *unbiased* when its expected value equals the parameter itself.
iii. Variability - the variance of the estimation bearing (which is also the variance of the estimation error)

Since the direct computation of the bias and variance of the estimated DOA parameters is in general difficult to achieve, the usual procedure is to derive a lower bound on the variance of each estimated parameter. A popular lower bound on the variance var $(\hat{\phi}_k)$ of any unbiased estimate $\hat{\phi}_k$ of a parameter ϕ_k is provided by the *Cramér-Rao lower bound* (CRLB), the determination of which is closely linked to the *Fisher information matrix*. The $k'k''$th element of the latter $K\times K$ matrix $\mathbf{J}$ is defined as:

$$J_{k'k''} = \mathcal{E}\{[\frac{\partial \ln f_{\boldsymbol{u}}(\boldsymbol{u}|\boldsymbol{\phi})}{\partial \phi_{k'}}]\,[\frac{\partial \ln f_{\boldsymbol{u}}(\boldsymbol{u}|\boldsymbol{\phi})}{\partial \phi_{k''}}]\} = -\mathcal{E}[\frac{\partial^2 \ln f_{\boldsymbol{u}}(\boldsymbol{u}|\boldsymbol{\phi})}{\partial \phi_{k'}\,\partial \phi_{k''}}] \qquad \cdots (5.2.1)$$

provided the derivatives exist and are absolutely integrable. In *(5.2.1)* $\boldsymbol{u}$ is a random vector of the received array data, represented by the observed sample vector $\boldsymbol{u}$, $f_{\boldsymbol{u}}(\boldsymbol{u}|\boldsymbol{\phi})$ is the conditional joint probability density function (PDF) for the random vector $\boldsymbol{u}$, viewed as a function of the DOA parameter vector $\boldsymbol{\phi}$, and $\mathcal{E}$ is the expectation operator. It can be shown [VAN 68], [RAO 73] that for an unbiased vector estimate $\hat{\boldsymbol{\phi}}$

$$\text{cov}\,(\hat{\boldsymbol{\phi}}) \geq \mathbf{J}^{-1} \qquad \cdots (5.2.2)$$

where $\mathbf{J}^{-1}$ is the inverse of $\mathbf{J}$, cov $(\hat{\boldsymbol{\phi}})$ is the covariance matrix for the estimated parameter vector (or in other words the estimation error covariance matrix) and the matrix inequality is in the sense that the difference matrix [cov $(\hat{\boldsymbol{\phi}}) - \mathbf{J}^{-1}$] is positive

semi-definite. One consequence of *(5.2.2)* is that the CRLB for the variance of each of the K parameters $\{\hat{\phi}_k\}$ is given by:

$$\text{var}(\hat{\phi}_k) \geq [\mathcal{J}^{-1}]_{kk} \quad , \quad 0 \leq k \leq K\text{-}1 \qquad \cdots (5.2.3)$$

where $[\mathcal{J}^{-1}]_{kk}$ is the k'th diagonal element of $\mathbf{J}^{-1}$.

An estimator is said to be *efficient* if its covariance matrix equals $\mathbf{J}^{-1}$. Note however that the stochastic and deterministic (or any other non-Gaussian signal) models each leads to a different Fisher information matrix and therefore to a different CRLB [STO 90b], [OTT 92].

5.2.2 DATA MODEL

For a given observation interval $(t\text{-}NT,\ t]$ the observed sample vector $\boldsymbol{u}$ may denote a stacked tempo-spatial vector of the form:

$$\begin{aligned} \boldsymbol{u} &= [\boldsymbol{x}^T(t_0)\ \boldsymbol{x}^T(t_1) \cdots\cdots \boldsymbol{x}^T(t_{N-1})]^T \\ t_n &= t - nT \quad , \quad 0 \leq n \leq N\text{-}1 \end{aligned} \qquad \cdots (5.2.4)$$

where each of the N temporally delayed vectors (or 'snapshots') $\{\boldsymbol{x}(t_n)\}_{n=0}^{N-1}$, being a statistical sample of a corresponding random vector $\boldsymbol{x}(t_n)$, groups the complex (analytical) representation of signals received by the array sensors. For an M-element array we denote:

$$\boldsymbol{x}(t_n) = [x_0(t_n)\ x_1(t_n) \cdots\cdots x_{M-1}(t_n)]^T \qquad \cdots (5.2.5)$$

and similarly,

$$\boldsymbol{X}(t_n) = [X_0(t_n)\ X_1(t_n) \cdots\cdots X_{M-1}(t_n)]^T \qquad \cdots (5.2.6)$$

where $X_m(t_n)$ is a random variable of the received data at the m'th array sensor at time t_n, represented by the observed sampled value $x_m(t_n)$. An alternative representation of *(5.2.4)* is via an $M \times N$ data matrix $\mathbf{X}$:

$$\mathbf{X} = [\boldsymbol{x}(t_0)\ \boldsymbol{x}(t_1) \cdots\cdots \boldsymbol{x}(t_{N-1})] \qquad \cdots (5.2.7)$$

Under wideband formulation, each snapshot $x_m(t_n)$ is often represented over the relevant sub-interval $(t_n - T/2, t_n + T/2)$ by its (assumed bandlimited) Fourier series coefficients $\{X_m(\omega_\ell; t_n)\}_\ell$ so that for each discrete frequency, the sample data vector (denoted here by U) is given by:

$$U = [X^T(\omega_\ell; t_0)\, X^T(\omega_\ell; t_1) \cdots\cdots X^T(\omega_\ell; t_{N-1})]^T \qquad \cdots (5.2.8)$$

where

$$X(\omega_\ell; t_n) = [X_0(\omega_\ell; t_n)\, X_1(\omega_\ell; t_n) \cdots\cdots X_{M-1}(\omega_\ell; t_n)]^T \qquad \cdots (5.2.9)$$

represents the corresponding random vector $\boldsymbol{X}(\omega_\ell; t_n)$, and

$$\omega_\ell = (2\pi/T)\ell \quad , \quad \ell_{LO} \le \ell \le \ell_{HI} \qquad \cdots (5.2.10)$$

are the discrete frequencies in the passband $[\omega_{\ell_{LO}}, \omega_{\ell_{HI}}]$ of the Fourier series coefficients.

Under stochastic formulation the signal delivered by the m'th sensor of an M-element array is generally modelled as a random noise process $x_{*m}(t)$ added to a sum of K delayed random signals $\{s_k(t)\}_{k=0}^{K-1}$ convolved with respective 'steering impulse responses' $\{a_{mk}(t)\}_{k=0}^{K-1}$:

$$x_m(t) = \sum_{k=0}^{K-1} a_{mk}(t) * s_k(t - \tau_m(\phi_k)) + x_{*m}(t) \quad , \quad 0 \le m \le M-1 \qquad \cdots (5.2.11)$$

The noise may be internally (thermally) generated at the sensor channels or picked up by the array sensors from a variety of external sources (see [WEN 62], [URI 83] for a detailed review of ocean noise). In the latter case it is usually modelled as a continuous far-field noise distribution that is statistically independent with respect to direction. The delayed signals emanate from K sources (including multipath 'image sources'), each at a different bearing and (in general) a different range from the array centre, and it is assumed that $K < M$. The steering impulse response $a_{mk}(t)$ is the response of the m'th array sensor to a temporal impulse arriving from direction ϕ_k of the k'th source, and $\tau_m(\phi_k)$ is the propagation delay to the m'th sensor from that source direction, referred to the corresponding delay to the array centre (or some other stationary reference point); the propagation delay of each of the signals from its respective source (or 'image source') to the reference point is assumed to be 'contained' in the function form $s_k(\cdot)$. The corresponding deterministic data model is

similar in form to the above, except that the delayed signals are non-random. The distinction between the stochastic and the deterministic models is particularly relevant for spectral estimators (such as the ML method – see sub-section 5.2.5) based on a statistical inference approach.

Under single-frequency narrowband conditions i.e. when the (Fourier-transformed) steering responses are constant over the common bandwidth of the signals, and the bandwidth, with centre frequency ω_0, is also much smaller than the reciprocal of the propagation delay across the array, *(5.2.11)* may be modified to the following matrix form:

$$\boldsymbol{x}(t) = \mathbf{A}(\omega_0)\boldsymbol{s}(t) + \boldsymbol{x}_n(t) \qquad \cdots (5.2.12)$$

where $\boldsymbol{s}(t) = [s_0(t)\ s_1(t) \cdots\cdots\ s_{K-1}(t)]^T$ and $\boldsymbol{x}_n(t) = [x_{n_0}(t)\ x_{n_1}(t) \cdots\cdots\ x_{n_{M-1}}(t)]^T$ are the corresponding narrowband random signal and noise vectors and $\mathbf{A}(\omega_0) = \mathbf{A}(\boldsymbol{\phi}, \omega_0)$ is an $M \times K$ steering matrix[3] whose mk'th element corresponds to the spatial response of the m'th array sensor to a plane wave at frequency ω_0 arriving from the k'th source, i.e.

$$A_{mk} = \int_{-\infty}^{\infty} dt\, a_{mk}(t-\tau_m(\phi_k))e^{-j\omega_0 t} = e^{-j\omega_0\tau_m(\phi_k)}\int_{-\infty}^{\infty} dt\, a_{mk}(t)e^{-j\omega_0 t} \qquad \cdots (5.2.13)$$

It is common to assume that the K columns of $\mathbf{A}(\omega_0)$ are linearly independent, and in the case of a linear array of equally spaced sensors this is indeed true by virtue of its Vandermonde structure for non-coincident sources[4]. The spatial covariance matrix $\mathbf{R} = \mathcal{E}\boldsymbol{x}\boldsymbol{x}^H$ may thus be written in terms of a signal covariance matrix $\mathbf{R}_s = \mathcal{E}\boldsymbol{s}\boldsymbol{s}^H$, a noise covariance matrix $\mathbf{R}_n = \sigma_n^2\mathcal{E}\boldsymbol{x}_n\boldsymbol{x}_n^H$ and a full-rank steering matrix[5] $\mathbf{A}$:

---

3 The steering matrix $\mathbf{A}$ obviously depends on the DOA parameter vector $\boldsymbol{\phi}$. For both notational convenience and clarity, especially when dealing with search-based superresolution schemes, we denote the functional form of the steering matrix by $\mathbf{A}(\varphi, \omega)$, and use $\mathbf{A}(\omega_0) = \mathbf{A}(\varphi = \boldsymbol{\phi}, \omega = \omega_0)$ to indicate the steering matrix associated with the actual sources. In a similar manner, the k'th column of $\mathbf{A}$ will be given by: $\mathbf{A}_k(\omega_0) = \mathbf{A}(\varphi = \phi_k, \omega = \omega_0)$

4 The steering matrix $\mathbf{A}$ has a Vandermonde structure when the array sensors are omni-directional. In the more general case of array sensors having a common element pattern, $\mathbf{A}$ is a Vandermonde matrix multiplied by a diagonal $K \times K$ matrix whose kk'th element equals A_{0k}. Obviously, an element pattern null in the direction of one of the incoming signals reduces the rank of $\mathbf{A}$. This also happens in the case of two signals arriving from equivalent ('grating-lobe') directions; herein we assume that the array inter-sensor spacing is such that grating-lobe propagation is suppressed.

5 It is common to refer to $\mathbf{R}_s = \mathbf{A}\mathbf{R}_s\mathbf{A}^H$ as the *signal-only covariance matrix.*

$$\mathbf{R} = \mathbf{R}_s + \sigma_n^2\mathbf{R}_n = \mathbf{A}\mathbf{R}_S\mathbf{A}^H + \sigma_n^2\mathbf{R}_n \qquad \cdots (5.2.14)$$

where $\mathbf{R}_n$ is usually normalised (through σ_n^2) such that its trace equals M. The noise is generally assumed to be *spatially-white* and *homoscedastic* (or *spatially-stationary*[6]), in which case *(5.2.14)* becomes:

$$\mathbf{R} = \mathbf{A}\mathbf{R}_S\mathbf{A}^H + \sigma_n^2\mathbf{I} \qquad \cdots (5.2.15)$$

where $\mathbf{I}$ is the $M \times M$ identity matrix and σ_n^2 is the noise power at each of the array sensors. For the wideband case, the temporal Fourier transform of the covariance of *(5.2.11)* yields the following expression for the cross-spectral density matrix $\mathbf{P}(\omega)$:

$$\begin{aligned}\mathbf{P}(\omega) = \int_{-\infty}^{\infty} d\tau \mathbf{R}(\tau)e^{-j\omega\tau} &= \mathbf{A}(\omega)\mathbf{P}_S(\omega)\mathbf{A}^H(\omega) + \mathbf{P}_n(\omega) \\ &= \mathbf{A}(\omega)\mathbf{P}_S(\omega)\mathbf{A}^H(\omega) + \eta_n(\omega)\,\mathbf{I} \qquad \cdots (5.2.16)\end{aligned}$$

where $\eta_n(\omega)$ is the spatially white noise power density at each array sensor, and each element A_{mk} of the steering matrix $\mathbf{A}(\omega)$ is the temporal Fourier transform of the corresponding steering impulse response $a_{mk}(t-\tau_m(\phi_k))$. $\mathbf{R}(\tau) = \mathcal{E}\boldsymbol{x}(t)\boldsymbol{x}^H(t-\tau)$ is the tempo-spatial covariance matrix, and for similarly defined respective signal and noise covariance matrices, $\mathbf{R}_S(\tau) = \mathcal{E}\boldsymbol{s}(t)\boldsymbol{s}^H(t-\tau)$ and $\sigma_n^2(\tau)\mathbf{R}_n(\tau) = \mathcal{E}\boldsymbol{x}_n(t)\boldsymbol{x}_n^H(t-\tau)$:

$$\mathbf{P}_S(\omega) = \int_{-\infty}^{\infty} d\tau \mathbf{R}_S(\tau)e^{-j\omega\tau}$$

and

$$\mathbf{P}_n(\omega) = \int_{-\infty}^{\infty} d\tau \sigma_n^2(\tau)\mathbf{R}_n(\tau)e^{-j\omega\tau}$$

are the corresponding signal and noise cross-spectral density matrices. Assuming the time interval T to be much longer than the propagation delay across the array, *(5.2.11)* leads to the following matrix expression for the Fourier series coefficient vectors:

---

6 The noise at the array sensors is said to be *homoscedastic* if all elements on the main diagonal of the noise covariance matrix $\sigma_n^2\mathbf{R}_n = \mathcal{E}\boldsymbol{x}_n\boldsymbol{x}_n^H$ are equal. It is *spatially-stationary* if $\mathbf{R}_n$ has a Toeplitz structure, i.e. if elements on its main diagonal or on any diagonal parallel to it, are equal. If the noises at the array sensors are pairwise uncorrelated, $\mathbf{R}_n$ is diagonal and the noise is said to be *spatially-white*.

$$\boldsymbol{X}(\omega_\ell; t_n) = \mathbf{A}(\omega_\ell)\boldsymbol{S}(\omega_\ell; t_n) + \boldsymbol{X}_n(\omega_\ell; t_n) \quad \cdots (5.2.17)$$

where $\omega_{\ell_{LO}} \leq \omega_\ell \leq \omega_{\ell_{HI}}$ for ω_ℓ as defined by *(5.2.10)*. If T is also large compared to the correlation time of the processes involved, then the frequency-domain vectors $\boldsymbol{X}(\omega_{\ell'}; t_n)$ and $\boldsymbol{X}(\omega_{\ell''}; t_n)$ are approximately uncorrelated for $\ell' \neq \ell''$ and,

$$\mathcal{E}\boldsymbol{X}(\omega_\ell; t_n)\boldsymbol{X}^H(\omega_\ell; t_n) = \frac{1}{T}\int_{-T}^{T} d\tau\, \mathbf{R}(\tau)\,[1 - \frac{|\tau|}{T}]e^{-j\omega_\ell \tau} \approx \frac{1}{T}\mathbf{P}(\omega_\ell) \quad \cdots (5.2.18)$$

5.2.3 CONVENTIONAL BEAMFORMING

In the conventional ('delay and sum') beamforming approach the output of each array sensor is shaded with a constant-amplitude weight[7] whose phase is delay-matched for a given look ('scan') direction of the array. The weighted outputs are then summed to form a spatial pattern whose maxima, above a prescribed threshold level, indicate the presence and the angular locations of radiation sources. The choice of the threshold depends on the dynamic range of the receiver, but also on the sidelobe levels of the 'dynamic' radiation patterns of the array.[8] The sidelobes may be reduced by applying a low-sidelobe weighting taper, but only at the expense of a wider mainlobe. Estimates for the maximum of the sum beam are obtained by such techniques as monopulse or conical scan, and for a single-source environment this method is asymptotically (for a large number of sensors or snapshots) unbiased and efficient [HIN 72], [NIC 87]. This is also nearly true for a low-sidelobe antenna receiving signals from two or more sources that are angularly several beamwidths apart. Pattern peaks contributed by more closely spaced sources will interfere and will become unresolvable at an angular separation of approximately one null-to-null beamwidth (depending on the degree of correlation of the sources and on signal-to-noise conditions). Under the above scheme, the bearing estimation accuracy and resolution of the array may only be improved by increasing the physical size of the array aperture.

---

7 The term *constant-amplitude weight* refers here to a pre-determined amplitude taper that does not depend on the received signal.

8 The *dynamic pattern* of a phased array refers to its radiation characteristics from a stationary far-field source, as a function of its look direction (the angle to which it is scanned). The 'ordinary' radiation pattern, on the other hand, is measured as a function of the relative direction of the far-field source, for a given look direction of the array.

The array power pattern for the delay and sum beamformer is given for the narrowband case by:

$$\mathcal{P}(\varphi) = \mathcal{E}|w^H(\varphi, \omega_0)\boldsymbol{X}|^2 = w^H(\varphi, \omega_0)\mathbf{R}w(\varphi, \omega_0) \qquad \cdots (5.2.19)$$

where the random vector $\boldsymbol{X}(t) = [x_0(t)\ x_1(t) \cdots\cdots\ x_{M-1}(t)]^T$ groups the temporal signals received by the array sensors, $w(\varphi, \omega) = [w_0(\varphi, \omega)\ w_1(\varphi, \omega) \cdots\cdots\ w_{M-1}(\varphi, \omega)]^T$ is the weight vector, with

$$w_m(\varphi, \omega) = |w_m|e^{-j\omega\tau_m(\varphi)} \quad , \quad 0 \le m \le M\text{-}1 \qquad \cdots (5.2.20)$$

and $\tau_m(\varphi)$ is the relative delay from a far-field source at angular direction φ to the m'th array sensor. For the special case of uniform (amplitude) weighting, one obtains the *Bartlett estimate*:

$$\mathcal{P}_B(\varphi) = \boldsymbol{E}^H(\varphi, \omega_0)\mathbf{R}\boldsymbol{E}(\varphi, \omega_0) \qquad \cdots (5.2.21)$$

where,

$$\boldsymbol{E}(\varphi, \omega) = [e^{-j\omega\tau_0(\varphi)}\ e^{-j\omega\tau_1(\varphi)} \cdots\cdots\ e^{-j\omega\tau_{M-1}(\varphi)}]^T \qquad \cdots (5.2.22)$$

For wideband signals observed over a time interval whose duration T is much larger than the propagation delay across the array and is also large compared to the correlation time of the processes, the beam power contained at a discrete frequency slice centred around $\omega_\ell = 2\pi\ell/T \quad , \quad \ell_{LO} \le \ell \le \ell_{HI}$ is given by:

$$\mathcal{P}(\varphi, \omega_\ell) = \mathcal{E}|w^H(\varphi, \omega_\ell)\boldsymbol{X}(\omega_\ell)|^2 = \frac{1}{T}w^H(\varphi, \omega_\ell)\mathbf{P}(\omega_\ell)w(\varphi, \omega_\ell) \qquad \cdots (5.2.23)$$

where $\boldsymbol{X}(\omega_\ell) = [X_0(\omega_\ell)\ X_1(\omega_\ell) \cdots\cdots\ X_{M-1}(\omega_\ell)]^T$ is a random vector of the ℓ'th Fourier series coefficients of the received signals over the interval T. The Bartlett estimate for the corresponding frequency slice is subsequently given by:

$$\mathcal{P}_B(\varphi, \omega_\ell) = \frac{1}{T}\boldsymbol{E}^H(\varphi, \omega_\ell)\mathbf{P}(\omega_\ell)\boldsymbol{E}(\varphi, \omega_\ell) \qquad \cdots (5.2.24)$$

5.2.4 SCALAR-SEARCH SUPERRESOLUTION ALGORITHMS

In the conventional beamforming approach described in sub-section 5.2.3, each direction-of-arrival angle is estimated by locating the corresponding peak in the

dynamic power pattern of the array when excited by the received signals, independently of all other maxima. The source directions are thus evaluated one at a time in what constitutes a scalar (or 'one-dimensional') parameter search. The algorithms to be considered next are also of the scalar-search type – each is characterised by a spectral pattern $\mathcal{P}(\varphi)$ whose peaks are assumed to indicate directions of arrival, and it is again the maxima of $\mathcal{P}(\varphi)$ (or alternatively the minima of the inverse pattern $1/\mathcal{P}(\varphi)$) that one tries to locate.[9] The processors are, however, adaptive in that their spectral patterns are formed using information provided by the received signals, outperforming conventional beamformers in accuracy and resolution, and are therefore denoted here as scalar-search superresolution algorithms. Although the conceptual framework under which such estimation methods were originally formulated varies from one algorithm to another, they may nevertheless be generally described as linearly-constrained minimum-variance schemes in which the weight vector $\boldsymbol{w}$ of the array beamformer is optimised so as to minimise the average power in the beam. The constraint may relate to the look direction in what may be viewed as the dynamic radiation pattern of the processor, where signals arriving from that direction are 'safeguarded' or even enhanced while all other signals are suppressed. $\mathcal{P}(\varphi)$ is then taken as the optimised dynamic power pattern excited by the received signals, sometimes normalised to $|\boldsymbol{w}|^2$ (which, for spatially white noise, is proportional to the noise power). Alternatively, $\boldsymbol{w}$ is optimised under a single linear constraint that does not 'protect' any look directions. The optimised ordinary radiation pattern (i.e. the array response to a single far-field source as a function of its relative angular position) is then characterised by minima in the directions of the incoming signals, and the squared inverse of that pattern is subsequently taken (to within a constant) as the spectral pattern of the processor. We shall identify estimation algorithms that follow the above two approaches as *Minimum Variance Protected Response (MVPR)* and *Minimum Variance Inverse Response (MVIR)* methods respectively.

Under narrowband formulation, the MVPR optimisation problem may be expressed as follows:

$$\min_{\boldsymbol{w}} \boldsymbol{w}^H \mathbf{R} \boldsymbol{w} \quad , \quad \boldsymbol{w}^H \boldsymbol{\Pi} \mathbf{A}(\varphi, \omega_0) = 1 \qquad \cdots (5.2.25)$$

where $\boldsymbol{\Pi}$ is some $M \times M$ transformation matrix whose choice depends on the particular algorithm, and $\mathbf{A}(\varphi, \omega) = [A_0(\varphi, \omega)\, A_1(\varphi, \omega) \cdots\cdots A_{M-1}(\varphi, \omega)]^T$ is a steering vector whose m'th element denotes the response of the corresponding array sensor to a

9 $1/\mathcal{P}(\varphi)$ is commonly referred to as the *null pattern.*

plane wave at frequency ω arriving from direction φ. In the case of omni-directional sensors:

$$\boldsymbol{A}(\varphi, \omega) = \boldsymbol{E}(\varphi, \omega)$$

The processor is thus constrained to have unity gain for some linear transformation of the response of the sensor array to a plane wave impinging on it from direction φ. With the aid of a Lagrange multiplier χ, *(5.2.25)* is solved by minimising

$$\mathcal{E}(w, \varphi) = w^H \mathbf{R} w + \chi^* [\mathbf{A}^H(\varphi, \omega_0)\mathbf{\Pi}^H w - 1] + [w^H \mathbf{\Pi A}(\varphi, \omega_0) - 1]\chi \quad \cdots (5.2.26)$$

which yields:

$$w_{opt} = \frac{\mathbf{R}^{-1}\mathbf{\Pi A}(\varphi, \omega_0)}{\mathbf{A}^H(\varphi, \omega_0)\mathbf{\Pi}^H \mathbf{R}^{-1}\mathbf{\Pi A}(\varphi, \omega_0)} \quad \cdots (5.2.27)$$

resulting in the following expression for the total power, which is also the MVPR spectral pattern:

$$\mathcal{P}(\varphi) = w_{opt}^H \mathbf{R} w_{opt} = \frac{1}{\mathbf{A}^H(\varphi, \omega_0)\mathbf{\Pi}^H \mathbf{R}^{-1}\mathbf{\Pi A}(\varphi, \omega_0)} \quad \cdots (5.2.28)$$

In the case of wideband signals observed over T-long snapshot intervals where T is much larger than the propagation delay across the array and is also large compared to the correlation time of the processes involved, a similar minimisation procedure may be carried out for the beam power at discrete frequency slices centred around frequencies $\omega_\ell = 2\pi\ell/T \quad , \quad \ell_{LO} \le \ell \le \ell_{HI}$, leading to:

$$\mathcal{P}(\varphi, \omega_\ell) = \frac{1}{T} w_{opt}^H \mathbf{P}(\omega_\ell) w_{opt} = \frac{1/T}{\mathbf{A}^H(\varphi, \omega_\ell)\mathbf{\Pi}^H \mathbf{P}^{-1}(\omega_\ell)\mathbf{\Pi A}(\varphi, \omega_\ell)} \quad \cdots (5.2.29)$$

Expression *(5.2.29)* is used in *incoherent* MVPR-type spatial spectral estimation methods – see sub-section 5.2.7.

The narrowband formulation for the MVIR minimisation problem is:

$$\min_w w^H \mathbf{R} w \quad , \quad w^H \mathbf{B} = \boldsymbol{\kappa}^T \quad \cdots (5.2.30)$$

where $\mathbf{B}$ is a rectangular $M \times K'$ matrix of rank K' with $1 \le K' \le M-K$, and $\boldsymbol{\kappa} \neq \boldsymbol{0}$ is a real constant $K' \times 1$ vector. The narrowband cost function to be minimised this time is:

$$\mathcal{L}(w) = w^H \mathbf{R} w + \chi^H [\mathbf{B}^H w - \kappa] + [w^H \mathbf{B} - \kappa^H] \chi \qquad \cdots (5.2.31)$$

where χ is a $K' \times 1$ vector Lagrange multiplier. The resulting weight vector is:

$$w_{opt} = \mathbf{R}^{-1}\mathbf{B}(\mathbf{B}^H\mathbf{R}^{-1}\mathbf{B})^{-1}\kappa \qquad \cdots (5.2.32)$$

the received (noise) power is:

$$w_{opt}^H \mathbf{R} w_{opt} = \kappa^H(\mathbf{B}^H\mathbf{R}^{-1}\mathbf{B})^{-1}\kappa \qquad \cdots (5.2.33)$$

the radiation power pattern of the optimised array is given by:

$$|w_{opt}^H \mathbf{A}(\varphi, \omega_0)|^2 = |\mathbf{A}^H(\varphi, \omega_0)\mathbf{R}^{-1}\mathbf{B}(\mathbf{B}^H\mathbf{R}^{-1}\mathbf{B})^{-1}\kappa|^2 \qquad \cdots (5.2.34)$$

and the MVIR spectral pattern is taken as

$$\mathcal{P}(\varphi) = \frac{w_{opt}^H \mathbf{R} w_{opt}}{|w_{opt}^H \mathbf{A}(\varphi, \omega_0)|^2} = \frac{\kappa^H(\mathbf{B}^H\mathbf{R}^{-1}\mathbf{B})^{-1}\kappa}{|\mathbf{A}^H(\varphi, \omega_0)\mathbf{R}^{-1}\mathbf{B}(\mathbf{B}^H\mathbf{R}^{-1}\mathbf{B})^{-1}\kappa|^2} \qquad \cdots (5.2.35)$$

The corresponding MVIR spectral pattern for the (incoherently solved) wideband case is given at each discrete frequency by:

$$\mathcal{P}(\varphi, \omega_\ell) = \frac{1}{T}\frac{w_{opt}^H \mathbf{P}(\omega_\ell) w_{opt}}{|w_{opt}^H \mathbf{A}(\varphi, \omega_\ell)|^2} = \frac{(1/T)\,\kappa^H(\mathbf{B}^H\mathbf{P}^{-1}(\omega_\ell)\mathbf{B})^{-1}\kappa}{|\mathbf{A}^H(\varphi, \omega_\ell)\mathbf{P}^{-1}(\omega_\ell)\mathbf{B}(\mathbf{B}^H\mathbf{P}^{-1}(\omega_\ell)\mathbf{B})^{-1}\kappa|^2} \qquad \cdots (5.2.36)$$

Of course the true correlation matrix $\mathbf{R}$ and cross-spectral density matrix $\mathbf{P}(\omega_\ell)$ are not available to the processor. Assuming stationarity throughout the duration NT of the record, they may be consistently estimated from the respective sample matrices [AND 84][10]:

$$\hat{\mathbf{R}} = \frac{1}{N}\sum_{n=0}^{N-1} x(t_n)x^H(t_n) = \frac{1}{N}\mathbf{X}\mathbf{X}^H \qquad \cdots (5.2.37)$$

$$\hat{\mathbf{P}}(\omega_\ell) = \frac{1}{NT}\sum_{n=0}^{N-1} X(\omega_\ell; t_n)X^H(\omega_\ell; t_n) \qquad \cdots (5.2.38)$$

[10] It may be shown [AND 84] that each sample matrix is a maximum-likelihood estimate of the true correlation matrix, and as such is *consistent*, i.e. converges in probability to its true values.

More optimal estimates are possible if *a priori* structural information of these matrices is available [BUR 82], [SHA 88a], [ZIS 90].

Expressions *(5.2.28)* (or *(5.2.29)*) and *(5.2.35)* (or *(5.2.36)*) are generic for a number of well known algorithms to be considered next in this sub-section. Estimation schemes derived from the MVIR spectral pattern are ordinarily restricted to equally spaced linear arrays, for which the radiation pattern (which is essentially the MVIR null pattern) is given by:

$$w^H\mathbf{A}(\varphi,\omega) = A_0(\varphi,\omega)\sum_{m=0}^{M-1} w_m^* z^{-m} \quad , \quad z = e^{-j(\omega d/c)\sin\varphi} \qquad \cdots (5.2.39)$$

where c is the speed of propagation and d is the inter-element spacing. This is a polynomial expression of order M-1 which is therefore characterised by M-1 zeros on the complex z-plane. K of these zeros may be forced by the MVIR minimisation procedure *(5.2.30)* to lie on the unit circle at points $\{e^{-j(\omega d/c)\sin\phi_k}\}_{k=0}^{K-1}$ corresponding to the sought after directions of arrival, provided that $1 \le K' \le M-K$. Unless $K = M$-1, spurious nulls or minima may also result due to extraneous roots that lie close to the unit circle $|z| = 1$ — these may be suppressed by a prudent choice of $\mathbf{B}$ and $\boldsymbol{\kappa}$[11].

a. Minimum Variance Distortionless Response (MVDR) method

This method developed by Capon [CAP 69] has been formerly referred to as the *Maximum Likelihood Method* (MLM), although it has little to do with the standard approach used in maximum-likelihood estimates. Its spectral pattern is given (for the narrowband model) by:

$$\mathcal{P}_{\mathrm{MVDR}}(\varphi) = \frac{1}{\mathbf{A}^H(\varphi,\omega_0)\mathbf{R}^{-1}\mathbf{A}(\varphi,\omega_0)} \qquad \cdots (5.2.40)$$

and is obtained from the MVPR pattern *(5.2.28)* by setting: $\mathbf{\Pi} = \mathbf{I}$, where $\mathbf{I}$ is the identity matrix. Physically it means that the beam power (or variance) is minimised subject to the condition that there is a distortionless response to a plane wave incident from the look direction. If the noise covariance matrix is available, trapezoidal-diagonal factorisation may be used to alleviate the numerical instability inherent in

[11] K'-1 columns of $\mathbf{B}$ together with the corresponding elements of $\boldsymbol{\kappa}$ may be chosen so that the extraneous zeros in the z-domain radiation pattern are evenly distributed within the unit circle. This very effect is achieved with a specific vector $\mathbf{B}$ (K'=1) in the *Minimum Norm method* reviewed later in this sub-section.

the inversion of $\mathbf{R}$ [BRA 86][12].

b. Adaptive Angular Response (AAR) method

This method, introduced by Borgiotti and Kaplan [BOR 79] and later by Lagunas-Hernandez and Gasull-Llampallas [LAG 84] is a derivative of the MVDR technique in which the (dynamic) power pattern of the array is normalised to $|w|^2$. For spatially white noise this normalises the processor pattern to the noise power pattern, suppressing the effect of the latter on the spectral pattern. From *(5.2.27)*:

$$w_{opt}^{H} w_{opt} = \frac{\mathbf{A}^H(\varphi, \omega_0)\mathbf{\Pi}^H\mathbf{R}^{-2}\mathbf{\Pi}\mathbf{A}(\varphi, \omega_0)}{|\mathbf{A}^H(\varphi, \omega_0)\mathbf{\Pi}^H\mathbf{R}^{-1}\mathbf{\Pi}\mathbf{A}(\varphi, \omega_0)|^2} \qquad \cdots (5.2.41)$$

$$\frac{w_{opt}^{H}\mathbf{R}w_{opt}}{w_{opt}^{H}w_{opt}} = \frac{\mathbf{A}^H(\varphi, \omega_0)\mathbf{\Pi}^H\mathbf{R}^{-1}\mathbf{\Pi}\mathbf{A}(\varphi, \omega_0)}{\mathbf{A}^H(\varphi, \omega_0)\mathbf{\Pi}^H\mathbf{R}^{-2}\mathbf{\Pi}\mathbf{A}(\varphi, \omega_0)} \qquad \cdots (5.2.42)$$

and by setting $\mathbf{\Pi} = \mathbf{I}$ in the above expression, one obtains the AAR spectral pattern:

$$\mathcal{P}_{\mathrm{AAR}}(\phi) = \frac{\mathbf{A}^H(\varphi, \omega_0)\mathbf{R}^{-1}\mathbf{A}(\varphi, \omega_0)}{\mathbf{A}^H(\varphi, \omega_0)\mathbf{R}^{-2}\mathbf{A}(\varphi, \omega_0)} \qquad \cdots (5.2.43)$$

c. Maximum Entropy (ME) method

The idea behind the ME method, as devised by Burg [BUR 67], [BUR 68], [BUR 75] for the spectral estimation of time series, was to extrapolate the autocorrelation function of an assumed stationary stochastic process beyond a set of known values, so that the entropy of the process (or, in other words, its 'randomness') is maximised. The problem is akin to that of linear prediction, and the corresponding power spectrum may be shown to be given by the transfer function of the forward prediction-error filter for the time series, as well as by the synthesised output of an autoregressive (all-pole) process generator, excited by the received noise power. The corresponding narrowband spatial processing problem is restricted to linear uniformly-spaced arrays, in which context the order of the appropriate prediction filter or of the autoregressive process generator (for an M-sensor array) is given by M-1. The power spectrum for the (narrowband) ME array processor is of the form:

---

12 Note that the rank of the signal-only component of $\mathbf{R}$ (which is assumed dominant) is K (or less, for coherent signals) which means that $\mathbf{R}$ is 'almost' singular.

$$\mathcal{P}_{ME}(\varphi) = \frac{I_0^T \mathbf{R}^{-1} I_0}{|\mathbf{A}^H(\varphi, \omega_0)\mathbf{R}^{-1} I_0|^2} = \frac{[R^{-1}]_{00}}{|\mathbf{A}^H(\varphi, \omega_0)[R^{-1}]_0|^2} \quad \cdots (5.2.44)$$

where $[R^{-1}]_{00}$ is the element on the first row and first column of the matrix $\mathbf{R}^{-1}$, the vector $[R^{-1}]_0$ denotes the first column of the matrix $\mathbf{R}^{-1}$ and the $M\times 1$ vector I_0 is given by:

$$I_0 = [1\ 0\ 0 \cdots\cdots 0]^T \quad \cdots (5.2.45)$$

Although the rationale behind the ME method is rather different from the argument leading to *(5.2.35)*, it is in fact a special case of the latter MVIR expression with:

$$\mathbf{B} = I_0 \qquad (\Rightarrow K' = 1)$$

It has also been shown [NIC 88] that (for the case of an equally spaced linear array):

$$\frac{1}{\mathcal{P}_{MVDR}(\varphi)} = \sum_{m=1}^{M} \frac{1}{\mathcal{P}_{ME}^{(m)}(\varphi)}$$

where $\mathcal{P}_{ME}^{(m)}(\varphi)$ refers to the ME power spectrum from an m-sensor array and $\mathcal{P}_{MVDR}(\varphi)$ pertains as before to an M-element array.

d. MUltiple SIgnal Classification (MUSIC) method

The MUSIC algorithm as introduced by Schmidt [SCH 79], [SCH 81] and independently by Bienvenu and Kopp [BIE 80] is based on eigenvector-eigenvalue decomposition of the spatial covariance matrix. Referring to the narrowband model described by equation *(5.2.15)*, the signal sources are assumed to have distinct bearings and not to be fully correlated. This implies that in:

$$\mathbf{R} = \mathbf{A}\mathbf{R}_S\mathbf{A}^H + \sigma_n^2\mathbf{I} \quad \cdots (5.2.46)$$

both the signal covariance matrix $\mathbf{R}_S$ and (at least for the case of a uniformly spaced linear array of equi-pattern sensors that cover the relevant source regions) the $M\times K$ steering matrix $\mathbf{A}$ are full rank. If $\lambda_0 \geq \lambda_1 \geq \cdots\cdots \geq \lambda_{M-1}$ and $\varsigma_0 \geq \varsigma_1 \geq \cdots\cdots \geq \varsigma_{M-1}$ denote the eigenvalues of the covariance matrix $\mathbf{R}$ and of the signal-only covariance

matrix $\mathbf{R}_x = \mathbf{A}\mathbf{R}_S\mathbf{A}^H$ respectively,[13] then from *(5.2.46)*:

$$\lambda_i = \varsigma_i + \sigma_w^2 \quad , \quad i = 0, 1, \cdots, M-1 \qquad \cdots (5.2.47)$$

Assuming $\mathbf{A}$ and $\mathbf{R}_S$ to be full rank, it follows that:

$$\varsigma_K = \varsigma_{K+1} = \cdots\cdots = \varsigma_{M-1} = 0$$

and consequently,

$$\lambda_K = \lambda_{K+1} = \cdots\cdots = \lambda_{M-1} = \sigma_w^2$$

The covariance matrix $\mathbf{R}$, being Hermitian, may be characterised by a set of M orthonormal eigenvectors $\{V_i\}_{i=0}^{M-1}$, each associated with its respective eigenvalue λ_i. Obviously:

$$\mathbf{A}\mathbf{R}_S\mathbf{A}^H V_i = \mathbf{0} \quad , \quad K \le i \le M-1 \qquad \cdots (5.2.48)$$

where $\mathbf{0}$ is a vector of zeros. Since $\mathbf{A}$ and $\mathbf{R}_S$ are full rank we may multiply both sides of *(5.2.48)* from the left by $\mathbf{R}_S^{-1}(\mathbf{A}^H\mathbf{A})^{-1}\mathbf{A}^H$ to obtain:

$$\mathbf{A}^H V_i = \mathbf{0} \quad , \quad K \le i \le M-1 \qquad \cdots (5.2.49)$$

In other words, the subspace spanned by the eigenvectors $\{V_i\}_{i=K}^{M-1}$ is orthogonal to the subspace spanned by the columns of $\mathbf{A}$. The latter subspace is therefore also spanned by the complementary set of eigenvectors $\{V_i\}_{i=0}^{K-1}$. The space spanned by the eigenvectors of $\mathbf{R}$ thus consists of two disjoint subspaces:

i. the *signal subspace* which is spanned by the eigenvectors of $\mathbf{R}$ associated with the K largest eigenvalues, and also by the columns of the steering matrix $\mathbf{A}$

ii the *noise subspace* which is spanned by the eigenvectors of $\mathbf{R}$ associated with the M-K smallest eigenvalues; all vectors in this subspace are orthogonal to the columns of $\mathbf{A}$.

The spectral pattern of the (narrowband) MUSIC estimator is given by:

---

13 Note that the sensor noise has to be both spatially white and homoscedastic. If this is not the case, and $\mathbf{R}_w$ is available, one must resort to *generalised* eigen-decomposition [BEL 70] of the matrix pencil $(\mathbf{R}, \mathbf{R}_w)$, or equivalently, perform the appropriate pre-whitening transformation – see appendix E.1.

$$\mathcal{P}_{\text{MUSIC}}(\varphi) = \frac{1}{\sum_{i=K+1}^{M-1} |\mathbf{A}^H(\varphi, \omega_0) V_i|^2} = \frac{1}{\mathbf{A}^H(\varphi, \omega_0)\mathbf{V}_n\mathbf{V}_n^H\mathbf{A}(\varphi, \omega_0)}$$

$$= \frac{1}{\mathbf{A}^H(\varphi, \omega_0)(\mathbf{I} - \mathbf{V}_s\mathbf{V}_s^H)\mathbf{A}(\varphi, \omega_0)} \qquad \cdots (5.2.50)$$

where

$$\mathbf{V}_s = [V_0\ V_1 \cdots\cdots V_{K-1}] \qquad \cdots (5.2.51)$$

$$\mathbf{V}_n = [V_K\ V_{K+1} \cdots\cdots V_{M-1}] \qquad \cdots (5.2.52)$$

As effectively noted by Johnson and Degraff [JOH 82a], [JOH 82b], $\mathcal{P}_{\text{MUSIC}}(\phi)$ may be derived from the MVPR pattern *(5.2.28)* by setting:

$$\mathbf{\Pi} = \sum_{i=K}^{M-1} V_i \lambda_i^{1/2} V_i^H = \sigma_n \mathbf{V}_n \mathbf{V}_n^H$$

and noting that:

$$\mathbf{R}^{-1} = \mathbf{V}[\text{diag}\,(\lambda_0^{-1}\ \lambda_1^{-1} \cdots\cdots \lambda_{M-1}^{-1})]\mathbf{V}^H = \sum_{i=0}^{M-1} V_i(1/\lambda_i)V_i^H \qquad \cdots (5.2.53)$$

where

$$\mathbf{V} = [\mathbf{V}_s\mathbf{V}_n] = [V_0\ V_1 \cdots\cdots V_{M-1}] \qquad \cdots (5.2.54)$$

and diag $(\lambda_0^{-1}\ \lambda_1^{-1} \cdots\cdots \lambda_{M-1}^{-1})$ is an $M \times M$ diagonal matrix whose ii'th element is equal to $1/\lambda_i$. The above setting means that the constraint on the MVPR minimisation problem *(5.2.25)* does not just ensure a 'distortionless response' at the look direction, but forces a projection of $\mathbf{A}(\varphi, \omega_0)$ onto the noise subspace to be equal to one. When φ approaches a DOA angle ϕ_k of one of the incident signals, $\mathbf{A}(\varphi, \omega_0)$ coincides with the corresponding column of the steering matrix $\mathbf{A}$, and $\mathbf{V}_n\mathbf{V}_n^H\mathbf{A}(\varphi, \omega_0)$, its projection onto the noise subspace therefore falls to zero. Constraining the optimal weight vector to form a finite array response with $\mathbf{V}_n\mathbf{V}_n^H\mathbf{A}(\varphi, \omega_0)$, therefore means that (the norm of the) optimal weight vector must increase, thus enhancing the (dynamic) power pattern in that look direction. If the true $\mathbf{R}^{-1}$ matrix and its eigenvectors (rather than estimates thereof) were available, the spectral pattern $\mathcal{P}_{\text{MUSIC}}(\varphi)$ would indeed be characterised by infinitely high pattern peaks at the required DOA angles. The MUSIC algorithm

may thus be viewed as an enhanced MVDR-type scheme and has in fact been shown to possess an MVDR spectral pattern that uses a covariance matrix corresponding to infinite signal-to-noise ratio [NIC 88].

e. Minimum Norm (MN) method

The MN method proposed by Reddy [RED 79] and reformulated by Kumaresan and Tufts [KUM 83a] is another popular eigen-decomposition scheme, but one which tries to represent the noise subspace by a single vector. The underlying idea is based on prediction theory and as such is restricted to equi-spaced linear arrays, although its application to arbitrary arrays has been suggested [VAC 89]. The (narrowband) MN spectral pattern is given by:

$$\mathcal{P}_{MN}(\varphi) = \frac{1}{|\mathbf{A}^H(\varphi, \omega_0)\boldsymbol{b}|^2} \qquad \cdots (5.2.55)$$

where $\boldsymbol{b} = [b_0\, b_1 \cdots\cdots b_{M-1}]^T$ is the vector with least Euclidean norm whose first element b_0 is equal to one, belonging to the noise subspace. Obviously, $\mathbf{A}^H(\varphi, \omega_0)\boldsymbol{b}$ falls to zero whenever φ approaches one of the K DOA angles ϕ_k, and it has been shown by Kumaresan [KUM 83b] that this choice of a weight vector $\boldsymbol{b}$ ensures (for a linear uniformly-spaced array) that the (M-1-K) extraneous zeros of the pattern

$$\sum_{m=0}^{M-1} b_m z^{-m} \quad , \quad z = e^{-j(\omega d/c)\sin\varphi}$$

are approximately uniformly distributed in angle within the unit circle in the z-plane[14]. Denoting:

$$\boldsymbol{b} = [1\ \boldsymbol{\beta}^T]^T$$

and letting

$$\mathbf{V}_s = [\boldsymbol{V}_0\, \boldsymbol{V}_1 \cdots\cdots \boldsymbol{V}_{K-1}\,] = [\boldsymbol{\upsilon}_s\, \mathbf{Y}_s]^H$$

$$\mathbf{V}_n = [\boldsymbol{V}_K\, \boldsymbol{V}_1 \cdots\cdots \boldsymbol{V}_{M-1}] = [\boldsymbol{\upsilon}_n\, \mathbf{Y}_n]^H$$

the orthogonality of $\boldsymbol{b}$ to the columns of $\mathbf{V}_s$ may be expressed as:

$$\mathbf{Y}_s\boldsymbol{\beta} = -\boldsymbol{\upsilon}_s$$

---

14 In the context of array processing [KUM 83b] is actually formulated in terms of a signal-only spatially-smoothed version of the (single-) sample covariance matrix.

which (assuming that $K < M\text{-}1$) is an underdetermined matrix equation for $\boldsymbol{\beta}$, whose least-squares solution subject to $\boldsymbol{\beta}$ having minimum norm is:

$$\boldsymbol{\beta} = -\mathbf{Y}_s^H(\mathbf{Y}_s\mathbf{Y}_s^H)^{-1}\boldsymbol{\upsilon}_s = -\mathbf{Y}_s^H\boldsymbol{\upsilon}_s(1 - |\boldsymbol{\upsilon}_s|^2)^{-1} = \mathbf{Y}_a\boldsymbol{\upsilon}_a|\boldsymbol{\upsilon}_s|^{-2} \qquad \cdots (5.2.56)$$

where use has been made of

$$\mathbf{Y}_s\mathbf{Y}_s^H = \mathbf{V}_s^H\mathbf{V}_s - \boldsymbol{\upsilon}_s\boldsymbol{\upsilon}_s^H = \mathbf{I} - \boldsymbol{\upsilon}_s\boldsymbol{\upsilon}_s^H$$

as well as of the Woodbury identity (matrix inversion lemma)[15]

$$(\mathbf{I} - \boldsymbol{\upsilon}_s\boldsymbol{\upsilon}_s^H)^{-1} = \mathbf{I} + \boldsymbol{\upsilon}_s(1 - |\boldsymbol{\upsilon}_s|^2)^{-1}\boldsymbol{\upsilon}_s^H$$

and of the easily checked identities:

$$|\boldsymbol{\upsilon}_a|^2 = 1 - |\boldsymbol{\upsilon}_s|^2$$

$$\mathbf{Y}_a\boldsymbol{\upsilon}_a = -\mathbf{Y}_s\boldsymbol{\upsilon}_s$$

From *(5.2.56)* we also have:

$$\boldsymbol{b} = \mathbf{V}_a\boldsymbol{\upsilon}_a/|\boldsymbol{\upsilon}_a|^2 = \sum_{i=K}^{M-1} V_i V_{0i}^* \Big/ \sum_{i=K}^{M-1} |V_{0i}|^2 \qquad \cdots (5.2.57)$$

where V_{0i}^* denotes the complex conjugate of the i'th element in the first row of $\mathbf{V}$. It is apparent that by setting:

$$\mathbf{B} = \boldsymbol{b} \qquad (\Rightarrow K' = 1)$$

in the MVIR spectral pattern *(5.2.35)* one obtains:

$$\mathcal{P}(\varphi) = \frac{\sigma_a^2 \sum_{i=K}^{M-1} |V_{0i}|^2}{|\mathbf{A}^H(\varphi, \omega_0)\boldsymbol{b}|^2}$$

which (to within a constant) is the MN spectral pattern. The MN method may therefore be viewed as an enhanced version of the ME scheme and $\mathcal{P}_{MN}(\varphi)$ is in fact

15 The matrix inversion lemma version used here relates to a $K\times L$ matrix $\mathbf{A}$ and an $L\times K$ matrix $\mathbf{B}$, and states that: $(\mathbf{I}_{K\times K} + \mathbf{AB})^{-1} = \mathbf{I}_{K\times K} - \mathbf{A}\,(\mathbf{I}_{L\times L} + \mathbf{BA})^{-1}\,\mathbf{B}$
where $\mathbf{I}_{K\times K}$ and $\mathbf{I}_{L\times L}$ are the respective $K\times K$ and $L\times L$ identity matrices.

related to $\mathcal{P}_{ME}(\varphi)$ in exactly the same way that $\mathcal{P}_{MUSIC}(\varphi)$ is related to $\mathcal{P}_{MVDR}(\varphi)$ [NIC 88]: $\mathcal{P}_{MN}(\varphi)$ possesses an ME spectral pattern that uses a correlation matrix corresponding to infinite signal-to-noise ratio.

5.2.5 SEARCH-FREE SUPERRESOLUTION ALGORITHMS

The DOA parameter search involved in forming the spectral patterns of scalar-search estimation schemes (see sub-section 5.2.4), although straightforward to implement, does pose a considerable computational burden on those algorithms. This adds to the typically large amounts of data storage associated with the crucial but non-trivial task of calibrating the responses of the array sensors. Both these drawbacks are essentially removed in the spatial estimators described in this sub-section: the evaluation of the angles of arrival requires no search procedure nor does it depend on a knowledge of the sensor characteristics being available to the estimator. The structural requirements of these techniques as well as their independence of the actual sensor patterns are similar to those encountered in conventional phase-comparison direction-finding, and they may indeed be viewed as extended phase-comparison schemes that are pertinent to a noisy multiple-source environment. Since no parameter search is involved, these methods are referred to here as search-free superresolution algorithms.

a. Estimation of Signal Parameters via Rotational Invariance Techniques (ESPRIT)

The ESPRIT method introduced by Paulraj, Roy and Kailath is an eigen-structure scheme that exploits a known translational invariance in the array structure in order to ease the computational and storage requirements that characterise scalar-search eigen-decomposition algorithms such as MUSIC or the MN method. The required structural constraint is that the array be comprised of two identical sub-arrays, displaced by a known vector (with respect to which all bearings are to be defined). In the original form of ESPRIT [PAU 85], [PAU 86], [ROY 86a], [ROY 86b] the required DOA parameters appear as the largest generalised eigenvalues of the signal-only covariance matrix of one sub-array in the metric of the cross-covariance matrix of the two sub-arrays. In later more numerically robust developments of the algorithm [ROY 87], [ROY 89], [OTT 91] two sets of vectors that span the sub-array signal sub-space are obtained by pre-multiplying the complementary of the full-array noise-space eigenvector matrix by the full-array noise covariance matrix, and partitioning in accordance with the two sub-arrays. The DOA parameters are then estimated as the full set of eigenvalues of

the matrix operator that maps, in the least squares (or preferably in the total least squares) sense, one of these sets of vectors into the other. Other modifications include the reformulation of (total-least-squares) ESPRIT as a (vector-search) subspace fitting scheme [VIB 91a], its extension to the wideband problem [OTT 88], [OTT 90a] and its application to polarisation-sensitive (antenna) arrays as a combined DOA and signal-polarisation estimator [LIC 91].

For the mathematical formulation of ESPRIT, let K incoherent far-field sources illuminate a sensor array possessing at least one translational invariance so that it can be viewed as two M''-element sub-arrays of identical geometries with a vector displacement of Δ between them, and let $K < M''$[16]. The $M' = 2M''$ narrowband signals $[\boldsymbol{x}^T \boldsymbol{y}^T]^T$ at the outputs of the two sub-arrays may be expressed as:

$$\begin{bmatrix} \boldsymbol{x} \\ \boldsymbol{y} \end{bmatrix} = \begin{bmatrix} \mathbf{A}_x \\ \mathbf{A}_x \boldsymbol{\Psi} \end{bmatrix} \boldsymbol{s} + \begin{bmatrix} \boldsymbol{x}_n \\ \boldsymbol{y}_n \end{bmatrix} \qquad \cdots (5.2.58)$$

where $\boldsymbol{x}_n$ and $\boldsymbol{y}_n$ denote the additive $M''\times 1$ noise vectors for the two sets of sensors, $\boldsymbol{s}$ is the $K\times 1$ signal vector, $\mathbf{A}_x$ is the $M''\times K$ sub-array steering matrix and $\boldsymbol{\Psi}$ is a $K\times K$ diagonal matrix of the phase delays between the corresponding sensors of the two sub-arrays:

$$\boldsymbol{\Psi} = \mathrm{diag}[e^{j(\omega_0 \Delta/c)\sin\phi_0}\, e^{j(\omega_0 \Delta/c)\sin\phi_1} \ldots\ldots e^{j(\omega_0 \Delta/c)\sin\phi_{K-1}}] \qquad \cdots (5.2.59)$$

In *(5.2.59)* $\Delta = |\boldsymbol{\Delta}|$ and spatial angles are measured with respect to a vector perpendicular to $\boldsymbol{\Delta}$. The covariance matrix $\bar{\mathbf{R}}$ for the combined ESPRIT array is given by[17]:

$$\bar{\mathbf{R}} = \begin{pmatrix} \mathbf{R}_x & \mathbf{R}_{xy} \\ \mathbf{R}_{yx} & \mathbf{R}_y \end{pmatrix} = \begin{pmatrix} \mathbf{A}_x \mathbf{R}_s \mathbf{A}_x^H & \mathbf{A}_x \mathbf{R}_s \boldsymbol{\Psi}^H \mathbf{A}_x^H \\ \mathbf{A}_x \boldsymbol{\Psi} \mathbf{R}_s \mathbf{A}_x^H & \mathbf{A}_x \boldsymbol{\Psi} \mathbf{R}_s \boldsymbol{\Psi}^H \mathbf{A}_x^H \end{pmatrix} + \sigma_n^2 \begin{pmatrix} \mathbf{R}_{nx} & \mathbf{R}_{nxy} \\ \mathbf{R}_{nyx} & \mathbf{R}_{ny} \end{pmatrix}$$

$$= \bar{\mathbf{A}} \mathbf{R}_s \bar{\mathbf{A}}^H + \sigma_n^2 \bar{\mathbf{R}}_n \qquad \cdots (5.2.60)$$

where $\bar{\mathbf{R}}_n$ and $\bar{\mathbf{A}} = [\mathbf{A}_x^T \;\; \boldsymbol{\Psi}^T \mathbf{A}_x^T]^T$ are respectively the combined noise matrix and combined steering matrix for the two sub-arrays[18]. Note that in the case of spatially-

16 For an M-sensor array consisting of two non-overlapping sub-arrays we are restricted to $K < M/2$. An equally-spaced linear array possesses more than one translational invariance, so that overlapping sub-arrays may be formed. By selecting: $M'' = M-1$ the above restriction is relaxed to $K < M-1$.

17 For non-overlapping sub-arrays, $\bar{\mathbf{R}}$ is simply the full-array covariance matrix $\mathbf{R}$.

18 For non-overlapping sub-arrays, $\bar{\mathbf{R}}_n$ and $\bar{\mathbf{A}}$ are simply the full-array noise matrix $\mathbf{R}_n$ and steering matrix $\mathbf{A}$ respectively.

white homoscedastic noise:

$$\mathbf{R}_{\epsilon x} = \mathbf{R}_{\epsilon y} = \mathbf{I}$$

and if the two sub-arrays are non-overlapping, then also,

$$\mathbf{R}_{\epsilon xy} = \mathbf{R}_{\epsilon yx} = \mathbf{0}$$

Following the original ESPRIT formulation let us denote:

$$\mathbf{R}_{\phi x} = \mathbf{R}_x - \sigma_\epsilon^2 \mathbf{R}_{\epsilon x} \qquad \cdots (5.2.61)$$

$$\mathbf{R}_{\phi xy} = \mathbf{R}_{xy} - \sigma_\epsilon^2 \mathbf{R}_{\epsilon xy} \qquad \cdots (5.2.62)$$

and consider the matrix pencil $(\mathbf{R}_{\phi x}, \mathbf{R}_{\phi xy})$. Clearly:

$$\mathbf{R}_{\phi x} - \psi \mathbf{R}_{\phi xy} = \mathbf{A}_x \mathbf{R}_s (\mathbf{I} - \psi \mathbf{\Psi}^H) \mathbf{A}_x^H \qquad \cdots (5.2.63)$$

and for full-rank $\mathbf{A}_x$, $\mathbf{R}_s$ and $(\mathbf{I} - \psi \mathbf{\Psi}^H)$ matrices –

$$\text{rank}[\mathbf{A}_x \mathbf{R}_s (\mathbf{I} - \psi \mathbf{\Psi}^H) \mathbf{A}_x^H] = \text{rank}[\mathbf{A}_x \mathbf{R}_s \mathbf{A}_x^H] = K$$

But whenever:

$$\psi = \psi_k = e^{j(\omega_0 \Delta / c) \sin \phi_k} \quad , \quad 0 \le k \le K\text{-}1$$

the k'th row of $(\mathbf{I} - \psi \mathbf{\Psi}^H)$ becomes a row of zeros and rank$[\mathbf{R}_{\phi x} - \psi \mathbf{R}_{\phi xy}]$ drops to K-1, which by definition means that $\{\psi_k\}_{k=0}^{K-1}$ are generalised eigenvalues of the matrix pair $(\mathbf{R}_{\phi x}, \mathbf{R}_{\phi xy})$. Since both $\mathbf{R}_{\phi x} = \mathbf{A}_x \mathbf{R}_s \mathbf{A}_x^H$ and $\mathbf{R}_{\phi xy} = \mathbf{A}_x \mathbf{R}_s \mathbf{\Psi}^H \mathbf{A}_x^H$ span the same sub-space, the M''-K generalised eigenvalues corresponding to their common null-space will be zero[19], and the DOA parameters are thus estimated by evaluating the K largest generalised eigenvalues of the matrix pair $(\mathbf{R}_{\phi x}, \mathbf{R}_{\phi xy})$.

---

19 Notice that this is a *singular* generalised eigen-decomposition problem in that the matrix $\mathbf{R}_{\phi xy}$ in the pair $(\mathbf{R}_{\phi x}, \mathbf{R}_{\phi xy})$ is singular. This means that $|\mathbf{R}_{\phi x} - \psi \mathbf{R}_{\phi xy}| = 0$ and $(\mathbf{R}_{\phi x} - \psi \mathbf{R}_{\phi xy})\mathbf{v} = \mathbf{0}$ for a vector $\mathbf{v}$ in the common null space of $\mathbf{R}_{\phi x}$ and $\mathbf{R}_{\phi xy}$, are satisfied by any value of ψ. Two procedures for solving this problem based on the factorisation of $\mathbf{R}_{\phi xy}$ are suggested in [Zoi 87a], [Zoi 87b]. Both procedures evaluate the generalised eigenvalues corresponding to the range space of $\mathbf{R}_{\phi xy}$, and in the second procedure the extraneous M''-K null-space eigenvalues are obtained as zero.

b. Least Squares (LS) and Total Least Squares (TLS) ESPRIT

In these versions of ESPRIT the K generalised eigenvectors $\{\bar{V}_0, \bar{V}_1, \cdots, \bar{V}_{K-1}\}$ corresponding to the K largest generalised eigenvalues of the matrix pair $(\bar{\mathbf{R}}, \bar{\mathbf{R}}_{\epsilon})$ are used to define the $M' \times K$ matrix $\tilde{\mathbf{V}}_{\epsilon} = \bar{\mathbf{R}}_{\epsilon}[\bar{V}_0\, \bar{V}_1 \cdots \bar{V}_{K-1}]$ whose columns span the same sub-space as do the columns of the combined steering matrix $\bar{\mathbf{A}}$ – see appendix E.1. There must therefore exist a unique nonsingular $K \times K$ transformation matrix T such that:

$$\tilde{\mathbf{V}}_{\epsilon} = \begin{bmatrix} \tilde{\mathbf{V}}_x \\ \tilde{\mathbf{V}}_y \end{bmatrix} = \begin{bmatrix} \mathbf{A}_x\mathbf{T} \\ \mathbf{A}_x\mathbf{\Psi}\mathbf{T} \end{bmatrix} = \bar{\mathbf{A}}\mathbf{T} \qquad \cdots (5.2.64)$$

where $\tilde{\mathbf{V}}_{\epsilon}$ has been partitioned in accordance with the two sub-arrays. $\mathbf{A}_x$ may be eliminated from the above equation, resulting in:

$$\tilde{\mathbf{V}}_y = \tilde{\mathbf{V}}_x\mathbf{T}^{-1}\mathbf{\Psi}\mathbf{T} \qquad \cdots (5.2.65)$$

The elements of $\mathbf{\Psi}$ are therefore the eigenvalues of the operator that maps the columns of $\tilde{\mathbf{V}}_x$ onto $\tilde{\mathbf{V}}_y$. In LS-ESPRIT, this operator

$$\mathbf{F} = \mathbf{T}^{-1}\mathbf{\Psi}\mathbf{T} \qquad \cdots (5.2.66)$$

is estimated through a least-squares minimisation procedure

$$\min_{\mathbf{F}} \|\tilde{\mathbf{V}}_y - \tilde{\mathbf{V}}_x\mathbf{F}\|_F^2 \qquad \cdots (5.2.67)$$

or, alternatively:

$$\min_{\mathbf{F}^{-1}} \|\tilde{\mathbf{V}}_y\mathbf{F}^{-1} - \tilde{\mathbf{V}}_x\|_F^2 \qquad \cdots (5.2.68)$$

where $\|\mathbf{A}\|_F^2 = \mathrm{tr}(\mathbf{A}^H\mathbf{A})$ is the squared *Frobenius norm* of the matrix $\mathbf{A}$.[20] Procedures *(5.2.67)* and *(5.2.68)* above result in the following two respective expressions for F:

$$\mathbf{F} = (\tilde{\mathbf{V}}_x^H\tilde{\mathbf{V}}_x)^{-1}\tilde{\mathbf{V}}_x^H\tilde{\mathbf{V}}_y \qquad \cdots (5.2.69)$$

$$\mathbf{F} = (\tilde{\mathbf{V}}_y^H\tilde{\mathbf{V}}_x)^{-1}\tilde{\mathbf{V}}_y^H\tilde{\mathbf{V}}_y \qquad \cdots (5.2.70)$$

---

[20] Note that the Frobenius norm of $\mathbf{A} = [\boldsymbol{A}_0\, \boldsymbol{A}_1 \cdots \boldsymbol{A}_{K-1}]$ is also given by: $\|\mathbf{A}\|_F^2 = \sum_{k=0}^{K-1} |\boldsymbol{A}_k|^2$

Although both these expressions are equivalent in theory[21], this is not so in practice, where only an estimate of $\tilde{\mathbf{V}}_s = [\tilde{\mathbf{V}}_x^H \ \tilde{\mathbf{V}}_y^H]^H$ is available. The non-symmetrical nature of the least-squares formulation with respect to $\tilde{\mathbf{V}}_x$ and $\tilde{\mathbf{V}}_y$ means that DOA estimates based on the above solutions will in fact be non-identical and biased [GOL 84].

A more symmetric approach for extracting $\mathbf{F}$ based on the total least squares criterion [GOL 80], [GOL 84] is employed in TLS-ESPRIT. The minimisation procedure pursued here is:

$$\min_{\mathbf{F}_x, \mathbf{F}_y} \|\tilde{\mathbf{V}}_x\mathbf{F}_x + \tilde{\mathbf{V}}_y\mathbf{F}_y\|_F^2 \qquad \cdots (5.2.71)$$

constrained by the non-triviality condition

$$\mathbf{F}_x^H\mathbf{F}_x + \mathbf{F}_y^H\mathbf{F}_y = \mathbf{I} \qquad \cdots (5.2.72)$$

Denoting:

$$\begin{aligned} \tilde{\mathbf{V}}_{xy} &= [\tilde{\mathbf{V}}_x \ \ \tilde{\mathbf{V}}_y] \\ \mathbf{F}_{xy} &= [\mathbf{F}_x^T \ \ \mathbf{F}_y^T]^T \end{aligned} \qquad \cdots (5.2.73)$$

the total least squares minimisation problem described by *(5.2.71)* and *(5.2.72)* may be rewritten as

$$\min_{\mathbf{F}_{xy}} \|\tilde{\mathbf{V}}_{xy}\mathbf{F}_{xy}\|_F^2 \quad , \quad \mathbf{F}_{xy}^H\mathbf{F}_{xy} = \mathbf{I} \qquad \cdots (5.2.74)$$

the solution for which is obtained in terms of the eigenvector matrix $\mathbf{U}$ of $\tilde{\mathbf{V}}_{xy}^H\tilde{\mathbf{V}}_{xy}$ whose columns (eigenvectors of $\tilde{\mathbf{V}}_{xy}^H\tilde{\mathbf{V}}_{xy}$) are arranged in decreasing order of the corresponding eigenvalues (see appendix E.2 for details):

$$\mathbf{F}_{xy} = \begin{bmatrix} \mathbf{F}_x \\ \mathbf{F}_y \end{bmatrix} = \begin{bmatrix} \mathbf{U}_{12} \\ \mathbf{U}_{22} \end{bmatrix} \qquad \cdots (5.2.75)$$

where $\mathbf{U}_{12}$ and $\mathbf{U}_{22}$ are $K \times K$ sub-matrices of –

$$\mathbf{U} = \begin{bmatrix} \mathbf{U}_{11} & \mathbf{U}_{12} \\ \mathbf{U}_{21} & \mathbf{U}_{22} \end{bmatrix} \qquad \cdots (5.2.76)$$

21 This can be easily checked by substituting $\tilde{\mathbf{V}}_y = \tilde{\mathbf{V}}_x\mathbf{F}$ for $\tilde{\mathbf{V}}_y$ in *(5.2.70)*.

The required operator **F** is finally given by:

$$\mathbf{F} = -\mathbf{F}_x\mathbf{F}_y^{-1} = -\mathbf{U}_{12}\mathbf{U}_{22}^{-1} \qquad \cdots (5.2.77)$$

and the DOA parameters may be directly evaluated from the eigenvalues obtained from its eigen-decomposition.

c. Toeplitz Approximation Method (TAM)

In the context of array processing, TAM is a search-free spatial spectral estimation scheme, based on extracting signal-bearing information from an operator that transforms between two sets of vectors spanning the signal-subspace of two overlapping sub-arrays. The method has been originally formulated under state-space representation as a solution for the harmonic retrieval problem [KUN 83] and later proposed by Kung *et al.* [KUN 86] as a spatial estimator, in which context it is inherently restricted to linear equi-spaced arrays. TAM does, however, bear strong resemblance to ESPRIT, and it has in fact been shown that TAM and LS-ESPRIT (and asymptotically, also TLS-ESPRIT) are statistically equivalent [RAO 88], [RAO 89], [LIV 91].

The state-space formulation for a set of K narrowband incoherent signals, incident on an M-sensor linear uniformly-spaced array is as follows:

$$\begin{aligned} \xi_{m+1}(t) &= \Psi\,\xi_m(t) && 0 \le m \le M\text{-}2 \\ x_{s_m}(t) &= \alpha\,\xi_m(t) = \alpha\Psi^m\,\xi_0(t) && 1 \le m \le M\text{-}1 \end{aligned} \qquad \cdots (5.2.78)$$

In *(5.2.78)* ξ_m is a K-dimensional state-vector with initial value equal to

$$\xi_0(t) = \mathbf{s}(t)$$

α is a row vector denoting the spatial response of the first sensor at the K different source directions, x_{s_m} is the signal-only output at the m'th array sensor, and

$$\Psi = \mathrm{diag}[e^{j(\omega_0 d/c)\sin\phi_0}\, e^{j(\omega_0 d/c)\sin\phi_1} \ldots\ldots e^{j(\omega_0 d/c)\sin\phi_{K-1}}] \qquad \cdots (5.2.79)$$

which is the same as the ESPRIT diagonal matrix defined in *(5.2.59)*, but with the inter-array spacing Δ set equal to the inter-sensor spacing d. It is easy to see that the

covariance matrix for the array outputs takes the familiar form:

$$\mathbf{R} = \mathbf{A}\mathbf{R}_S\mathbf{A}^H + \sigma_n^2\mathbf{R}_n$$

with the steering matrix $\mathbf{A}$ being given by:

$$\mathbf{A} = \begin{bmatrix} \alpha \\ \alpha\Psi \\ \vdots \\ \alpha\Psi^{M-1} \end{bmatrix} = \begin{bmatrix} \mathbf{B} \\ \alpha\Psi^{M-1} \end{bmatrix} = \begin{bmatrix} \alpha \\ \mathbf{B}\Psi \end{bmatrix} \qquad \cdots (5.2.80)$$

where the $(M\text{-}1)\times K$ matrix $\mathbf{B}$ comprises the top M-1 rows of $\mathbf{A}$. The signal-only covariance matrix may be factorised as follows:

$$\mathbf{R}_s = \mathbf{A}\mathbf{R}_S\mathbf{A}^H = [\mathbf{R}_n\mathbf{V}_s(\Lambda_s - \sigma_n^2\mathbf{I})^{1/2}][\mathbf{R}_n\mathbf{V}_s(\Lambda_s - \sigma_n^2\mathbf{I})^{1/2}]^H \qquad \cdots (5.2.81)$$

where Λ_s is a diagonal $K\times K$ matrix of the K largest generalised eigenvalues of $\mathbf{R}$ (arranged in decreasing order), $(\Lambda_s - \sigma_n^2\mathbf{I})^{1/2}$ has the square roots of the generalised eigenvalues of $\mathbf{R}_s$ on its main diagonal and $\mathbf{V}_s$ is the corresponding generalised eigenvector (sub-) matrix – see appendix E.1. Denoting the top and bottom M-1 rows of $\mathbf{R}_n\mathbf{V}_s(\Lambda_s - \sigma_n^2\mathbf{I})^{1/2}$ by the sub-matrices $\tilde{\mathbf{V}}_{s_1}$ and $\tilde{\mathbf{V}}_{s_2}$ respectively, we then have:

$$\begin{bmatrix} \mathbf{B} \\ \mathbf{B}\Psi \end{bmatrix}\mathbf{R}_S\begin{bmatrix} \mathbf{B}^H & \Psi^H\mathbf{B}^H \end{bmatrix} = \begin{bmatrix} \tilde{\mathbf{V}}_{s_1} \\ \tilde{\mathbf{V}}_{s_2} \end{bmatrix}\begin{bmatrix} \tilde{\mathbf{V}}_{s_1}^H & \tilde{\mathbf{V}}_{s_2}^H \end{bmatrix} \qquad \cdots (5.2.82)$$

Since $\mathbf{B}$, $\mathbf{R}_S$ and Ψ are full rank it follows that the columns of $[\ \mathbf{B}^H \quad \Psi^H\mathbf{B}^H\ ]^H$ and $[\ \tilde{\mathbf{V}}_{s_1}^H \quad \tilde{\mathbf{V}}_{s_2}^H\ ]^H$ span the same sub-space, which means that for some non-singular transformation $\mathbf{T}$ we have:

$$\begin{bmatrix} \tilde{\mathbf{V}}_{s_1} \\ \tilde{\mathbf{V}}_{s_2} \end{bmatrix} = \begin{bmatrix} \mathbf{B} \\ \mathbf{B}\Psi \end{bmatrix}\mathbf{T} \qquad \cdots (5.2.82)$$

When $\mathbf{B}$ is eliminated from the above equation, Ψ is obtained as the eigenvalue matrix of the operator $\mathbf{F}$ that transforms the columns of $\tilde{\mathbf{V}}_{s_1}$ onto $\tilde{\mathbf{V}}_{s_2}$:

$$\tilde{\mathbf{V}}_{s_2} = \tilde{\mathbf{V}}_{s_1}\mathbf{T}^{-1}\Psi\mathbf{T} = \tilde{\mathbf{V}}_{s_1}\mathbf{F} \qquad \cdots (5.2.83)$$

The above transformation is of exactly the same form as the corresponding ESPRIT mapping given by *(6.5.65)*, and the least-squares solution for **F** is similarly given by:

$$\mathbf{F} = (\tilde{\mathbf{V}}_{s_1}^H \tilde{\mathbf{V}}_{s_1})^{-1} \tilde{\mathbf{V}}_{s_1}^H \tilde{\mathbf{V}}_{s_2} \qquad \cdots (5.2.84)$$

Comparing the TAM formulation to ESPRIT, it is clear that the TAM operator $\mathbf{F}_{TAM}$ is related to the ESPRIT operator $\mathbf{F}_{ESPRIT}$ (for the case of a linear equi-spaced array where $M'' = M\text{-}1$) by the diagonal similarity transformation:

$$\mathbf{F}_{TAM} = (\mathbf{\Lambda}_s - \sigma_w^2 \mathbf{I})^{-1/2} \mathbf{F}_{ESPRIT} (\mathbf{\Lambda}_s - \sigma_w^2 \mathbf{I})^{1/2} \qquad \cdots (5.2.85)$$

5.2.6 VECTOR-SEARCH SUPERRESOLUTION ALGORITHMS

The performance of search-free and scalar-search spatial estimators depends on the non-singularity of the signal covariance matrix $\mathbf{R}_s$, degrading substantially when coherent signals are encountered. As discussed in section 5.4 of this chapter, signal coherence can be tackled by resorting to pre-processing in the form of spatial smoothing with its attendant loss of resolution, frequency-domain smoothing which only applies to wideband signals or both. A different approach is to seek a more optimal algorithm which is inherently insensitive to the presence of coherent signals. Such algorithms are reviewed in this sub-section under the heading of vector-search superresolution methods, as they all require a multivariate search of the K-dimensional parameter space of DOA vectors. The superiority of these algorithms is also exhibited under low SNR conditions ('threshold region'), or when the number of available snapshots is small[22] [TUF 82], [MAT 89], [VIB 91a], [KAV 91], [STO 91]. The price paid for the improved performance and robustness of these algorithms is the high computational load involved in the simultaneous parameter search which they employ.

a. Iterative Multi-Parameter (IMP) method

The IMP algorithm proposed by Clarke [CLA 88], [MAT 89], [CLA 91] is conceptually very simple. It employs an iterative search that utilises conventional beamforming for alternately estimating the bearing of each of the sources while nulling the estimated bearings of all others. The multivariate parameter search is thus transformed into a

22 Note that if the number of snapshots N is smaller than the number of array sensors M, then the sample covariance matrix *(5.2.37)* is rank deficient.

series of single-parameter maximisations, an approach similar to the *alternating projection technique* that has been suggested for the numeric solution of the DML method reviewed later in this sub-section [ZIS 87], [ZIS 88].

The IMP algorithm begins by searching for an initial estimate ϕ_{00} for the direction of arrival ϕ_0 of the first (and presumably strongest) signal. This is taken as the largest peak of the (dynamic) power-pattern of a conventional beamformer that forms a spatial matched filter in each scanned directions φ:

$$\phi_{00} = \arg\max_{\varphi}\{\boldsymbol{A}^H(\varphi,\omega_0)\mathbf{R}\boldsymbol{A}(\varphi,\omega_0) / \boldsymbol{A}^H(\varphi,\omega_0)\boldsymbol{A}(\varphi,\omega_0)\} \qquad \cdots (5.2.86)$$

where $\boldsymbol{A}(\varphi,\omega_0)$ is the array steering vector and $\mathbf{R}$, the array covariance matrix is estimated in the usual way[23]. Next, a projection matrix onto the null-space of $\boldsymbol{A}_{00} = \boldsymbol{A}(\phi_{00},\omega_0)$ is formed:

$$\boldsymbol{\Pi}(\boldsymbol{A}_{00}) = \mathbf{I} - \boldsymbol{A}_{00}(\boldsymbol{A}_{00}^H\boldsymbol{A}_{00})^{-1}\boldsymbol{A}_{00}^H$$

and the search for a second signal is conducted with projected steering vectors $\boldsymbol{\Pi}(\boldsymbol{A}_{00})\boldsymbol{A}(\varphi,\omega_0)$ so that the initial estimate ϕ_{10} for the direction of arrival ϕ_1 of the second signal is obtained as:

$$\phi_{10} = \arg\max_{\varphi}\mathcal{P}(\boldsymbol{\Pi}(\boldsymbol{A}_{00}),\ \varphi)$$

where[24]

$$\mathcal{P}(\boldsymbol{\Pi},\ \varphi) = \boldsymbol{A}^H(\varphi,\omega_0)\boldsymbol{\Pi}\mathbf{R}\boldsymbol{\Pi}\boldsymbol{A}(\varphi,\omega_0) / \boldsymbol{A}^H(\varphi,\omega_0)\boldsymbol{\Pi}\boldsymbol{A}(\varphi,\omega_0) \qquad \cdots (5.2.87)$$

A subsequent estimate ϕ_{01} is then evaluated for ϕ_0 –

$$\phi_{01} = \arg\max_{\varphi}\mathcal{P}(\boldsymbol{\Pi}(\boldsymbol{A}_{10}),\ \varphi)$$

where $\boldsymbol{\Pi}(\boldsymbol{A}_{10})$ is a projection matrix onto the null-space of $\boldsymbol{A}_{10} = \boldsymbol{A}(\phi_{10},\omega_0)$, and the process continues with similar iterations for ϕ_{11}, ϕ_{02}, ϕ_{12} etc. until stable respective

---

23 Note that in *(5.2.86)* $\varphi = \phi_{00}$ maximises the SNR provided the noise is spatially white and homoscedastic. In the more general case of an arbitrary but known noise covariance matrix $\mathbf{R}_{nn}$, *(5.2.86)* should be modified to:

$$\phi_{00} = \arg\max_{\varphi}\{\boldsymbol{A}^H(\varphi,\omega_0)\mathbf{R}\boldsymbol{A}(\varphi,\omega_0) / \boldsymbol{A}^H(\varphi,\omega_0)\mathbf{R}_{nn}\boldsymbol{A}(\varphi,\omega_0)\}$$

24 when the noise covariance matrix is not equal to the identity matrix then *(5.2.87)* ought to be modified to: $\mathcal{P}(\boldsymbol{\Pi},\ \varphi) = \boldsymbol{A}^H(\varphi,\omega_0)\boldsymbol{\Pi}\mathbf{R}\boldsymbol{\Pi}\boldsymbol{A}(\varphi,\omega_0) / \boldsymbol{A}^H(\varphi,\omega_0)\boldsymbol{\Pi}\mathbf{R}_{nn}\boldsymbol{\Pi}\boldsymbol{A}(\varphi,\omega_0)$

estimates (re-denoted here as ϕ_{00} and ϕ_{10}) for ϕ_0 and ϕ_1 are obtained. Next, $\mathbf{\Pi}$ is redefined as a projection matrix onto the null space of the columns of a matrix $\mathbf{A}$:

$$\mathbf{\Pi}(\mathbf{A}) = \mathbf{I} - \mathbf{A}(\mathbf{A}^H\mathbf{A})^{-1}\mathbf{A}^H$$

and the iterations restart with:

$$\phi_{20} = \arg\max_{\varphi} \mathcal{P}(\mathbf{\Pi}(\boldsymbol{A}_{00}\ \boldsymbol{A}_{10}),\ \varphi)$$

$$\phi_{01} = \arg\max_{\varphi} \mathcal{P}(\mathbf{\Pi}(\boldsymbol{A}_{10}\ \boldsymbol{A}_{20}),\ \varphi)$$

$$\phi_{11} = \arg\max_{\varphi} \mathcal{P}(\mathbf{\Pi}(\boldsymbol{A}_{01}\ \boldsymbol{A}_{20}),\ \varphi)$$

and so on, until convergence to stable estimates for ϕ_0, ϕ_1 and ϕ_2 is achieved. The process continues until all sources have been localised, or (if K is not known) until some pre-determined criterion for the flatness of the residual spatial spectrum $\mathcal{P}(\mathbf{\Pi}(\boldsymbol{A}_{00}\ \boldsymbol{A}_{10} \cdots \boldsymbol{A}_{(K-1)0}),\ \varphi)$ is satisfied.

b. Stochastic ('unconditional') Maximum Likelihood (SML) method

The statistical inference technique known as the maximum-likelihood (ML) method was among the first approaches to be pursued for estimating the directions of arrival of signals in a multiple emitters environment using a sensor array [SCH 68], [LIG 73], [OWS 81], [WAX 83]. The idea is to estimate the K-dimensional DOA parameter vector $\boldsymbol{\phi}$ by its most likely value, given the observed sample vector $\boldsymbol{u}$. Assuming a uniform *a priori* PDF for $\boldsymbol{\phi}$ and noting the monotonic nature of the logarithmic transformation, this is equivalent to seeking a $K\times1$ vector $\boldsymbol{\varphi}$ that will maximise the log-likelihood function $\ln f_{\boldsymbol{u}}(\boldsymbol{u}|\boldsymbol{\varphi})$. In the context of a general data vector of length L, the ML estimator exhibits a number of desirable asymptotic ($L \rightarrow \infty$) properties [VAN 68]: it is asymptotically Gaussian, unbiased and efficient, and it is *consistent* in that it converges in probability (for $L \rightarrow \infty$) to the true parameter value.

In the context of array processing, two different signal models, namely the stochastic (unconditional) and the deterministic (conditional) models, have formed the basis for two statistically different versions of the ML estimator [STO 90b], [OTT 92]. For the *Stochastic Maximum-Likelihood* method [BAN 71], [BOH 86], [JAF 88] one assumes the sources to be stationary zero-mean jointly complex Gaussian random

processes, uncorrelated with the additive noises. The latter are taken as stationary zero-mean uncorrelated ("spatially white") complex Gaussian processes. The (assumed statistically independent) samples of the received array data are then zero-mean complex Gaussian vectors with a log-likelihood function given by:[25]

$$\ln f_{\boldsymbol{U}}(\boldsymbol{u}|\boldsymbol{\varphi}) = -N \ln(\pi^M |\mathcal{E}\boldsymbol{X}(\boldsymbol{\varphi})\boldsymbol{X}^H(\boldsymbol{\varphi})|) - \sum_{n=0}^{N-1} \boldsymbol{x}^H(t_n)[\mathcal{E}\boldsymbol{X}(\boldsymbol{\varphi})\boldsymbol{X}^H(\boldsymbol{\varphi})]^{-1}\boldsymbol{x}(t_n)$$

$$= -NM\ln\pi - N\ln|\mathbf{R}(\boldsymbol{\varphi})| - N\,\mathrm{tr}[\hat{\mathbf{R}}(\boldsymbol{u})\,\mathbf{R}^{-1}(\boldsymbol{\varphi})] \qquad \cdots (5.2.88)$$

where $|\mathbf{R}|$ denotes the determinant of the array covariance matrix $\mathbf{R}$ given the parameter vector $\boldsymbol{\varphi}$, $\mathbf{R}^{-1}$ is its inverse, and $\hat{\mathbf{R}}$ is the sample covariance matrix defined in *(5.2.37)*. Under wideband conditions, data snapshots may be represented by their Fourier series coefficients as discussed in section 5.2, sub-section 5.2.2. The log-likelihood function for $\boldsymbol{U} = [\boldsymbol{X}^T(\omega_\ell; t_0)\ \boldsymbol{X}^T(\omega_\ell; t_1) \cdots\cdots \boldsymbol{X}^T(\omega_\ell; t_{N-1})]^T$ being also a zero-mean complex Gaussian vector, is similarly given by:

$$\ln f_{\boldsymbol{U}}(\boldsymbol{U}|\boldsymbol{\varphi}) =$$

$$-N\ln(\pi^M |\mathcal{E}\boldsymbol{X}(\omega_\ell|\boldsymbol{\varphi})\boldsymbol{X}^H(\omega_\ell|\boldsymbol{\varphi})|) - \sum_{n=0}^{N-1} X^H(\omega_\ell; t_n)[\mathcal{E}\boldsymbol{X}(\omega_\ell|\boldsymbol{\varphi})\boldsymbol{X}^H(\omega_\ell|\boldsymbol{\varphi})]^{-1}X(\omega_\ell; t_n)$$

$$\approx NM\ln(T/\pi) - N\ln|\mathbf{P}(\omega_\ell|\boldsymbol{\varphi})| - N\,\mathrm{tr}[\hat{\mathbf{P}}(\boldsymbol{U}; \omega_\ell)\mathbf{P}^{-1}(\omega_\ell|\boldsymbol{\varphi})] \qquad \cdots (6.2.89)$$

where $\mathbf{P}$ is the array cross-spectral density matrix given the parameter vector $\boldsymbol{\varphi}$, and $\hat{\mathbf{P}}$ is the sample spectral density matrix as defined by *(5.2.38)*. The ML maximisation described by[26]

$$\hat{\boldsymbol{\phi}} = \arg\max_{\boldsymbol{\varphi}} \ln f_{\boldsymbol{U}}(\boldsymbol{u}|\boldsymbol{\varphi}) \qquad \text{or} \qquad \hat{\boldsymbol{\phi}} = \arg\max_{\boldsymbol{\varphi}} \ln f_{\boldsymbol{U}}(\boldsymbol{U}|\boldsymbol{\varphi})$$

constitutes a non-linear optimisation problem that is numerically solvable via Newton-Raphson iterations or by the method of steepest descent[27], as well as by a number of other techniques [SHA 88b], [SHA 89].

---

25 Here $\boldsymbol{u}$ is taken as the tempo-spatial vector defined in *(5.2.4)*, and the conditional joint PDF for the random $M\times 1$ vector $\boldsymbol{U}$ is given by [WHA 71]:

$$f_{\boldsymbol{U}}(\boldsymbol{u}|\boldsymbol{\varphi}) = f_{\boldsymbol{U}}(\mathbf{X}|\boldsymbol{\varphi}) = \prod_{n=0}^{N-1} \frac{1}{\det[\pi\mathbf{R}]} e^{-\boldsymbol{x}^H(t_n)\mathbf{R}^{-1}\boldsymbol{x}(t_n)} = \frac{1}{[\pi^M|\mathbf{R}|]^N} \exp[-\sum_{n=0}^{N-1} \boldsymbol{x}^H(t_n)\mathbf{R}^{-1}\boldsymbol{x}(t_n)]$$

26 An equivalent large-sample SML estimation problem is [BOH 86], [JAF 88]:

$$\hat{\boldsymbol{\phi}} = \arg\min_{\boldsymbol{\varphi}} \ln|\boldsymbol{\Pi}_{\mathbf{A}}(\boldsymbol{\varphi})\hat{\mathbf{R}}\,\boldsymbol{\Pi}_{\mathbf{A}}(\boldsymbol{\varphi}) + (M\text{-}K)^{-1}\,\mathrm{tr}\{[\mathbf{I} - \boldsymbol{\Pi}_{\mathbf{A}}(\boldsymbol{\varphi})]\hat{\mathbf{R}}\}[\mathbf{I} - \boldsymbol{\Pi}_{\mathbf{A}}(\boldsymbol{\varphi})]| \ , \quad \boldsymbol{\Pi}_{\mathbf{A}} = \mathbf{A}(\mathbf{A}^H\mathbf{A})^{-1}\mathbf{A}^H$$

27 See [WAX 83] for a brief description of these iterative methods.

c. Deterministic ('conditional') Maximum Likelihood (DML) method

For the formulation of the *Deterministic Maximum-Likelihood* estimator [BOH 84], [BOH 85], [WAX 85a] the additive noises are taken as before to be stationary zero-mean uncorrelated complex Gaussian processes, but the sources are assumed to be non-random and the signals are consequently modelled as arbitrary deterministic sequences. The log-likelihood function for a narrowband tempo-spatial array data vector is then given by:[28]

$$\ln f_{\boldsymbol{u}}(\boldsymbol{u}|\boldsymbol{\varphi}) =$$

$$-N\ln(\pi^M|\mathbf{R}_{\boldsymbol{\varepsilon}}|) - \sum_{n=0}^{N-1} [\boldsymbol{x}^H(t_n) - \boldsymbol{s}^H(t_n)\mathbf{A}^H(\boldsymbol{\varphi}, \omega_0)]\mathbf{R}_{\boldsymbol{\varepsilon}}^{-1}[\boldsymbol{x}(t_n) - \mathbf{A}(\boldsymbol{\varphi}, \omega_0)\boldsymbol{s}(t_n)]$$

$$= -NM\ln(\pi\sigma_{\boldsymbol{\varepsilon}}^2) - \frac{1}{\sigma_{\boldsymbol{\varepsilon}}^2}\sum_{n=0}^{N-1} |\boldsymbol{x}(t_n) - \mathbf{A}(\boldsymbol{\varphi}, \omega_0)\boldsymbol{s}(t_n)|^2 \qquad \cdots (5.2.90)$$

Holding the signals $\{\boldsymbol{s}(t_n)\}_n$ and $\boldsymbol{\varphi}$ fixed, the log-likelihood function may be maximised with respect to $\sigma_{\boldsymbol{\varepsilon}}^2$ yielding,

$$\hat{\sigma}_{\boldsymbol{\varepsilon}}^2 = \frac{1}{NM}\sum_{n=0}^{N-1} |\boldsymbol{x}(t_n) - \mathbf{A}(\boldsymbol{\varphi}, \omega_0)\boldsymbol{s}(t_n)|^2 \qquad \cdots (5.2.91)$$

Substitution of $\hat{\sigma}_{\boldsymbol{\varepsilon}}^2$ for $\sigma_{\boldsymbol{\varepsilon}}^2$ in *(5.2.90)* leaves us with the following ML maximisation problem:

$$\max_{\boldsymbol{\varphi},\, \boldsymbol{s}(t_0), \cdots, \boldsymbol{s}(t_{N-1})} \{ -NM[\ln\pi + 1 + \ln(\frac{1}{NM}\sum_{n=0}^{N-1} |\boldsymbol{x}(t_n) - \mathbf{A}(\boldsymbol{\varphi}, \omega_0)\boldsymbol{s}(t_n)|^2)] \}$$

or equivalently,

$$\min_{\boldsymbol{\varphi},\, \boldsymbol{s}(t_0), \cdots, \boldsymbol{s}(t_{N-1})} \{\sum_{n=0}^{N-1} |\boldsymbol{x}(t_n) - \mathbf{A}(\boldsymbol{\varphi}, \omega_0)\boldsymbol{s}(t_n)|^2 \} \qquad \cdots (5.2.92)$$

The minimisation of *(5.2.92)* with respect to each $\boldsymbol{s}(t_n)$ yields

---

28 The conditional joint PDF for the random vector $\boldsymbol{u}$ is given this time by:

$$f_{\boldsymbol{u}}(\boldsymbol{u}|\boldsymbol{\varphi}) =$$

$$\prod_{n=0}^{N-1} \frac{1}{\det[\pi\mathbf{R}_{\boldsymbol{\varepsilon}}]} e^{-[\boldsymbol{x}(t_n) - \mathbf{A}(\boldsymbol{\varphi}, \omega_0)\boldsymbol{s}(t_n)]^H\mathbf{R}_{\boldsymbol{\varepsilon}}^{-1}[\boldsymbol{x}(t_n) - \mathbf{A}(\boldsymbol{\varphi}, \omega_0)\boldsymbol{s}(t_n)]} = (\pi\sigma_{\boldsymbol{\varepsilon}}^2)^{-NM}\exp[-\frac{1}{\sigma_{\boldsymbol{\varepsilon}}^2}\sum_{n=0}^{N-1} |\boldsymbol{x}(t_n) - \mathbf{A}(\boldsymbol{\varphi}, \omega_0)\boldsymbol{s}(t_n)|^2]$$

$$\hat{s}(t_n) = [\mathbf{A}^H(\boldsymbol{\varphi}, \omega_0)\mathbf{A}(\boldsymbol{\varphi}, \omega_0)]^{-1}\mathbf{A}^H(\boldsymbol{\varphi}, \omega_0)x(t_n) \qquad \cdots (5.2.93)$$

These may be substituted back into *(5.2.92)* leading to the following minimisation problem:

$$\hat{\boldsymbol{\phi}} = \arg\min_{\boldsymbol{\varphi}} \{ \sum_{n=0}^{N-1} |[\mathbf{I}-\boldsymbol{\Pi}_{\mathbf{A}}(\boldsymbol{\varphi})]x(t_n)|^2 \} \qquad \cdots (5.2.94)$$

where

$$\boldsymbol{\Pi}_{\mathbf{A}}(\boldsymbol{\varphi}) = \mathbf{A}(\boldsymbol{\varphi}, \omega_0)[\mathbf{A}^H(\boldsymbol{\varphi}, \omega_0)\mathbf{A}(\boldsymbol{\varphi}, \omega_0)]^{-1}\mathbf{A}^H(\boldsymbol{\varphi}, \omega_0) \qquad \cdots (5.2.95)$$

is the projection operator onto the space spanned by the columns of $\mathbf{A}(\boldsymbol{\varphi}, \omega_0)$. Equivalently, the maximum-likelihood estimate of $\boldsymbol{\phi}$ is obtained by the maximisation process:

$$\hat{\boldsymbol{\phi}} = \arg\max_{\boldsymbol{\varphi}} \frac{1}{N}\sum_{n=0}^{N-1} |\boldsymbol{\Pi}_{\mathbf{A}}(\boldsymbol{\varphi})x(t_n)|^2 = \arg\max_{\boldsymbol{\varphi}} \mathrm{tr}\,[\boldsymbol{\Pi}_{\mathbf{A}}(\boldsymbol{\varphi})\hat{\mathbf{R}}(u)] \qquad \cdots (5.2.96)$$

where $\hat{\mathbf{R}}(u)$ is the sample covariance matrix as given by *(5.2.37)*. The numerical solution of *(5.2.94)* or *(5.2.96)* involving a nonlinear search for the DOA parameter vector, is implementable by various algorithms such as the alternating projection method of Ziskind and Wax [ZIS 87], [ZIS 88] or Kaufman's variable projection method [KAU 75], [VIB 91b].

The statistical properties of both the SML and the DML method have been asymptotically analysed by a number of authors [SAN 87], [STO 89], [STO 90b]. It has been shown that whereas the SML estimator is asymptotically efficient in that the covariance matrix of DOA errors approaches the ('stochastic') Cramér-Rao bound $\mathbf{J}_S^{-1}$ as the number of samples N tends to infinity, this is not true of the DML estimator which, for a finite number of elements M, never reaches the corresponding 'deterministic' Cramér-Rao bound $\mathbf{J}_D^{-1}$. In fact it has been proved that [OTT 90b], [STO 90b], [OTT 92]:

$$\mathbf{C}_D \geq \mathbf{C}_S = \mathbf{J}_S^{-1} \geq \mathbf{J}_D^{-1}$$

where $\mathbf{C}_D$ and $\mathbf{C}_S$ are the asymptotic DOA error covariance matrices for the deterministic and stochastic maximum-likelihood estimators respectively, and each matrix inequality is in the sense of positive (semi-) definiteness of the corresponding difference matrix.

d. Weighted Subspace Fitting (WSF) method

The WSF method introduced by Ottersten and Viberg [OTT 89], [VIB 91a], [VIB 91b] searches for the K-dimensional DOA parameter vector $\boldsymbol{\phi}$ by trying to fit, in the least-squares sense, the column space of a search-dependent steering matrix $\mathbf{A}(\boldsymbol{\varphi}, \omega_0)$ to the estimated signal subspace that is contained in the column space of the actual steering matrix $\mathbf{A}(\omega_0) = \mathbf{A}(\boldsymbol{\phi}, \omega_0)$. When applied to a general arbitrarily-shaped sensor array, the sub-space fitting process involves a computationally intense optimisation search that is of the same order as the parameter search required for the ML method.

Mathematically, the $K\times1$ parameter vector $\boldsymbol{\phi}$ pertaining to K far-field narrowband possibly coherent sources illuminating an M-sensor array, is estimated under homoscedastic white noise conditions by seeking the vector $\boldsymbol{\varphi}$ that minimises:

$$\min_{\boldsymbol{\varphi},\,\mathbf{T}} \| \mathbf{V}_s\mathbf{W}^{1/2} - \mathbf{A}(\boldsymbol{\varphi}, \omega_0)\mathbf{T} \|_F^2 \qquad \cdots (5.2.97)$$

where, for a signal covariance matrix $\mathbf{R}_s$ of rank K', $\mathbf{V}_s$ is the $M\times K'$ signal eigenvector matrix

$$\mathbf{V}_s = [V_0\ V_1 \cdots\cdots V_{K'-1}]$$

whose columns, the eigenvectors corresponding to the K' largest eigenvalues of the array covariance matrix $\mathbf{R}$, span the 'signal subspace' that lies in the column space of $\mathbf{A}(\omega_0)$, $\mathbf{W} = \mathbf{W}^{1/2}[\mathbf{W}^{1/2}]^H$ is a $K'\times K'$ hermitian positive-definite 'weight' matrix and $\mathbf{T}$ is a full-rank $K\times K'$ matrix[29]. Minimisation of *(5.2.97)* with respect to $\mathbf{T}$ yields:

$$\mathbf{T} = (\mathbf{A}^H\mathbf{A})^{-1}\mathbf{A}^H\mathbf{V}_s\mathbf{W}^{1/2}$$

which when plugged back into *(5.2.97)* and use is made of the definition of the Frobenius norm and of the invariance of the trace operator to matrix commutation, leads to the following optimisation problem

$$\hat{\boldsymbol{\phi}} = \arg\min_{\boldsymbol{\varphi}} \operatorname{tr}\{\ [\mathbf{I} - \boldsymbol{\Pi}_{\mathbf{A}}(\boldsymbol{\varphi})]\mathbf{V}_s\mathbf{W}\mathbf{V}_s^H\ \} \qquad \cdots (5.2.98)$$

or, equivalently:

$$\hat{\boldsymbol{\phi}} = \arg\max_{\boldsymbol{\varphi}} \operatorname{tr}\{\ \boldsymbol{\Pi}_{\mathbf{A}}(\boldsymbol{\varphi})\mathbf{V}_s\mathbf{W}\mathbf{V}_s^H\ \} \qquad \cdots (5.2.99)$$

---

29 Note that in the case of incoherent signals, $\mathbf{R}_s$ has full rank and $K' = K$.

where $\mathbf{\Pi}_{\mathbf{A}} = \mathbf{A}(\mathbf{A}^H\mathbf{A})^{-1}\mathbf{A}^H$ is the projection matrix onto the column space of $\mathbf{A}$.

The weighting matrix $\mathbf{W}$ affects the asymptotic properties of the estimation error. The optimal choice (referred to as the WSF choice) that leads to the lowest asymptotic estimation error variance, which under the Gaussian signal assumption coincides with the stochastic CRLB, has been shown to be [VIB 91a]

$$\mathbf{W} = [\hat{\mathbf{\Lambda}}_s - \hat{\sigma}_w^2\mathbf{I}]^2\hat{\mathbf{\Lambda}}_s^{-1}$$

where $\hat{\mathbf{\Lambda}}_s$ is the signal subspace eigenvalue matrix obtained by the eigen-decomposition of the sample covariance matrix, and $\hat{\sigma}_w^2$ is any consistent estimate of σ_w^2. If $\mathbf{W}$ is set equal to the identity matrix then *(5.2.97)* and *(5.2.99)* become:

$$\hat{\boldsymbol{\phi}} = \arg\min_{\boldsymbol{\varphi},\,\mathbf{T}} \| \mathbf{V}_s - \mathbf{A}(\boldsymbol{\varphi}, \omega_0)\mathbf{T} \|_F^2 = \arg\max_{\boldsymbol{\varphi}} \mathrm{tr}\{ \mathbf{\Pi}_{\mathbf{A}}(\boldsymbol{\varphi})\mathbf{V}_s\mathbf{V}_s^H \}$$

which describes the vector-search algorithm suggested by Cadzow [CAD 88], also known as the *Multidimensional MUSIC (MD-MUSIC)* estimator [SCH 81], [ROY 87], [VIB 91a]. The same choice of $\mathbf{W}$ but with a translated sub-array parametrisation for $\mathbf{A}$ leads to the following vector-search formulation for TLS-ESPRIT [VIB 91a]:

$$\hat{\mathbf{\Psi}} = \arg\min_{\mathbf{\Psi},\,\mathbf{T}} \| \mathbf{V}_s - \bar{\mathbf{A}}\mathbf{T} \|_F^2$$

$$\bar{\mathbf{A}} = [\mathbf{A}_X \quad \mathbf{\Psi}^H\mathbf{A}_X^H] \quad , \quad \{\hat{\phi}_k\}_{k=0}^{K-1} \text{ are eigenvalues of } \hat{\mathbf{\Psi}}$$

This algorithm, like the search-free version of ESPRIT described in sub-section 5.2.5, requires no knowledge of the sensor characteristics and geometry save for a known sub-array displacement vector, but is also unable to resolve coherent signals. Note also that the WSF optimisation problem *(5.2.99)* is very similar to the DML procedure *(5.2.96)*. By setting: $\mathbf{W} = \mathbf{\Lambda}_s - \sigma_w^2\mathbf{I}$ the maximisation problem *(5.2.99)* becomes:

$$\hat{\boldsymbol{\phi}} = \arg\max_{\boldsymbol{\varphi}} \mathrm{tr}\{ \mathbf{\Pi}_{\mathbf{A}}(\boldsymbol{\varphi})\mathbf{R}_S \}$$

which has been shown to be asymptotically equivalent to the DML problem *(5.2.96)* [VIB 91a].

5.2.7 WIDEBAND SPATIAL SPECTRAL ESTIMATION

Superresolution spatial spectral estimators have originally been formulated for a narrowband model, in terms of the covariance matrix of the array outputs. The underlying idea behind narrowband eigenstructure-based algorithms, such as MUSIC and the MN method, is that the rank of the signal-only covariance matrix $\mathbf{R}_s$ equals K, the number of (incoherent) sources, provided K is smaller than the number of sensors, M. In the case of wideband sources, this 'rank 1 per source' assumption is no longer valid (strictly speaking, it does not hold for sources of any non-zero bandwidth), and consequently narrowband estimators are not directly applicable.

In the so called *incoherent* approach to wideband spatial spectral estimation, the frequency band is divided into bins (explicitly, in terms of cross-spectral density matrices of the Fourier-transformed array outputs [WAX 84], or implicitly, by sampling the z-transformed covariance matrix [SUM 83]) where narrowband superresolution procedures are separately performed. The individual narrowband estimations obtained across the frequency band are then averaged to yield the final result.

In the *broad-band signal subspace spatial spectral estimation (BASS-ALE)* methods proposed by Buckley and Griffiths, the effective low-rank character of the signal-only tempo-spatial covariance matrix (TSCM)[30] is identified based on the expansion of a tempo-spatial source sample data vector using the TSCM eigenvectors as a basis[31] [BUC 86a], [BUC 86b], [BUC 87], [BUC 88]. It is claimed that over 99.99% of the power emanating from a flat-spectrum source in direction ϕ_k is represented by the TSCM eigenvectors corresponding to the K_e largest eigenvalues, with K_e, the *effective rank* being given by

$$K_e(\phi_k) = \lceil\, 1 + \Delta\omega [\max_{0 \le m', m'' \le M-1} (\tau_{m'}(\phi_k) - \tau_{m''}(\phi_k)) + (N-1)T]/\pi \,\rceil$$

where $\lceil x \rceil$ stands for the ceiling of (i.e. smallest integer equal or larger than) x, $\Delta\omega$ denotes the (angular) bandwidth of the source and the expression in the square brackets is the total temporal duration of the source in the array during the full observation interval of NT. Subsequent eigen-decomposition is based on the effective rank of the TSCM[32], the evaluation of which requires the approximated

30 TSCM refers here to the $NM \times NM$ correlation matrix formed from the stacked tempo-spatial data vector $\boldsymbol{u}$ as defined in *(5.2.4)-(5.2.6)*.

31 This is known as the *Karhunen-Loéve* expansion [AHM 75].

32 For K sources, the effective rank is taken as $\sum_{k=0}^{K-1} K_e(\phi_k)$.

knowledge of the source locations. In the special case of a circular sensor array, the dependence of the effective rank on source location can be practically removed [ROC 88], [MES 90].

In the *coherent signal subspace (CSS)* methods introduced by Wang and Kaveh [WAN 85], [WAN 87], [YAN 87] the narrowband cross-spectral density matrices are transformed via 'focusing matrices' which align their corresponding signal and noise subspaces, and are then averaged to form the 'focused' covariance matrix. The signal-only focused covariance matrix is thereby reduced to rank K, but is not made rank-deficient by the presence of fully correlated (but relatively delayed) sources. This obvious improvement over the incoherent approach, in addition to its greater statistical stability and lower threshold SNR [WAN 85], [HUN 87], [HUN 88], [KRO 91] has led to considerable interest in CSS methods. These methods are, however, vulnerable to DOA bias due to errors in estimating the focusing matrices (for which an initial estimate of source bearings is required) and from the uncertain spectral signature of the sources [SWI 89]. In the related *steered covariance matrix (STCM)* technique, the (analytic) time-domain spatial covariance matrix is focused or 'steered' by inserting a set of look-direction-dependent conventional steering delays at the array outputs [KRO 89]. This approach solves the source location bias problem while greatly increasing the computational complexity as a new steered covariance matrix has to be estimated for each look direction. The computational burden is somewhat alleviated in the *doubly-steered coherent signal subspace* method whereby steered covariance matrices are evaluated for a reduced number of steering directions, but this variant is also susceptible to source location bias [SWI 88]. An alternative technique which achieves the required focusing operation independently (and without using preliminary estimates) of the source directions is the *spatial resampling* method [CLE 89], [BIE 89], [KRO 90], [KRO 91]. The concept here, which is restricted to equi-spaced linear arrays, is to treat the array outputs as samples of a continuous array and 'resample' the continuous array such that the new inter-element spacing d is made inversely proportional to frequency. The required pre-processing transformation which can only be approximately realised, renders the steering matrix for the spatially resampled array independent of frequency, thus enabling the rank 1 modelling of each wideband source. In all coherent methods considered above, appropriately transformed narrowband cross-spectral density matrices are averaged over the frequency band to form a 'focused' covariance matrix. In that respect these schemes constitute *frequency-domain smoothing* by which multipathed signals originating from the same wideband source are effectively decorrelated. Frequency smoothing is further discussed in the context of circular sensor arrays in section 5.4.

5.2.8 BEAM-SPACE METHODS

Superresolution estimators have usually been described in the context of *element-space*, i.e. the algorithms have been directly applied to the signals received by the array elements without any spatial pre-filtering. Many Superresolution methods are equally applicable to a linearly transformed observation space. Such a spatial transformation could for instance be used to spatially pre-whiten the background noise, provided that the (assumed non-singular) noise-only covariance matrix $\mathbf{R}_{nn} = \mathcal{E}\mathbf{x}_n\mathbf{x}_n^H$ is known. If $\mathbf{R}_{nn}$ is not available, the noise is generally assumed to be spatially white, although its mis-modelling may lead to increased variances and biases. The linear transformation of element data into *beam-space* has been considered by a number of authors [BIE 84], [OWS 85], [FOR 87], [BYR 87] as a means of reducing the sensitivity of spatial spectral estimation algorithms to spatially coloured noise. It has been argued that clustering sets of directional beams in confined angular sectors has a whitening effect on the noise, as the spatial distribution of the background noise power approaches local uniformity over each sector. Beam-space algorithms have been shown in some cases to provide superior resolution [VAN 88], [LEE 88], [XUB 89], [XUB 90] although there is a great dependency on the specific beamformer used. If the number of beams in each sector is much smaller than the number of array sensors, then the beamforming pre-processing will also reduce the computational load of the subsequent superresolution algorithm employed.

5.2.9 DETECTION PROBLEM

A vital pre-processing step on which many superresolution schemes depend is the prior estimation of the number of sources K, or equivalently (when sources are not fully correlated), of the dimension of the signal subspace. This task, known as the detection problem, is ordinarily tackled via an information-theoretic approach, using *Akaike's Information Criterion (AIC)* [AIK 73], [WAX 85b] or the *Minimum Description Length (MDL)* criterion due to Rissanen [RIS 78], Wax and Ziskind [WAX 89] and Wax [WAX 91]. In [WAX 89] and [WAX 91] detection is accompanied by ML localisation of the sources based on the deterministic and stochastic signal models respectively. A brief review and a comparison of the above AIC and MDL criteria can be found in [HAY 92] and a 'coherent' extension to wideband sources is suggested in [WAN 85]. The detection problem is not addressed in this thesis and the number of sources is always assumed to be either known or correctly estimated by one of the above criteria.

5.3 APPLICATION TO CIRCULAR ARRAYS

5.3.1 GENERAL

Although the compatibility of certain spatial superresolution schemes with arbitrarily-shaped arrays had been noted in the past, the inherent symmetry and full peripheral coverage that characterise sensor arrays with circular geometry have, rather surprisingly, not attracted the interest of many authors in the field. A brief reference to a circular array arrangement has been made by Johnson [JOH 82b], by Li and Vaccaro [LIV 90] and by Viberg et. al. [VIB 91b], the latter two as the array configuration chosen for simulations, and all in the context of element-space spectral estimation. Simulations using a circular array have also been reported by Xu and Buckley [XUB 90] in both element-space and (eigen-) beam space.[33] The desirability of circular array geometry when full 360° coverage in DF is required has been noted by Zeytinoğlu, Litva and Qian [ZEY 91] who have modified an element-space superresolution algorithm to compensate for mutual coupling effects.[34] An interesting use of the special symmetry of circular arrays has been suggested by Messer and Rockah [ROC 88], [MES 90] for the localisation of multiple flat-spectrum broadband sources. Based on the fact that the projected aperture of a (continuous) circular array in any direction is equal to the array diameter, they have shown that the circular geometry renders the eigenstructure parameters of the (element-space) signal-only tempo-spatial covariance matrix (TSCM) practically independent of source direction, thus removing a major difficulty in the implementation of the Buckley and Griffiths TSCM-based estimation algorithms referred to in section 5.2, sub-section 5.2.7 [BUC 86a], [BUC 86b], [BUC 87], [BUC 88]. One important type of element-space to beam-space pre-processing, namely, the transformation into phase-mode space, has hitherto received very little attention.[35] In sub-section 5.3.2 we shall show that in mode-space, circular arrays can be treated essentially as uniformly-spaced linear arrays, thus allowing the application of estimation methods that are ordinarily restricted to the latter (element-space) geometry.

---

33 An eigen-beamformer is characterised by a transformation matrix whose columns are the (signal sub-space) eigenvectors of the spatial covariance matrix.

34 Under element-space formulation each circular array sensor receiving signals from a far-field source 'sees' a different field environment and is therefore differently affected by inter-element coupling. This is not so in an (infinitely long) uniformly-spaced linear array, where the incident field places a periodic boundary condition on the aperture.

35 A pre-processing transformation of circular array signals from element-space into phase-mode space, though not referred to as such, has in fact been suggested by Moody [Moo 80], [MIL 81] who subsequently applied a scheme akin to Prony's method for solving the multiple source problem.

5.3.2 MODE-SPACE FORMULATION

The pre-processing transformation of a circular sensor array from M-dimensional element-space into M'-dimensional mode-space, may be represented by the matrix operation:

$$\boldsymbol{y}(t) = \mathbf{Q}^H\mathbf{E}^H\boldsymbol{x}(t) \qquad \cdots (5.3.1)$$

where the $M\times 1$ vector $\boldsymbol{x}$ and the $M'\times 1$ vector $\boldsymbol{y}$ group the respective signals received by the array sensors and the linearly transformed signals at the beamformer outputs, the M' orthonormal columns of the phasing matrix $\mathbf{E} = [\boldsymbol{E}_{-\Lambda}\cdots\boldsymbol{E}_0\cdots\boldsymbol{E}_\Lambda]$, where $M' = 1+2\Lambda$, are given by:

$$\boldsymbol{E}_\mu = (1/M)^{1/2}[1\ e^{j(2\pi/M)\mu}\ e^{j(2\pi/M)2\mu}\ldots\ldots\ e^{j(2\pi/M)(M-1)\mu}]^T$$

$$-\Lambda\le\mu\le\Lambda \qquad \cdots (5.3.2)$$

$\mathbf{Q}$ is an $M'\times M'$ diagonal matrix whose $\mu\mu'$th element is given by:

$$Q_{\mu\mu} = 1/M^{1/2}C^*_{\mu 0}(\omega_0, \pi/2) \quad , \quad -\Lambda\le\mu\le\Lambda \qquad \cdots (5.3.3)$$

and $C_{\mu 0}(\omega_0, \pi/2)$ is the zero-order coefficient for phase-mode number μ at frequency ω_0 as defined in chapter 2, section 2.4. Under narrowband formulation, one obtains from *(5.2.12)*:

$$\boldsymbol{y}(t) = \mathbf{Q}^H\mathbf{E}^H\mathbf{A}(\omega_0)\boldsymbol{s}(t)+\mathbf{Q}^H\mathbf{E}^H\boldsymbol{x}_n(t) \qquad \cdots (5.3.4)$$

and the $M'\times M'$ covariance matrix for the transformed signals is given by:

$$\mathbf{R}_y = \mathcal{E}\boldsymbol{y}\boldsymbol{y}^H = \tilde{\mathbf{A}}\mathbf{R}_s\tilde{\mathbf{A}}^H + \tilde{\mathbf{R}}_n \qquad \cdots (5.3.5)$$

where:

$$\tilde{\mathbf{A}} = \mathbf{Q}^H\mathbf{E}^H\mathbf{A} \qquad \cdots (5.3.6)$$

$$\tilde{\mathbf{R}}_n = \mathbf{Q}^H\mathbf{E}^H\mathbf{R}_n\mathbf{E}\mathbf{Q} \qquad \cdots (5.3.7)$$

and for spatially white homoscedastic noise:

$$\tilde{\mathbf{R}}_{nn} = \sigma_n^2 \mathbf{Q}^H \mathbf{Q} \qquad \cdots (5.3.8)$$

where σ_n^2 is the noise power at the array sensors. Notice that although the (mode-space) noise remains spatially white, it is also heteroscedastic, i.e. the noise powers at the phase-mode outputs are not the same. They are in fact equal to:

$$\tilde{\sigma}_{n\mu}^2 = \sigma_n^2 / M |C_{\mu 0}(\omega_0, \pi/2)|^2 \quad , \quad -\Lambda \le \mu \le \Lambda \qquad \cdots (5.3.9)$$

However, the spatial whiteness assumption which leads to *(5.3.8)*, although reasonable as far as internally generated (thermal) noise is concerned, does not necessarily hold for spatial contributions from ambient noise fields. Denoting the spatial power density of the ambient noise field by $\mathcal{N}(\omega, \theta, \varphi)$, and the cross-spectral density matrix of the ambient noise field contribution at the M' mode outputs by $\tilde{\mathbf{P}}_{n_a}(\omega)$, we have for a spatially-white noise field that is statistically independent with respect to direction:

$$[\tilde{P}_{n_a}(\omega)]_{\mu'\mu''} \approx \int_0^{\pi} d\theta \frac{C_{\mu' 0}(\omega, \theta) C_{\mu'' 0}^*(\omega, \theta)}{C_{\mu' 0}(\omega_0, \pi/2) C_{\mu'' 0}^*(\omega_0, \pi/2)} \sin\theta \int_{-\pi}^{\pi} d\varphi \mathcal{N}(\omega, \theta, \varphi) e^{-j(\mu' - \mu'')\varphi}$$

$$\cdots (5.3.10)$$

where $[\tilde{P}_{n_a}]_{\mu'\mu''}$ denotes the $\mu'\mu''$'th element of $\tilde{\mathbf{P}}_{n_a}$ and use has been made of the approximate far-field phase-mode characteristics

$$\Phi_\mu(\theta, \varphi, \omega) / C_{\mu 0}(\omega, \theta) \approx e^{-j\mu\varphi} \qquad \cdots (5.3.11)$$

for an array of closely spaced sensors (see chapter 2, section 2.4). If the noise field is omnidirectional in φ and concentrated around zero ($\theta = \pi/2$) elevation, then:

$$\tilde{P}_{n_a \mu'\mu''}(\omega) = \begin{cases} 2\pi \int_0^{\pi} d\theta |C_{\mu' 0}(\omega, \theta) / C_{\mu' 0}(\omega_0, \pi/2)|^2 \mathcal{N}(\omega, \theta) \sin\theta \\ 0 \end{cases}$$

$$\approx \begin{cases} 2\pi \int_0^{\pi} d\theta |C_{\mu' 0}(\omega, \pi/2) / C_{\mu' 0}(\omega_0, \pi/2)|^2 \mathcal{N}(\omega, \theta) \sin\theta & \mu' = \mu'' \\ 0 & \mu' \ne \mu'' \end{cases} \qquad \cdots (5.3.12)$$

$\tilde{\mathbf{P}}_{n_a}(\omega_0)$ is then a diagonal matrix with equal elements, and, for the narrowband problem, so is the spatial covariance matrix contributed by the ambient noise field.

Note that a similar result is obtained for the (element-space) covariance matrix of a linear array in an isotropic noise field, provided that the array sensors are isotropic and spaced half a wavelength apart [BUR 91]. Taking the (internally-generated) thermal noise power to be negligibly small (which is a fair assumption in the case of a sonar system [BUR 91]), the noise at the phase-mode outputs of (a horizontal) circular-array is thus seen to be spatially white and homoscedastic, for a noise field that is omni-directional in azimuth and impulsive at zero elevation.[36] This noise model allows the convenient eigen-decomposition of the mode-space covariance matrix in estimation algorithms such as MUSIC and the MN method. In contrast, the element-space covariance matrix for a circular array or a linear array with non-isotropic sensors in an isotropic noise-field, or that of a horizontal linear array under an azimuthally omnidirectional noise-field that varies in elevation are not white – see appendix E.3.

From *(5.3.11)* it also follows that each column of $\tilde{\mathbf{A}}$ is approximately given by:

$$\tilde{A}_k = [1 \;\; z_k^{-1} \;\; z_k^{-2} \cdots\cdots z_k^{(M'-1)}]^T z_k^{\Lambda} \quad , \quad 0 \le k \le K\text{-}1 \qquad \cdots (5.3.12)$$

where for each direction of arrival ϕ_k:

$$z_k = e^{j\phi_k} \quad , \quad 0 \le k \le K\text{-}1 \qquad \cdots (5.3.13)$$

The modified $M' \times K$ steering matrix $\tilde{\mathbf{A}}$ may thus be written as:

$$\tilde{\mathbf{A}} = \begin{pmatrix} 1 & & 1 & & 1 \\ z_0^{-1} & & z_k^{-1} & & z_{K-1}^{-1} \\ z_0^{-2} & \cdots & z_k^{-2} & \cdots & z_{K-1}^{-2} \\ \vdots & & \vdots & & \vdots \\ z_0^{-(M'-1)} & & z_k^{-(M'-1)} & & z_{K-1}^{-(M'-1)} \end{pmatrix} \begin{pmatrix} z_0^{\Lambda} & & & \\ & \ddots & & 0 \\ & & z_k^{\Lambda} & \\ & 0 & & \ddots \\ & & & & z_{K-1}^{\Lambda} \end{pmatrix} \qquad \cdots (5.3.14)$$

The first matrix on the right hand side of *(6.3.14)* is characterised by a Vandermonde structure and consequently has full rank K for K distinct DOA angles $\{\phi_k\}$ (and therefore K distinct z_k's), while the diagonal matrix which multiplies it from the right is clearly nonsingular. $\tilde{\mathbf{A}}$ is thus a full rank matrix whose structure is identical to that of the steering matrix of a linear array of M' equal-pattern uniformly-spaced

36 If the internally-generated thermal noise power σ_n^2 is known (or measurable), one may subtract the matrix $\sigma_n^2 \mathbf{Q}^H \mathbf{Q}$ from the mode-space covariance matrix before proceeding with eigen-decomposition.

sensors[37]. Letting $\tilde{\mathbf{A}}(\varphi, \omega)$ denote the response of the M' phase-mode outputs to a plane wave at frequency ω arriving from direction φ, the modal radiation pattern is given, for a corresponding $M'\times 1$ weight vector $\tilde{w}$, by:

$$\tilde{w}^H \tilde{\mathbf{A}}(\varphi, \omega) = \tilde{A}_\Lambda(\varphi, \omega) \sum_{\mu=-\Lambda}^{\Lambda} w_\mu^* z^{-\mu} \qquad \cdots (5.3.15)$$

which is of exactly the same form as *(5.2.31)* for the radiation pattern of an equally-spaced linear array.

Since the mode-space signal-only covariance matrix and radiation pattern of an equally-spaced circular array are of the same structure as the corresponding signal-only covariance matrix and radiation pattern of an equally-spaced linear array under element-space formulation, and as, under isotropic noise-field conditions (for the linear array) and the more reasonable assumption of azimuthally-omnidirectional and elevationwise-impulsive noise (for the circular array), the noise covariance matrix is in both cases diagonal and with equal elements, it follows that superresolution schemes which are ordinarily restricted to uniformly-spaced linear arrays in element-space, are equally applicable to uniformly-spaced circular arrays in mode-space. That includes multiple-invariance (overlapped) ESPRIT and TAM, spatial spectral estimators whose spectral pattern is derived from the MVIR pattern, such as the ME and MN methods, as well as root-finding versions of all scalar-search algorithms. This means that in both circular-array mode-space and linear-array element-space the ME and MN null patterns are characterised by K nulls (provided K is smaller than the number of circular-array phase-modes or linear-array sensors), with spurious nulls in the latter pattern effectively suppressed. Under the rather ideal assumption of an isotropic noise-field, the performance of circular-array mode-space methods in the φ domain is not expected to be better than that of the corresponding linear-array element-space schemes in the $(\omega_0 d/c)\sin\varphi$ domain.[38] However, if the (unknown) horizontally omni-directional noise-field is concentrated around zero elevation, then while the phase-mode noise remains spatially white and homoscedastic, the linear-array element noise is no longer spatially white. Consequently, an eigen-structure based linear-array element-space estimator will be mis-modelled and therefore outperformed by the corresponding mode-space estimator.

---

37 In the linear array case with d the inter-element spacing, each z_k in the Vandermonde matrix is given by $z_k = e^{-j(\omega_0 d/c)\sin\phi_k}$ and the kk'th element of the diagonal matrix is the element pattern in direction ϕ_k.

38 The number of processed phase modes of the circular array is assumed to be equal to the number of processed linear-array sensors.

5.4 SPATIAL AND FREQUENCY-DOMAIN SMOOTHING

5.4.1 GENERAL

Pre-processing in the form of spatial or frequency smoothing is required by eigenstructure-based superresolution algorithms, such as MUSIC, MN and the ESPRIT method, to enable them to cope with coherent signals[39]. When some of the received signals are coherent, the signal covariance matrix $\mathbf{R}_s$ in *(5.2.46)* becomes rank-deficient, and consequently the subspace spanned by the eigenvectors of the covariance matrix $\mathbf{R}$ associated with the minimal eigenvalue of $\mathbf{R}$ is no longer orthogonal to the columns of the steering matrix $\mathbf{A}$. Thus, although these DOA estimators are asymptotically unbiased for uncorrelated or partially correlated signals, they may completely fail in the presence of multipath 'image sources' or when subjected to coherent jamming.

The spatial smoothing technique for the decorrelation of coherent signals was first introduced by Evans *et al.* [EVA 81], [EVA 82] and further developed and analysed by Shan *et al.* [SHA 85] and by a number of other authors [WIL 88], [PIL 89a], [PIL 89b], [RAO 90]. As formulated for an equally-spaced linear array of identical sensors, the spatial smoothing pre-processing scheme involves the reduction of the spatial covariance matrix into a set of 'partial' covariance matrices defined for a corresponding set of equal-size (interlaced) sub-arrays, each with a different phase-centre. These matrices are averaged to form the 'smoothed' covariance matrix, which may be shown to have the same structure as the covariance matrix for noncoherent signals. The effective size of the array is, however, reduced to the sub-array size, which implies a lower angular resolution.

---

39 We refer to two complex narrowband signals $s_0(t)$ and $s_1(t)$ as *coherent* when: $s_0(t) = \xi s_1(t)$, where ξ is a non-zero complex constant. The covariance matrix for the two signals is then given by:

$$\text{cov}\,(s_0\, s_1) = \begin{pmatrix} |\xi|^2 r(0) & \xi\, r(0) \\ \xi^* r(0) & r(0) \end{pmatrix} \quad \text{where} \quad r(\tau) = \mathcal{E} s_1(t) s_1^*(t-\tau) - |\mathcal{E} s_1|^2$$

Obviously, $\text{cov}\,(s_0\, s_1)$ is singular, the correlation coefficient is 1, and the signals are fully correlated. Under wideband conditions, $s_0(t)$ and $s_1(t)$ will be said to be *coherent* when: $s_0(t) = \xi s_1(t-t_0)$, where t_0 is some real time delay and ξ is again a non-zero complex constant. This time we have:

$$\text{cov}\,(s_0\, s_1) = \begin{pmatrix} |\xi|^2 r(0) & \xi\, r^*(t_0) \\ \xi^* r(t_0) & r(0) \end{pmatrix}$$

which is generally non-singular; the correlation coefficient is given by $|r(t_0)|/r(0)$ and $s_0(t)$ and $s_1(t)$ are only partially correlated.

Frequency smoothing refers to frequency-domain averaging of the pre-processed cross-spectral density matrix which has a decorrelating effect on wideband sources. Pre-processing is necessary to enable the (modified) steering matrix to maintain the same rank 1 description per source over the whole frequency band, so that (essentially narrowband) eigen-decomposition algorithms may be applied. A number of coherent 'focusing' techniques were considered in section 5.2, sub-section 5.2.7, of which the spatial resampling method was the only approach to provide true direction-independent focusing, with a single evaluation of the transformed covariance matrix that does not require preliminary estimates of source locations. However, as with spatial smoothing, the applicability of the spatial resampling method is limited to linear equi-spaced arrays.

In the following sub-sections we examine spatial smoothing and omni-directional frequency smoothing in the context of circular-array mode-space, and show that this (circular-array) configuration and (phase-mode) pre-processing does indeed allow the extension of the above techniques from equi-spaced linear-array geometry.

5.4.2 SPATIAL SMOOTHING

Consider the M' aligned[40] outputs of phase-modes $\{-\Lambda, -\Lambda+1, \cdots\cdots, \Lambda\}$ formed by applying the pre-processing transformation *(5.3.1)* to the element channels of an M-sensor circular array, and let the approximate far-field radiation pattern of the phase-modes in the above set be given by *(5.3.11)*. Next, form the following $(M'-M''+1)$ overlapping subsets of M'' aligned phase-modes:

$$\{-\Lambda, -\Lambda+1, \cdots\cdots, -\Lambda+M''-1\}, \{-\Lambda+1, -\Lambda+2, \cdots\cdots, -\Lambda+M''\},$$
$$\cdots\cdots, \{\Lambda-M''+1, \Lambda-M''+2, \cdots\cdots, -\Lambda\}$$

and denote by $\boldsymbol{y}_v$, $v=0, 1, \cdots, M'-M''$ the vector of aligned phase-modes belonging to the v'th subset. Under narrowband formulation we then have:

$$\boldsymbol{y}_v(t) = \mathbf{B}(\omega_0)\boldsymbol{\Psi}^v(\boldsymbol{\phi})\boldsymbol{s}(t) + \boldsymbol{y}_{nv}(t) \quad , \quad v=0, 1, \cdots, M'-M'' \qquad \cdots (5.4.1)$$

where $\boldsymbol{y}_{nv}(t)$ is the mode-space additive noise vector belonging to the v'th subset, the $M''\times K$ matrix $\mathbf{B}(\omega_0)$ consists of the top M'' rows of the modified steering matrix $\tilde{\mathbf{A}}(\omega_0)$, and $\boldsymbol{\Psi}^v$ denotes the v'th power of the $K\times K$ diagonal matrix

---

40 We assume that each phase-mode pattern to be normalised to its zero-order coefficient $C_{\mu 0}$

$$\Psi(\phi) = \mathrm{diag}(e^{j\phi_0}\, e^{j\phi_1} \ldots\ldots e^{j\phi_{K-1}}) \qquad \ldots (5.4.2)$$

The covariance matrix of the v'th subset is given by:

$$\mathbf{R}_v = \mathcal{E}\mathbf{y}_v\mathbf{y}_v^H = \mathbf{B}\Psi^v\mathbf{R}_s\Psi^{Hv}\mathbf{B}^H + \tilde{\sigma}_e^2\mathbf{I} \qquad \ldots (5.4.3)$$

where $\tilde{\sigma}_e^2$ is the (white homoscedastic) noise power at the phase-mode outputs, and $\mathbf{I}$ is the $M''\times M''$ identity matrix. The construction of a spatially smoothed covariance matrix $\bar{\mathbf{R}}$ follows that suggested for an equi-spaced linear array [SHA 85], according to which $\bar{\mathbf{R}}$ is simply given by the sample mean of the subset covariances:

$$\bar{\mathbf{R}} = \frac{1}{M'-M''+1}\sum_{v=0}^{M'-M''}\mathbf{R}_v = \mathbf{B}\bar{\mathbf{R}}_s\mathbf{B}^H + \tilde{\sigma}_e^2\mathbf{I} \qquad \ldots (5.4.4)$$

where $\bar{\mathbf{R}}_s$, the modified signal covariance matrix, is given by:

$$\bar{\mathbf{R}}_s = \frac{1}{M'-M''+1}\sum_{v=0}^{M'-M''}\Psi^v\mathbf{R}_s\Psi^{Hv} \qquad \ldots (6.4.5)$$

The modified signal covariance matrix $\bar{\mathbf{R}}_s$ will be full-rank provided that:

$$(M'-M''+1) \geq K \qquad \ldots (5.4.6)$$

This, together with the condition $M'' > K$ needed for the subsequent eigen-decomposition procedure, means that we must also have:

$$M' \geq 2K \qquad \ldots (5.4.7)$$

In other words, the number of processed phase-modes must be no less than twice the total number of sources. The above claim is proved in appendix E.4 which follows the lines of a similar proof for the case of an equi-spaced linear array found in [SHA 85]. Since the smoothed covariance matrix $\bar{\mathbf{R}}$ is of exactly the same signal and noise structure as the (unsmoothed) covariance matrix for the incoherent case, it is equally applicable to eigen-structure based spatial spectral estimation algorithms. The dimension of the covariance matrix is, however, reduced from $M'\times M'$ to $M''\times M''$, which may be viewed as a decrease in the effective aperture of the array.[41]

[41] Recall that circular-array phase-modes play a similar role to that of linear-array sensors in forming an array radiation pattern.

5.4.3 FREQUENCY-DOMAIN SMOOTHING

Consider again the pre-processing transformation *(5.3.1)* of a circular sensor array from M-dimensional element-space into M'-dimensional mode-space, but this time let each phase-mode be (digitally-) filtered so that the response of its zero-order coefficient is deconvolved over the relevant frequency band as described in chapter 3. This means that the elements of the time-domain diagonal matrix $\mathbf{Q}$ in *(5.3.1)* are replaced by convolution operators, such that in the frequency domain the following expression for the mode-space cross-spectral density matrix (CSDM) results:

$$\mathbf{P}_y(\omega) = \int_{-\infty}^{\infty} d\tau \mathbf{R}_y(\tau) e^{-j\omega\tau} = \tilde{\mathbf{A}}(\omega)\mathbf{P}_s(\omega)\tilde{\mathbf{A}}^H(\omega) + \tilde{\mathbf{P}}_n(\omega) \qquad \cdots (5.4.8)$$

where,

$$\tilde{\mathbf{P}}_n(\omega) = \int_{-\infty}^{\infty} d\tau \tilde{\mathbf{R}}_n(\tau) e^{-j\omega\tau} \qquad \cdots (5.4.9)$$

is the mode-space noise CSDM, the steering matrix is modified to

$$\tilde{\mathbf{A}}(\omega) = \tilde{\mathbf{Q}}^H(\omega)\mathbf{E}^H\mathbf{A}(\omega) \qquad \cdots (5.4.10)$$

and in the relevant frequency band, the $\mu\mu$'th element of $\tilde{\mathbf{Q}}(\omega)$ is given by:

$$\tilde{Q}_{\mu\mu}(\omega) = 1/M^{1/2} C^*_{\mu 0}(\omega, \pi/2) \quad , \quad -\Lambda \leq \mu \leq \Lambda \qquad \cdots (5.4.11)$$

In the incoherent approach to wideband superresolution, equation *(5.2.16)*, which is of exactly the same form as *(5.4.8)* (or an approximation thereof via spatial covariances of the Fourier-series coefficients – see *(5.2.18)*), serves as the model under which effectively narrowband estimations are separately performed at a number of discrete frequencies in the operating band. In the case of eigenstructure-based algorithms such as MUSIC, the MN method or ESPRIT, this approach may completely fail when some of the received signals are coherent, as the signal cross-spectral density matrix $\mathbf{P}_s(\omega)$ is then singular irrespective of frequency – see appendix E.5. Although the wideband signal covariance matrix $\mathbf{R}_s$ would in general

remain non-singular (assuming the bandwidth is larger than the inverse of the relative delays of the coherent signals – see appendix E.5), the steering matrix $\mathbf{A}(\omega)$ is frequency-dependent, having a different column space at each frequency, the model *(5.2.15)* does not apply, nor does the rank 1 per source assumption for the (now full-rank) signal-only covariance matrix $\mathbf{R}_s$.

In the context of a general sensor array, frequency smoothing refers to a two-stage process that enables a wideband source to be represented by a rank 1 model. First, the array outputs are pre-processed with the aim of transforming the CSDM in such a way that renders the (transformed) steering matrix independent of frequency while maintaining its rank.[42] The modified CSDM is then Fourier-transformed at zero correlation time (or, in other words, frequency-averaged) to yield a 'frequency-smoothed' covariance matrix that has the same structure as the CSDM (or of a narrowband covariance matrix), but is characterised by a generally full-rank (modified) signal covariance matrix. As noted before, a single 'omni-directional' frequency-smoothed covariance matrix may be approximately implemented by pre-processing an equi-spaced linear array with a spatial resampling filter.

Returning now to the wideband mode-space formulation of *(5.4.8)* we note that $\tilde{\mathbf{A}}$ as defined by *(5.4.10)* is approximately given by *(5.3.14)* throughout the frequency band and is thus independent of frequency. This means that wideband phase-mode pre-processing of a circular array is inherently also a frequency smoothing operation that allows eigen-decomposition to be based on the mode-space covariance matrix, and it may be viewed as a simple extension of the spatial resampling technique from equi-spaced linear arrays to equi-spaced circular arrays. Although the signal covariance matrix will generally remain non-singular in the presence of coherent wideband signals when their relative delays are larger than $2\pi/(\omega_{HI}-\omega_{LO})$ (ω_{HI} and ω_{LO} are the respective upper and lower angular frequencies in the band), its robustness to signal coherence may be further enhanced via a spatial smoothing procedure that will add to the automatic frequency-smoothing process.

42 This is sometimes referred to as *focusing*.

5.5 SIMULATIONS AND SUMMARY

5.5.1 GENERAL

A quantitative assessment of the superresolution capabilities of circular sensor arrays in phase-mode space may be obtained via illustrative and comparative Monte-Carlo simulations. The objective is to estimate and compare, under different signal and noise scenarios, the resolvability, bias and variability of such algorithms, when applied to (possibly pre-processed) arrays of different shape (e.g. linear and circular geometries), dimensions and radiation properties. An exhaustive performance study would have to relate to the following parameters:

a. Type of estimator – different methods and specific implementations of algorithms inevitably lead to different absolute as well as comparative results
b. Geometry – the relevant parameters are the array type, its orientation, the number of array sensors and the inter-sensor spacing
c. Radiation properties – radiation patterns of array sensors as a function of frequency
d. Signal model – signals may emanate from deterministic or stochastic sources which are either narrowband or broadband (for different bandwidths)
e. Signal scenario – we refer here to the number of sources, their location and their level of coherence
f. Noise model – narrowband or bandpass noise may be internally-generated at the array sensors, or it may be received from ambient noise-fields of different types
g. Pre-processing –
- optional pre-whitening transformation
- beamforming transformations:
  - none (sensor-space)
  - beam-space: type and number of available beams
  - circular-array mode-space: number of available modes
- smoothing: extent of spatial or frequency-domain smoothing

h. Sensitivity to errors – performance under different sensor calibration and position errors

Other important parameters include the number of snapshot samples N, the (appropriately defined) SNR and the number of times each experiment is repeated for the evaluation of the pseudo-statistical averages. In order to keep the set of results manageable and within the scope of a supplementary section of a single chapter, the extent of our simulations has been limited herein to include:

a. One representative scalar-search superresolution method, namely MUSIC

b. Selected geometries:
   - a 5-sensor narrowband equi-spaced linear array with inter-element spacing of half a wavelength
   - a 10-sensor equi-spaced circular array (of which 5 phase modes are used) with arc-wise inter-element spacing of:
     – 0.3 of a wavelength for the narrowband problem
     – 0.15 to 0.3 of a wavelength for the wideband problem

c. The following frequency-independent (voltage) element patterns:
   - isotropic (linear array)
   - $g(\theta, \varphi)=\sin^{1/2}\theta \cos^2(\varphi/2)$ (horizontal circular array)

d. Narrowband and octave-bandwidth gaussian signal sources – see sub-section 5.5.2 for model description

e. The following respective signal scenarios for the linear and circular arrays:
   - 2 equi-power sources at ϕ_0=-3.82° and ϕ_1=3.82° ($180°\sin\phi_{0,1}=\pm 12°$) on the azimuth ($\theta = 90°$) plane (angular spacing of one third of the Rayleigh resolution for the above specified narrowband linear array)
   - 2 equi-power sources at ϕ_0=-12° and ϕ_1=12° on the azimuth plane (angular spacing of one third of the mode-space Rayleigh resolution for the above specified circular array)

   The following levels of signal coherence:
   - incoherence
   - 99% coherence
   - full coherence

f. Noise modelled as the integrated contribution of ambient noise fields of 2 types:
   - isotropic or hemispherically-isotropic noise:
   - elevation-wise spatially impulsive noise at $\theta = 90°$:

   See sub-section 5.5.2 for model details

g. The following pre-processing transformations:
   - no pre-whitening
   - no beamforming transformation for the linear array
   - transformation of the circular array into phase-mode space
   - optional spatial smoothing using three 3-element linear-array sub-arrays
   - optional spatial smoothing using three 3-mode circular-array sub-sets
   - no frequency-domain smoothing for the linear array case; inherent mode-space frequency smoothing is demonstrated in the case of the circular array

h. Full error-free knowledge of the position and radiation properties of the array sensors is assumed.

The simulations were conducted on a Macintosh computer using the Mathematica programming language (version 2.0), for 30 snapshot samples and varying levels of SNR, and were each repeated 30 times for the evaluation of the angular bias and variance. The models used for simulating the discrete signal sources and the continuous noise fields are detailed in sub-section 5.5.2. The results are presented and explained in sub-section 5.5.3, with a discussion and a summary of the whole chapter in sub-section 5.5.4.

5.5.2 SIGNAL AND NOISE MODELS

Signals were modelled as emanating from a couple of (pseudo-) random spatially-impulsive (discrete point) sources in the far-field region of the array. The following specific formulation was used for simulating the k'th narrowband signal at time t_n:

$$s_k(t_n) = (S_{kn}^{RE} + jS_{kn}^{IM}) e^{j\omega_0(t_n - t_{c_k})} \quad , \quad 0 \le k \le K\text{-}1 \quad , \quad 0 \le n \le N\text{-}1$$

where the data $\{S_{kn}^{RE}, S_{kn}^{IM}\}_{k,n}$ were obtained from a zero-mean pseudo-random gaussian generator set to a variance of[43] $\sigma^2 = (1/2) \times 10^{SNR/10}$, ω_0 is the (angular) frequency at which the inter-element spacing in wavelengths is as specified in sub-section 5.5.1-b, and t_{c_k} is some time delay specific to the k'th source.[44] For the wideband case we used:[45]

$$s_k(t_n) = \sum_{\ell=8}^{16} (S_{kn\ell}^{RE} + jS_{kn\ell}^{IM}) e^{j(\ell\omega_{HI}/16)(t_n - t_{c_k})} \quad , \quad 0 \le k \le K\text{-}1 \quad , \quad 0 \le n \le N\text{-}1$$

where the data $\{S_{kn\ell}^{IM}, S_{kn\ell}^{IM}\}_{k,n,\ell}$ were obtained as before from a zero-mean (pseudo-) random gaussian generator, and ω_{HI} is the (angular) frequency at which the inter-element spacing in wavelengths reaches the highest value specified in sub-section 5.5.1-b. The signals were received at the array sensors (or phase mode outputs) through the usual complex (normalised) responses of the array sensors or (aligned) phase modes.

---

43 SNR is defined here as (10 times the logarithm to the base 10 of) the ratio of signal to noise power received by a (linear- array) sensor or an aligned (circular-array) phase mode, due to the presence of a single signal source and the given noise field. Note that S_{kn}^{RE} and S_{kn}^{IM} are assumed to be uncorrelated, so that:

$$\mathcal{E}|S_{kn}^{RE} + jS_{kn}^{IM}|^2 = 2\sigma^2$$

44 This is important for frequency-domain smoothing – see appendix E.5.

45 Flat-spectrum broadband signals are assumed which, for an approximately finite time response, dictates the minimum number of sampling points needed to cover the passband.

Signals s_0 and s_1 with a coherence level of $100p\%$ were synthesised under the respective narrowband and wideband models as:

$$s_0(t_n)=\{[\frac{1+(1-p^2)^{1/2}}{2}]^{1/2}(S_{0n}^{RE}+jS_{0n}^{IM})+[\frac{1-(1-p^2)^{1/2}}{2}]^{1/2}(S_{1n}^{RE}+jS_{1n}^{IM})\}e^{j\omega_0(t_n-t_{c0})}$$

$$s_1(t_n)=\{[\frac{1-(1-p^2)^{1/2}}{2}]^{1/2}(S_{0n}^{RE}+jS_{0n}^{IM})+[\frac{1+(1-p^2)^{1/2}}{2}]^{1/2}(S_{1n}^{RE}+jS_{1n}^{IM})\}e^{j\omega_0(t_n-t_{c1})}$$

$$0\le p\le 1$$

and

$$s_0(t_n)=$$

$$\sum_{\ell=8}^{16}\{[\frac{1+(1-p^2)^{1/2}}{2}]^{1/2}(S_{0n\ell}^{RE}+jS_{0n\ell}^{IM})+[\frac{1-(1-p^2)^{1/2}}{2}]^{1/2}(S_{1n\ell}^{RE}+jS_{1n\ell}^{IM})\}e^{j(\ell\omega_{HI}/16)(t_n-t_{c0})}$$

$$s_1(t_n)=$$

$$\sum_{\ell=8}^{16}\{[\frac{1-(1-p^2)^{1/2}}{2}]^{1/2}(S_{0n\ell}^{RE}+jS_{0n\ell}^{IM})+[\frac{1+(1-p^2)^{1/2}}{2}]^{1/2}(S_{1n\ell}^{RE}+jS_{1n\ell}^{IM})\}e^{j(\ell\omega_{HI}/16)(t_n-t_{c1})}$$

$$0\le p\le 1$$

and the time delays t_{c0}, t_{c1} were chosen as: $t_{c0}=0$, $\omega_{HI}t_{c1}=3.6\,\pi$.

Both hemispherically-isotropic and elevation-wise impulsive noise fields were considered. Ideally, these would have been formulated (for a hemispherically-isotropic noise field under the narrowband model) as:

$$x_{*m}(t_n)=$$

$$e^{j\omega_0 t_n}\int_{-\pi}^{\pi}d\varphi\int_{0}^{\pi/2}d\theta\sin\theta[N_n^{RE}(\theta,\varphi)+jN_n^{IM}(\theta,\varphi)]g(\theta,\varphi)e^{j(\omega_0 d/c)m\sin\theta\sin\varphi}$$

$$y_{*\mu}(t_n)=$$

$$e^{j\omega_0 t_n}\int_{-\pi}^{\pi}d\varphi\int_{0}^{\pi/2}d\theta\sin\theta[N_n^{RE}(\theta,\varphi)+jN_n^{IM}(\theta,\varphi)]\,\Phi_\mu(\theta,\varphi,\omega_0)/C_{\mu 0}(\omega_0,\pi/2)$$

where $x_{*m}(t_n)$ and $y_{*\mu}(t_n)$ refer to the narrowband noise ('voltage') received at time t_n by the m'th linear-array sensor and by the μ'th circular array phase-mode respectively, $g(\theta,\varphi)$ denotes the radiation pattern of a linear-array sensor, $\Phi_\mu(\theta,\varphi,\omega_0)/C_{\mu 0}(\omega_0,\pi/2)$ describes the μ'th phase-mode pattern aligned on the

azimuth ($\theta=\pi/2$) plane, and $\{N_n^{RE,IM}(\theta,\varphi)\}_n$ denote spatially-continuous normally-distributed zero-bias noise fields.

In fact, in order to save computer time, a much simpler scheme was used. Spatial whiteness of the (circular-array) mode-space noise has been assumed (which is the approximate case for an elevationwise-impulsive ambient noise field at $\theta=\pi/2$, and it was consequently modelled as:

$$y_{\alpha\mu}(t_n) = (N_n^{RE}+jN_n^{IM})e^{j\omega_0 t_n}$$

and

$$y_{\alpha\mu}(t_n) = \sum_{\ell=8}^{16} (N_{n\ell}^{RE}+jN_{n\ell}^{IM})e^{j(\ell\omega_H/16)t_n}$$

for the narrowband and wideband scenarios respectively, with $\{N_n^{RE,IM}, N_{n\ell}^{RE,IM}\}$ generated by a zero-mean pseudo-random gaussian generator of variance 1/2. A similar scheme was also used for simulating the linear-array element-space noise caused by a hemispherically-isotropic noise field (see footnote 2 in appendix E.3). The case of a linear array under an elevation-impulsive noise field at $\theta=\pi/2$ required a somewhat more complex model. Here, element noises were formulated as:

$$x_{\alpha\mu}(t_n) = \mathbf{H}\,[N_n^{RE}+N_n^{IM}]e^{j\omega_0 t_n}$$

where the data

$$N_n^{RE,IM} = [N_{n0}^{RE,IM}\ N_{n1}^{RE,IM}\ \cdots\ N_{n(M-1)}^{RE,IM}]^T$$

are generated from a zero-mean pseudo-random gaussian generator of variance 1/2, and the $M\times M$ matrix $\mathbf{H}$ is the hermitian square root of the Toeplitz matrix $\mathbf{R}_\alpha$ whose elements are given by [BUR 91]:

$$[R_\alpha]_{m'm''} = (1/2)J_0[\pi(m'-m'')] \quad , \quad 0\le m', m''\le M-1$$

In other words,

$$\mathbf{R}_\alpha = \mathbf{H}\,\mathbf{H}^H$$

$$\mathbf{H} = \mathbf{U}\,\mathbf{\Lambda}^{1/2}\,\mathbf{U}^H$$

where $\mathbf{\Lambda}$ and $\mathbf{U}$ are, respectively, the eigenvalue matrix and eigenvector matrix of $\mathbf{R}_\alpha$, and $\mathbf{\Lambda}^{1/2}$ has the square roots of the eigenvalues of $\mathbf{R}_\alpha$ on its main diagonal.

5.5.3 SIMULATION RESULTS

The simulated results shown in *Fig. 5.5.1* to *Fig. 5.5.6* are aimed both at demonstrating mode-space superresolution processing and at comparing the performance of a (mode-space) circular array with that of an (element-space) linear array. It is important to realise that there is an inherent resolution factor of approximately π in favour of the latter[46] for sources close to broadside, when the number of processed circular-array phase modes equals the number of linear-array elements, and as in general, not all M phase modes excited in an M-element circular array are usable, a simple comparison may prove misleading. We have thus chosen to

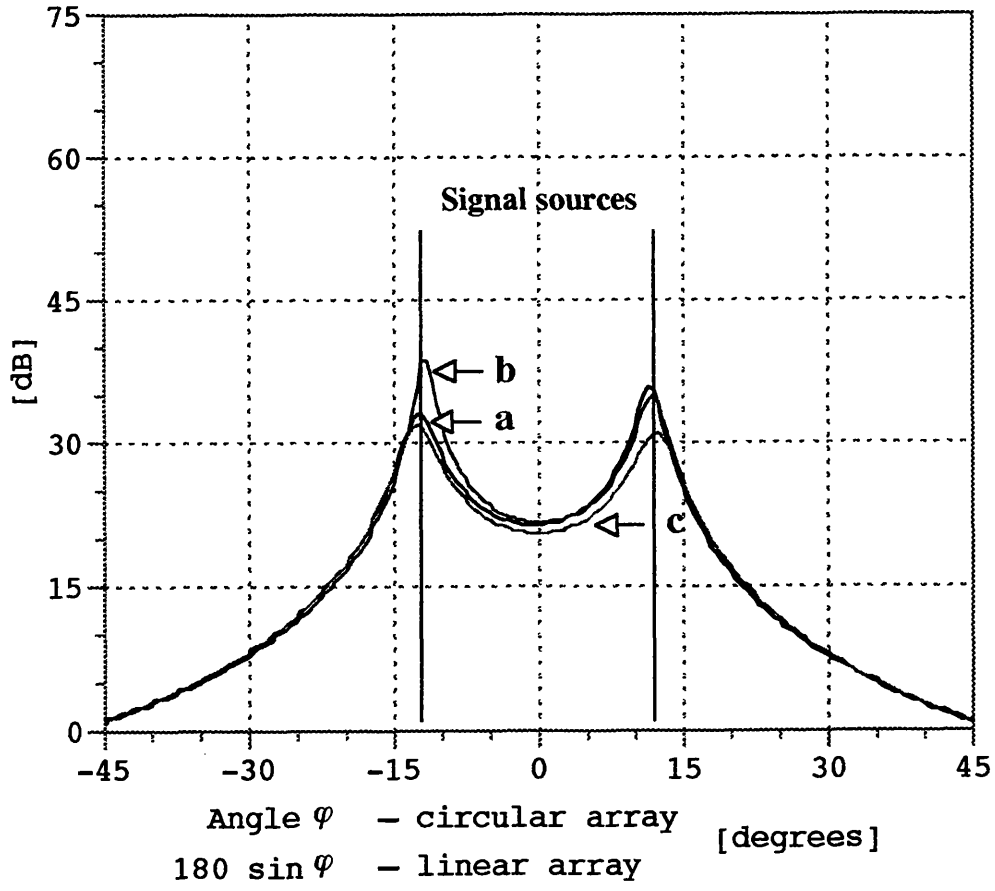

Fig. 5.5.1 MUSIC spectral pattern for two uncorrelated sources (SNR = 25 dB)
a. 5-sensor linear array in (full or hemispherically) isotropic noise
b. 5-sensor linear array in elevationwise-impulsive noise
c. 10-sensor/5-mode circular array in elevationwise-impulsive noise

[46] See *(3.2.2)* in chapter 3 for a linear-array inter-element spacing of half a wavelength

simulate the following arrays:

i a 10-element equi-spaced circular array of directional sensors, with superresolution processing applied to 5 aligned phase modes no. {-2 to 2}. The array is embedded in an elevationwise-impulsive ambient noise field

ii a 5-element equi-spaced linear array of isotropic sensors embedded in an isotropic or semi-isotropic ambient noise field

iii a 5-element equi-spaced linear array of isotropic sensors embedded in an elevationwise-impulsive ambient noise field at $\theta = \pi/2$.

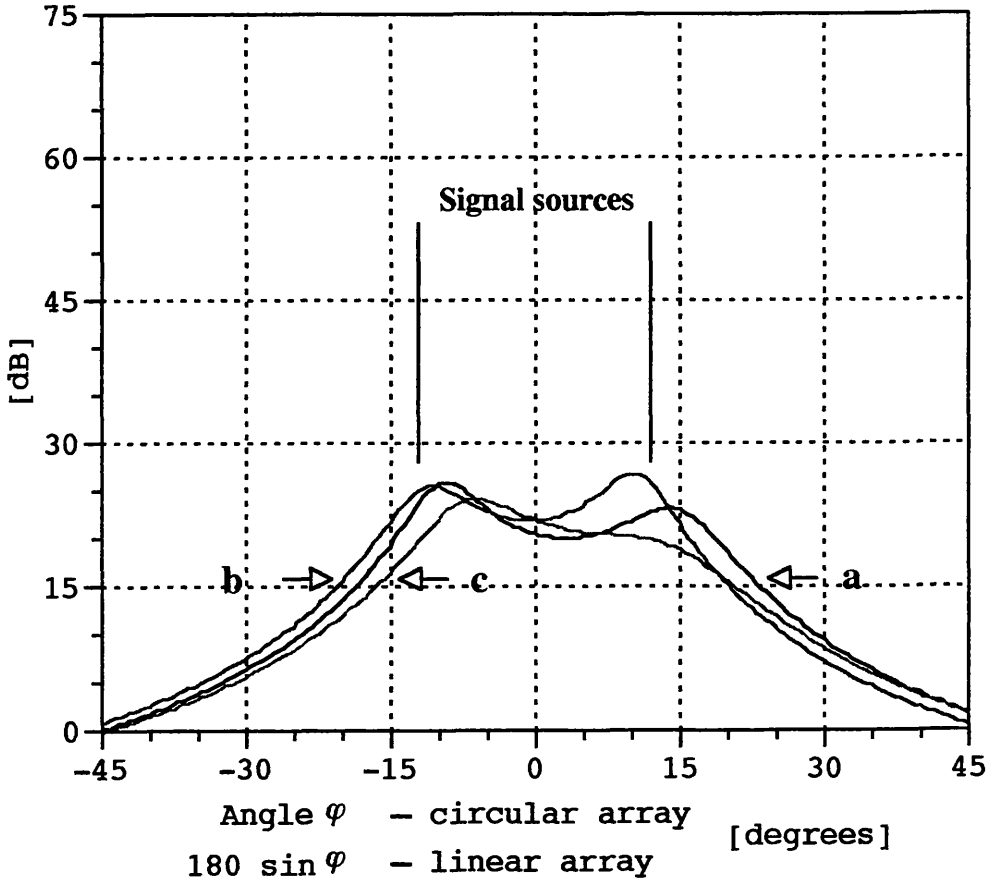

Fig. 5.5.2 MUSIC spectral pattern for unsmoothed arrays excited by two 99% correlated sources (SNR = 30 dB)

a. 5-sensor linear array in (full or hemispherically) isotropic noise

b. 5-sensor linear array in elevationwise-impulsive noise

c. 10-sensor/5-mode circular array in elevationwise-impulsive noise

Note that even though the simulated circular array comprises twice the number of linear-array elements, its diameter (for $\lambda/3$ inter-element spacing) is in fact smaller than the long dimension of the corresponding ($\lambda/2$-spaced) linear array by an approximate factor of π. As far as our graphical output is concerned, all circular-array results are displayed in angle φ° space, whereas the linear-array outputs have been plotted versus $180^\circ \sin\varphi$, which, for $\lambda/2$ inter-element spacing of the linear array sensors, corresponds to the coordinate transformation *(3.2.2)*.

Fig. 5.5.1 depicts the narrowband MUSIC spectral patterns for the two arrays when excited by two equi-power sources. The power received from each of the

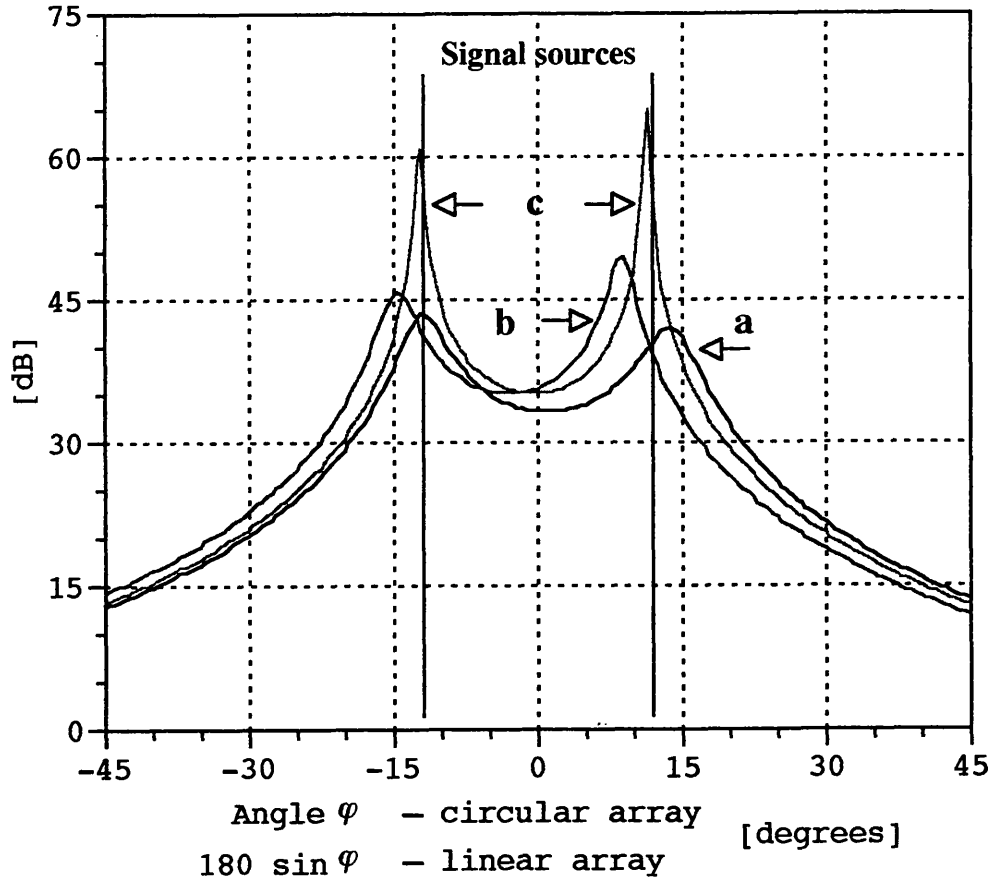

Fig. 5.5.3 MUSIC spectral pattern for spatially-smoothed arrays excited by two 99% correlated sources (SNR = 30 dB)

a. 5-sensor linear array in (full or hemispherically) isotropic noise

b. 5-sensor linear array in elevationwise-impulsive noise

c. 10-sensor/5-mode circular array in elevationwise-impulsive noise

sources corresponds to a signal-to-noise ratio of 25 dB. We notice that the two sources are easily resolved both by the linear array (under both noise models) and by the circular array, although the linear-array resolution appears to be somewhat higher. In *Fig. 5.5.2*, there is a 99% correlation between the two sources, which are now also 5 dB more powerful. As no processing has been applied to 'decorrelate' the sources, the result is an almost complete loss of resolution. This situation is remedied by applying spatial smoothing to the arrays, with the linear-array elements and similarly, the circular-array phase modes, divided into three sets of three interlaced elements and phase modes, respectively. The resulting spectral patterns are shown in *Fig. 5.5.3*. Both the linear and the circular array have fully regained their resolving power, with the highest resolution exhibited by the circular array. But also note that

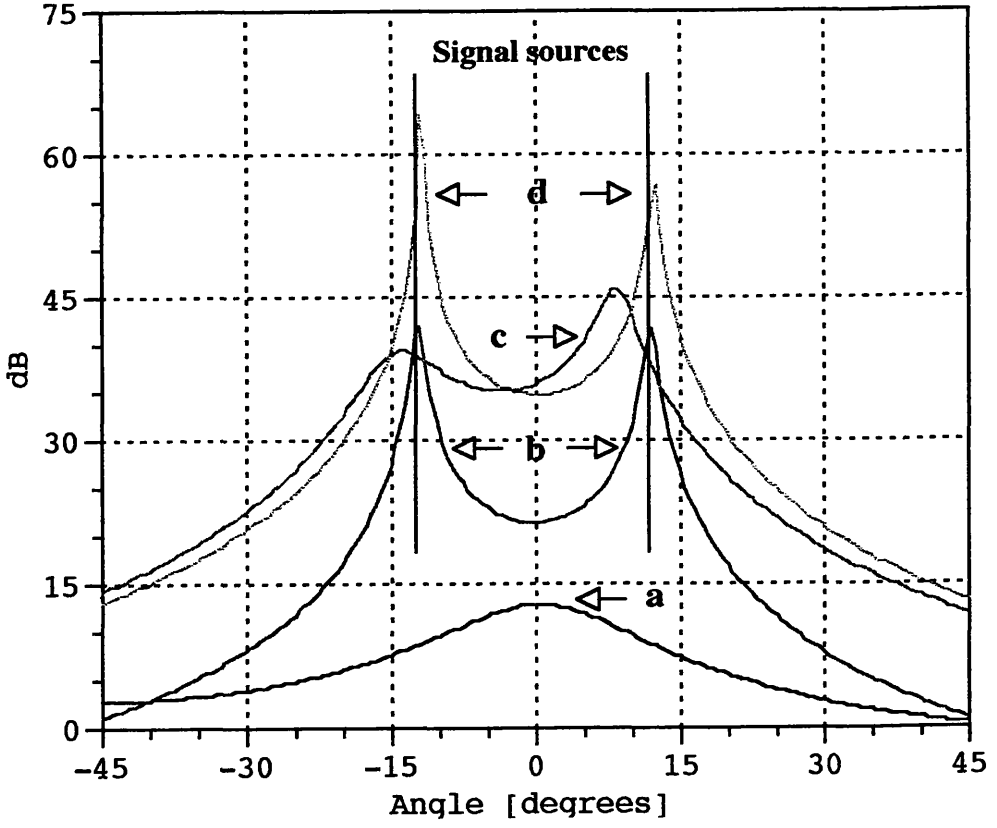

Fig. 5.5.4 MUSIC spectral pattern for a 10-sensor/5-mode circular array excited by two fully correlated sources (SNR = 30 dB)

a. unsmoothed array

b. under inherent frequency-domain smoothing (octave bandwidth)

c. spatially smoothed array

d. spatial smoothing + inherent frequency-domain smoothing

the spatially-smoothed result for the linear array under an elevationwise impulsive noise field is biased by approximately 3 (transformed) degrees[47], which may be attributed to its element noise not being spatially white. No such bias has been noticed in the smoothed MUSIC pattern for the circular array or for the linear array when the ambient noise field is isotropic.

Fig. 5.5.4 is wholly devoted to the simulated circular array which is now illuminated by two fully-correlated signal sources. The narrowband result is a complete loss of resolution as depicted by plot **a**. In plot **b**, an octave-bandwidth is assumed for the signals, noises and phase modes, which allows the inherent frequency-domain smoothing mechanism of broadband mode-space processing to

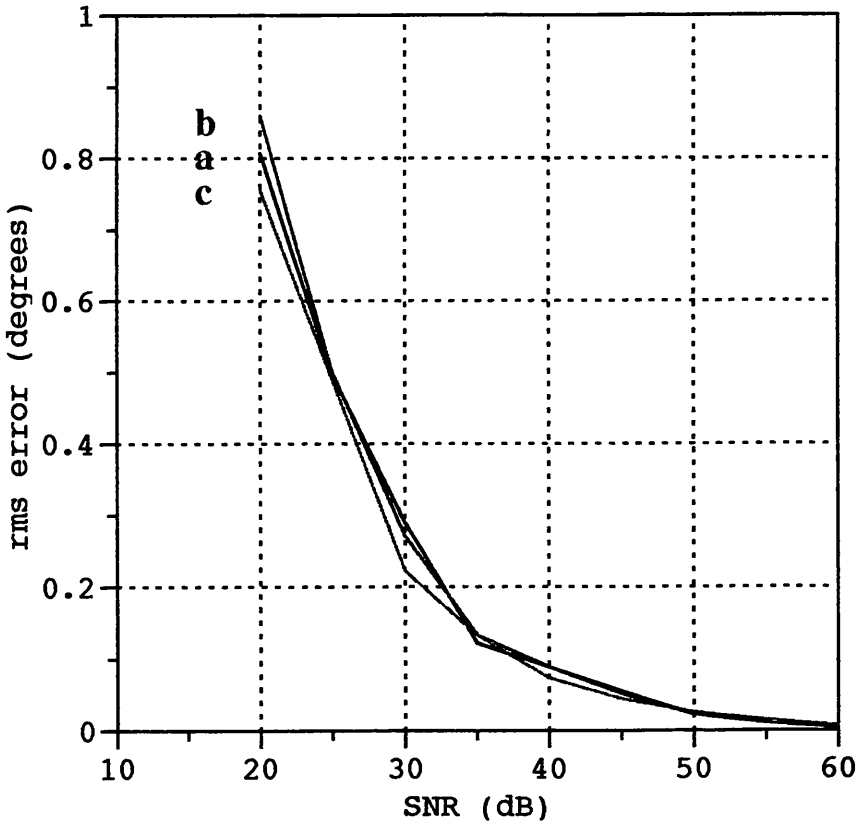

Fig 5.5.5 Application of spectral MUSIC for two uncorrelated sources: rms error patterns (φ-space for circular array, 180° sinφ-space for linear array)
a. 5-sensor linear array in (full or hemispherically) isotropic noise
b. 5-sensor linear array in elevationwise-impulsive noise
c. 10-sensor/5-mode circular array in elevationwise-impulsive noise

47 The bias in degrees is $\sin^{-1}(3°/180°)$.

take effect[48], leading to the fully regained resolution of the two sources. Plot **c** demonstrates the application of narrowband spatial smoothing, which partially recovers resolvability, albeit with noticeable bias, whereas plot **d** illustrates the benefit of combining wide bandwidth (yielding frequency-domain smoothing) with spatial smoothing. The statistical angular bias and rms error[49] attendant to the MUSIC estimator as applied to the linear and circular arrays, are finally plotted in *Fig. 5.5.5* and *Fig. 5.5.6* respectively for the case of two uncorrelated sources. The bias and variance (or rms error) are both seen to fall to zero when the signal to noise ratio is increased, which, after all, was to be expected from the MUSIC estimator.

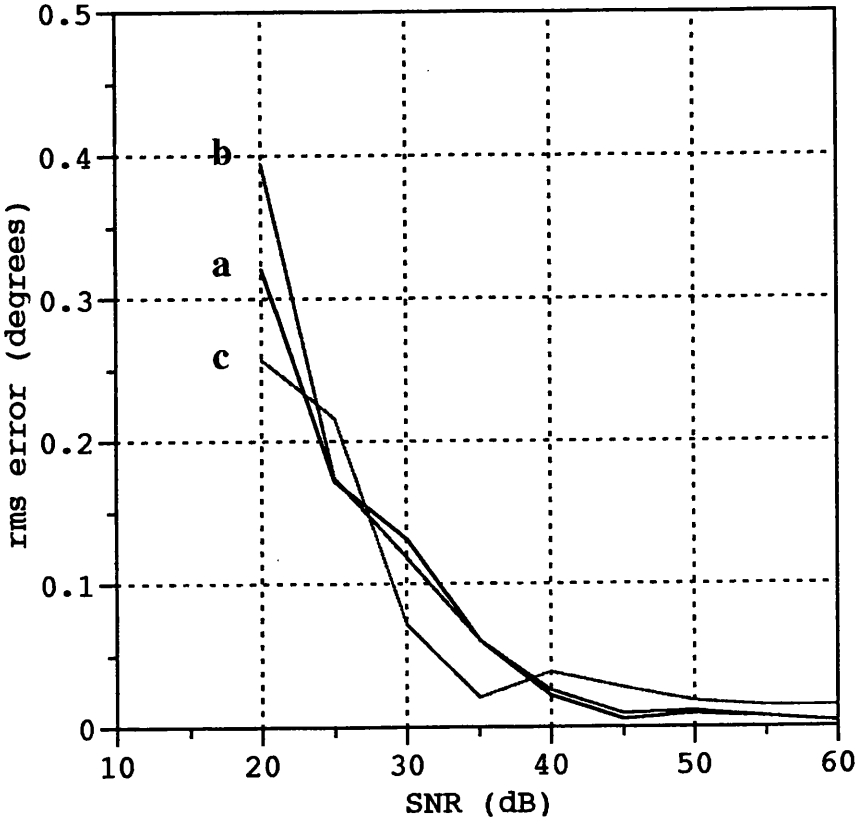

Fig 5.5.6 Application of spectral MUSIC for two uncorrelated sources: angular bias patterns (φ-space for circular array, 180° sinφ-space for linear array)
a. 5-sensor linear array in (full or hemispherically) isotropic noise
b. 5-sensor linear array in elevationwise-impulsive noise
c. 10-sensor/5-mode circular array in elevationwise-impulsive noise

[48] Note again that the presence of a non-zero time delay t_c between the two received signals is crucial for their decorrelation – see appendix E.5.

[49] By rms error we refer to the square root of the variance of the estimation bearing, or equivalently, to the variance of the estimation error.

5.5.4 SUMMARY

This chapter has been devoted to the application of high-resolution spatial estimators in circular-array mode space. Noting the structural identity between the mode-space steering matrix and the corresponding element-space matrix for a uniformly-spaced linear array, together with the spatially-white and homoscedastic mode-space noise received from a circumferentially-omnidirectional and elevationwise-impulsive ambient field, we have concluded and partially illustrated in simulations, that superresolution schemes that have hitherto been relevant to equi-spaced linear arrays are in fact equally applicable to equi-spaced circular arrays in mode space.

An important aspect of mode-space processing which we have demonstrated, is its compatibility with the spatial smoothing technique and (in the case of broadband sources and phase modes) the inherent omnidirectional frequency-domain smoothing mechanism which allows such algorithms as MUSIC and MN to cope with a coherent signal environment. Spatial smoothing has been extended from an established linear-array element-space version, whereas true direction-independent frequency-domain smoothing, free from preliminary estimation of source locations, has ordinarily involved spatial resampling, a technique that is again limited to linear arrays.

It should be noted that the linear-array to circular-array coordinate transformation mentioned in chapter 3, means that an M-element linear array receiving signals from direction ϕ, has a resolution factor of approximately (for half-wavelength inter-element spacing) $\pi\cos\phi$ in its favour when compared with the M-fold mode-space processing of a circular array. This factor equals π for sources near broadside, but becomes smaller and eventually less than unity (for $|\phi| \geq 72°$) as the location of sources moves away from broadside, and of course the linear array lacks the full circumferential coverage of the circular array. Also, although the generation of a set of M' 'well behaved' phase modes, generally requires a larger number of array elements, the physical size of the array will usually remain smaller than the length of a linear array of M' elements.

In conclusion, we have shown circular-array high-resolution mode-space processing to be a viable and beneficial alternative to high-resolution linear-array element-space techniques.

6. CONCLUSIONS

The application of mode-space beamforming, null-steering and direction-finding techniques to circular sonar arrays appears to have some appealing attractions. The sonar frequencies are sufficiently low to enable all signal processing to be realised digitally, allowing the implementation of complex processing schemes which are readily calibrated and are not limited by the imperfect nature of analogue components. In this thesis we have been examining several aspects pertaining to the analysis and processing of circular array systems with digital beamforming architecture. The general context has been that of sonar systems where noise is mainly contributed by external fields, and where one has the benefit of low frequencies, making complex digital processing more feasible, as well as manageable array dimensions due to the low velocity of propagation; but evidently, much of the material is relevant, at least in parts, to antenna arrays.

The basic concepts of beam-cophased and phase-mode excitation were briefly reviewed in chapter 2 and the transient circular array patterns associated with the reception of wideband pulses were discussed. It was pointed out that even when an array is delay-compensated (or 'co-delayed') in a certain look direction (i.e. of its main beam), it remains uncompensated in all other directions and the transient array pattern will depart (e.g. in the sidelobe region) from its steady-state radiation pattern. This is clearly manifested by the (approximately linear) change of co-delayed beamwidth with frequency. In contrast, beam patterns formed by the linear combination of phase modes that have been aligned (for a given elevation angle) over a wide frequency band, are effectively frequency independent, rendering the circular array 'delay matched' over the full constant-elevation azimuth cut.

In chapter 3 we considered conventional mode-space techniques that are applicable in the context of full digital beamforming. It was shown that omnidirectional phase modes may be linearly combined to form sectoral sets of beams with (almost) identical directional amplitude patterns but different phase gradients of locally linear slopes corresponding to 'effective mode numbers'. Such beams with phase-mode-like phase characteristics and directivity that may be

compromised for a steeper maximum phase gradient, were duly named *sectoral phase modes*. They may find application in a direction-finding scheme that combines the high resolution of multimodal phase-comparison DF with the inherent immunity of directional low-sidelobe beams to interference from a multi-source environment. Null steering may also be used for dealing with a multi-source environment, and it was shown that the incorporation of sectoral phase modes allows nulls to be independently steered for each directional beam in a multiple-beam network. An extension of this idea could incorporate independently steered nulls in a directional phase-comparison direction-finding system.

Also considered in chapter 3 were wideband extensions to the foregoing schemes. It was noted that with the exception of omnidirectional phase-comparison direction-finding (multimodal DF) which, subject to a 'favourable' element pattern, was shown to cover a wide bandwidth by virtue of symmetry, mode-space techniques generally rely on wideband mode alignment that will deconvolve the frequency-dependent zero-order phase mode coefficients. A digital filtering approach was subsequently proposed and its viability shown to depend on the directional properties of the array elements.

The effect of aperture and mode-space errors on the sidelobe level of mode-space beams was examined in chapter 4, where the rms sidelobe level was found to be constant either in the case of mode-space excitation errors of equal variance, or under equi-variance aperture errors, provided the array elements are omnidirectional. Various calibration-based pattern correction and alignment algorithms for optimising in the 'least squares' sense the array performance were then considered, and it was demonstrated that trying to optimise the array for multiple mode-space beams may be equivalent to a multimodal scheme in which the set of phase modes used for the synthesis of the beams, is aligned. For wideband alignment, digital filters have to be implemented at the phase mode outputs, based on one of the schemes discussed in chapter 3.

Finally, in chapter 5 we set out to exploit the benefits of mode-space formulation in the rapidly growing field of high-resolution processing. After an overview of scalar-search ('one-dimensional'), vector-search ('multidimensional') and search-free spatial estimators, the applicability of algorithms ordinarily restricted to equi-spaced linear arrays was demonstrated, in terms of both the signal and noise covariance matrices. In fact it was shown that the ambient noise model for circular arrays in mode space is less restrictive than that for its linear array counterpart, especially when the directivity in elevation is increased by a cylindrical arrangement of rings. Another

important aspect of mode-space processing demonstrated in this chapter was the applicability of the spatial smoothing technique and (in the case of broadband signals) the direction-independent frequency-domain smoothing inherent in wideband phase modes. Mode-space spatial smoothing for the decorrelation of narrowband coherent signals is a direct extension of the element space version of that technique, which has hitherto been restricted to equi-spaced linear arrays. The decorrelation of wideband coherent signals through frequency-domain smoothing is both omnidirectional and automatic in (wideband) mode space. In contrast, true direction-independent frequency-domain smoothing in element space that does not depend on preliminary estimates of source locations, is restricted to equi-spaced linear arrays and requires pre-processing in the form of spatial resampling. Mode-space versions of popular algorithms such as MUSIC (including its root version) and the Minimum Norm method are thus readily usable even in scenarios of fully correlated signals.

The main contributions of this work cover both conventional beamforming and superresolution processing and may be summarised as follows:

i The introduction of sectoral phase modes and their applications in direction finding and in null steering

ii The digital broadband alignment of phase modes and its dependence on the directional properties of the element patterns

iii The compatibility of circular arrays in mode space with linear-array estimators

iv The extension of the spatial smoothing technique from equi-spaced linear-array element space to circular-array mode space

v The inherent omnidirectional frequency-domain smoothing effect on broadband mode-space signals

The study which has been undertaken here is by no means complete. Various other aspects relating to the analysis and applications of sonar and antenna ring arrays and similar structures merit further investigation. An interesting and potentially promising topic for further research involves the use of sectoral phase modes in 'beam-space' spatial estimation. The idea is to enable the array to handle more (evenly spaced) sources and to reduce its susceptibility to a non-isotropic ambient noise field by confining the modes to sectors of locally isotropic noise, while continuing to enjoy the benefits of mode-space processing, namely:

- 360° coverage through the multibeam excitation of sectoral phase modes
- compatibility with linear-array estimators and spatial smoothing techniques
- automatic handling of broadband multipath signals through inherent frequency-domain smoothing.

Another area that deserves serious consideration pertains to the implementation of two-dimensional beamformers and direction-finders using arrays of related geometries. These may include elements in a cylindrical, conical or spherical arrangement as well as a toroidal array (i.e. a horizontal ring of vertical ring arrays) which is perhaps the most 'natural' two-dimensional extension to the single ring geometry. An interesting geometry that could well be worth investigating is that of an elliptical array, or of a cylindrical structure with elliptical cross-section. On the practical side, such an array may more easily conform to the hull of a sea vessel, while the (possibly phase-mode) analysis could make use of the fact that a (continuous) circular ring array would also look elliptical to an elevated far-field source. Since each azimuth bearing of the source would be equivalent to a different tilt of the circular array, one would have to angularly sectorise the operation of the array through the possible use of sectoral phase modes or their elliptical equivalent.

Other configurations are of course possible and are open to analysis. It is hoped that the work presented in this thesis together with some of the ideas suggested above will stimulate other researchers in the sonar and antenna array communities as well as authors in the field of high-resolution spatial processing, to focus more attention on circular arrays.

7. REFERENCES

7.1 REFERENCES FOR CHAPTER 1

[ADC 19] **Adcock, F.**: 'Improvements in means for determining the direction of a distant source of electromagnetic radiation', *British patent 130490, 1919*

[AND 60] **Anderson, V. C.**: 'Digital array phasing', *J. Acoust. Soc. Am., Vol. 32, pp 867-870, 1960*

[AND 63] **Anderson, V. C., Munson, J. C.**: 'Directivity of spherical receiving arrays', *J. Acoust. Soc. Am., Vol. 35, No. 8, pp 1162-1168, 1963*

[BAI 60] **Bain, W. C.**: 'Improvements in or relating to high frequency direction finding systems', *British Patent 853 662, 1960*

[BIE 84] **Bienvenu, G., Kopp, L.**: 'Decreasing high resolution method sensitivity by conventional beamformer preprocessing', *Proceedings of the IEEE International Conference on Acoustics, Speech and Signal Processing (ICASSP), San Diego, CA, pp 33.2.1-33.2.4, April 1984*

[BOY 68] **Boyns, J. E., Munger, A. D., Provencher, J. H., Reindel, J., Small, B. I.**: 'A lens feed for a ring array', *IEEE Transactions on Antennas and Propagation, Vol. AP-16, pp 264-267, March 1968*

[BOY 70] **Boyns, J. E., Gorham, C. W., Munger, A. D., Provencher, J. H., Reindel, J., Small, B. I.**: 'Step-scanned circular-array antenna', *IEEE Transactions on Antennas and Propagation, Vol. AP-18, No. 5, pp 590-595, September 1970*

[BOG 74] **Bogner, B. F.**: 'Circularly symmetric RF commutator for cylindrical phased arrays', *IEEE Transactions on Antennas and Propagation, Vol. AP-22, pp 78-81, January 1974*

[BUR 91] **Burdic S. B.**: 'Underwater acoustic system analysis', 2nd edition, *Signal Processing Series, Prentice Hall, New Jersey, 1991*

[BUT 61] **Butler, J., Lower, R.**: 'Beam-forming matrix simplifies design of electronically scanned antennas', *Electronic Design, pp 170-173, April 1961*

[CAR 43] **Carter, P. S.**: 'Antenna arrays around cylinders', *Proc. IRE, Vol. 31, pp 671-693, December 1943*

[CHA 62] **Chadwick, G. G., Glass, J. C.**: 'Investigations of a multiple beam scanning circular array', *Scientific Report No. 1, Contract AF19(628)367, Project A-1035, AFCRL, U.S. Air Force, Bedford, Mass., U.S.A., December 1962*

[CHE 67] **Cheng, D. K., Tseng, F. I.**: 'Maximisation of directive gain for circular and elliptical arrays', *Proc. IEE, Vol. 114, pp 589-594, May 1967*

[CHI 36] **Chireix, H.**: 'Antennes à rayonnement zénithal réduit', *L'Onde Élec., Vol. 15, pp 440-456, July 1936*

[CHO 66] **Chow, P. E. K., Fenby, R. G.**: 'Electronic beam-rotation for circular arrays using matrix networks', *NATO 12th AGARD Symposium of the Avionics Panel, Dusseldorf, 1966*

[CHO 67] **Chow, P. E. K., Davies, D. E. N.**: 'Wide bandwidth Butler matrix network', *Electronics Letters, Vol. 3, No. 6, pp 252-253, June 1967*

[CHR 74] **Christopher, E. J.**: 'Electronically scanned TACAN antenna', *IEEE Transactions on Antennas and Propagation, Vol. AP-22, pp 12-16, January 1974*

[CHU 59] **Chu, T. S.**: 'On the use of uniform circular arrays to obtain omnidirectional patterns', *IRE Transactions on Antennas and Propagation, Vol. AP-7, pp 436-438, October 1959*

[COL 69] **Collin, R. E., Zucker, F. J.**: 'Antenna Theory Part I', *McGraw-Hill, New York, 1969*

[COL 70] **Coleman, H. P.**: 'An iterative technique for reducing sidelobes of circular arrays', *IEEE Transactions on Antennas and Propagation, Vol. AP-18, No. 4, pp 566-567, July 1970*

[CRA 47] **Crampton, C.**: 'Naval radio direction-finding', *J. IEE, Vol. 94, Pt. IIIA, pp 132-153, 1947*

[CUR 80] **Curtis, T. E., Ward, R. J.**: 'Digital beam forming for sonar systems', *IEE Proceedings Pt F: Commun., Radar & Signal Process., Vol. 127, No. 4, pp 257-265, August 1980*

[CVE 88a] **Cvetkovic, M.**: 'HF direction finding and null steering using circular arrays', *Ph.D. Thesis, University of London, May 1988*

[CVE 88b] **Cvetkovic, M., Davies, D. E. N., Griffiths, H. D., Collins, B. S.**: 'An HF direction-finding and null steering system employing a four-element circular array', *Proc. 4th IEE Intl. Conf. on HF Radio Systems and Techniques, London, IEE Conf. Publ. No. 284, pp 221-225, April 1988*

[DAV 65a] **Davies, D. E. N., McCartney, B. S.**: 'Cylindrical arrays with electronic beam scanning', *Proc. IEE, Vol. 112, No. 3, pp 497-505, 1965*

[DAV 65b] **Davies, D. E. N.**: 'A transformation between the phasing techniques required for linear and circular aerial arrays', *Proc. IEE, Vol. 112, No. 11, pp 2041-2045, November 1965*

[DAV 69] **Davies, D. E. N., Chow, P. E. K.**: 'An experimental array with electronic beam rotation', *Proc. Eur. Microwave Conf., London, pp 129-132, September 1969*

[DAV 77] **Davies, D. E. N., Rizk, M. S. A. S.**: 'Electronic steering of multiple-nulls for circular arrays', *Electronics Letters, Vol. 13, No. 22, pp 669-670, October 1977*

[DAV 78a] **Davies, D. E. N., Rizk, M. S. A. S.**: 'A small radius circular array with 360° null steering capability', *IEE Conf. Publ. 169, Antennas and Propagation, pp 60-64, 1978*

[DAV 78b] **Davies, D. E. N., Rizk, M. S. A. S.**: 'A broadband experimental null-steering antenna system for mobile communications', *Radio Electron Engnr., Vol. 48, No. 10, pp 511-517, Oct. 1978*

[DAV 81a] **Davies, D. E. N.**: 'Circular arrays: their properties and potential applications', *Invited Review Paper, Proc. 2nd IEE Intl. Conf. on Antennas and Propagation, York, IEE Conf. Publ. No. 195, Pt. I, pp 1-10, April 1981*

[DAV 81b] **Davies, D. E. N., Guy, J. R. F.**: 'A UHF communication antenna employing open-loop control null steering', *Joint International IEEE/AP-S Symposium, National Radio Science Meeting and International IEEE/MTT symposium on Antennas and Propagation, Vol. 1, pp 276-279, June 1981*

[DAV 83] **Davies, D. E. N.**: 'Circular arrays', *Chapter 12 in The Handbook of Antenna Design, Vol. II, A. W. Rudge, K. Milne, A. D. Olver and P. Knight eds, Peter Peregrinus, Stevenage 1983*

[DUH 52] **DuHamel, R. H.**: 'Pattern synthesis for antenna arrays on circular, elliptical and spherical surfaces', *Univ. of Illinois, Urbana, Elec. Engrg. Res. Tech. Rept. 16, Contract N6-ori-71 pp 27-59, May 1952*

[EAR 47] **Earp, C. W., Godfrey, R. M.**: 'Radio direction finding by the cyclic differntial measurement of phase', *J. IEE, Vol. 94, Pt.IIIA, pp 705-721, 1947*

[FEN 65a] **Fenby, R. G.**: 'A study of phase-compensated circular aerial arrays for electronic beam-scanning radar systems', *M.Sc. Thesis, Dept. of Electronic and Electrical Engineering, University of Birmingham, 1965*

[FEN 65b] **Fenby, R. G.**: 'Limitations on directional patterns of phase compensated circular arrays', *Radio Electron Engnr., Vol. 30, pp 206-222, October 1965*

[FEN 68] **Fenby R. G., Davies, D. E. N.**: 'Circular array providing fast 360° electronic beam rotation', *Proc. IEE, Vol. 115, pp 78-86, January 1968*

[GET 66] **Gething, P. J. D.**: 'High-frequency direction finding', *Proc. IEE, Vol. 113, No. 1, pp 49-61, January 1966*

[GET 78] **Gething, P. J. D.**: 'Radio direction finding and the resolution of multicomponent wave-fields', *Peter Pereginus, IEE Electromagnetic Series 4, 1978*

[GOT 70] **Goto, N., Cheng, D. K.**: 'On the synthesis of concentric ring arrays', *Proc. IEEE, Vol. 58, pp 839-840, 1970*

[GOT 77] **Goto, N., Tsunoda, Y.**: 'Sidelobe reduction of circular arrays with a constant excitation amplitude', *IEEE Transactions on Antennas and Propagation, Vol. AP-25, No. 6, pp 896-898, November 1977*

[GRA 84] **Gray, D. A.**: 'Theoretical and experimental comparisons of optimum element, beam and eigen space array processors', *NATO Advanced Study Institute on Adaptive Methods in Underwater Acoustics, Lüneburg, Germany, pp 34.1-34.6, July-August 1984*

[GRE 74] **Gregorwich, W. S.**: 'An electronically despun array flush-mounted on a cylindrical spacecraft', *IEEE Transactions on Antennas and Propagation, Vol. AP-22, pp 71-74, Jan. 1974*

[GRI 86] **Griffiths, H. D., Karavassilis, N., Jones, M. R., Davies, D. E. N.**: 'Broadband nulls from a circular array', *Proc. 4th IEE Intl. Conf. on Antennas and Propagation, Warwick, IEE Conf. Publ. No. 248, pp 304-306, 1985*

[GUY 81] **Guy, J. R. F.**: 'Circular arrays incorporating adaptive pattern control for communications', *Ph.D. Thesis, University of London, April 1981*

[GUY 83a] **Guy, J. R. F., Davies, D. E. N.**: 'Studies of the Adcock direction finder in terms of phase-mode excitation around circular arrays', *The Radio and Electronic Engineer, Vol. 53, No. 1, pp 33-38, January 1983*

[GUY 83b] **Guy, J. R. F., Davies, D. E. N.**: 'Novel method of multiplexing radiocommunication antennas using circular-array configuration', *IEE Proceedings Pt. H, Vol. 130, No. 6, pp 410-414, June 1983*

[HAN 38] **Hansen, W. W., Woodyard, J. R.**: 'A new principle in directional antenna design', *Proc. IRE, Vol. 26, pp 333-345, March 1938*

[HAN 39] **Hansen, W.W., Hollingsworth, L. M.**: 'Design of flat-shooting antenna arrays', *Proc. IRE, Vol. 27, pp 137-143, February 1939*

[HAN 53] **Hansel, P. G.**: 'Doppler-effect omnirange', *Proc. IRE, Vol. 41, pp 1750-1756, December 1953*

[HAY 20] **Hayes, H. C.**: 'Detection of submarines', *Proc. Am. Phil. Soc., Vol. 59, pp 1-47, 1920*

[HIC 60] **Hickman, C. E.**: 'Current distribution and terminal impedance of a circular antenna array', *Master's Thesis, University of Tennessee, Knoxville, Tenn., August 1960*

[HIC 61] **Hickman, C. E., Neff, H. P., Tillman, J. D.**: 'The theory of a single ring circular antenna array', *Trans. Amer. Inst. Elec. Engrs., Vol. 80, Part 1, pp 110-115, May 1961*

[HIC 63] **Hickman, C. E.**: 'First order impedance of a circular antenna array', *Scientific Report No. 5, Dept. of Elec. Engrg., University of Tennessee, Knoxville, Tenn., March 1963*

[HOL 47] **Holt, L. E.**: 'The German use of sonic listening', *J. Acoust. Soc. Am., Vol 19, pp 678-681, 1947*

[HOL 74] **Holley, A. E., Dufort, E. C., Dell-Imagine, R. A.**: 'An electronically scanned beacon antenna', *IEEE Transactions on Antennas and Propagation, Vol. AP-22, pp 3-12, January 1974*

[JAM 65] **James, P. W.**: 'Polar patterns of phase corrected circular arrays', *Proc. IEE, Vol. 112, pp 1839-1848, 1965*

[JOH 86] **Johnson, R. L., Miner, G. E.:** 'Comparison of superresolution algorithms for radio direction finding', *IEEE Transactions on Aerospace and Electronic Systems, Vol. AES-22, No. 4, pp 432-441, July 1986*

[JON 89] **Jones, M. R., Griffiths, H. D.:** 'Broadband pattern synthesis from a circular array', *Proc. 6th IEE Intl. Conf. on Antennas and Propagation, IEE Conf. Publ. No. 301, Pt. I, pp 55-59, April 1989*

[JON 90] **Jones, M. R.:** 'A study of wide bandwidth directional patterns from circular arrays', *Ph.D. Thesis, Univ. of London, April 1990*

[KAR 86] **Karavassilis, N., Davies, D. E. N., Guy, C. G.:** 'Experimental HF circular array with direction finding and null steering capabilities', *IEE Proceedings, Pt. H, Vol. 133, No. 2, pp 147-154, April 1986*

[KIN 56] **King, R. W. P.:** 'Theory of linear antennas', *Harvard University Press, Cambridge, Mass., 1956*

[KIN 68] **King, R. W. P., Mack, R. B., Sadler, S. S.:** 'Arrays of cylindrical dipoles', *Cambridge University Press, 1968*

[KUM 83a] **Kummer, W. H.:** 'Broad-band microwave electronically scanned direction finder', *IEEE Transactions on Antennas and Propagation, Vol. AP-31, No. 1, pp 18-26, January 1983*

[KUM 83b] **Kumaresan, R., Tuft, D. W.:** 'Estimating the angles of arrival of multiple plane waves', *IEEE Transactions on Aerospace and Electronic Systems, Vol. AES-19, No 1, pp 134-139, January 1983*

[KUM 83c] **Kumaresan, R.:** 'On the zeros of the linear prediction-error filter for deterministic signals', *IEEE Transactions on Acoustics, Speech and Signal Processing, Vol. ASSP-31, No. 1, pp 217-220, February 1983*

[KUN 51] **Kundsen, H. L.:** 'The necessary number of elements in a directional ring array', *J. Appl. Phys., Vol. 22, No. 1, pp 1299-1306, Nov. 1951*

[KUN 53] **Kundsen, H. L.:** 'The field radiated by a ring of quasi-array of an infinite number of tangential or radial dipoles', *Proc. IRE, Vol. 41, pp 781-789, June 1953*

[KUN 56] **Kundsen, H. L.:** 'Radiation from ring quasi-arrays', *IRE Transactions on Antennas and Propagation, Vol. AP-4, pp 452-472, July 1956*

[LEE 92] **Lee, T.:** 'Fast implementation of root-form eigen-based methods for detecting closely spaced sources', *IEE Proceedings. Pt. F: Commun., Radar & Signal Process., Vol. 139, No. 4, August 1992*

[LEP 50] **Le Page, W. R., Roys, C. S., Seely, S.**: 'Radiation from circular current sheets', *Proc. IRE, Vol. 38, pp 1069-1072, 1950*

[LIM 75] **Lim, J. C., Davies, D. E. N.**: 'Synthesis of a single null response in an otherwise omni-directional pattern using a circular array', *Proc. IEE, Vol. 122, No. 4, pp 349-352, April 1975*

[LIM 77] **Lim, J. C.**: 'Introduction of a sharp steerable null response in an otherwise omnidirectional pattern using a circular array', *Radio Electron Engr., Vol. 47, pp 30-32, Jan./Febr. 1977*

[LON 67] **Longstaff, I. D., Chow, P. E. K., Davies, D. E. N.**: 'Directional properties of circular arrays', *Proc. IEE, Vol. 114, No. 6, pp 713-718, June 1967*

[LON 68] **Longstaff, I. D., Davies, D. E. N.**: 'A wideband circular array for HF communications', *Radio Electron Engr., Vol. 35, pp 321-327, June 1968*

[MAC 63] **Mack, R. B.**: 'A study of circular arrays', *Cruft Laboratory, Harvard University, technical reports 381-386, 1963*

[MAW 68] **Ma, M. T., Walters, L. C.**: 'Synthesis of concentric ring antenna arrays yielding approximately equal sidelobes', *Radio Science, Vol. 3 (New Series) pp 465-470, May 1968*

[MCC 63] **McCartney, B. S.**: 'Proposals for an electronically scanned circular array', *Proc. IEE, Vol. 110, No. 7, pp 1220-1222, 1963*

[MIT 59] **Mitchell, T. A.**: 'The design of cylindrical aerials by means of equivalent linear arrays', *Admiralty Surface Weapons Establishment, Portsmouth, Technical Note RX2-59-16, 1959*

[MOT 68] **Mott, H., Dudgeon, J. E.**: 'On circular array pattern synthesis using a digital computer', *Proceedings of the IEEE, Vol. 56, pp 369-370, March 1968*

[NAG 78] **Nagayama, A., Yoshida, G., Watanabe, F., Goto, N.**: 'Experimental study on sidelobe suppression of circular arrays excited in a constant voltage', *Trans. IECE Japan ISAP, Vol. A-1-3, August 1978*

[NEF 50] **Neff, H. P., Patton, W. T., Pierce, J. F., Tillman, J. D.**: 'An amplitude scanned circular array', *Univ. of Tennessee, Dept. Elec. Engrg., AF Cambridge Research Center, Final report, Contract AF 19(604)-1537, October 1950*

[NEF 60] **Neff, H. P., Tillman, J. D.**: 'An electronically scanned circular antenna array', *IRE Int. Conv. Record, Pt. 1, pp 41-48, 1960*

[NIC 87] **Nickel, U.**: 'Angular superresolution with phased array radar: a review of algorithms and operational constraints', *IEE Proceedings Pt F: Commun., Radar & Signal Process.,Vol. 134, No. 1, pp 53-59, February 1987*

[PAG 48a] **Page, H.**: 'Radiation resistance of ring aerials', *Wireless Engineer, Vol. 25, pp 102-109, April 1948*

[PAG 48b] **Page, H.**: 'Ring aerial systems', *Wireless Engineer, Vol. 25, pp 308-315, October 1948*

[PRO 72] **Provencher, J. H.**: 'A survey of circular symmetric arrays', *in Phased-Array Antennas, Oliner, A. A. and Knittel, G. H. Eds., Artech House, pp 292-300, 1972*

[QUE 70] **Queens, W. C.**: 'The directivity of sonar receiving arrays', *J. Acoust. Soc. Am., Vol. 47, No. 3, pp 711-720, 1970*

[RAH 80] **Rahim, T.**: 'Directional pattern synthesis in circular arrays of directional antennas', *Ph.D. Thesis, Univ. of London, 1980*

[RAH 81] **Rahim, T., Guy, J. R. F., Davies, D. E. N.**: 'A wideband UHF circular array', *Proc. 2nd International Conference on Antennas and Propagation, IEE Conf. Publ. 195, pp 447-450, April 1981*

[RAH 82] **Rahim, T., Davies, D. E. N.**: 'Effect of directional elements on the directional response of circular antenna arrays', *IEE Proceedings Pt. H, Vol. 129, No. 1, pp 18-22, February 1982*

[RED 70] **Redlich, R. W.**: 'Sampling synthesis of ring arrays', *IEEE Transactions on Antennas and Propagation, Vol. AP-18, No. 1, pp 116-118, January 1970*

[REH 80] **Rehnmark, S.**: 'Improved angular discrimination for digital ESM systems', 2nd Military Microwaves *(MM80) Conf. Proc., pp 157-162, Microwave Exhibitions and Publishers Ltd., Sevenoaks, Kent, October 1980*

[RIN 56] **Rindfleisch, H.**: 'Die Grossbasis-Peilanlage Wullenwever', *Nachrichtentechnische Zeitschrift, Vol. 9, pp 119-123, March 1956*

[RIZ 77] **Rizk, M. S. A. S.**: 'Null steering antennas for mobile communications', *Ph.D. Thesis, University of London, February 1977*

[ROY 64] **Royer, G. M.**: 'Directivity and impedance of a phased ring array of antennas', *M.S. Thesis, University of Toronto, Ontario, Canada, June* ***1964***

[ROY 66] **Royer, G. M.**: 'Directive gain and impedance of a ring array of antennas', *IEEE Transactions on Antennas and Propagation, Vol. AP-14, No. 5, pp 566-573, September* ***1966***

[SHE 68] **Sheleg, B.**: 'A matrix-fed circular array for continuous scanning', *Proceedings of the IEEE, Vol. 56, pp 2016-2027, November* ***1968***

[SHE 70] **Sheleg, B., Wright, B. D.**: 'A 3-D electronically scanned S-band cylindrical array', *Proc. of conformal array antenna conference, NELC, San-Diego, CA., January* ***1970***

[SHE 74] **Shestag, L. N.**: 'A cylindrical array for the TACAN system', *IEEE Transactions on Antennas and Propagation, Vol. AP-22, pp 17-25, January* ***1974***

[SKA 75] **Skahill, G., White, W. D.**: 'A new technique for feeding a cylindrical array', *IEEE Transactions on Antennas and Propagation, Vol. AP-23, pp 253-256, March* ***1975***

[STA 69] **Starbuck, J. T.**: 'A multiple-beam HF receiving aerial system', *Radio Electron Engr., Vol. 37, pp 229-235, April* ***1969***

[STE 29] **Stenzel, H.**: 'Uber die Richtcharakteristic von in einer Ebene Angeordneten Strahlern', *Elektrische Nachrichten-Technik, Berlin, Germany, Vol. 6, pp 165-181, May* ***1929***

[STE 65] **Stearn, C. O., Stewart, A. C.**: 'An investigation of concentric ring antennas with low sidelobes', *IEEE Transactions on Antennas and Propagation, Vol. AP-13, pp 856-863, November* ***1965***

[TAN 62] **Tanner, R. L., Andreason, M. G.**: 'A wire grid lens antenna of wide application. I. The wire-grid lens – concept and experimental confirmation', *IRE Transactions on Antennas and Propagation, Vol. AP-10, No. 4, pp 408-415, July* ***1962***

[TAY 52] **Taylor, T. T.**: 'A synthesis method for circular and cylindrical antennas composed of discrete elements', *IRE Transactions on Antennas and Propagation, Vol. PGAP-3, pp 251-261, August* ***1952***

[TIL 55] **Tillman, J., Patton, W. T., Blakey, C. E., Schultz, F. V.**: 'The use of a ring array as a ship range antenna', *Proc. IRE, Vol. 43, pp 1655-1660, November* ***1955***

[TSE 68] **Tseng, F. I., Cheng, D. K.**: 'Pattern synthesis of circular arrays with many directive elements', *IEEE Transactions on Antennas and Propagation, Vol. AP-16, pp 758-759, November 1968*

[URI 83] **Urick, R. J.**: 'Principles of underwater sound', 3rd edition, *MacGraw-Hill Inc., 1983*

[WAI 58] **Wait, J. R.**: 'Electromagnetic radiation from sources on and near cylindrical surfaces', *National Bureau of Standards, Rep. 5553, January 1958*

[WAT 80] **Watanabe, F., Goto, N., Nagayama, A., Yashida, G.**: 'A pattern synthesis of circular arrays by phase adjustment', *IEEE Transactions on Antennas and Propagation, Vol. AP-28, pp 857-863, November 1980*

[WIT 69] **Withers, M. J.**: 'Frequency-insensitive phase-shift networks and their use in a wide-bandwidth Butler matrix', *Electronics Letters, Vol. 5, pp 496-497, October 1969*

[WUN 66] **Wundt, R. M.**: 'Wullenweber arrays', *12th Symposium of the AGARD Avionics Panel on Radio Antennas for Aircraft and Aerospace Vehicles and Signal Processing Arrays, 1966*

[XUB 89] **Xu, X. L., Buckley, K M.**: 'A statistical performance comparison of MUSIC in element-space and beam-space', *Proceedings of the IEEE International Conference on Acoustics, Speech and Signal Processing (ICASSP), Glasgow, Scotland, pp 2124-2127, May 1989*

[XUB 90] **Xu, X. L., Buckley, K M.**: 'A comparison of element and beam space spatial-spectrum estimation for multiple source clusters', *Proceedings of the IEEE International Conference on Acoustics, Speech and Signal Processing (ICASSP), Albuquerque, New Mexico, Vol. 5, pp 2643-2646, April, 1990*

[ZIE 64] **Ziehm, G.**: 'Optimum directional pattern synthesis of circular arrays', *Radio Electron Engnr., Vol. 28, pp 341-355, November 1964*
[reprinted from the Proc. of the Symposium on "Signal Processing in Radar and Sonar Directional Systems", Birmingham, July 1964]

7.2 REFERENCES FOR CHAPTER 2

[AMI 72] **Amitay, N., Galindo, Y., Wu, C. P.**: 'Theory and analysis of phased array antennas', *Wiley-Interscience, New York, 1972*

[BRE 80] **Brekhovskikh, L. M.**: 'Waves in layered media', 2nd edition, *Academic Press, New York, 1980*

[COL 91] **Collin, R. E.**: 'Field theory of guided waves', 2nd edition, *IEEE Press, New York, 1991*

[DYS 67] **Dyson, J. D.**: 'Determination of the phase center and phase patterns of antennas', *in Radio antennas for aircraft and aerospace vehicles, W. T. Blackband, Ed., AGARD Conference Proceedings No. 15, Slough, England, 1967*

[FEN 65] **Fenby, R. G.**: 'Limitations on directional patterns of phase compensated circular arrays', *Radio Electron Engnr., Vol. 30, pp 206-222, October 1965*

[HAR 61] **Harrington, R. F.**: 'Time-harmonic electromagnetic fields', *McGraw-Hill Inc., New York, 1961*

[LON 68] **Longstaff, I. D., Davies, D. E. N.**: 'A wideband circular array for HF communications', *Radio Electron Engr., Vol. 35, pp 321-327, June 1968*

[STA 69] **Starbuck, J. T.**: 'A multiple-beam HF receiving aerial system', *Radio Electron Engr., Vol. 37, pp 229-235, April 1969*

7.3 REFERENCES FOR CHAPTER 3

[ANT 79] **Antoniou, A.**: 'Digital filters: analysis and design', *McGraw-Hill Inc., 1979*

[BRA 83] **Brandwood, D. H.**: 'A complex gradient operator and its application in adaptive array theory', *IEE Proceedings, Vol. 130, Parts F and H, No. 1, pp 11-16, February 1983*

[CLA 68] **Clarke, J.**: 'Steering of zeros in the directional pattern of a linear array', *Transactions on Antennas and Propagation, Vol. AP-16, pp 267-268, 1968*

[CVE 88a] **Cvetkovic, M., Davies, D. E. N., Griffiths, H. D., Collins, B. S.**: 'An HF direction-finding and null steering system employing a four-element circular array', *Proc. 4th IEE Intl. Conf. on HF Radio Systems and Techniques, London, IEE Conf. Publ. No. 284, pp 221-225, April 1988*

[CVE 88b] **Cvetkovic, M.**: 'HF direction finding and null steering using circular arrays', *Ph.D. Thesis, Univ. of London, May 1988*

[DAV 65] **Davies, D. E. N.**: 'A transformation between the phasing techniques required for linear and circular aerial arrays', *Proc. IEE, Vol. 112, No. 11, pp 2041-2045, November 1965*

[DAV 67] **Davies, D. E. N.**: 'Independent angular steering of each zero of the directional pattern for a linear array', *IEEE Transactions on Antennas and Propagation, Vol. AP-15, pp 296-298, March 1967*

[DAV 77] **Davies, D. E. N., Rizk, M. S. A. S.**: 'Electronic steering of multiple-nulls for circular arrays', *Electronics Letters Vol. 13, No. 22, pp 669-670, October 1977*

[DAV 78a] **Davies, D. E. N., Rizk, M. S. A. S.**: 'A small radius circular array with 360° null steering capability', *IEE Conf. Publ. 169, Antennas and Propagation, pp 60-64, 1978*

[DAV 78b] **Davies, D. E. N., Rizk, M. S. A. S.**: 'A broadband experimental null-steering antenna system for mobile communications', *Radio Electron Engnr., Vol. 48, No. 10, pp 511-517, Oct. 1978*

[DAV 81] **Davies, D. E. N., Guy, J. R. F.**: 'A UHF communication antenna employing open-loop control null steering', *Joint International IEEE/AP-S Symposium, National Radio Science Meeting and International IEEE/MTT symposium on Antennas and Propagation, Vol. 1, pp 276-279, June 1981*

[GOL 69] **Gold, B., Rader, C.**: 'Digital processing of signals', *McGraw-Hill Inc., 1969*

[GRI 85] **Griffiths, H. D., Karavassilis, N., Jones, M. R., Davies, D. E. N.**: 'Broadband nulls from a circular array', *Proc. 4th IEE Intl. Conf. on Antennas and Propagation, Warwick, IEE Conf. Publ. No. 248, pp 304-306, 1985*

[JUR 64] **Jury, E. I.**: 'Theory and application of the z-transform method', *Wiley, New York, 1964*

[KAR 86] **Karavassilis, N., Davies, D. E. N., Guy, C. G.**: 'Experimental HF circular array with direction finding and null steering capabilities', *IEE Proceedings Pt. H, Vol. 133, No. 2, pp 147-154, April 1986*

[LIM 75] **Lim, J. C., Davies, D. E. N.**: 'Synthesis of a single null response in an otherwise omni-directional pattern using a circular array', *Proc. IEE, Vol. 122, No. 4, pp 349-352, April 1975*

[LIM 77] **Lim, J. C.**: 'Introduction of a sharp steerable null response in an otherwise omnidirectional pattern using a circular array', *Radio Electron Engr., Vol. 47, pp 30-32, Jan./Febr. 1977*

[MEL 70] **Mellors, M., Davies, D. E. N., Withers, M. J.**: 'Zero steering in the directional pattern of a linear array in the presence of mutual coupling', *Proc. IEE, Vol. 117, No. 1, pp 35-40, 1970*

[OPP 76] **Oppenheim, A.V., Schafer, R. W.**: 'Digital signal processing', *Prentice-Hall Inc., Englewood Cliffs, New Jersey 1976*

[REH 80] **Rehnmark, S.**: 'Improved angular discrimination for digital ESM systems', 2nd Military Microwaves *(MM80) Conf. Proc., pp 157-162, Microwave Exhibitions and Publishers Ltd., Sevenoaks, Kent, October 1980*

[RIZ 77] **Rizk, M. S. A. S.**: 'Null steering antennas for mobile communications', *Ph.D. Thesis, Univ. of London, Feb. 1977*

7.4 REFERENCES FOR CHAPTER 4

[BAR 80] **Barton, P.**: 'Digital beam forming for radar', *IEE Proceedings Pt. F: Commun., Radar & Signal Process., Vol. 127, No. 4, pp 266-277, August 1980*

[WAR 89] **Wardrop, B.**: 'Digital beamforming and adaptive techniques', *i n Tutorial Meeting of IEE Professional Group E15 on Phased Array Radar, University College London, pp 3/1-3/28, 18th September, 1989*

[LON 85a] **Long, N. R. W.**: 'A procedure for the alignment of phased arrays' *Proceedings of 5th IEE Conference on Antennas and Propagation, Warwick, IEE Conference Publication No. 248, April 1985*

[LON 85b] **Long, N. R. W.**: 'Correcting phased arrays for multipath or for conformal topography', *Electronics Letters, Vol. 21, No. 15, pp 639-640, 18th July 1985*

[RON 59] **Rondinelli, L. A.**: 'Effects of random errors on the performance of antenna arrays of many elements', *IRE Nat. Conv. Rec., Pt. 1, pp 174-189, 1959*

[RUZ 52] **Ruze, J.**: 'The effect of aperture errors on the antenna radiation pattern', *Nuovo Cimento, Vol. 9, 9th Suppl., No. 3, pp 364-380, 1952*

[SKO 80] **Skolnik, M. I.**: 'Introduction to radar systems', *McGraw-Hill Inc., 1980*

7.5 REFERENCES FOR CHAPTER 5

[AHM 75] **Ahmed, N., Rao, K. R.**: 'Orthogonal transformations for digital signal processing', *Springer-Verlag, New York, 1975*

[AKA 73] **Akaike, H.**: 'A new look at the statistical model identification', *IEEE Transactions on Automatic Control, Vol. AC-19, pp 716-723, 1973*

[AND 84] **Anderson, T. W.**: 'An introduction to multivariate statistical analysis', *2nd edition, John Wiley and Sons, 1984*

[BAN 71] **Bangs, W. J.**: 'Array processing with generalized beamformers', *Ph.D dissertation, Yale University, New Haven, CT, 1971*

[BAN 73] **Bangs, W. J., Schultheiss, P. M.**: 'Space-time processing for optimal parameter estimation', *in Signal Processing (Proceedings of the NATO Advanced Study Institute on Signal Processing with particular reference to Underwater Acoustics, Loughborough, U.K., August 1972), J. W. R. Griffiths, P. L. Stocklin and C. Van Schooneveld, Eds., pp 577-590, Academic Press, London, 1973*

[BAR 83] **Barabell, A. J.**: 'Improving the resolution performance of eigenstructure-based direction-finding algorithms', *Proceedings of IEEE International Conference on ASSP, Boston, pp 336-339, 1983*

[BAR 75] **Barton, D. K.** (Ed.): 'Radars, Vol. 4: radar resolution and multipath effects', *Artech House, 1975*

[BEL 70] **Bellman, R.**: 'Introduction to matrix analysis', *McGraw-Hill, New York, 1970*

[BIE 80] **Bienvenu, G., Kopp, L.**: 'Adaptivity to background noise spatial coherence for high resolution passive methods', *Proceedings of the IEEE International Conference on Acoustics, Speech and Signal Processing (ICASSP), Denver, CO, pp 307-310, April 1980*

[BIE 81] **Bienvenu, G., Kopp, L.**: 'Source power estimation method associated with high resolution bearing estimation', *Proceedings of the IEEE International Conference on Acoustics, Speech and Signal Processing (ICASSP), Atlanta, GA, pp 302-305, 1981*

[BIE 83] **Bienvenu, G., Kopp, L.**: 'Optimality of high resolution array processing using the eigensystem approach', *IEEE Transactions on Acoustics, Speech, and Signal Processing, Vol. ASSP-31, pp 1235-1248, 1983*

[BIE 84] **Bienvenu, G., Kopp, L.**: 'Decreasing high resolution method sensitivity by conventional beamformer preprocessing', *Proceedings of the IEEE International Conference on Acoustics, Speech and Signal Processing (ICASSP), San Diego, CA, pp 33.2.1-33.2.4, April 1984*

[BIE 89] **Bienvenu, G., Fuerxer, P., Vezzosi, G., Kopp, L., Florin, F.**: 'Coherent wide band high resolution processing for linear array', *Proceedings of the IEEE International Conference on Acoustics, Speech and Signal Processing (ICASSP), Glasgow, Scotland, Vol. 4, pp 2799-2802, May 1989*

[BOH 84] **Böhme, J. F.**: 'Estimation of source parameters by maximum likelihood and nonlinear regression', *Proceedings of the IEEE International Conference on Acoustics, Speech and Signal Processing (ICASSP), San Diego, CA, pp 7.3.1-7.3.4, April 1984*

[BOH 85] **Böhme, J. F.**: 'Source parameter estimation by approximate maximum likelihood and non-linear regression', *IEEE J. Oceanic Eng. (special issue on beamforming) Vol. OE-10, pp 206-212, 1985*

[BOH 86] **Böhme, J. F.**: 'Estimation of spectral parameters of correlated signals in wavefields', *Signal Processing, Vol. 10, pp 329-337, 1986*

[BOR 79] **Borgiotti, G. V., Kaplan, L. J.**: 'Superresolution of uncorrelated interference sources by using adaptive array techniques', *IEEE Transactions on Antennas and Propagation, Vol. AP-27, No. 6, pp 842-845, November 1979*

[BRA 83] **Brandwood, D. H.**: 'A complex gradient operator and its application in adaptive array theory', *IEE Proceedings Pt. F: Commun, Radar & Signal Process., Vol. 138, No. 5, pp 11-16, February 1983*

[BRA 86] **Brandwood, D. H.**: 'Stable matrix inverse method for array DF using trapezoidal factorisation', *Electronics Letters, Vol. 22, No. 4, p 177, 13th February 1986*

[BUC 86a] **Buckley, K. M., Griffiths, L. J.**: 'Eigenstructure based broadband source location estimation', *Proceedings of the IEEE International Conference on Acoustics, Speech and Signal Processing (ICASSP), Tokyo, Vol. 3, pp 1869-1872, April 1986*

[BUC 86b] **Buckley, K. M., Griffiths, L. J.**: 'Direct broad-band array data processing for source location estimation', *Proc. IEEE 3rd Acoustics, Speech and Signal Processing Workshop on Spectrum Estimation and Modeling, pp 145-148, November 1986*

[BUC 87] **Buckley, K. M.**: 'Spatial/spectral filtering with linearly constrained minimum variance beamformers', *IEEE Transactions on Acoustics, Speech and Signal Processing, Vol. ASSP-35, No. 3, pp 249-266, March 1987*

[BUC 88] **Buckley, K. M., Griffiths, L. J.**: 'Broad-band signal-subspace spatial-spectrum (BASS-ALE) estimation', *IEEE Transactions on Acoustics, Speech and Signal Processing, Vol. ASSP-36, No. 7, pp 953-964, July 1988*

[BUR 82] **Burg, J. P., Luenberger, D. J., Wenger, D. L.**: 'Estimation of structured covariance matrices', *Proceedings of the IEEE, Vol. 70, pp 963-974, 1982*

[BUR 91] **Burdic, W. S.**: 'Underwater acoustic system analysis', Second edition, *Prentice-Hall Signal Processing Series, A. V. Oppenheim, Ed., Englewood Cliffs, New Jersey, 1991*

[BUR 67] **Burg, J. P.**: 'Maximum entropy spectral analysis', *Proc. 37th Annual Int. Meeting of the Society of Exploration of Geophysists, Orlando FL, 1967*

[BUR 68] **Burg, J. P.**: 'A new analysis technique for time series data' *NATO Advanced Study Institute on Signal Processing with Emphasis on Underwater Acoustics, Enschede, The Netherlands, 1968*

[BUR 72] **Burg, J. P.**: 'The relationship between maximum entropy spectra and maximum likelihood spectra', *Geophysics, Vol. 37, No. 2, pp 375-376, April 1972*

[BUR 75] **Burg, J. P.**: 'Maximum entropy spectral analysis', *Ph.D. dissertation, Dept. Geophys., Stanford Univ., Stanford, CA, 1975*

[BYR 87] **Byrne, C. L., Steele, A. K.**: 'Sector-focussed stability for high resolution array processing', *Proceedings of the IEEE International Conference on Acoustics, Speech and Signal Processing (ICASSP), Dallas, TX, pp 2340-2343, April 1987*

[CAD 81] **Cadzow, J. A., Ogino, R.**: 'Two-dimensional spectral estimation', *IEEE Transactions on Acoustics, Speech, and Signal Processing, Vol. ASSP-29, pp 396-401, 1981*

[CAD 88] **Cadzow, J. A.**: 'A high resolution direction-of-arrival algorithm for narrow-band coherent and incoherent sources', *IEEE Transactions on Acoustics, Speech, and Signal Processing, Vol. ASSP-36, pp 965-979, July 1988*

[CAP 69] **Capon, J.**: 'High resolution frequency wave number spectrum analysis', *Proc. IEEE, Vol. 57, pp 1408-1418, 1969*

[CAP 79] **Capon, J.**: 'Maximum-likelihood spectral estimation', *in Nonlinear methods of spectral analysis, S. Haykin, Ed., pp 155-179, Springer, New York, 1979*

[CHI 78] **Childers, D. G.** (Ed.): 'Modern spectrum analysis', *IEEE Press, New York, 1978*

[CLA 88] **Clarke, I. J.**: 'High-discrimination detection bound and model order control', *SPIE Proceedings, Vol. 975-33, Advanced Algorithms and Architectures for Signal Processing, III, pp 344-351, San-Diego, CA, 1988*

[CLA 91] **Clarke, I. J.**: 'Supervised interpretation of sampled data using efficient implementations of higher-rank spectrum estimation', *Chapter 2 in Advances in spectrum analysis and array processing, Vol. II, S. Haykin, Ed., pp 263-325, Prentice-Hall Inc., Englewood Cliffs, New Jersey, 1991*

[CLE 89] **Clergeot, H., Michel, O.**: 'New simple implementation of the coherent signal subspace method for wideband direction of arrival estimation', *Proceedings of the IEEE International Conference on Acoustics, Speech and Signal Processing (ICASSP), Glasgow, Scotland, Vol. 4, pp 2764-2767, May 1989*

[EDE 67] **Edelblute, D. J., Fisk, J. M., Kinnison, G. L.**: 'Criteria for optimum-signal-detection theory for arrays', *J. Acoust. Soc. Amer., Vol. 41, No. 1, pp 199-205, 1967*

[EVA 81] **Evans, J. E., Johnson, J. R., Sun, D. F.**: 'High resolution angular spectrum estimation techniques for terrain scattering analysis and angle of arrival estimation', *Proceedings of the IEEE Acoustics, Speech, Signal Processing and Spectral Estimation Workshop I, Hamilton, Ont., Canada, pp 134-139, 1981*

[EVA 82] **Evans, J. E., Johnson, J. R., Sun, D. F.**: 'Application of advanced signal processing techniques to angle of arrival estimation in ATC navigation and surveillance systems', *MIT Lincoln Lab., Technical Report 582, Lexington, MA, June 1982*

[FOR 87] **Forster, P., Vezzosi, G.**: 'Application of spheroidal sequences to array processing', *Proceedings of the IEEE International Conference on Acoustics, Speech and Signal Processing (ICASSP), Dallas, TX, pp 2267-2271, April 1987*

[GOL 80] **Golub, G. H., Van Loan, C. F.**: 'An analysis of the total least squares problem', *SIAM Journal of Numerical Analysis, Vol. 17, pp 883-893, 1980*

[GOL 84] **Golub, G. H., Van Loan, C. F.**: 'Matrix computations', *Baltimore, MD, John Hopkins University Press, 1984*

[HAY 91] **Haykin, S.**: 'Adaptive filter theory', *2nd edition, Prentice-Hall Inc., Englewood Cliffs, New Jersey, 1991*

[HAY 92] **Haykin, S., Reilly, J. P., Kezys, V., Vertatschitsch, E.**: 'Some aspects of array signal processing', *IEE Proceedings Pt. F: Commun., Radar & Signal Process., Vol. 139, No. 1, pp 1-26, February 1992*

[HIN 72] **Hinich, M. J., Shaman, P.**: 'Parameter estimation for an r-dimensional plane wave observed with additive independent Gaussian errors', *Ann. Stat., Vol. 43, pp 153-169, 1972*

[HUN 83] **Hung, E., Turner, R.**: 'Fast beamforming algorithms for large arrays', *IEEE Trans. Aerosp. Electron. Syst., Vol. AES-19, pp 598-607, 1983*

[HUN 87] **Hung, H., Kaveh, M.**: 'On the statistical sufficiency of the coherently averaged covariance matrix for the estimation of the parameters of wideband sources', *Proceedings of the IEEE International Conference on Acoustics, Speech and Signal Processing (ICASSP), Dallas, Tx, Vol. 1, pp 33-36, April 1987*

[HUN 88] **Hung, H., Kaveh, M.**: 'Focusing matrices for coherent signal-subspace processing', *IEEE Transactions on Acoustics, Speech and Signal Processing, Vol. ASSP-36, No. 8, pp 1272-1281, August 1988*

[JAF 88] **Jaffer, A. G.**: 'Maximum likelihood direction finding of stochastic sources: a separable solution', *Proceedings of the IEEE International Conference on Acoustics, Speech and Signal Processing (ICASSP), New York, Vol. 5, pp 2893-2896, April 1988*

[JOH 82a] **Johnson, D. H., DeGraaf, S. R.**: 'Improving the resolution of bearing in passive sonar arrays by eigenvalue analysis', *IEEE Transactions on Acoustics, Speech and Signal Processing, Vol. ASSP-30, No. 4, pp 638-647, August 1982*

[JOH 82b] **Johnson, D. H**: 'The application of spectral estimation methods to bearing estimation problems', *Proceedings of the IEEE, Vol. 70, No. 9, pp 1018-1028, September 1982*

[JOH 86] **Johnson, R. L, Miner, G. E.**: 'Comparison of superresolution algorithms for radio direction finding', *IEEE Transactions on Aerospace and Electronic Systems, Vol. AES-22, No 4, pp 432-441, July 1986*

[KAU 75] **Kaufman, L.**: 'A variable projection method for solving separable nonlinear least squares problems', *BIT, Vol. 15, pp 49-57, 1975*

[KAV 91] **Kaveh, M., Wang, H.**: 'Threshold properties of narrow-band signal-subspace array processing methods', *Chapter 5 in Advances in spectrum analysis and array processing, Vol. II, S. Haykin, Ed., pp 263-325, Prentice-Hall Inc., Englewood Cliffs, New Jersey, 1991*

[KAY 81] **Kay, S. M., Marple, L. L.**: 'Spectrum analysis – a modern perspective', *Proc. IEEE, Vol. 69, pp 1380-1419, 1981*

[KRO 89] **Krolik, J., Swingler, D.**: 'Multiple broad-band source location using steered covariance matrices', *IEEE Transactions on Acoustics, Speech and Signal Processing, Vol. ASSP-37, No. 10, pp 1481-1494, October 1989*

[KRO 90] **Krolik, J., Swingler, D.**: 'Focused wideband array processing via spatial resampling', *IEEE Transactions on Acoustics, Speech and Signal Processing, Vol. ASSP-38, No. 2, pp 356-360, February 1990*

[KRO 91] **Krolik, J.**: 'Focused wide-band array processing for spatial spectral estimation', *Chapter 6 in Advances in spectrum analysis and array processing, Vol. II, S. Haykin, Ed., pp 221-267, Prentice-Hall Inc., Englewood Cliffs, New Jersey, 1991*

[KUM 83a] **Kumaresan, R., Tuft, D. W.**: 'Estimating the angles of arrival of multiple plane waves', *IEEE Transactions on Aerospace and Electronic Systems, Vol. AES-19, No 1, pp 134-139, January 1983*

[KUM 83b] **Kumaresan, R.**: 'On the zeros of the linear prediction-error filter for deterministic signals', *IEEE Transactions on Acoustics, Speech and Signal Processing, Vol. ASSP-31, No. 1, pp 217-220, February 1983*

[KUN 83] **Kung, S. Y., Bhaskar Rao, D. V., Arun, K. S.**: 'New state space and singular value decomposition based approximate modeling methods for harmonic retrieval', *Proceedings of the IEEE Acoustics, Speech, Signal Processing and Spectral Estimation Workshop II, pp 266-271,1983*

[KUN 86] **Kung, S. Y., Lo, C. K., Foka, R.**: 'A Toeplitz approximation approach to coherent source direction finding', *Proceedings of the IEEE International Conference on Acoustics, Speech and Signal Processing (ICASSP), Tokyo, Japan, April 1986*

[LAG 84] **Lagunas-Hernandez, M. A., Gasull-Llampallas, A.**: 'An improved maximum likelihood method for power spectral density estimation', *IEEE Transactions on Acoustics, Speech and Signal Processing, Vol. ASSP-32, No. 1, pp 170-173, February 1984*

[LAN 80] **Lang, S. W., McClellan, J. H.**: 'Frequency estimation with maximum entropy spectral estimators', *IEEE Transactions on Acoustics, Speech, and Signal Processing, Vol. ASSP-28, pp 716-724, 1980*

[LEE 88] **Lee, H. B., Wengrovitz, M. S.**: 'Improved high resolution direction-finding through use of homogeneous constraints', *Proc. IEEE ASSP Fourth Workshop Spectrum Estimation, Modeling, pp 152-157, August 1988*

[LIC 91] **Li, J., Compton, R. T.**: 'Angle and polarization estimation using ESPRIT with a polarization sensitive array', *IEEE Transactions on Antennas and Propagation, Vol. AP-39, No. 9, pp 1376-1383, September 1991*

[LIG 73] **Ligget, W. S.**: 'Passive sonar: fitting models to multiple time-series', *in Signal Processing (Proceedings of the NATO Advanced Study Institute on Signal Processing with particular reference to Underwater Acoustics, Loughborough, U.K., August 1972), J. W. R. Griffiths, P. L. Stocklin and C. Van Schooneveld, Eds., pp 327-345, Academic Press, London, 1973*

[LIV 90] **Li, F., Vaccaro, J.**: 'Analysis of min-norm and MUSIC with arbitrary array geometry', *IEEE Transactions on Aerospace and Electronic Systems, Vol. AES-26, No. 6, pp 976-985, November 1990*

[LIV 91] **Li, F., Vaccaro, J., Tufts, D. W.**: 'Performance analysis of the state-space realization (TAM) and ESPRIT algorithms for DOA estimation', *IEEE Transactions on Antennas and Propagation, Vol. AP-39, No. 3, pp 418-423, March 1991*

[MAK 75] **Makhoul, J.**: 'Linear prediction: A tutorial review', *Proc. IEEE, Vol. 63, pp 561-580, 1975*

[MAP 80] **Marple, S. L.**: 'A new autoregressive spectrum analysis algorithm', *IEEE Trans. Acoust., Speech, Signal Processing, Vol. ASSP-27, pp 441-454, 1980*

[MAT 89] **Mather, J. L.**: 'Characterisation of the iterative multi-parameter (IMP) algorithm', *Proceedings of the Institute of Acoustics, Vol. 11, Pt. 8, pp 189-197, 1989*

[MCD 79] **McDonough, R. N.**: 'Application of the maximum-likelihood method and the maximum entropy method in array processing', *in Nonlinear Methods of Spectral Analysis, S. Haykin, Ed., pp 181-243, Springer, New York, 1979*

[MES 90] **Messer, H., Rockah, Y.**: 'On the eigenstructure of the signal-only tempo-spatial covariance matrix of broad-band sources using a circular array', *IEEE Transactions on Acoustics, Speech and Signal Processing, Vol ASSP-38, No. 3, pp 557-559, March 1990*

[MIL 81] **Miller, E. K.**: 'Comments on "Resolution of coherent sources incident on a circular antenna array"', *Proceedings of the IEEE, Vol. 69, No. 1, pp 122-123, January 1981*

[MIR 55] **Mirsky, L.**: 'Linear algebra', *Oxford, New York, 1955*

[MOO 80] **Moody, M. P.**: 'Resolution of coherent sources incident on a circular antenna array', *Proc. IEEE, Vol. 68, No. 2, pp 276-277, February 1980*

[MUI 82] **Muirhead, R. J.**: 'Aspects of multivariate statistical theory', *John Wiley and Sons, 1982*

[NIC 82] **Nickel, U.**: 'Angular resolution of closely spaced targets with antenna arrays', *Dissertation, Fakultät für Elektrotechnik, RWTH, Aachen, 1982 (in German)*

[NIC 83] **Nickel, U.**: 'Superresolution by spectral line fitting', in Schüssler, H. W. (Ed.): 'Signal processing II. Theories and applications', *Elsevier Science Publishers BV, North-Holland, EURASIP, pp 645-648, 1983*

[NIC 87] **Nickel, U.**: 'Angular superresolution with phased array radar: a review of algorithms and operational constraints', *IEE Proceedings Pt. F: Commun., Radar & Signal Process., Vol. 134, No. 1, pp 53-59, February 1987*

[NIC 88] **Nickel, U.**: 'Algebraic formulation of Kumaresan-Tuft superresolution method, showing relation to ME and MUSIC methods', *IEE Proceedings Pt. F: Commun., Radar & Signal Process., Vol. 135, No. 1, pp 7-10, February 1988*

[OTT 88] **Ottersten, B., Kailath, T.**: 'Wideband direction-of-arrival estimation using the ESPRIT algorithm', *Proceedings of the IEEE International Conference on Acoustics, Speech and Signal Processing (ICASSP), New York, Vol. 5, pp 2666-2669, April **1988***

[OTT 89] **Ottersten, B., Viberg, M.**: 'Analysis of subspace fitting based methods for sensor array processing', *Proceedings of the IEEE International Conference on Acoustics, Speech and Signal Processing (ICASSP), Glasgow, Scotland, Vol. 4, pp 2807-2810, May **1989***

[OTT 90a] **Ottersten, B., Kailath, T.**: 'Direction-of-arrival estimation for wide-band signals using the ESPRIT algorithm', *IEEE Transactions on Acoustics, Speech, and Signal Processing, Vol. ASSP-38, No. 2, pp 317-327, February **1990***

[OTT 90b] **Ottersten, B., Viberg, M.**: 'Asymptotic robustness of sensor array processing methods', *Proceedings of the IEEE International Conference on Acoustics, Speech and Signal Processing (ICASSP), Albuquerque, New Mexico, Vol. 5, pp 2635-2638, April **1990***

[OTT 91] **Ottersten, B., Viberg, M., Kailath, T.**: 'Performance analysis of the total least squares ESPRIT algorithm', *IEEE Transactions on signal processing, Vol. SP-39, No. 5, pp 1122-1135, May **1991***

[OTT 92] **Ottersten, B., Viberg, M., Kailath, T.**: 'Analysis of subspace fitting and ML techniques for parameter estimation from sensor array data', *IEEE Transactions on signal processing, Vol. SP-40, No. 3, pp 590-599, March **1992***

[OWS 81] **Owsley, N. L., Swope, G.**: 'Time delay estimation in a sensor array', *IEEE Transactions on Acoustics, Speech, and Signal Processing, Vol. ASSP-29, pp 519-523, June **1981***

[OWS 85] **Owsley, N. L.**: 'Signal subspace based minimum-variance spatial array processing', *Proc. 19th Asilomar Conf. Circuits, Syst., Comput., Asilomar, CA, pp 94-97, November **1985***

[PAR 85] **Parthasarathy, S., Tufts, D.**: 'Maximum-likelihood estimation of parameters of exponentially damped sinusoids', *Proc. IEEE, Vol. 73, pp 1528-1530, **1985***

[PAU 85] **Paulraj, A., Roy, R., Kailath, T.**: 'Estimation of signal parameters via rotational invariance techniques – ESPRIT', *Proceedings of the 19th Asilomar Conference on Circuits, Systems and Computers pp 83-89, Asilomar, CA, November **1985***

[PAU 86] **Paulraj, A., Roy, R., Kailath, T.**: 'A subspace rotation approach to signal parameter estimation', *Proceedings of the IEEE, Vol. 74, No. 7, pp 1044-1045, July 1986*

[PIL 89a] **Pillai, S. U., Kwon, B. H.**: 'Forward-backward spatial smoothing techniques for the coherent signal identification', *IEEE Transactions on Acoustics,Speech, and Signal Processing, Vol. ASSP-37, No. 1, pp 8-15, January 1989*

[PIL 89b] **Pillai, S. U., Kwon, B. H.**: 'Performance analysis of MUSIC-type high resolution estimators for direction finding in correlated and coherent scenes', *IEEE Transactions on Acoustics, Speech, and Signal Processing, Vol. ASSP-37, No. 8, pp 1176-1189, August 1989*

[PIS 72] **Pisarenko, V. F.**: 'On the estimation of spectra by means of non-linear functions of the covariance matrix', *Geophys. J. R. Astron. Soc., Vol. 28, pp 511-531, 1972*

[PIS 73] **Pisarenko, V. F.**: 'The retrieval of harmonics from a covariance function', *Geophys. J. Roy. Aastron. Soc., Vol. 33, pp 347-366, 1973*

[RAO 73] **Rao, C. R.**: 'Linear statistical inference and its applications', *2nd edition, John Wiley and Sons, New York, 1973*

[RAO 88] **Rao, B. D., Hari, K. V. S.**: 'Performance analysis of subspace based methods', *Proceedings of IEEE 4th Acoustics, Speech and Signal Processing Workshop on Spectrum Estimation and Modeling, pp 92-97, August 1988*

[RAO 89] **Rao, B. D., Hari, K. V. S.**: 'Performance analysis of ESPRIT and TAM in determining the direction of arrival of plane waves in noise', *IEEE Transactions on Acoustics, Speech, and Signal Processing, Vol. ASSP-37, No. 12, pp 1990-1995, December 1989*

[RAO 90] **Rao, B. D., Hari, K. V. S.**: 'Effect of spatial smoothing on the performance of MUSIC and the minimum-norm method', *IEE Proceedings. Pt. F: Commun., Radar & Signal Process., Vol. 137, No. 6, pp 449-458, December 1990*

[RED 79] **Reddi, S. S.**: 'Multiple source location – a digital approach', *IEEE Transactions on Aerospace and Electronic Systems, Vol. 15, No. 1, pp 95-105, January 1979*

[REI 82] **Reilly, J. P., Haykin, S.**: 'Maximum-likelihood receiver for low-angle tracking radar. Part 2: the nonsymmetric case', *IEE Proceedings Pt F: Commun., Radar & Signal Process., Vol. 129, No. 5, pp 331-340, 1982*

[RIS 78] **Rissanen, J.**: 'Modelling by shortest data description', *Automatica (GB), Vol. 14, pp 465-475, 1978*

[ROC 88] **Rockah, Y., Messer, H.**: 'Broadband source direction estimation using a circular array', *Proceedings of the IEEE International Conference on Acoustics, Speech and Signal Processing (ICASSP), New York, Vol. 5, pp 2654-2657, April 1988*

[ROY 86a] **Roy, R., Paulraj, A., Kailath, T.**: 'Direction-of-arrival estimation by subspace rotation methods - ESPRIT', *Proceedings of the IEEE International Conference on Acoustics, Speech and Signal Processing (ICASSP), Vol. 4, Tokyo, Japan, pp 2495-2498, April 1986*

[ROY 86b] **Roy, R., Paulraj, A., Kailath, T.**: 'ESPRIT – a subspace rotation approach to estimation of parameters of cisoids in noise', *IEEE Transactions on Acoustics, Speech, and Signal Processing, Vol. ASSP-34, No. 10, pp 1340-1342, October 1986*

[ROY 87] **Roy, R., H.**: 'ESPRIT, estimation of signal parameters via rotational invariance techniques', *Ph.D, dissertation, Stanford University, Stanford, CA, August 1987*

[ROY 89] **Roy, R., H., Kailath, T.**: 'ESPRIT - estimation of signal parameters via rotational invariance techniques', *IEEE Transactions on Acoustics, Speech, and Signal Processing, Vol. ASSP-37, No. 7, pp 984-995, November 1989*

[SAN 85] **Sandkühler, U., Böhme, J. F.**: 'Location and power estimation of multiple sources by non-linear regression', *Proceedings of the international conference on array signal processing, Loughborough, UK, 1985*

[SAN 87] **Sandkühler, U., Böhme, J. F.**: 'Accuracy of maximum likelihood estimates for array processing', *Proceedings of the IEEE International Conference on Acoustics, Speech and Signal Processing (ICASSP), Dallas, TX, pp 2015-2018, April 1987*

[SCH 68] **Schweppe, F. C.**: 'Sensor array data processing for multiple signal sources', *IEEE Transactions on Information Theory, Vol. IT-14, pp 294-305, 1968*

[SCH 79] **Schmidt, R. O.**: 'Multiple emitter location and signal parameter estimation', *IEEE Transactions on Antennas and Propagation, Vol. AP-34, No. 3, pp 276-280, March 1986*
[reprinted from: RADC Spectrum Estimation Workshop, Griffiss AFB, NY, pp 243-258, 1979]

[SCH 81] **Schmidt, R. O.**: 'A signal subspace approach to multiple emitter location and spectral estimation', *Ph.D. dissertation, Stanford University, Stanford, CA, November 1981*

[SHA 85] **Shan, T. J., Wax, M., Kailath, T.**: 'On spatial smoothing for direction-of-arrival estimation of coherent signals', *IEEE Transactions on Acoustics, Speech and Signal Processing, Vol. ASSP-33, No. 4, pp 806-811, August 1985*

[SHA 88a] **Shaw, A. K., Kumaresan, R.**: 'Some structured matrix approximation problems', *Proceedings of the IEEE International Conference on Acoustics, Speech and Signal Processing (ICASSP), New York, NY, Vol. 5, pp 2324-2327, April 1988*

[SHA 88b] **Sharman, K.**: 'Maximum likelihood estimation by simulated annealing', *Proceedings of the IEEE International Conference on Acoustics, Speech and Signal Processing (ICASSP), New York, NY, pp 2741-2744, April 1988*

[SHA 89] **Sharman, K., McClurkin, G. D.**: 'Genetic algorithms for maximum likelihood parameter estimation', *Proceedings of the IEEE International Conference on Acoustics, Speech and Signal Processing (ICASSP), Glasgow, Scotland, pp 2716-2719, May 1989*

[STO 89] **Stoica, P., Nehorai, A.**: 'MUSIC, maximum likelihood and Cramér-Rao bound', *IEEE Transactions on Acoustics, Speech and Signal Processing, Vol. ASSP-37, No. 5, pp 720-741, May 1989*

[STO 90a] **Stoica, P., Sharman, K. C.**: 'Maximum likelihood methods for direction-of-arrival estimation', *IEEE Transactions on Acoustics, Speech and Signal Processing, Vol. ASSP-38, No. 7, pp 1132-1143, July 1990*

[STO 90b] **Stoica, P., Nehorai, A.**: 'Performance study of conditional and unconditional direction-of-arrival estimation', *IEEE Transactions on Acoustics, Speech and Signal Processing, Vol. ASSP-38, No. 10, pp 1783-1795, October 1990*

[STO 91] **Stoica, P., Nehorai, A.**: 'Statistical efficiency study of direction estimation methods', *Chapters 7 and 8 in Advances in spectrum analysis and array processing, Vol. II, S. Haykin, Ed., pp 263-325, Prentice-Hall Inc., Englewood Cliffs, New Jersey, 1991*

[SUM 83] **Su, G., Morf, M.**: 'Signal subspace approach for multiple wide-band emitter location', *IEEE Transactions on Acoustics, Speech and Signal Processing, Vol. ASSP-31, No. 6, pp 1502-1522, December 1983*

[SWI 88] **Swingler, D. N., Walker, R. S., Krolik, J.**: 'High-resolution broadband beamforming using a doubly-steered coherent signal-subspace approach', *Proceedings of the IEEE International Conference on Acoustics, Speech and Signal Processing (ICASSP), New York, NY, Vol. 5, pp 2658-2661, April 1988*

[SWI 89] **Swingler, D. N., Krolik, J.**: 'Source location bias in the coherently focused high-resolution broad-band beamformer', *IEEE Transactions on Acoustics, Speech and Signal Processing, Vol. ASSP-37, No. 1, pp 143-145, January 1989*

[TUF 82] **Tufts, D. W., Kumaresan, R.**: 'Estimation of frequencies of multiple sinusoids: making linear prediction perform like maximum likelihood', *Proceedings of the IEEE, Vol 70, pp 975-989, September 1982*

[URI 83] **Urick, R. J.**: 'Principles of underwater sound', Third edition, *McGraw-Hill Book Company, New York, 1983*

[VAC 89] **Vaccaro, L. F., Tuft, D. W.**: 'Min-norm linear prediction for arbitrary sensor array', *Proceedings of the IEEE International Conference on Acoustics, Speech and Signal Processing (ICASSP), Glasgow, Scotland, pp 2613-2616, May 1989*

[VAN 68] **Van Trees, H. L.**: 'Detection, estimation and linear modulation theory', *Part 1 of Detection, estimation and modulation theory, John Wiley and Sons Inc., New York, 1968*

[VAN 88] **Van Veen, B., Williams, B.**: 'structured covariance matrices and dimensionality reduction in array processing', *IEEE ASSP Fourth Workshop Spectrum Estimation Modeling, pp 168-171, August 1988*

[VIB 91a] **Viberg, M., Ottersten, B.**: 'Sensor array processing based on subspace fitting', *IEEE Transactions on Signal Processing, Vol. SP-39, No. 5, pp 1110-1121, May 1991*

[VIB 91b] **Viberg, M., Ottersten, B., Kailath, T.**: 'Detection and estimation in sensor arrays using weighted subspace fitting', *IEEE Transactions on Signal Processing, Vol. SP-39, No. 11, pp 2436-2449, November 1991*

[WAN 85] **Wang, H., Kaveh, M.**: 'Coherent signal-subspace for the detection and estimation of angles of arrival of multiple wide-band sources', *IEEE Transactions on Acoustics, Speech, and Signal Processing, Vol. ASSP-33, No. 4, pp 823-831, August 1985*

[WAN 87] **Wang, H., Li, C. C., Zhu, J. X.**: 'High-resolution direction finding in the presence of multipath: a frequency-domain smoothing approach', *Proceedings of the IEEE International Conference on Acoustics, Speech and Signal Processing (ICASSP), Dallas, TX, pp 2276-2279, April 1987*

[WAX 83] **Wax, M., Kailath, T.**: 'Optimum localization of multiple sources by passive arrays', *IEEE Transactions on Acoustics, Speech, and Signal Processing, Vol. ASSP-31, No. 5, pp 1210-1218, October 1983*

[WAX 84] **Wax, M., Shan, T. J., Kailath, T.**: 'Spatio-temporal spectral analysis by eigenstructure methods', *IEEE Transactions on Acoustics, Speech, and Signal Processing, Vol. ASSP-32, No. 4, pp 817-827, August 1984*

[WAX 85a] **Wax, M.**: 'Detection and estimation of superimposed signals', *Ph.D dissertation, Stanford University, Stanford, CA, March 1985*

[WAX 85b] **Wax, M., Kailath, T.**: 'Detection of signals by information theoretical criteria', *IEEE Transactions on Acoustics, Speech, and Signal Processing, Vol. ASSP-33, No. 2, pp 387-392, April 1985*

[WAX 89] **Wax, M., Ziskind, I.**: 'Detection of the number of coherent signals by the MDL principle', *IEEE Transactions on Acoustics, Speech, and Signal Processing, Vol. ASSP-37, No. 8, pp 1190-1196, August 1989*

[WAX 91] **Wax, M.**: 'Detection and localization of multiple sources via the stochastic signals model', *IEEE Transactions on Signal Processing, Vol. SP-39, No. 11, pp 2450-2456, November 1991*

[WEN 62] **Wenz, G. M.**: 'Acoustic ambient noise in the ocean: spectra and sources', *Journal of Acoustic Society of America, Vol. 34, No. 12, pp 1936-1956, December 1962*

[WHA 71] **Whalen, A. D.**: 'Detection of signals in noise', *Academic Press, New York, 1971*

[WIL 88] **Williams, R. T., Prasad, S., Mahalanabis, A. K., Sibul, L. H.**: 'An improved spatial smoothing technique for bearing estimation in a multipath environment', *IEEE Transactions on Acoustics, Speech, and Signal Processing, Vol. ASSP-36, No. 4, pp 425-432, April 1988*

[WYL 75] **Wylie, C. R.**: 'Advanced engineering mathematics', *4th edition, McGraw-Hill Inc., New York 1975*

[XUB 89] **Xu, X. L., Buckley, K M.**: 'A statistical performance comparison of MUSIC in element-space and beam-space', *Proceedings of the IEEE International Conference on Acoustics, Speech and Signal Processing (ICASSP), Glasgow, Scotland, pp 2124-2127, May 1989*

[XUB 90] **Xu, X. L., Buckley, K M.**: 'A comparison of element and beam space spatial-spectrum estimation for multiple source clusters', *Proceedings of the IEEE International Conference on Acoustics, Speech and Signal Processing (ICASSP), Albuquerque, New Mexico, Vol. 5, pp 2643-2646, April, 1990*

[YAN 87] **Yang, J. F., Kaveh, M.**: 'Wideband adaptive arrays based on the coherent signal-subspace transformation', *Proceedings of the IEEE International Conference on Acoustics, Speech and Signal Processing (ICASSP), Dallas, TX, Vol. 4, pp 2011-2014, April 1987*

[ZEY 91] **Zeytinoğlu, M., Litva, J., Qian, J.**: 'High-resolution direction finding using circular arrays', *Proceedings of the IEEE International Conference on Acoustics, Speech and Signal Processing (ICASSP), Toronto, Ontario, Vol. 5, pp 3341-3344, May 1991*

[ZIS 87] **Ziskind, I., Wax, M.**: 'Maximum likelihood estimation via the alternating projection maximization algorithm', *Proceedings of the IEEE International Conference on Acoustics, Speech and Signal Processing (ICASSP), Dallas, TX, Vol. 4, pp 2280-2283, April 1987*

[ZIS 88] **Ziskind, I., Wax, M.**: 'Maximum localization of multiple source by alternating projection', *IEEE Transactions on Acoustics, Speech, and Signal Processing, Vol. ASSP-36, No. 10, pp 1553-1560, October 1988*

[ZIS 90] **Ziskind, I., Wax, M.**: 'Resolution enhancement by periodicity constrAints', *IEEE Transactions on Acoustics, Speech, and Signal Processing, Vol. ASSP-38, No. 4, pp 687-694, April 1990*

[ZOL 87a] **Zoltowski, M. D.**: 'Solving the semi-definite generalized eigenvalue problem with application to ESPRIT', *Proceedings of the IEEE International Conference on Acoustics, Speech and Signal Processing (ICASSP), Dallas, Tx, Vol. 4, pp 2316-2319, April 1987*

[ZOL 87b] **Zoltowski, M. D.**: 'Solving the generalized eigenvalue problem with singular forms', *Proceedings of the IEEE, Vol. 75, No. 11, pp 1546-1548, November 1987*

A. ABBREVIATIONS AND SYMBOLS

A.1 LIST OF ABBREVIATIONS

AAR	Adaptive Angular Response method – see chapter 5, sub-section 5.2.3
AIC	Akaike's Information Criterion – see chapter 5, sub-section 5.2.9
BASS-ALE	Broad-bAnd Signal subspace Spatial spectrAL Estimation methods – see chapter 5, sub-section 5.2.7
CRLB	Cramér-Rao Lower Bound – see chapter 5, sub-section 5.2.1
CSS	Coherent Signal Subspace methods – see chapter 5, sub-section 5.2.7
CW	Continuous Wave (monotonic)
DF	direction finding
DFT	Discrete Fourier Transform
DML	Deterministic Maximum Likelihood method – see chapter 5, sub-section 5.2.6
DOA	Direction Of Arrival (of signals relative to the array)
ERP	Effective radiated power – see footnote 2 in chapter 2
ESPRIT	Estimation of Signal Parameters via Rotational Invariance Techniques – see chapter 5, sub-section 5.2.5
FIR	Finite Impulse Response (refers to a non-recursive digital filter)
FM	Frequency Modulation – see in connection with the response to a linear FM pulse in chapter 2, section 2.3 and in appendix B.1
HF	High Frequency (3 – 30 MHz)
IDFT	Inverse Discrete Fourier Transform
IIR	Infinite Impulse Response (refers to a recursive digital filter)
IMP	Iterative Multi-Parameter method – see chapter 5, sub-section 5.2.6
LS	Least Squares – see in connection with LS-ESPRIT in chapter 5, sub-section 5.2.5
MDL	Minimum Description length – see chapter 5, sub-section 5.2.9
ME	Maximum Entropy (Burg's method) – see chapter 5, sub-section 5.2.4
ML	Maximum Likelihood method – see chapter 5, sub-section 5.2.6
MN	Minimum Norm method (also known as the TK method) – see chapter 5, sub-section 5.2.4

MLM	Maximum Likelihood Method (former name for Capon's method) – see chapter 5, sub-section 5.2.4
MUSIC	MUltiple SIgnal Classification method – see chapter 5, sub-section 5.2.4
MVDR	Minimum Variance Distortionless Response (Capon's method) – see chapter 5, sub-section 5.2.4
MVIR	Minimum Variance Inverse Response – see chapter 5, sub-section 5.2.4
MVPR	Minimum Variance Protected Response – see chapter 5, sub-section 5.2.4
PDF	Probability Density Function
RMS	Root Mean Square – see in connection with rms sidelobes in chapter 4, sections 4.2 to 4.4
SML	Stochastic Maximum Likelihood method – see chapter 5, sub-section 5.2.6
STCM	STeered Covariance Matrix technique – see chapter 5, sub-section 5.2.7
SNR	Signal to Noise Ratio
SPM	Sectoral Phase Mode – see chapter 3, section 3.5
TAM	Toeplitz Approximation Method – see chapter 5, sub-section 5.2.5
TLS	Total Least Squares – see in connection with TLS-ESPRIT in chapter 5, sub-section 5.2.5
TSCM	Tempo-Spatial Covariance Matrix – see chapter 5, sub-section 5.2.7
UHF	Ultra High Frequency (300 – 3000 MHz)
VHF	Very High Frequency (30 – 300 MHz)
WSF	Weighted Subspace Fitting – see chapter 5, sub-section 5.2.6

A.2 LIST OF SYMBOLS

$[\cdot]^{-1}$	inverse of a matrix
$[\cdot]^{*}$	complex conjugate of a scalar, a vector or a matrix
$[\cdot]^{T}$	transpose of a vector or a matrix
$[\cdot]^{H}$	transpose conjugate of a vector or a matrix
$[\cdot]^{-H}$	inverse of the transpose conjugate matrix
$\lvert\cdot\rvert$	determinant of a matrix, Euclidean norm of a vector, absolute value of a scalar
$\lVert\cdot\rVert_F$	Frobenius norm of a matrix: $\lVert\mathbf{A}\rVert_F^2 = \mathrm{tr}(\mathbf{A}^H\mathbf{A})$
$\lceil\cdot\rceil$	ceiling of (smallest integer larger than) an expression
$[x]_{\mathrm{mod}\,2\pi}$	modulo-2π value of a real number x
$\boldsymbol{0}$	null vector
$\mathbf{0}$	null matrix
a_m	complex weighting applied to the m'th array element – see *(2.2.2)* and *(2.3.5)* in chapter 2
$a_{mk}(t)$	steering impulse response of the m'th array sensor in the direction of the k'th far-field source – see chapter 5, sub-section 5.2.2
$A(\varphi)$	amplitude pattern of a sectoral phase mode – see chapter 3, section 3.5
A	signal amplitude – see appendix C.1
$\mathbf{A}(\omega)$	array steering matrix, equals to $\mathbf{A}(\boldsymbol{\varphi}=\boldsymbol{\phi}, \omega)$ – see chapter 5, sub-section 5.2.2
A_{mk}	mk'th element of the steering matrix $\mathbf{A}$
$\tilde{\mathbf{A}}$	mode-space steering matrix – see chapter 5, sub-section 5.3.2
$\bar{\mathbf{A}}$	combined ESPRIT steering matrix – see chapter 5, sub-section 5.2.5
$\mathbf{A}_x$, $\mathbf{A}_y$	ESPRIT sub-array steering matrix – see chapter 5, sub-section 5.2.5
$\boldsymbol{A}$	steering vector – see chapter 5, sub-section 5.2.4
$\mathbf{A}(\boldsymbol{\varphi}, \omega)$	functional form of steering matrix – see footnote 1 in chapter 5, sub-section 5.2.2
$\underset{\boldsymbol{\varphi}}{\mathrm{argmax}}\,\mathcal{F}(\boldsymbol{\varphi})$	maximising vector $\boldsymbol{\varphi}$ in the expression $\mathcal{F}(\boldsymbol{\varphi})$
$\underset{\boldsymbol{\varphi}}{\mathrm{argmin}}\,\mathcal{F}(\boldsymbol{\varphi})$	minimising vector $\boldsymbol{\varphi}$ in the expression $\mathcal{F}(\boldsymbol{\varphi})$
$\{\boldsymbol{b}_q\}$	vectors defined in appendix C.3
$\mathbf{B}$	constraint matrix in an MVIR algorithm – see chapter 5, sub-section 5.2.4, TAM sub-matrix comprising the top rows of $\mathbf{A}$ – see *(5.2.80)* in chapter 5, spatial-smoothing sub-matrix comprising the top M'' rows of $\tilde{\mathbf{A}}$ – see *(5.4.1)* in chapter 5

b	vector of least Euclidean norm whose first element equals to one, that belongs to the noise subspace – see chapter 5, sub-section 5.2.4
c	speed of propagation
C_D, C_S	asymptotic DML and SML DOA error covariance matrices – see chapter 5, sub-section 5.2.6
$C_{\mu q}(\omega, \theta)$	q'th order coefficient for the μ'th phase-mode – see chapter 2, section 2.4
$\boldsymbol{C}_q$	the vector $[C_{(-\Lambda)q}, \cdots, C_{0q}, \cdots, C_{\Lambda q}]^t$ – see *(C.3.6)* in appendix C.3
$C_{\mu n}$	unaliased component of $\mathcal{D}_\mu(e^{j\omega_n \Delta t})$ – see *(C.4.1)* in appendix C.4
cov ($\boldsymbol{u}$)	covariance matrix of a random vector $\boldsymbol{u}$
d	inter-element spacing in a uniformly-spaced linear array – see *(3.2.2)* in chapter 3
$\{ d_{\mu k} \}_k$	(inverse) DFT coefficients of $\{ \mathcal{D}_\mu(e^{j2\pi n/N}) \}_n$ – see *(3.6.21)* in chapter 3
$\mathbf{D}$	block matrix defined by *(E.4.3)* in appendix E.4
$\mathcal{D}_\mu(z)$	transfer function of FIR block in IIR mode-alignment filter – see *(3.6.18)* in chapter 3
det[·]	determinant of a matrix
diag($\boldsymbol{z}$)	diagonal matrix whose main diagonal comprises the elements of $\boldsymbol{z}$
$\mathcal{E}$	general cost function in a minimisation process, DOA estimation error defined by *(C.1.1)* in appendix C.1
$\boldsymbol{E}$	delay-only steering vector – see expression *(5.2.22)* in chapter 5, sub-section 5.2.3
$\mathbf{E}_\mu$	$M \times M$ diagonal mode-phasing matrix defined by *(4.5.13)* in chapter 4
$\mathbf{E}$	mode-phasing matrix as defined by *(5.3.2)* in chapter 5, sub-section 5.3.2
$\boldsymbol{E}_\mu$	a column of $\mathbf{E}$ – see definition *(5.3.2)* sub-section 5.3.2
$\boldsymbol{\mathcal{E}}(\cdot)$	expectation operator
e^z	exponential function
$f_{\boldsymbol{u}}(\boldsymbol{u})$	probability density function of a random vector $\boldsymbol{u}$
$f_{\boldsymbol{u}}(\boldsymbol{u}\|\boldsymbol{\phi})$	conditional probability density function of a random vector $\boldsymbol{u}$, given the second random vector $\boldsymbol{\phi}$ – see chapter 5, sub-section 5.2.1
$F(\theta, \varphi, \omega)$	far-field (steady-state) array radiation pattern – see *(2.2.2)*, *(2.3.5)* in chapter 2
$F_m(\varphi)$	(nominal) mode-space beam pointing in direction $2\pi m/M$ – see *(3.2.3)* in chapter 3
$\tilde{F}_m(\varphi)$	nominal mode-space beam $F_m(\varphi)$ at a modified array radius – see chapter 4, section 4.4
$\mathcal{F}_m(\varphi)$	perturbed mode-space beam pointing in direction $2\pi m/M$ – see chapter 4, sections 4.2, 4.3, 4.4

$|\Delta F|^2, |\Delta F_m|^2$ rms error pattern – see chapter 4, sections 4.2, 4.3, 4.4

$\boldsymbol{F}$ $L\times 1$ array far-field pattern vector – see *(4.5.4)* in chapter 4

$F_\nu^{m\Lambda_0}(\varphi)$ a sectoral phase mode pointing in direction $2\pi m/M$, having an effective mode number of ν – see chapter 3, section 3.5

$\mathbf{G}$ $L\times M$ element pattern matrix – see *(4.5.5)* in chapter 4, block matrix defined by *(E.4.7)* in appendix E.4

$\bar{\mathbf{G}}, \bar{\mathbf{G}}^H, \overline{\mathbf{G}^H\mathbf{G}}$ frequency and elevation averaged matrices, defined by *(4.7.3)* - *(4.7.5)* in chapter 4

$g(\theta, \varphi)$ (frequency-independent) element (voltage) pattern shared by all the array elements

$g_m(\theta, \varphi, \omega)$ element (voltage) pattern for the m'th array element

$g_\theta(\theta)\, g_\phi(\varphi)$ separable element pattern – see appendix C.3

$\mathcal{G}$ array gain factor defined by *(4.2.8)* in chapter 4

$\mathbf{H}$ hermitian square root of $\mathbf{R}_{\boldsymbol{\nu}}$ – see chapter 5, sub-section 5.52, and also *(E.1.3)* in appendix E.1

$h_i(\theta)$ the i'th angular Fourier coefficient of an element pattern – see *(2.2.4)* in chapter 2

$\boldsymbol{h}$ the vector $[h_{-I} \cdots h_{-1}\ h_0\ h_1 \cdots h_I]^T$ – see *(C.3.5)* in appendix C.3

$\{ h_{\mu k} \}_k$ (inverse) DFT of $\{ 1/\mathcal{D}_\mu(e^{j2\pi n/N}) \}_n$ – see *Fig. 3.6.5* in chapter 3

$\mathcal{H}_{\mu n}$ complex weights in an FIR mode-alignment filter – see *(3.2.4)* in chapter 3

$\mathcal{H}_\mu(z)$ transfer function of IIR mode-alignment filter – see *(3.6.20)* in chapter 3

$H_\mu(s)$ transfer function of an analogue deconvolution filter for phase mode coefficients – see chapter 3, section 3.6

i index referring to the i'th angular Fourier coefficient of an element pattern – see *(2.2.4)*,
index in the range $0 \le i \le M\text{-}1$ referring to the i'th eigenvalue (in decreasing order) or corresponding eigenvector of the covariance matrix

I the order of the highest non-vanishing term in the angular Fourier-series representation *(2.2.4)* for the element-patterns

$\mathbf{I}$ identity matrix

I_0 first column of $\mathbf{I}$

$I_\nu(x)$ modified Bessel function of the first kind of order ν and argument x

Int (x) integer part of the real number x

j square root of -1

$\mathbf{J}$ Fisher information matrix – see chapter 5, sub-section 5.2.1

$\mathbf{J}_D^{-1}$, $\mathbf{J}_S^{-1}$ CRLB matrices for the deterministic and stochastic signal model – see chapter 5, sub-sections 5.2.1 and 5.2.6

$J_{k'k''}$ $k'k''$'th element of $\mathbf{J}$ – see chapter 5, sub-section 5.2.1

$J_\nu(x)$	Bessel function of the first kind of order ν and argument x
$\hat{J}_\nu(t)$	(inverse) Fourier transform of $J_\nu(\omega R/c)$ – see *(3.6.9)* in chapter 3
$\mathbf{J}_q$	$(2\Lambda+1)\times(2I+1)$ matrix of coefficients of the q'th terms in the series expressions for a set of phase modes $\{\Phi_\mu(\theta, \phi, \omega)\}_{\mu=-\Lambda}^{\Lambda}$ – see *(C.3.7)* in appendix C
k_x	function defined by *(3.5.2)* in chapter 3 as: $k_x = \mathrm{Int}(\lvert x\rvert + 1/2)$
k	index in the range $0 \le k \le K-1$ referring to the k'th far-field source in a multiple-source environment – see chapter 5
K	number of far-field signal sources in a multiple-source environment – see chapter 5
K'	rank of $\mathbf{R_S}$: $K' = K - K_0$ – see chapter 5, sub-section 5.2.6-d
K_0	rank deficiency of $\mathbf{R_S}$ – see chapter 5, sub-section 5.4.2
K_e	effective rank – see chapter 5, sub-section 5.2.7
$K_q(\omega, \theta, \varphi)$	coefficient of the q'th term in the series expression for the radiation beam of a co-phased uniformly excited array – see *(2.2.14)* in chapter 2
$\mathbf{K}$	$M\times M$ diagonal co-phase weighting matrix – see chapter 4, section 4.5
ℓ	index in the range $0 \le \ell \le L-1$ referring to the ℓ'th angular sample of an array pattern – see *(4.5.1)* in chapter 4, (frequency-) index of the Fourier series coefficients in the range $\ell_{LO} \le \ell \le \ell_{HI}$ – see chapter 5, sub-section 5.2.2
ℓ_{LO}, ℓ_{HI}	lower and upper (frequency-) index defining the passband for the Fourier series coefficients – see chapter 5, sub-section 5.2.2
L	Number of points at which an array pattern is sampled – see chapter 4, section 4.5
$\ln(\cdot)$	natural logarithm
m	index in the range $0 \le m \le M-1$ referring to the m'th array element
M	number of array elements
M'	number of processed phase modes: $M' = 1+2\Lambda$ – see chapter 5, sub-section 5.3.2, twice the number of sub-array sensors in ESPRIT – see chapter 5, sub-section 5.2.5
M''	number of phase-modes in a spatial-smoothing scheme subset – see chapter 5, sub-section 5.4.2, number of sub-array sensors in ESPRIT – see chapter 5, sub-section 5.2.5
$\max(\cdot)$	a number equal to the largest of a (parenthesised) set of real numbers
$\min(\cdot)$	a number equal to the smallest of a (parenthesised) set of real numbers
n	time index in the range $0 \le n \le N-1$

N order of FIR block in IIR mode alignment filter – see chapter 3, section 3.6,
number of combined modes in the synthesis of sharp nulls – see chapter 3, section 3.4 and appendix C.2
number of temporal snapshots – see chapter 5, sub-section 5.2.2

N_ω order of FIR mode alignment filter – see chapter 3, sections 3.2, 3.6

$\mathcal{N}(\varphi)$ sharp pattern null – see *(3.4.3)* and *(C.2.1)* in chapter 3 and in appendix C.2, respectively

$\mathcal{N}(\omega, \theta, \phi)$ spatial power density of ambient noise – see chapter 5, sub-section 5.3.2

$\{N_{n(\ell)}^{RE,\,IM}\}$ pseudo-random data set as described in chapter 5, sub-section 5.5.2

$\{N_n^{RE,\,IM}\}$ pseudo-random data vectors as described in chapter 5, sub-section 5.5.2

p coherence coefficient – see chapter 5, sub-section 5.5.2

$p(t)$ a pulse in the time domain – see *(2.3.2)* and *(B.1.1)* in chapter 2 and appendix B.1, respectively

$p_m(\theta, \varphi, t)$ time-domain signal received by the m'th array element – see *(B.1.2)* in appendix B.1

$\hat{p}_m(\theta, \varphi, \omega)$ frequency-domain signal received by the m'th array element – see *(B.1.6)* in appendix B.1

$P(\theta, \varphi, t)$ Summed time-domain response of full array – see *(2.3.6)* and *(B.1.4)* in chapter 2 and appendix B.1, respectively

$\hat{P}(\theta, \varphi, \omega)$ Summed frequency-domain response of full array – see *(2.3.4)* in chapter 2

$p_{k'k''}(\omega)$ $k'k''$'th element of $\mathbf{P}_s(\omega)$ – see definition *(E.5.2)* in appendix E.5

$\mathbf{P}(\omega)$ cross-spectral density matrix for the array outputs – see chapter 5, sub-section 5.2.2

$\hat{\mathbf{P}}$ estimated cross-spectral density matrix – see *(5.2.38)* in chapter 5

$\mathbf{P}_\varepsilon(\omega)$ cross-spectral density matrix for the sensor noises – see chapter 5, sub-section 5.2.2

$\tilde{\mathbf{P}}_{\varepsilon_a}(\omega)$ cross-spectral density matrix of phase-mode noises contributed by the ambient noise-field – see chapter 5, sub-section 5.3.2

$\mathbf{P}_s(\omega)$ cross-spectral density matrix for the source signals – see chapter 5, sub-section 5.2.2

$\mathcal{P}(\phi)$ dynamic power pattern of a conventional beamformer, or spectral power of a general scalar-search superresolution estimator – see chapter 5, sub-sections 5.2.3 and 5.2.4

$\mathcal{P}_B(\phi)$ spectral pattern for the Bartlett estimator – see chapter 5, sub-section 5.2.3

$\mathcal{P}(\Pi, \varphi)$ residual spatial spectral pattern of IMP estimator – see chapter 5, sub-section 5.2.6

q	index in the range $-Q \le q \le Q$ referring to the q'th term in the series expression for a phase mode pattern – see *(2.4.10), (C.3.8)* in chapter 2 and in appendix C, respectively
Q	maximum order of distortion terms assumed in the series expression for a phase mode
$\mathbf{Q}$	diagonal matrix defined by *(5.3.3)* in chapter 5
$\tilde{\mathbf{Q}}(\omega)$	diagonal matrix defined by *(5.4.11)* in chapter 5
R	circular array radius
$\mathcal{R}$	'radius' defined via *(2.2.6)* in chapter 2
Δr	range resolution – see appendix B.1
$\{r_m\}_m$	an ensemble of random fractional radial displacement errors – see chapter 4, section 4.4
$r_{k'k''}(\tau)$	$k'k''$'th element of $\mathbf{R}_s(\tau)$ – see definition *(E.5.2)* in appendix E.5
$\mathbf{R} = \mathcal{E}\mathbf{x}\mathbf{x}^H$	spatial covariance matrix of $\mathbf{x}(t)$ – see chapter 5, sub-section 5.2.2
$\hat{\mathbf{R}}$	estimated spatial covariance matrix – see expression *(5.2.37)* in chapter 5
$\mathbf{R}_y$	mode-space covariance matrix – see chapter 5, sub-section 5.3.2
$\mathbf{R}_v$	v'th spatial-smoothing sub-matrix of the mode-space covariance matrix – see chapter 5, sub-section 5.4.2
$\bar{\mathbf{R}}$	spatially-smoothed mode-space covariance matrix – see chapter 5, sub-section 5.4.2, covariance matrix for the combined ESPRIT array – see *(5.2.60)* in chapter 5
$\mathbf{R}_x$, $\mathbf{R}_{xy}$	sub-matrices of $\bar{\mathbf{R}}$ used in ESPRIT – see *(5.2.60)* in chapter 5
$\mathbf{R}_{yx}$, $\mathbf{R}_y$	sub-matrices of $\bar{\mathbf{R}}$ used in ESPRIT – see *(5.2.60)* in chapter 5
$\mathbf{R}_n$	covariance matrix of sensor noises: $\mathbf{R}_n = \mathcal{E}\mathbf{x}_n\mathbf{x}_n^H$ – see chapter 5, sub-section 5.2.2
$\tilde{\mathbf{R}}_n$	mode-space noise covariance matrix – see chapter 5, sub-section 5.3.2
$\bar{\mathbf{R}}_n$	noise covariance matrix for the combined ESPRIT array – see *(5.2.60)* in chapter 5
$\mathbf{R}_{nx}$, $\mathbf{R}_{nxy}$	sub-matrices of $\bar{\mathbf{R}}_n$ used in ESPRIT – see *(5.2.60)* in chapter 5
$\mathbf{R}_{nyx}$, $\mathbf{R}_{ny}$	sub-matrices of $\bar{\mathbf{R}}_n$ used in ESPRIT – see *(5.2.60)* in chapter 5
$\mathbf{R}_s$	covariance matrix of source signals: $\mathbf{R}_s = \mathcal{E}\mathbf{s}\mathbf{s}^H$ – see chapter 5, sub-section 5.2.2
$\mathbf{R}_s$	signal-only covariance matrix: $\mathbf{R}_s = \mathbf{A}\mathbf{R}_s\mathbf{A}^H$ – see chapter 5, sub-section 5.2.2
$\mathbf{R}_{sx}$, $\mathbf{R}_{sxy}$	sub-matrices of $[\bar{\mathbf{R}} - \sigma_n^2\bar{\mathbf{R}}_n]$ – see *(5.2.61), (5.2.62)* in chapter 5
$\bar{\mathbf{R}}_s$	signal covariance matrix modified by (mode-space) spatial smoothing see chapter 5, sub-section 5.4.2

rank[·]	rank (number of linearly-independent rows or columns) of a matrix
$S(\Omega)$	sampling window function – see *(3.6.6)* in chapter 3
$\hat{S}(t)$	Fourier transform of $S(\Omega)$ – see chapter 3, section 3.6
$s_k(t)$	signal radiated by the k'th far-field source in a multi-source environment – see chapter 5, sub-section 5.2.2
$\boldsymbol{s}(t)$	vector of signals radiated by the K far-field sources – see chapter 5, sub-section 5.2.2
$\boldsymbol{S}(\omega_\ell; t_n)$	ℓ'th Fourier series coefficient of $\boldsymbol{s}(t)$ over the n'th temporal sub-interval – see chapter 5, sub-section 5.2.2
$\{S_{kn(\ell)}^{RE,\,IM}\}$	pseudo-random data set as described in chapter 5, sub-section 5.5.2
sgn(·)	sign function – equals to 1 (-1) for a positive (negative) argument.
t	time variable
t_c, t_d	time delays referred to in chapter 2, section 2.3
t_m	compensated delay to m'th array element – see *(2.3.3)* in chapter 2
t_n	discrete time variable – see chapter 5, sub-section 5.2.2
Δt	temporal sampling interval, equals to $\Delta t = 2\pi/\omega_s$ – see chapter 3, section 3.6
T	pulse length – see chapter 2, section 2.3, sampling time – see chapter 5, sub-section 5.2.2
$\mathcal{T}(\varphi)$	target pattern for sharp null – see *(3.4.4)* and *(C.2.2)* in chapter 3 and in appendix C.2, respectively
$\mathbf{T}$	non-singular transformation matrix used in the development of (LS and TLS-) ESPRIT – see chapter 5, sub-section 5.2.5
$T_n(x)$	Chebyshev polynomial of the first kind of order n, defined as: $T_n(x) = \cos(n \cos^{-1} x)$
u	a post-DFT correction vector of weights $\{u_\mu\}_\mu$ – see chapter 4, section 4.6, observed sample vector – see chapter 5, sub-sections 5.2.1, 5.2.2
$\boldsymbol{u}$	random observation vector – see chapter 5, sub-sections 5.2.1
U	vector of the (ℓ'th) Fourier series coefficient of $x(t)$ over all the N temporal sub-intervals – see chapter 5, sub-section 5.2.2
$\boldsymbol{U}$	vector of the (ℓ'th) Fourier series coefficient of $\boldsymbol{x}(t)$ over all the N temporal sub-intervals – see chapter 5, sub-section 5.2.2
U	eigenvector matrix of $\mathbf{R}_{\boldsymbol{u}}$ – see chapter 5, sub-section 5.5.2, eigenvector matrix of a 'pre-whitened' hermitian matrix – see appendix E.1, eigenvector matrix of $\mathbf{R}_{\boldsymbol{s}}$ – see appendix E.4

$\mathbf{r}$	a correction vector of array channel weights $\{v_m\}_m$ – see chapter 4, sections 4.5, 4.6
V_i	eigenvector corresponding to the i'th eigenvalue (in decreasing order) of $\mathbf{R}$ – see chapter 5,sub-section 5.2.4
$\bar{V}_i$	eigenvector corresponding to the i'th eigenvalue (in decreasing order) of $\bar{\mathbf{R}}$ – see chapter 5, sub-section 5.2.5
V	eigenvector matrix comprising M eigenvectors of $\mathbf{R}$ – see *(5.2.54)* in chapter 5
$\bar{V}$	eigenvector matrix for the combined ESPRIT array – see chapter 5, sub-section 5.2.5
V_s	matrix comprising K orthonormal eigenvectors of $\mathbf{R}$ corresponding to its largest eigenvalues – see chapter 5, sub-section 5.2.4
$\tilde{V}_s$	sub-matrix comprising the first K columns of $\bar{\mathbf{R}}_n\bar{\mathbf{V}}$ – see chapter 5, sub-section 5.2.5
V_n	matrix comprising $(M\text{-}K)$ orthonormal eigenvectors of $\mathbf{R}$ corresponding to its smallest eigenvalues – see chapter 5, sub-section 5.2.4
var $(\cdot)$	variance of a random variable
$\{w_n\}$	complex weights for the synthesis of sharp nulls – see *(3.4.5)* and *(C.2.3)* in chapter 3 and in appendix C.2, respectively
w	weight vector of a beamformer or of a minimum-variance estimator – see chapter 5, sub-sections 5.2.3 and 5.2.4
$\mathbf{W}$	$L\times L$ real diagonal weighting matrix – see *(4.5.7)* in chapter 4
$x_m(t_n)$	observed sampled (temporal) value of the signal at the m'th array sensor at time t_n – see chapter 5, sub-section 5.2.2
$x(t_n)$	vector of observed sampled (temporal) values of the signal at the array sensors at time t_n – see chapter 5, sub-section 5.2.2
$\chi_m(t)$	random variable of the received temporal data at the m'th array sensor – see chapter 5, sub-section 5.2.2
$\boldsymbol{\chi}(t)$	random vector of the received temporal data at the array sensors – see chapter 5, sub-section 5.2.2
$X_m(\omega_\ell; t_n)$	ℓ'th Fourier series coefficient of $x_m(t)$ over the n'th temporal sub-interval – see chapter 5, sub-section 5.2.2
$X(\omega_\ell; t_n)$	ℓ'th Fourier series coefficient of $x(t)$ over the n'th temporal sub-interval – see chapter 5, sub-section 5.2.2
$\boldsymbol{X}(\omega_\ell; t_n)$	ℓ'th Fourier series coefficient of $\boldsymbol{x}(t)$ over the n'th temporal sub-interval – see chapter 5, sub-section 5.2.2
$\chi_{nm}(t)$	random noise signal at the m'th array sensor – see chapter 5, sub-section 5.2.2

$\boldsymbol{x}_n(t)$ vector of random noise signals at the array sensors – see chapter 5, sub-section 5.2.2

$\boldsymbol{X}_n(\omega_\ell; t_n)$ ℓ'th Fourier series coefficient of $\boldsymbol{x}_n(t)$ over the n'th temporal sub-interval – see chapter 5, sub-section 6.2.2

$\boldsymbol{y}(t)$ mode-space data vector – see *(5.3.1)* in chapter 5,

$\boldsymbol{y}_v(t)$ v'th spatial-smoothing subset of the mode-space data vector – see chapter 5, sub-section 5.4.2

$\boldsymbol{y}_{nv}(t)$ v'th spatial-smoothing subset of the mode-space noise vector – see chapter 5, sub-section 5.4.2

z a complex number defined by *(5.2.39)* or by *(5.3.15)* in chapter 5 for equally-spaced linear arrays and circular arrays respectively

$\mathbf{Z}$ matrix defined in *(E.4.6)* in appendix E.4

α relative signal phase – see appendix C.1

$\{\alpha_\mu\}$ set of mode-space weights – see chapter 3, sections 3.2, 3.5

$\alpha_\mu(\omega, \theta, \varphi)$ function defined by *(3.3.5)* in chapter 3

$\boldsymbol{\alpha}$ mode-space weight vector – see *(4.6.14)* in chapter 4
first row of steering matrix – see *(5.2.78)* in chapter 5

$\{\beta_m\}_m$ an ensemble of random angular displacement errors – see chapter 4, section 4.4

$\beta_\mu(\omega, \theta, \varphi)$ function defined by *(3.3.6)* in chapter 3

β, β_1, β_2 null-steering control phases – see chapter 3, section 3.4

$\{\beta^m, \beta_i^m\}$ sectorally-controlled null-steering phases – see chapter 3, section 3.6

$\boldsymbol{\beta}$ vector obtained from $\boldsymbol{b}$ by removing its first element – see chapter 5, sub-section 5.2.4

$\{\gamma_\mu\}$ set of post-DFT minimisation parameters – see *(4.6.2)*, *(4.6.3)* in chapter 4

$\boldsymbol{\gamma}_k^H$ k'th row of matrix Γ – see definition *(E.4.8)* in appendix E.4

Γ matrix defined in chapter 4, section 4.5 as: $\Gamma = [\mathbf{G}^H\mathbf{G}]^{-1}\mathbf{G}^H$,
sub-matrix of $\mathbf{G}$ – see definition *(E.4.8)* in appendix E.4

$\boldsymbol{\Delta}$ ESPRIT sub-array displacement vector – see chapter 5, sub-section 5.2.5

Δ ESPRIT sub-array displacement: $\Delta = |\boldsymbol{\Delta}|$ – see chapter 5, sub-section 5.2.5

$\delta(n)$ Kronecker delta function defined as: $\delta(n) = \begin{cases} 1 & n = 0 \\ 0 & n \neq 0 \end{cases}$,

$\{\varepsilon_m\}_m$ an ensemble of random phase errors – see chapter 4, section 4.3,

$\{\varepsilon_{kn}, \varepsilon_{kn\ell}\}$ pseudo-random (phase) data as described in chapter 5, sub-section 5.5.2

ζ a stabilising parameter in the frequency-sampling implementation of a digital filter – see *(3.6.20)* in chapter 3

$\zeta_{k'k''}$ $k'k''$'th element of $\mathbf{U}\boldsymbol{\Lambda}^{1/2}$ as defined in appendix E.4

θ	angle relative to the vertical axis in a spherical coordinate system
$\tilde{\theta}$	θ-coordinate of desired beam pointing direction – see *(2.2.3)* in chapter 2
ϑ	'angle' defined via *(2.2.7)* and *(2.2.8)* in chapter 2
Θ	defines the elevation range of the array - see appendix C.3
η	sidelobe level in dB – see *(4.5.7)* in chapter 4
κ	constant defined in chapter 3, section 3.6: equals to the inverse of twice the inter-element spacing in wavelengths
κ_τ, κ_ω	constants defined by *(3.6.14)* in chapter 3
$\{\kappa_m\}_m$	an ensemble of random fractional amplitude errors – see chapter 4, section 4.3
$\boldsymbol{\kappa}$	constant vector used for the MVIR minimisation constraint – see chapter 5, sub-section 5.2.4
λ	wavelength – see *(3.2.2)* in chapter 3
λ_{HI}	wavelength at upper frequency ω_{HI}
λ_i	i'th eigenvalue (in decreasing order) of $\mathbf{R}$ – see expression *(5.2.47)* in chapter 5
$-\Lambda$, Λ	lower and upper index of processed phase-modes
Λ_0	number of phase modes out of the set $\{-\Lambda$ to $\Lambda\}$ that are left out in the synthesis of a sectoral phase mode – see chapter 3, section 3.5
$\boldsymbol{\Lambda}$	eigenvalue matrix for a general hermitian matrix
μ	index in the range $-\Lambda \le \mu \le \Lambda$ referring to the μ'th phase-mode. The notation in this thesis is that a positive μ corresponds to a negative phase slope [change of electrical phase with φ]
ξ	FM modulating coefficient – see *(B.1.1)* in appendix B.1, a complex constant used in *(E.5.1)* in appendix E.5
ξ_m	function defined by *(4.4.4)* in chapter 4
$\boldsymbol{\xi}$	TAM state-space vector – see *(5.2.78)* in chapter 5
Ξ	$L \times L$ diagonal phasing matrix defined by *(4.6.11)* in chapter 4
π	$4 \tan^{-1}1 = 3.14159...$
$\Pi(t)$	waveform envelope of a pulse – see *(2.3.2)* and *(B.1.1)* in chapter 2 and appendix B.1, respectively
$\hat{\Pi}(\omega)$	Fourier transform of $\Pi(t)$ as defined by *(2.3.2)* or *(B.1.1)*
$\boldsymbol{\Pi}$	transformation matrix in an MVPR algorithm – see chapter 5, sub-section 5.2.4, projection matrix in IMP algorithm – see chapter 5, sub-section 5.2.6
ρ	a positive real constant parameter in the exponential description of the element pattern – see *(2.4.3)* in chapter 2

σ^2 combined error variance as defined by *(4.2.5)* or *(4.4.7)* in chapter 4, signal-to-noise ratio as defined in chapter 5, sub-section 5.5.2

σ_ε^2, σ_κ^2 variances of random variables $\{\varepsilon_m\}$ and $\{\kappa_m\}$ – see chapter 4, section 4.3

σ_r^2, σ_ψ^2 variances of random variables $\{r_m\}$ and $\{\psi_m\}$ – see chapter 4, section 4.4

σ_n^2 noise power at the array sensors – see chapter 5, sub-section 5.2.2

$\tilde{\sigma}_n^2$ noise power at the mode-space 'elements' – see chapter 5, sub-section 5.4.2

ς_i i'th eigenvalue (in decreasing order) of $\mathbf{R}_{ss}$ – see expression *(5.2.47)* in chapter 5

$\tilde{\tau}_m$ co-phase delay for the m'th circular array element – see *(2.3.1)* in chapter 2

τ_{HI} maximum effective extent of $\hat{J}_V(t)*\hat{S}(t)$ in the time domain – see chapter 3, section 3.6

τ_s 'sampling time', defined by: $\tau_s = 2\pi/\Delta\omega$ – see chapter 3, section 3.6

$\tau_m(\phi_k)$ (referenced) propagation delay from the k'th source direction to the m'th array sensor – see chapter 5, sub-section 5.2.2

$\boldsymbol{v}_{ss}^H$, $\boldsymbol{v}_{nn}^H$ respective first row of $\mathbf{V}_{ss}$ and $\mathbf{V}_{nn}$ – see chapter 5, sub-section 5.2.4

$\mathbf{Y}_{ss}^H$, $\mathbf{Y}_{nn}^H$ matrices $\mathbf{V}_{ss}$ and $\mathbf{V}_{nn}$ with their respective first row removed – see chapter 5, sub-section 5.2.4

φ azimuth angle variable in a spherical coordinate system

$\tilde{\varphi}$ φ-coordinate of desired beam pointing direction – see *(2.2.3)* in chapter 2

$\boldsymbol{\varphi}$ K-dimensional vector variable of azimuth angles

ϕ_k k'th DOA parameter – see chapter 5, sub-section 5.2.1

$\hat{\phi}_k$ estimate of the k'th DOA parameter – see chapter 5, sub-section 5.2.1

$\boldsymbol{\phi}$ vector of K DOA parameters – see chapter 5, sub-section 5.2.1

$\hat{\boldsymbol{\phi}}$ estimate of the vector of DOA parameters – see chapter 5, sub-section 5.2.1

$\Phi_\mu(\theta, \varphi, \omega)$ radiation pattern of phase mode number μ

$\boldsymbol{\Phi}_\mu$ $L\times 1$ pattern vector of phase mode number μ – see *(4.5.10)* in chapter 4

$\hat{\boldsymbol{\Phi}}_\mu$ $L\times 1$ pattern vector of μ'th phase mode after pre-DFT correction – see *(4.5.15)*, *(4.6.5)* in chapter 4

$\overline{\hat{\boldsymbol{\Phi}}_\mu^H}$, $\overline{|\hat{\boldsymbol{\Phi}}_\mu|^2}$ frequency and elevation averaged vectors defined by *(4.7.9)*, *(4.7.10)*, elevation-averaged vectors defined by *(4.7.13)*, *(4,7,14)* in chapter 4

$\hat{\boldsymbol{\Phi}}$ matrix of vectors $\{\hat{\boldsymbol{\Phi}}_\mu\}$ – see *(4.6.13)* in chapter 4

χ scalar Lagrange multiplier – see *(5.2.26)* in chapter 5

$\boldsymbol{\chi}$ vector Lagrange multiplier – see *(5.2.31)* in chapter 5

χ_m function defined by *(4.3.5)* in chapter 4

$\{\psi_m\}_m$ an ensemble of random rotation errors – see chapter 4, section 4.4

ψ_k kk'th element of $\boldsymbol{\Psi}$ – see *(5.2.59)* in chapter 5

$\Psi^{\beta}_{\mu+1/2}$ a $\sin(\varphi/2)$-type pattern null formed by the phased subtraction of adjacent phase modes Φ_μ and $\Phi_{\mu+1}$

$\Psi_\mu(\varphi)$ target pattern for the μ'th phase mode: $\Psi_\mu(\varphi) = e^{-j\mu\varphi}$ – see chapter 4, section 4.5

$\boldsymbol{\Psi}_\mu$ $L\times 1$ ideal pattern vector of μ'th phase mode – see *(4.5.11)* in chapter 4

$\boldsymbol{\Psi}$ matrix of vectors $\{\boldsymbol{\Psi}_\mu\}$ – see *(4.6.10)* in chapter 4,
a diagonal phasing matrix defined by *(5.2.59)* in chapter 5,
a diagonal subset phasing matrix defined by *(5.4.2)* in chapter 5

Ω defined in appendix C.3 as $\Omega = (\omega R/c)\sin\theta$

ω angular (temporal) frequency

ω_0 centre frequency

ω_ℓ discrete angular frequency defined as $(2\pi/T)\ell$ – see chapter 5, sub-section 5.2.2

ω_s sampling (angular) frequency – see chapter 3, section 3.6

$\Delta\omega$ frequency sampling period for the digital reconstruction of a phase mode coefficient – see chapter 3, section 3.6

B. APPENDICES FOR CHAPTER 2

B.1 CIRCULAR ARRAY RESPONSE TO A LINEAR FM PULSE

Let us consider the following linear FM waveform with envelope $\Pi(t)$, propagating towards the circular array of *Fig. 2.2.1*:

$$p(t) = \Pi(t) e^{j[\omega_0 t + (\xi/2) t^2]} \quad , \quad |t| \le T/2 \qquad \cdots (B.1.1)$$

where $(\omega_0 + \xi t)$ is the instantaneous frequency and T is the pulse length. With t_c and $\{t_m\}$ defined as in section 2.3, the frequency-domain signal received at the m'th array element is given by:

$$\hat{p}_m(\theta, \varphi, \omega) = e^{-j\omega(t_c + t_m)} g_m(\theta, \varphi, \omega) \int_{-\infty}^{\infty} dt' \, \Pi(t') \, e^{j[\omega_0 t' + (\xi/2) t'^2]} e^{-j\omega t'} \qquad \cdots (B.1.2)$$

When all the received signals are eventually summed and passed through an equalising network whose frequency response is given by:

$$H(\omega) = e^{j(\omega - \omega_0)^2 / 2\xi} \qquad \cdots (B.1.3)$$

we obtain:

$$P(\theta, \varphi, t) =$$

$$\frac{1}{2\pi} \int_{-\infty}^{\infty} d\omega \, F(\theta, \varphi, \omega) e^{j\omega(t - t_c)} e^{j(\omega - \omega_0)^2 / 2\xi} \int_{-\infty}^{\infty} dt' \, \Pi(t') \, e^{j[\omega_0 t' + \xi t'^2/2]} e^{-j\omega t'}$$

$$\approx \frac{F(\theta, \varphi)}{2\pi} \int_{-\infty}^{\infty} d\omega \, e^{j\omega(t - t_c - t_d)} e^{j(\omega - \omega_0)^2 / 2\xi} \int_{-\infty}^{\infty} dt' \, \Pi(t') \, e^{j[\omega_0 t' + \xi t'^2/2]} e^{-j\omega t'} \quad \cdots (B.1.4)$$

provided that the steady-state array pattern $F(\theta, \varphi, \omega+\omega_0)$ is given by *(2.3.7)* over the full bandwidth of the signal. For a rectangular envelope $\Pi(t)$, the bandwidth of $p(t)$ is approximately given by $[(\xi T^2)+4\pi]/T$ about the central frequency ω_0, where the parenthesised term (ξT^2) is commonly referred to as the *time-bandwidth product.* Changing the order of integration leads after some manipulations to:

$$P(\theta, \varphi, t) = (\xi/2\pi)^{1/2}\, e^{j[\frac{\pi}{4}+\omega_0(t-t_c-t_d)-\frac{\xi}{2}(t-t_c-t_d)^2]} F(\theta, \varphi)\hat{\Pi}[-\xi(t-t_c-t_d)] \qquad \cdots (B.1.5)$$

which is a (negative-slope) linear FM pulse that follows the steady-state radiation pattern of the array. This output pulse is typically much narrower than T, its time length being approximately given by $4\pi T/(\xi T^2)$.

If $F(\theta, \varphi, \omega)$ is not frequency-independent over the full bandwidth of the signal, or equivalently, when the uncompensated delay across the array is not much smaller than $4\pi T/(\xi T^2)$ (which is also the time length of the pulsed contribution from each of the array elements), then at angle (θ, φ) the steady-state array pattern does not apply. Evaluating the separate time-domain contributions of the signal received by the various array elements, one obtains for the m'th array channel:

$$p_m(\theta, \varphi, t) = \frac{1}{2\pi}\int_{-\infty}^{\infty} d\omega\, \hat{p}_m(\theta, \varphi, \omega) e^{j(\omega-\omega_0)^2/2\xi}\, e^{j\omega t}$$

$$= (\xi/2\pi)^{1/2}\, e^{j[\pi/4+\omega_0(t-t_0-t_m)-\xi(t-t_c-t_m)^2/2]}\, g_m(\theta, \varphi)\hat{\Pi}(-\xi(t-t_c-t_m)) \quad \cdots (B.1.6)$$

where frequency-independent element patterns have been assumed. The time-varying array pattern is expressible (to within a constant) as:

$$P(\theta, \varphi, t) = \frac{1}{M} e^{j[\omega_0(t-t_c)-\xi(t-t_c)^2/2]}$$

$$\sum_{m=0}^{M-1} a_m g_m(\theta, \varphi) e^{-j[\omega_0 t_m+\xi t_m^2/2]}\, e^{-j\xi(t-t_0)t_m}\hat{\Pi}(-\xi(t-t_c-t_m)) \qquad \cdots (B.1.7)$$

In many practical cases the sum on the right hand side of *(B.1.7)* may be approximated by temporally-displaced short CW pulse term. Let Δr denote the range resolution the system is designed to achieve. It follows (for an active radar or sonar) that:

$$4\pi T/(\xi T^2) \approx 2\Delta r/c \qquad \cdots (B.1.8)$$

which in turn leads to:

$$\xi \approx (2\pi c/\Delta r)^2/(\xi T^2) \qquad \cdots (B.1.9)$$

Now assuming that the (arcwise) inter-element spacing is smaller than half a wavelength at the highest frequency of operation, it follows that:

$$|t_m| \leq \begin{cases} R/c \leq M\lambda_{HI}/4\pi c & \text{equi-delay excitation} \\ 2R/c \leq M\lambda_{HI}/2\pi c & \text{co-delayed excitation} \end{cases} \qquad \cdots (B.1.10)$$

where λ_{HI} is the wavelength at the highest frequency. Equation *(B.1.9)* together with inequality *(B.1.10)* subsequently lead to:

$$\frac{\xi}{2} t_m^2 \leq M^2/2(\xi T^2)(\Delta r/\lambda_{HI})^2 \qquad \cdots (B.1.11)$$

which for many practical cases is found to be negligibly small

$$M \leq 32 \ , \ (\Delta r/\lambda_{HI}) \geq 10 \ , \ (\xi T^2) \geq 1000 \ \Rightarrow$$

$$(\xi/2)t_m^2 \leq 0.00512 = (0.29°/360°)2\pi << 2\pi$$

Next, we note that $\hat{\Pi}(\alpha)$ effectively vanishes when $|\alpha| \geq 2\pi/T$. It follows that only the time interval given by:

$$|\xi(t-t_c-t_m)| \leq 2\pi/T \qquad \cdots (B.1.12)$$

is of consequence in the analysis. But when slightly rearranged and use is again made of *(B.1.8) – (B.1.11)* the above inequality takes the form

$$|\xi(t-t_c)|t_m \leq 2\pi t_m/T + \xi t_m^2 \leq \frac{1}{(\xi T^2)}\left[\frac{2\pi M}{(\Delta r/\lambda_{HI})} + \frac{M^2}{(\Delta r/\lambda_{HI})^2}\right] \qquad \cdots (B.1.13)$$

Substituting practical values for M, (ξT^2) and $(\Delta r/\lambda_{HI})$ we finally obtain:

$$M \leq 32 \ , \ (\Delta r/\lambda_{HI}) \geq 10 \ , \ (\xi T^2) \geq 1000 \ \Rightarrow$$

$$\xi|t-t_c|t_m \leq 0.0303 = (1.74°/360°)2\pi << 2\pi$$

Taking the effect of the phase terms $e^{-j(\xi/2)t_m^2}$ and $e^{-j\xi(t-t_c)t_m}$ in *(B.1.7)* to be negligible,

the array response may be approximated by a sum of time-shifted pulses all sharing the same linear-FM modulation:

$$P(\theta,\varphi,t)=\frac{1}{M}e^{j[\omega_0(t-t_c)-\frac{\xi}{2}(t-t_c)^2]}\sum_{m=0}^{M-1}a_m g_m(\theta,\varphi)e^{-j\omega_0 t_m}\hat{\Pi}[-\xi(t-t_c-t_m)] \quad \cdots (B.1.13)$$

where constant terms have again been omitted. In other words, transient effects in the array response are essentially representable by linear temporal displacements of (compressed) pulsed contributions from the array elements. The actual displacement $(t_{m'}-t_{m''})$ that can occur between pulses contributed by any two elements m' and m'', relative to the compressed pulse length $4\pi T/(\xi T^2)$, is bounded by virtue of *(B.1.8)* and *(B.1.10)* (which also applies to $|t_{m'}-t_{m''}|$):

$$\frac{|t_{m'}-t_{m''}|}{4\pi T/(\xi T^2)}\le\frac{M\lambda_{HI}/2\pi c}{2\Delta r/c}=\frac{(M/4\pi)}{\Delta r/\lambda_{HI}} \quad \cdots (B.1.13)$$

and for the previously assumed case of: $M\le 32$, $\Delta r/\lambda_{HI}\ge 10$, the maximum pulse-to-pulse displacement does not exceed about one quarter of the compressed pulse width.

B.2 DERIVATION OF *(2.4.11)*

We start from expression *(2.4.4)* for the far-field phase mode pattern:

$$\Phi_\mu(\theta, \varphi, \omega) = \frac{\rho h_0(\theta)}{M} \sum_{m=0}^{M-1} e^{-j(2\pi/M)\mu m} e^{j[(\omega R/c)+j\ln\rho]\sin\theta\cos(\varphi-2\pi m/M)} \quad \ldots (2.4.4)$$

and make use of the Bessel identity –

$$e^{j[(\omega R/c)+j\ln\rho]\sin\theta\cos(\varphi-2\pi m/M)} = \sum_{\nu=-\infty}^{\infty} j^\nu J_\nu[(\frac{\omega R}{c}+j\ln\rho)\sin\theta] e^{-j\nu(\varphi-2\pi m/M)}$$

to obtain:

$$\Phi_\mu(\theta, \varphi, \omega) = \rho h_0(\theta) \sum_{\nu=-\infty}^{\infty} j^\nu J_\nu[(\frac{\omega R}{c}+j\ln\rho)\sin\theta] e^{-j\nu\varphi}[\frac{1}{M}\sum_{m=0}^{M-1} e^{-j(2\pi/M)(\mu-\nu)m}] \quad \ldots (B.2.1)$$

Substitution of

$$\frac{1}{M}\sum_{m=0}^{M-1} e^{-j(2\pi/M)(\mu-\nu)m} = \sum_{q=-\infty}^{\infty} \delta(\mu-\nu+qM)$$

in *(B.2.1)* leads to:

$$\Phi_\mu(\theta, \varphi, \omega) = \rho h_0(\theta) \sum_{q=-\infty}^{\infty} j^{\mu+qM} J_{\mu+qM}[(\frac{\omega R}{c}+j\ln\rho)\sin\theta] e^{-j(\mu+qM)\varphi} \quad \ldots (B.2.2)$$

from which *(2.4.11)* immediately follows.

C. APPENDICES FOR CHAPTER 3

C.1 MAXIMUM DOA ERROR IN A MULTIMODAL DF DUE TO THE PRESENCE OF A SECOND SOURCE

Consider a circular multimodal array system receiving a strong signal from a source in direction ϕ, while a second signal from a weaker source at the same frequency reaches the array at amplitude A and phase α relative to the first signal. The angular error in estimating the direction of arrival of the strong signal using *(3.3.2)* is given by:

$$\mathcal{E} = \phi - \arg(e^{j\phi} + A\,e^{j\alpha}) + \arg(1 + A\,e^{j\alpha})$$

$$= \phi - \tan^{-1}\left[\frac{\sin\phi + A\sin\alpha}{\cos\phi + A\cos\alpha}\right] + \tan^{-1}\left[\frac{A\sin\alpha}{1 + A\cos\alpha}\right] \qquad \cdots (C.1.1)$$

where we have assumed, without loss of generality, that the second source is angularly located at $\varphi = 0$. To find the values of ϕ and α which maximise $\mathcal{E}$ we differentiate it with respect to ϕ and α and equate to zero:

$$\frac{\partial \mathcal{E}}{\partial \alpha} = A\left[-\frac{A + \cos(\phi - \alpha)}{1 + A^2 + 2A\cos(\phi - \alpha)} + \frac{A + \cos\alpha}{1 + A^2 + 2A\cos\alpha}\right] = 0 \qquad \cdots (C.1.2)$$

$$\frac{\partial \mathcal{E}}{\partial \phi} = A\frac{A + \cos(\phi - \alpha)}{1 + A^2 + 2A\cos(\phi - \alpha)} = 0 \qquad \cdots (C.1.3)$$

which lead to:

$$\cos\alpha = \cos(\phi - \alpha) = -A \qquad \cdots (C.1.4)$$

or

$$\alpha = \pi - \cos^{-1}A \qquad \cdots (C.1.5)$$

$$\phi = 2\alpha \qquad \cdots (C.1.6)$$

(The solution $\phi = 0$ leads to a minimum rather than a maximum error).
Inserting *(C.1.4)* - *(C.1.6)* in *(C.1.1)* we obtain:

$$\mathcal{E}_{max} = 2\alpha - \tan^{-1}\left[\frac{\sin 2\alpha - \cos\alpha \sin\alpha}{\cos 2\alpha - \cos^2\alpha}\right] + \tan^{-1}\left[\frac{-\cos\alpha \sin\alpha}{1-\cos^2\alpha}\right]$$

$$= 2\alpha - \tan^{-1}\left[\frac{-\cos(\pi-\alpha)}{-\sin(\pi-\alpha)}\right] + \tan^{-1}\left[\frac{\cos(\pi-\alpha)}{\sin(\pi-\alpha)}\right]$$

$$= 2\alpha - (\alpha+\pi/2) + (\alpha-\pi/2) = 2\alpha - \pi = 2\left[\frac{\pi}{2} - (\pi-\alpha)\right]$$

$$= 2\sin^{-1}A \qquad \cdots (C.1.7)$$

The 'maximum-error' geometry which yields *(C.1.7)* is illustrated in the phasor diagram of *Fig. C.1.1* and results for several values of A are tabulated in Table 3.3.1 in chapter 3.

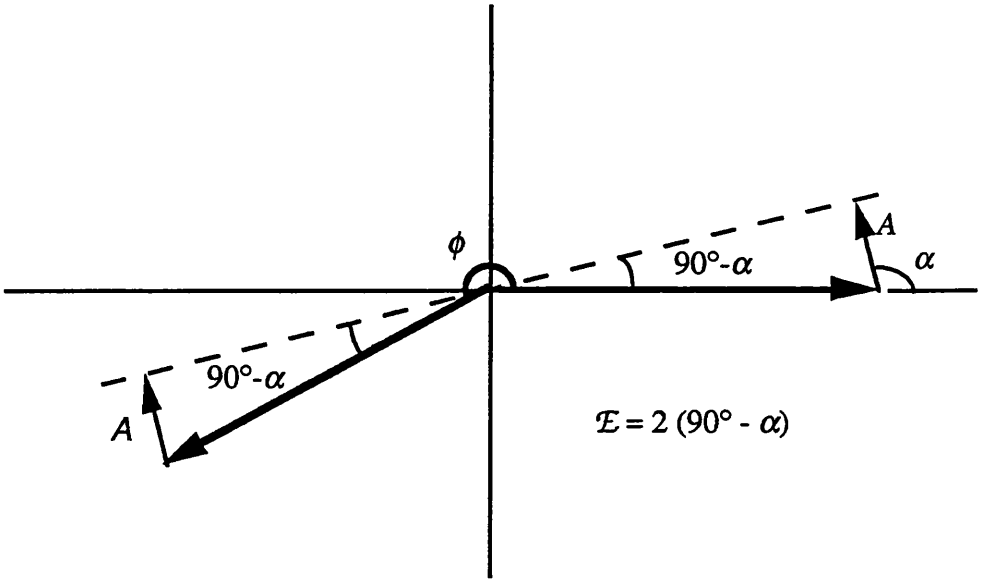

Fig. C.1.1 Maximum error in estimated angle of arrival

C.2 SYNTHESIS OF SECTORALLY-CONTROLLED SHARP NULLS

A multibeam set of directional beams with sectorally-controlled nulls that are sharper than $\sin[(\varphi-\beta_i^m-2\pi m/M)/2]$ may be synthesised (at the expense of increased complexity and wider beams or fewer sets of nulls) by linearly combining $N>2$ sectoral phase modes corresponding to the same angular sector and having adjacent (effective) mode numbers – see *Fig. C.2.1* for the case of $N = 3$.

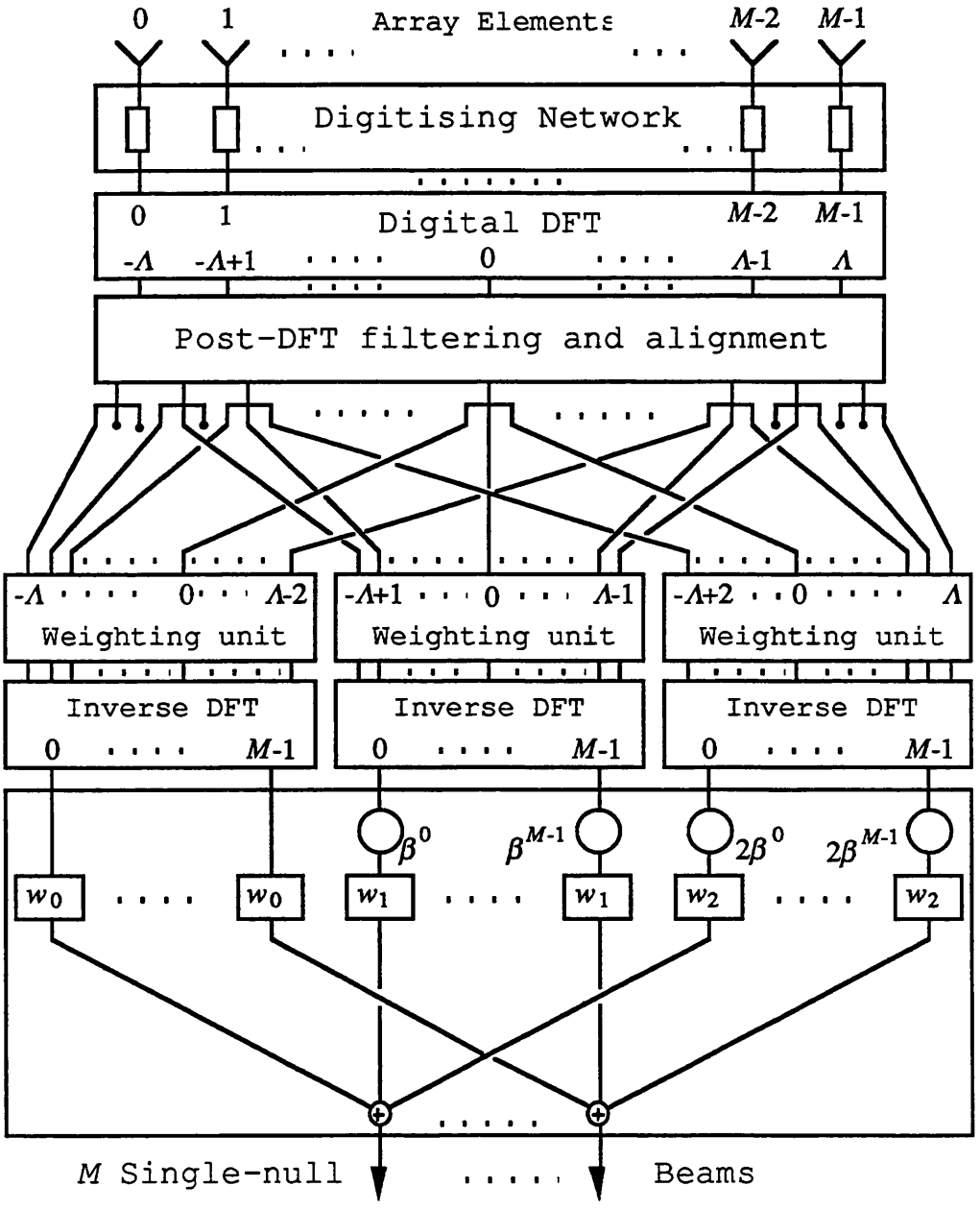

Fig. C.2.1 Sharp post-nulling with 3 sets of directional phase modes

The superscripts in $\beta^0, \beta^1, \cdots, \beta^m, \cdots, \beta^{M-1}$ are used for consistency with the notation of section 3.5 (see *Fig. 3.5.3*) and denote the directions $\{2\pi m/M\}$ of the corresponding beams in which the nulls are steered. The weighting and phasing scheme follows the lines described by *(3.4.3)* - *(3.4.6)* for the combination of omnidirectional phase modes. The m'th output pattern is accordingly given by:

$$\mathcal{N}_m(\varphi) = \sum_{n=0}^{N-1} w_n e^{jn\beta^m} F^{m(N-1)}_{n-(N-1)/2}(\varphi)$$

$$= e^{j(N-1)\beta^m/2} A(\varphi - 2\pi m/M) \sum_{n=0}^{N-1} w_n e^{-j[n-(N-1)/2](\varphi-\beta^m-2\pi m/M)}$$

$$0 \le m \le M-1 \quad \cdots (C.2.1)$$

where $A(\varphi)$ is given by *(3.5.4)* with Λ_0 set equal to N-1. The set of weights $\{w_n\}$ is evaluated, as outlined in section 3.4, by seeking a target pattern of the form:

$$\mathcal{T}_m(\varphi) = A(\varphi - 2\pi m/M) e^{j(N-1)\beta^m/2} e^{-j(\varphi-\beta^m-2\pi m/M)/2} \quad , \quad 0 \le m \le M-1 \quad \cdots (C.2.2)$$

which is characterised by a single null at direction $(\beta^m + 2\pi m/M)$, and using Fourier analysis to solve:

$$\sum_{n=0}^{N-1} w_n e^{-j[n-(N-1)/2](\varphi-\beta^m-2\pi m/M)} = e^{-j(\varphi-\beta^m-2\pi m/M)/2} \quad , \quad 0 \le m \le M-1 \quad \cdots (C.2.3)$$

The result for odd N is as given by *(3.4.6)*:

$$w_n = \frac{\sin[(n-N/2)\pi]}{(n-N/2)\pi} = \frac{(-1)^{n-(N-1)/2}}{(-n+N/2)\pi} \quad , \quad 0 \le n \le N-1$$

C.3 OPTIMAL ELEMENT PATTERN

Consider a circular array of M radially-symmetric identical elements in which a set $\{\Phi_\mu(\theta, \varphi, \omega)\}_{\mu=-\Lambda}^{\Lambda}$ of $2\Lambda+1$ phase modes is excited, where $\Lambda<M/2$. Assume frequency-independent and angularly separable element patterns:

$$g(\theta,\varphi) = g_\theta(\theta) \sum_{i=-\infty}^{\infty} h_i e^{ji\varphi} \qquad \cdots (C.3.1)$$

so that each phase mode pattern may be expressed by *(2.4.10)*, with each phase mode coefficients being given by:

$$C_{\mu q}(\omega, \theta) = g_\theta(\theta) \sum_{i=-I}^{I} j^{\mu+i+qM} h_i J_{\mu+i+qM}[(\omega R/c)\sin\theta] \qquad \cdots (C.3.2)$$

In our quest for the optimal element pattern, a set $\{h_i\}_{i=-I}^{I}$ of angular Fourier coefficients is sought that, over a given frequency band $\omega_{LO} \le \omega \le \omega_{HI}$ and elevation range $\pi/2-\Theta \le \theta \le \pi/2+\Theta$, would ideally:

i minimise the amplitude and phase variations between the set $\{C_{\mu 0}(\omega, \theta)\}_{\mu=-\Lambda}^{\Lambda}$ of zero-order phase mode coefficients

ii render the frequency response of the above coefficients linear in phase and constant in amplitude

iii minimise the amplitudes of higher order phase mode coefficients $\{\{C_{\mu q}(\omega, \theta)\}_{\mu=-\Lambda}^{\Lambda}\}_{|q|>0}$

The above conditions have been partially fulfilled by both types of element patterns discussed at the beginning of section 3.6. The first azimuth pattern of $g_\varphi(\varphi) = 1+\cos\varphi$, has been found to be asymptotically optimal in minimising amplitude and in phase variations between zero-order phase mode coefficients, and linearising the frequency responses of their arguments. Higher order phase mode coefficients had not been specifically minimised, but with $g_\varphi(\varphi)$ being represented by only three non-vanishing Fourier coefficients (h_0, h_{-1}, h_1), each higher order coefficient comprises three adjacent Bessel functions, that die down by virtue of their asymptotic behaviour for large orders.[1] The second azimuthally impulsive element pattern, whose Fourier coefficients had been uniformly weighted, has gone even

[1] When the order and argument of $J_{\mu+i+qM}[(\omega R/c)\sin\theta]$ are such that: $|\mu+i+qM| \gg (\omega R/c)\sin\theta$, then: $J_{\mu+i+qM}[(\omega R/c)\sin\theta] \sim [2\pi(\mu+i+qM)]^{-1/2}\{[e\omega R/2c(\mu+i+qM)]\sin\theta\}^{\mu+i+qM}$

further in achieving amplitude equalisation of each phase mode, but has also brought the total contributions from higher order modes to an impulsive level. We are evidently faced with a trade-off between full equalisation which requires a large number $2I+1$ of non-vanishing Fourier coefficients, and low distortion which is best served by reducing I. In that respect, the $(1+\cos\varphi)$-type element pattern seems to be closest to optimal, especially as the reasonably attractive asymptotic result of *(3.6.1)* is also obtained (to within a constant) by higher-order element patterns of the form $g_\varphi(\varphi) = 1+\cos\varphi+k(\cos 2\varphi+\cos 3\varphi)$.

Other solutions to the elusive ideal-pattern problem involve linear optimisation. Ignoring the term $g_\theta(\theta)$ in *(C.3.2)*, the set of equations relating $\{h_i\}_{i=-I}^{I}$ to the q'th coefficient of the set of phase modes $\{\Phi_\mu(\theta, \varphi, \omega)\}_{\mu=-\Lambda}^{\Lambda}$ may be put into the following matrix form:

$$\mathbf{J}_q(\Omega)\boldsymbol{h} = \boldsymbol{C}_q(\Omega) \qquad \cdots (C.3.3)$$

where:

$$\Omega = (\omega R/c)\sin\theta \qquad \cdots (C.3.4)$$

$$\boldsymbol{h} = [h_{-I} \cdots h_{-1}\ h_0\ h_1 \cdots h_I]^T \qquad \cdots (C.3.5)$$

$$\boldsymbol{C}_q(\Omega) = [C_{(-\Lambda)q}(\omega, \theta), \cdots, C_{0q}(\omega, \theta), \cdots, C_{\Lambda q}(\omega, \theta)]^T \qquad \cdots (C.3.6)$$

and $\mathbf{J}_q(\Omega)$ is a $(2\Lambda+1)\times(2I+1)$ matrix whose μi'th element is given by:

$$[J_q(\Omega)]_{\mu i} = j^{\mu+i+qM} J_{\mu+i+qM}(\Omega) \qquad \cdots (C.3.7)$$

Assuming $I < \Lambda$, we may define the following cost function to be minimised with respect to $\boldsymbol{h}$:

$$\mathcal{E} = \frac{1}{\Delta\Omega}\int_{\Omega_{LO}}^{\Omega_{HI}} d\Omega \sum_{q=-Q}^{Q} |\mathbf{J}_q(\Omega)\boldsymbol{h} - \boldsymbol{b}_q(\Omega)|^2 \qquad \cdots (C.3.8)$$

where,

$$\begin{aligned} \Omega_{LO} &= (\omega_{LO} R/c)\sin(\pi/2 - \Theta) \\ \Omega_{HI} &= \omega_{HI} R/c \end{aligned} \qquad \cdots (C.3.9)$$

$$\Delta\Omega = \Omega_{HI} - \Omega_{LO} \qquad \cdots (C.3.10)$$

$Q \geq 0$, the vectors $\{\boldsymbol{b}_q(\Omega)\}_{q\neq 0}$ are all zero and $\boldsymbol{b}_0(\Omega)$ is the target frequency response vector of the zero-order phase mode coefficients, which, in view of *(3.6.1)*, may be set equal to:

$$\boldsymbol{b}_0(\Omega) = [1\ 1 \cdots 1]^T e^{j\Omega}/\Omega^{1/2}$$

or even

$$\boldsymbol{b}_0(\Omega) = [1\ 1 \cdots 1]^T e^{j\Omega}$$

The cost function $\mathcal{E}$ may be minimised by differentiating it with respect to the real and imaginary parts of each h_i and equating to zero. Being a real-valued function, $\mathcal{E}$ may be equivalently minimised by equating to zero its complex gradient with respect to $\boldsymbol{h}^H$, where the notion of complex gradient has been defined and discussed in [BRA 83]. The result is:

$$\boldsymbol{h} = [\frac{1}{\Delta\Omega}\int_{\Omega_{LO}}^{\Omega_{HI}} d\Omega \sum_{q=-Q}^{Q} \mathbf{J}_q^H(\Omega)\mathbf{J}_q(\Omega)]^{-1}\ [\frac{1}{\Delta\Omega}\int_{\Omega_{LO}}^{\Omega_{HI}} d\Omega \mathbf{J}_0(\Omega)\boldsymbol{b}_0(\Omega)] \qquad \cdots (C.3.11)$$

where each vector or matrix integration is threaded over to the separate terms. Note that the value of Q affects the relative emphasis given in the minimisation procedure to higher order terms. For even more control, the sum on the right hand side of *(C.3.8)* may be changed into a weighted sum

$$\sum_{q=-Q}^{Q} w_q |\mathbf{J}_q(\Omega)\boldsymbol{h} - \boldsymbol{b}_q(\Omega)|^2$$

with a user-defined weighting sequence $\{w_q\}$, leading to:

$$\boldsymbol{h} = [\frac{1}{\Delta\Omega}\int_{\Omega_{LO}}^{\Omega_{HI}} d\Omega \sum_{q=-Q}^{Q} (w_q/w_0)\mathbf{J}_q^H(\Omega)\mathbf{J}_q(\Omega)]^{-1}\ [\frac{1}{\Delta\Omega}\int_{\Omega_{LO}}^{\Omega_{HI}} d\Omega \mathbf{J}_0(\Omega)\boldsymbol{b}_0(\Omega)]$$

C.4 SAMPLING OF PHASE MODE COEFFICIENTS

Denoting:

$$C_{\mu n} = S(\omega_n \Delta t) C_{\mu 0}(\omega_n, \pi/2) \quad , \quad 0 \le n \le N\text{-}1 \qquad \cdots (C.4.1)$$

the frequency samples $\{\mathcal{D}_\mu(e^{j\omega_n \Delta t})\}_{n=0}^{N-1}$ used in *(3.6.18)* are respectively given for odd and even N, by:[2]

$$\begin{aligned} \mathcal{D}_\mu(e^{j\omega_n \Delta t}) &= e^{-j(\pi/N)(N-1)n} S(\omega_n \Delta t) C_{\mu 0}(\omega_n, \pi/2) \\ &\quad + e^{j(\pi/N)(N-1)(N-n)} S(-\omega_n \Delta t) C_{\mu 0}(-\omega_{N-n}, \pi/2) \\ &= e^{-j(\pi/N)(N-1)n} (C_{\mu n} + C^*_{\mu(N-n)}) \quad , \quad 0 \le n \le N\text{-}1 \qquad \cdots (C.4.2) \end{aligned}$$

and

$$\begin{aligned} \mathcal{D}_\mu(e^{j\omega_n \Delta t}) &= e^{-j(\pi/N)(N-1)(n+1/2)} S(\omega_n \Delta t) C_{\mu 0}(\omega_n, \pi/2) \\ &\quad + e^{j(\pi/N)(N-1)(N-n-1/2)} S(-\omega_n \Delta t) C_{\mu 0}(-\omega_{N-n-1}, \pi/2) \\ &= e^{-j(\pi/N)(N-1)(n+1/2)} (C_{\mu n} - C^*_{\mu(N-n-1)}) \quad , \quad 0 \le n \le N\text{-}1 \qquad \cdots (C.4.3) \end{aligned}$$

and under the assumption that (see *Fig. 3.6.1* in chapter 3):

$$S(\Omega) = 0 \quad , \quad |\Omega| > 2\pi - \omega_{HI} \Delta t$$

there will be no aliasing within the operating frequency band of the array.[3]

The actual frequency samples for each of the the phase mode coefficients $\{C_{\mu 0}(\omega_n, \pi/2) \quad , \quad -\Lambda \le \mu \le \Lambda\}$ are obtainable from calibration measurements of the element patterns – this is treated under the heading of 'post-DFT correction' in sections 4.6 and 4.7 of chapter 4. The application of one of the least-squares mode-alignment schemes described in chapter 4, leads to:

---

2 Here $S(\Omega)$ is assumed real, and note also that: $C_{\mu 0}(-\omega, \pi/2) = C^*_{\mu 0}(\omega, \pi/2)$

3 The sampling window function should not fall to zero at $|\omega| < \omega_{s/2}$ so as not to introduce zeros on the unit circle. This may give rise to some frequency-domain aliasing of $C_{\mu 0}(\omega, \pi/2)$, especially when a gradual rather than an ideal rectangular window is implemented. However, the sampling frequency can always be so chosen that the affected interval is kept outside the band $|\omega| \le \omega_{HI}$.

$$C_{\mu n} = \frac{1}{L} S(\omega_n \Delta t) \sum_{\ell=0}^{L-1} e^{j(2\pi/L)\mu\ell} \frac{1}{M^{1/2}} \sum_{m=0}^{M-1} e^{-j(2\pi/M)\mu m} G_{\ell m}(\omega_n, \pi/2) \quad \cdots (C.4.4)$$

where $G_{\ell m}(\omega, \pi/2)$ is the measured complex pattern of the m 'th array element at angle ($\theta = \pi/2$, $\varphi = 2\pi\ell/L$) and angular frequency ω, and $L>M$ is an integer. Invoking *(2.4.10)*, we can rewrite *(C.4.4)* as:

$$C_{\mu n} = \frac{1}{L} S(\omega_n \Delta t) \sum_{\ell=0}^{L-1} e^{j(2\pi/L)\mu\ell} \sum_{q=-\infty}^{\infty} C_{\mu q}(\omega_n, \pi/2)\, e^{-j(\mu+qM)(2\pi/L)\ell}$$

$$= S(\omega_n \Delta t) \sum_{q=-\infty}^{\infty} C_{\mu(Kq)}(\omega_n, \pi/2) \quad \cdots (C.4.5)$$

where K is the smallest integer such that KM is an integer multiple of L. Assuming contributions from higher order modes to decrease with order, it is evident from *(3.6.22)* that the larger we make K, the more accurate is the approximation *(C.4.4)* for the zero-order phase mode coefficient.

Note finally that if the available data cover only part of the frequency band 0 to $(2\pi/\Delta t)$-ω_{HI}, then in order to avoid zeros of $\mathcal{D}_\mu(z)$ on the unit circle, the data may be 'analytically continued' as follows:

$$G_{\ell m}(\omega_{HI} \le \omega < \omega_s - \omega_{HI}, \pi/2) =$$

$$G_{\ell m}(\omega_{HI}, \pi/2) e^{-j(\omega-\omega_{HI})(R/c)[1-\cos(2\pi\ell/L - 2\pi m/M)]} \quad \cdots (C.4.6)$$

$$G_{\ell m}(0 \le \omega < \omega_{LO}, \pi/2) =$$

$$G_{\ell m}(\omega_{LO}, \pi/2) e^{-j(\omega-\omega_{LO})(R/c)[1-\cos(2\pi\ell/L - 2\pi m/M)]} \quad \cdots (C.4.7)$$

D. APPENDICES FOR CHAPTER 4

D.1 DERIVATION OF EXPRESSION *(4.6.4)*

We start from expressions *(4.6.2)* for the cost function, which we differentiate with respect to $\boldsymbol{v}^H$ and $\{\gamma_\mu^*\}_{\mu\neq 0}$ and equate to zero to obtain:

$$[\sum_{\mu=-\Lambda}^{\Lambda} \mathbf{E}_\mu \mathbf{G}^H \mathbf{G} \mathbf{E}_\mu^H] \boldsymbol{v} = \sum_{\mu=-\Lambda}^{\Lambda} \mathbf{E}_\mu \mathbf{G}^H \boldsymbol{\Psi}_\mu \gamma_\mu \qquad \cdots (D.1.1)$$

$$\boldsymbol{\Psi}_\mu^H \mathbf{G} \mathbf{E}_\mu^H \boldsymbol{v} = |\boldsymbol{\Psi}_\mu|^2 \gamma_\mu \quad , \quad \mu = -\Lambda, \cdots, -1, 1, \cdots, \Lambda \qquad \cdots (D.1.2)$$

We proceed by inserting $\{\gamma_\mu\}_\mu$ from *(D.1.2)* and from *(4.6.3)* into *(D.1.1)*, which yields:

$$[\sum_{\mu=-\Lambda}^{\Lambda} \mathbf{E}_\mu \mathbf{G}^H \mathbf{G} \mathbf{E}_\mu^H] \boldsymbol{v} = \mathbf{E}_0 \mathbf{G}^H \boldsymbol{\Psi}_0 + [\sum_{\substack{\mu=-\Lambda \\ \mu\neq 0}}^{\Lambda} \mathbf{E}_\mu \mathbf{G}^H \boldsymbol{\Psi}_\mu |\boldsymbol{\Psi}_\mu|^{-2} \boldsymbol{\Psi}_\mu^H \mathbf{G} \mathbf{E}_\mu^H] \boldsymbol{v}$$

$$= \mathbf{G}^H \boldsymbol{\Psi}_0 + \frac{1}{L} [\sum_{\substack{\mu=-\Lambda \\ \mu\neq 0}}^{\Lambda} \mathbf{E}_\mu \mathbf{G}^H \boldsymbol{\Psi}_\mu \boldsymbol{\Psi}_\mu^H \mathbf{G} \mathbf{E}_\mu^H] \boldsymbol{v} \qquad \cdots (D.1.3)$$

The terms in the above equation are finally rearranged leading to

$$[\mathbf{G}^H \mathbf{G} + \sum_{\substack{\mu=-\Lambda \\ \mu\neq 0}}^{\Lambda} \mathbf{E}_\mu (\mathbf{G}^H \mathbf{G} - \frac{1}{L} \mathbf{G}^H \boldsymbol{\Psi}_\mu \boldsymbol{\Psi}_\mu^H \mathbf{G}) \mathbf{E}_\mu^H] \boldsymbol{v} = \mathbf{G}^H \boldsymbol{\Psi}_0 \qquad \cdots (D.1.4)$$

from which *(4.6.4)* immediately follows.

D.2 DERIVATION OF EXPRESSION *(4.7.2)*

We start from expression *(4.7.1)* for the cost function, which we differentiate with respect to v^H and $\{\gamma_\mu^*\}_{\mu\neq 0}$ and equate to zero to obtain:

$$[\sum_{\mu=-\Lambda}^{\Lambda} \mathbf{E}_\mu \frac{1}{\Delta\omega}\int_{\omega_{LO}}^{\omega_{HI}} d\omega \frac{1}{2\Theta}\int_{\pi/2-\Theta}^{\pi/2+\Theta} d\theta \mathbf{G}^H(\omega,\theta)\mathbf{G}(\omega,\theta)\mathbf{E}_\mu^H]v =$$

$$\sum_{\mu=-\Lambda}^{\Lambda} \mathbf{E}_\mu \frac{1}{\Delta\omega}\int_{\omega_{LO}}^{\omega_{HI}} d\omega \frac{1}{2\Theta}\int_{\pi/2-\Theta}^{\pi/2+\Theta} d\theta \mathbf{G}^H(\omega,\theta)\,\boldsymbol{\Psi}_\mu\gamma_\mu \qquad \cdots (D.2.1)$$

$$\boldsymbol{\Psi}_\mu^H \frac{1}{\Delta\omega}\int_{\omega_{LO}}^{\omega_{HI}} d\omega \frac{1}{2\Theta}\int_{\pi/2-\Theta}^{\pi/2+\Theta} d\theta \mathbf{G}(\omega,\theta)\mathbf{E}_\mu^H v = |\boldsymbol{\Psi}_\mu|^2\gamma_\mu$$

$$\mu = -\Lambda, \cdots, -1, 1, \cdots, \Lambda \qquad \cdots (D.2.2)$$

We proceed by inserting $\{\gamma_\mu\}_\mu$ from *(D.2.2)* and from *(4.6.3)* into *(D.2.1)*, which yields:

$$[\sum_{\mu=-\Lambda}^{\Lambda} \mathbf{E}_\mu \bar{\mathbf{G}}^H\mathbf{G}\,\mathbf{E}_\mu^H]v = \mathbf{E}_0\bar{\mathbf{G}}^H\boldsymbol{\Psi}_0 + [\sum_{\substack{\mu=-\Lambda \\ \mu\neq 0}}^{\Lambda} \mathbf{E}_\mu\bar{\mathbf{G}}^H\boldsymbol{\Psi}_\mu\,|\boldsymbol{\Psi}_\mu|^{-2}\boldsymbol{\Psi}_\mu^H\bar{\mathbf{G}}\,\mathbf{E}_\mu^H]v$$

$$= \bar{\mathbf{G}}^H\boldsymbol{\Psi}_0 + \frac{1}{L}[\sum_{\substack{\mu=-\Lambda \\ \mu\neq 0}}^{\Lambda} \mathbf{E}_\mu\bar{\mathbf{G}}^H\boldsymbol{\Psi}_\mu\boldsymbol{\Psi}_\mu^H\bar{\mathbf{G}}\,\mathbf{E}_\mu^H]v \qquad \cdots (D.2.3)$$

where $\bar{\mathbf{G}}$, $\bar{\mathbf{G}}^H$ and $\overline{\mathbf{G}^H\mathbf{G}}$ are defined in *(4.7.3)* to *(4.7.5)*. Finally, rearrangement of the terms in *(D.2.3)* leads, after matrix inversion, to *(4.7.2)*.

E. APPENDICES FOR CHAPTER 5

E.1 SIGNAL AND NOISE SUBSPACES UNDER GENERALISED EIGEN-DECOMPOSITION

The generalised eigen-structure of the matrix pair ($\mathbf{R}_x$, $\mathbf{R}_n$) may be represented by the equation

$$\mathbf{R}_x\mathbf{V} = \mathbf{R}_n\mathbf{V}\mathbf{\Lambda} \qquad \cdots (E.1.1)$$

where the $M\times M$ matrices $\mathbf{\Lambda}$ and $\mathbf{V} = [V_0\ V_1 \cdots\cdots V_{M-1}]$ are the diagonal generalised eigenvalue matrix and the generalised eigenvector matrix respectively. In *(E.1.1)* $\mathbf{R}_x$ is the narrowband spatial covariance matrix modelled as:

$$\mathbf{R}_x = \mathbf{A}\mathbf{R}_s\mathbf{A}^H + \sigma_n^2\mathbf{R}_n \qquad \cdots (E.1.2)$$

where $\mathbf{R}_s$ is the $K\times K$ signal covariance matrix, $\mathbf{R}_n$ is a known $M\times M$ non-singular covariance matrix of the sensor noises and $\mathbf{A}$ is the $M\times K$ steering matrix; all three matrices are assumed to be of full rank and $K < M$. Denoting the hermitian square root of $\mathbf{R}_n$ by:

$$\mathbf{R}_n = \mathbf{H}\mathbf{H}^H \qquad \cdots (E.1.3)$$

equation *(E.1.1)* may be recast into the following equivalent form:

$$\mathbf{R}_y\mathbf{U} = \mathbf{U}\mathbf{\Lambda} \qquad \cdots (E.1.4)$$

where the hermitian matrix $\mathbf{R}_y$ and the unitary matrix $\mathbf{U}$ are given by:

$$\mathbf{R}_y = \mathbf{H}^{-1}\mathbf{R}_x\mathbf{H}^{-H} = \mathbf{H}^{-1}\mathbf{A}\mathbf{R}_s\mathbf{A}^H\mathbf{H}^{-H} + \sigma_n^2\mathbf{I} \qquad \cdots (E.1.5)$$

$$\mathbf{U} = \mathbf{H}^H\mathbf{V} \qquad \cdots (E.1.6)$$

with $\mathbf{I}$ standing for the $M \times M$ identity matrix and $\mathbf{H}^{-H}$ denoting the transpose conjugate of $\mathbf{H}^{-1}$. The (diagonal) elements of $\mathbf{\Lambda}$ and the columns of $\mathbf{U}$ are clearly the ordinary eigenvalues of $\mathbf{R}_{\boldsymbol{y}}$ and their associated eigenvectors, respectively. The operation

$$\boldsymbol{y} = \mathbf{H}^{-1}\boldsymbol{x}$$

that leads to the above transformation is commonly referred to as *pre-whitening*. From *(E.1.4)* and *(E.1.5)* we have:

$$[\mathbf{H}^{-1}\mathbf{A}\mathbf{R}_{\boldsymbol{s}}\mathbf{A}^{H}\mathbf{H}^{-H}]\mathbf{U} = \mathbf{U}\,[\mathbf{\Lambda} - \sigma_{\boldsymbol{w}}^2\mathbf{I}] \qquad \cdots (E.1.7)$$

and since $\text{rank}(\mathbf{A}\mathbf{R}_{\boldsymbol{s}}\mathbf{A}^{H}) = K$ while $\mathbf{H}$ and $\mathbf{U}$ are full rank matrices, it follows that $(M\text{-}K)$ eigenvalues of $[\mathbf{H}^{-1}\mathbf{A}\mathbf{R}_{\boldsymbol{s}}\mathbf{A}^{H}\mathbf{H}^{-H}]$ on the main diagonal of $[\mathbf{\Lambda} - \sigma_{\boldsymbol{w}}^2\mathbf{I}]$ must vanish, or, in other words, the $(M\text{-}K)$ smallest eigenvalues of $\mathbf{R}_{\boldsymbol{y}}$ (or, equivalently, generalised eigenvalues of $(\mathbf{R}_{\boldsymbol{x}}, \mathbf{R}_{\boldsymbol{w}})$) must be equal to $\sigma_{\boldsymbol{w}}^2$. Inserting *(E.1.6)* in *(E.1.7)* (or alternatively, starting from *(E.1.1)* and *(E.1.2)*) we also have:

$$\mathbf{A}\mathbf{R}_{\boldsymbol{s}}\mathbf{A}^{H}\mathbf{V} = \mathbf{R}_{\boldsymbol{w}}\mathbf{V}[\mathbf{\Lambda} - \sigma_{\boldsymbol{w}}^2\mathbf{I}] \qquad \cdots (E.1.8)$$

Arranging eigenvalues in decreasing order of magnitude it immediately follows that:

$$\mathbf{A}\mathbf{R}_{\boldsymbol{s}}\mathbf{A}^{H}\boldsymbol{V}_i = \boldsymbol{0} \quad , \quad K \le i \le M\text{-}1$$

which, when pre-multiplied by $\mathbf{R}_{\boldsymbol{s}}^{-1}(\mathbf{A}^{H}\mathbf{A})^{-1}\mathbf{A}^{H}$ yields

$$\mathbf{A}^{H}\boldsymbol{V}_i = \boldsymbol{0} \quad , \quad K \le i \le M\text{-}1 \qquad \cdots (E.1.9)$$

The set of generalised eigenvectors $\{\boldsymbol{V}_i\}_{i=K}^{M-1}$ associated with the smallest $(M\text{-}K)$ generalised eigenvalues of $(\mathbf{R}_{\boldsymbol{x}}, \mathbf{R}_{\boldsymbol{w}})$ therefore spans the 'noise sub-space' of vectors that are orthogonal to the columns of $\mathbf{A}$. In addition, as the bottom $(M\text{-}K)$ rows of $[\mathbf{\Lambda} - \sigma_{\boldsymbol{w}}^2\mathbf{I}]$ are zero, *(E.1.8)* leads to:

$$\mathbf{A}\mathbf{R}_{\boldsymbol{s}}\mathbf{A}^{H}[\boldsymbol{V}_0\,\boldsymbol{V}_1 \cdots\cdots \boldsymbol{V}_{K-1}] = \mathbf{R}_{\boldsymbol{w}}[\boldsymbol{V}_0\,\boldsymbol{V}_1 \cdots\cdots \boldsymbol{V}_{K-1}][\mathbf{\Lambda}_s - \sigma_{\boldsymbol{w}}^2\mathbf{I}] \quad \cdots (E.1.10)$$

where $\mathbf{\Lambda}_s$ comprises the top K rows of $\mathbf{\Lambda}$ and $\mathbf{I}$ is the $K \times K$ identity matrix. It is evident from *(E.1.10)* that the column space of $\mathbf{A}$ is spanned by the columns of $\mathbf{R}_{\boldsymbol{w}}[\boldsymbol{V}_0\,\boldsymbol{V}_1 \cdots\cdots \boldsymbol{V}_{K-1}]$. Consequently, the set of vectors $\{\mathbf{R}_{\boldsymbol{w}}\boldsymbol{V}_i\}_{i=0}^{K-1}$ spans the signal sub-space corresponding to the steering matrix $\mathbf{A}$.

Note that the vectors sets $\{V_0, V_1, \cdots, V_{M-1}\}$ and $\{\mathbf{R}_{\alpha}V_0, \mathbf{R}_{\alpha}V_1, \cdots, \mathbf{R}_{\alpha}V_{M-1}\}$ are not orthogonal. This means that although the noise and signal sub-spaces corresponding to the steering matrix $\mathbf{A}$ are spanned by the sets $\{V_i\}_{i=K}^{M-1}$ and $\{\mathbf{R}_{\alpha}V_i\}_{i=0}^{K-1}$ respectively, they are not spanned by the respective complementary vector sets $\{\mathbf{R}_{\alpha}V_i\}_{i=K}^{M-1}$ and $\{V_i\}_{i=0}^{K-1}$. On the other hand, the signal and noise sub-spaces corresponding to the pre-whitened steering matrix $\mathbf{H}^{-1}\mathbf{A}$ are spanned by the orthonormal vector sets $\{\mathbf{H}^H V_i\}_{i=0}^{K-1}$ and $\{\mathbf{H}^H V_i\}_{i=K}^{M-1}$ respectively[1].

The (narrowband) MUSIC spectral pattern

$$\mathcal{P}_{\text{MUSIC}}(\varphi) = \frac{1}{\mathbf{A}^H(\varphi, \omega_0)\mathbf{V}_{\alpha}\mathbf{V}_{\alpha}^H\mathbf{A}(\varphi, \omega_0)} \qquad \cdots (E.1.11)$$

is obtained from the MVPR pattern for the pre-whitened array

$$\mathcal{P}(\varphi) = \frac{1}{[\mathbf{H}^{-1}\mathbf{A}(\varphi, \omega_0)]^H\Pi^H\mathbf{R}_{\tilde{y}}^{-1}\Pi[\mathbf{H}^{-1}\mathbf{A}(\varphi, \omega_0)]}$$

by setting:

$$\Pi = \sigma_{\alpha}(\mathbf{H}^H\mathbf{V}_{\alpha})(\mathbf{H}^H\mathbf{V}_{\alpha})^H$$

where,

$$\mathbf{V}_{\alpha} = [V_K\, V_{K+1} \cdots\cdots V_{M-1}] \qquad \cdots (E.1.12)$$

(E.1.11) is also obtainable from the MVPR pattern for the unprocessed array:

$$\mathcal{P}(\varphi) = \frac{1}{\mathbf{A}^H(\varphi, \omega_0)\Pi^H\mathbf{R}_X^{-1}\Pi\mathbf{A}(\varphi, \omega_0)}$$

when Π is set to:

$$\Pi = \sigma_{\alpha}\mathbf{R}_{\alpha}\mathbf{V}_{\alpha}\mathbf{V}_{\alpha}^H$$

---

1 [Roy 89] mistakenly assumes $\{\mathbf{R}_{\alpha}V_i\}_{i=K}^{M-1}$ to spans the noise sub-space corresponding to A. This does not affect the development of the ESPRIT algorithm which depends on the (correct) use of $\{\mathbf{R}_{\alpha}V_i\}_{i=0}^{K-1}$ as a vector set that spans the signal sub-space, but it does lead to an incorrect expression for the spectral pattern of MUSIC.

E.2 TOTAL-LEAST-SQUARES MINIMISATION OF *(5.2.74)*

Denoting: $\mathbf{F}_{xy} = [F_{xy_0} F_{xy_1} \cdots\cdots F_{xy_{K-1}}]$, the minimisation of the Frobenius norm in *(5.2.74)* is equivalent to the minimisation of:

$$\min_{F_{xy0}, F_{xy1}, \cdots, F_{xyK-1}} \sum_{k=0}^{K-1} F_{xy_k}^H \tilde{\mathbf{V}}_{xy}^H \tilde{\mathbf{V}}_{xy} F_{xy_k}$$

$$F_{xy_{k'}}^H F_{xy_{k''}} = \begin{cases} 1 & k' = k'' \\ 0 & k' \neq k'' \end{cases} \quad , \quad 0 \leq k', k'' \leq K\text{-}1 \qquad \cdots (E2.1)$$

which may be performed with the aid of a set of K real Lagrange multipliers $\chi_0, \chi_1, \cdots\cdots, \chi_{K-1}$:

$$\frac{\partial}{\partial F_{xy_k}^H} \{ \sum_{k=0}^{K-1} [F_{xy_k}^H \tilde{\mathbf{V}}_{xy}^H \tilde{\mathbf{V}}_{xy} F_{xy_k} + \chi_k (1 - F_{xy_k}^H F_{xy_k})] \} = 0 \quad , \quad 0 \leq k \leq K\text{-}1 \qquad \cdots (E2.2)$$

In *(E.2.2)*, $\frac{\partial}{\partial F_{xy_k}^H}$ denotes the complex gradient operator of differentiation with respect to a complex vector as defined and explained in [BRA 83] and also in appendix B of [HAY 91]. The result is:

$$[\tilde{\mathbf{V}}_{xy}^H \tilde{\mathbf{V}}_{xy}] F_{xy_k} = F_{xy_k} \chi_k \quad , \quad 0 \leq k \leq K\text{-}1 \qquad \cdots (E2.3)$$

which means that $\chi_0, \chi_1, \cdots, \chi_{K-1}$ and $F_{xy_0}, F_{xy_1}, \cdots, F_{xy_{K-1}}$ must be eigenvalues of the hermitian matrix $[\tilde{\mathbf{V}}_{xy}^H \tilde{\mathbf{V}}_{xy}]$ and their corresponding eigenvectors, respectively. Pre-multiplying *(E.2.3)* by $F_{xy_k}^H$ and invoking the constraint from *(E.2.1)* we obtain:

$$F_{xy_k}^H \tilde{\mathbf{V}}_{xy}^H \tilde{\mathbf{V}}_{xy} F_{xy_k} = \chi_k \quad , \quad 0 \leq k', k'' \leq K\text{-}1 \qquad \cdots (E2.4)$$

which immediately leads to

$$\| \tilde{\mathbf{V}}_{xy} \mathbf{F}_{xy} \|_F^2 = \sum_{k=0}^{K-1} \chi_k \qquad \cdots (E2.5)$$

From *(E.2.5)* it is clear that $\| \tilde{\mathbf{V}}_{xy} F_{xy_k} \|_F^2$ is minimised when the orthonormal columns of $\mathbf{F}_{xy}$ are the eigenvectors corresponding to the K smallest eigenvalues of $[\tilde{\mathbf{V}}_{xy}^H \tilde{\mathbf{V}}_{xy}]$.

E.3 ELEMENT-SPACE COVARIANCE MATRIX FOR A CIRCULAR ARRAY UNDER AN ISOTROPIC NOISE FIELD

Consider a circular array of M equally-spaced radially-symmetric sensors, arranged on a ring of radius R on the (horizontal) xy-plane, and assume the sensors to be horizontally omni-directional, i.e. be characterised by element patterns that are independent of the azimuth angle φ. Denote the spatial power density of the ambient noise field by $\mathcal{N}(\omega, \theta, \varphi)$, and the cross-spectral density matrix of the ambient noise field contribution at the M array sensors by $\mathbf{P}_{n_a}(\omega)$. For a spatially-white noise-field that is statistically independent with respect to direction we then have:

$$[P_{n_a}(\omega)]_{m'm''} \approx \frac{1}{M}\int_0^{\pi} d\theta\, g_\theta^2(\theta,\omega)\sin\theta$$

$$\int_{-\pi}^{\pi} d\varphi\, \mathcal{N}(\omega,\theta,\varphi)\, e^{j(\omega R/c)[\cos(\varphi-2\pi m'/M)-\cos(\varphi-2\pi m''/M)]\sin\theta} \qquad \cdots (E3.1)$$

where $[P_{n_a}]_{m'm''}$ is the $m'm''$'th element of $\mathbf{P}_{n_a}$ and $g_\theta(\theta,\omega)$ is the common elevation pattern of the sensors. But the last term on the right hand side of *(E.3.1)* is given by:

$$e^{j(\omega R/c)[\cos(\phi-2\pi m'/M)-\cos(\phi-2\pi m''/M)\sin\theta} =$$

$$\sum_{\nu'=-\infty}^{\infty}\sum_{\nu''=-\infty}^{\infty} j^{\nu'-\nu''} J_{\nu'}\left(\frac{\omega R}{c}\sin\theta\right) J_{\nu''}\left(\frac{\omega R}{c}\sin\theta\right) e^{j(2\pi/M)(m'\nu'-m''\nu'')} e^{-j(\nu'-\nu'')\phi} \qquad \cdots (E3.2)$$

where $J_\nu(x)$ is Bessel function of the first kind of order ν and argument x. Inserting *(E.3.2)* into *(E.3.1)* leads, for a horizontally isotropic noise field $\mathcal{N} = \mathcal{N}(\omega, \theta)$, to:

$$[P_{n_a}(\omega)]_{m'm''} = \frac{1}{M}\int_0^{\pi} d\theta \sum_{\nu'=-\infty}^{\infty}\sum_{\nu''=-\infty}^{\infty} j^{\nu'-\nu''} J_{\nu'}\left(\frac{\omega R}{c}\sin\theta\right) J_{\nu''}\left(\frac{\omega R}{c}\sin\theta\right)$$

$$e^{j(2\pi/M)(m'\nu'-m''\nu'')} g_\theta^2(\theta,\omega)\mathcal{N}(\omega,\theta)\sin\theta \int_{-\pi}^{\pi} d\varphi\, e^{-j(\nu'-\nu'')\varphi}$$

$$= \frac{2\pi}{M}\int_0^{\pi} d\theta \sum_{\nu=-\infty}^{\infty} J_\nu^2\left(\frac{\omega R}{c}\sin\theta\right) e^{j(2\pi/M)(m'-m'')\nu} g_\theta^2(\theta,\omega)\mathcal{N}(\omega,\theta)\sin\theta$$

$$= \frac{2\pi}{M}\int_0^{\pi} d\theta\, J_0\left(\frac{2\omega R}{c}\sin[\pi(m'-m'')/M]\sin\theta\right) g_\theta^2(\theta,\omega)\mathcal{N}(\omega,\theta)\sin\theta \qquad \cdots (E3.3)$$

where use has been made of the Bessel identity:

$$\sum_{\nu=-\infty}^{\infty} J_\nu^2(x)e^{j\nu y} = J_0(2x\sin(y/2)) \qquad \cdots (E3.4)$$

Let us now consider two extreme cases: *i* an impulsive noise field at some angle θ_0
ii isotropic noise-field and element pattern

In the first case, *(E3.3)* simplifies to:

$$\begin{aligned}[P_{nn}(\omega)]_{m'm''} &= \eta_a(\omega)J_0\left(\frac{2\omega R}{c}\sin[\pi(m'-m'')/M]\sin\theta_0\right) \\ \eta_a(\omega) &= (2\pi/M)\mathcal{N}(\omega,\theta_0)g_\theta^2(\theta_0,\omega)\sin\theta_0\end{aligned} \qquad \cdots (E3.5)$$

whereas in the isotropic case we may use the Bessel identity

$$\int_0^\pi d\theta J_0(x\sin\theta)\sin\theta = 2\sin x/x \qquad \cdots (E3.6)$$

to obtain:

$$[P_{nn}(\omega)]_{m'm''} = \eta_a(\omega)\sin[(2\omega R/c)\sin(\pi(m'-m'')/M)]/[(2\omega R/c)\sin(\pi(m'-m'')/M)]$$

$$\eta_a(\omega) = (4\pi/M)\mathcal{N}(\omega)g_\theta^2(\omega) \qquad \cdots (E3.7)$$

Under an impulsive noise-field, it is clear from *(E3.5)* that for the pairwise cross-spectral power density (and therefore also the narrowband covariance) to fall to zero, $(2\omega R/c)\sin((m'-m'')\pi/M)$ must be equal to one of the zeros of J_0. But since the zeros of J_0 are not uniformly spaced, there can be no frequency and array radius at which the noise of *all* pairs of sensors becomes uncorrelated (or, in other words, spatially-white). This point is illustrated in Table E.3.1 for an 8-sensor circular array under an impulsive noise field at $\theta_0 = \pi/2$, where the different (arcwise) inter-element spacings required to decorrelate the noise at different array elements are listed.

In the case of isotropic noise and element pattern, it follows from *(E3.7)* that in order to decorrelate the noise at the array sensors, we must have:

$$(2\omega R/c)\sin(\pi(m'-m'')/M) = (m'-m'')\pi \qquad \cdots (E3.8)$$

Obviously, *(E.3.8)* cannot be simultaneously satisfied by all $(m'-m'')$ and full spatial whiteness of the noise cannot be achieved. Note though that the noise between (isotropic) neighbouring sensors of a large circular array is nearly decorrelated if the arcwise inter-element spacing is set to half a wavelength. This follows directly from *(E.3.8)* when $(m'-m'')/M << 1$, and is also evident from Table E.3.2 which lists the (arcwise) inter-element spacings required to decorrelate the noise at different isotropic elements of an 8-sensor array under an isotropic noise field; for $m'-m'' = \pm 1$ the decorrelating inter-element spacing is close to half a wavelength.

$m'-m''$	±1, ±7	±2, ±6	±3, ±5	±4
d/λ	0.393	0.488	0.585	0.737

Table E.3.1: Inter-element spacing (in wavelengths) d/λ at which $[P_{nn_a}(\omega)]_{m'm''} = 0$ for an 8-element circular array under an impulsive noise field at zero elevation ($\theta_0 = \pi/2$)

$m'-m''$	±1, ±7	±2, ±6	±3, ±5	±4
d/λ	0.513	0.555	0.638	0.785

Table E.3.2: Inter-element spacing (in wavelengths) d/λ at which $[P_{nn_a}(\omega)]_{m'm''} = 0$ for an 8-element circular array of isotropic sensors under an isotropic noise field

In the case of an equally-spaced horizontal linear array, true spatial whiteness is only achieved in an isotropic or hemispherically-isotropic noise-field when the sensors are isotropic and spaced half a wavelength apart – see [BUR 91] for cross-spectral noise densities under isotropic, semi-isotropic[2], impulsive and surface noise distributions.

---

2 The derivation presented in [BUR 91] for the cross-spectral power density in a linear array under semi-isotropic noise-field appears to be erroneous. Using our nomenclature, the expression for $[P_{nn_a}]_{m'm''}$ under a semi-isotropic noise-field $\mathcal{N}(\omega, \theta)=[\eta_a(\omega)/2\pi(1-\cos\theta_0)][1+\mathrm{sgn}(\theta-\theta_0)]$ is:

$$[P_{nn_a}(\omega)]_{m'm''}=\frac{\eta_a(\omega)}{(1-\cos\theta_0)}\int_0^{\theta_0} d\theta \sin\theta J_0[\frac{\omega d}{c}(m''-m')\sin\theta]$$

which only equals $(2\theta_0/\pi)\eta_a(\omega)\sin[\frac{\omega d}{c}(m''-m')\sin\theta_0]/[\frac{\omega d}{c}(m''-m')\sin\theta_0]$ as suggested in [BUR 91] when $\theta_0=\pi/2$ or π.

E.4 RANK OF THE MODIFIED SIGNAL COVARIANCE MATRIX

Consider the $K \times K$ covariance matrix $\mathbf{R_S}$ of the received signals, and let its rank be given by $(K-K_0)$. We may express $\mathbf{R_S}$ (conveniently normalised to $(M'-M''+1)$, the number of phase-mode subsets formed in the spatial smoothing scheme of section 5.4, sub-section 5.4.2) in terms of its eigenvalue matrix $\mathbf{\Lambda}$ and the corresponding (orthonormal) eigenvector matrix $\mathbf{U}$:

$$\frac{1}{(M'-M''+1)}\mathbf{R_S} = \mathbf{U\Lambda U}^H \qquad \cdots (E.4.1)$$

Note that $\mathbf{U}$ is full-rank whereas the diagonal matrix $\mathbf{\Lambda}$ has rank $(K-K_0)$ with K_0 zero eigenvalues on the main diagonal. Expression *(5.4.5)* for the modified signal covariance matrix $\bar{\mathbf{R}}_\mathbf{S}$ may be rewritten as:

$$\bar{\mathbf{R}}_\mathbf{S} = \sum_{v=0}^{M'-M''} \mathbf{\Psi}^v \mathbf{U\Lambda U}^H \mathbf{\Psi}^{Hv} = \mathbf{DD}^H \qquad \cdots (E.4.2)$$

where $\mathbf{\Psi}$ is defined by *(5.4.2)*, and

$$\mathbf{D} = [\mathbf{I}\ \mathbf{\Psi}\ \mathbf{\Psi}^2 \ldots\ldots \mathbf{\Psi}^{M'-M''}] \begin{pmatrix} \mathbf{U} & & & & \\ & \mathbf{U} & & & \\ & & \ddots & & \\ & & & \mathbf{U} & \\ & & & & \mathbf{U} \end{pmatrix} \begin{pmatrix} \mathbf{\Lambda}^{1/2} & & & & \\ & \mathbf{\Lambda}^{1/2} & & & \\ & & \ddots & & \\ & & & \mathbf{\Lambda}^{1/2} & \\ & & & & \mathbf{\Lambda}^{1/2} \end{pmatrix}$$

$$= [\mathbf{U\Lambda}^{1/2}\ \ \mathbf{\Psi U\Lambda}^{1/2}\ \ \mathbf{\Psi}^2\mathbf{U\Lambda}^{1/2} \ldots\ldots \mathbf{\Psi}^{M'-M''}\mathbf{U\Lambda}^{1/2}] \qquad \cdots (E.4.3)$$

and $\mathbf{\Lambda}^{1/2}$ has the square roots of the eigenvalues of $\mathbf{R_S}$ on its main diagonal. Clearly,

$$\text{rank}\ \bar{\mathbf{R}}_\mathbf{S} = \text{rank}\ \mathbf{D} \qquad \cdots (E.4.4)$$

and by rearranging the columns of $\mathbf{D}$ (which has no effect on the rank of the matrix), we obtain:

$$\text{rank}\mathbf{D} = \text{rank}(\mathbf{ZG}) \qquad \cdots (E.4.5)$$

where:

$$\mathbf{Z} = \begin{pmatrix} \zeta_{00} & 0 & \cdots & 0 & \zeta_{01} & 0 & \cdots & 0 & \zeta_{0(K-1)} & 0 & \cdots & 0 \\ 0 & \zeta_{10} & & \vdots & 0 & \zeta_{11} & & \vdots & 0 & \zeta_{1(K-1)} & & \vdots \\ \vdots & & \ddots & 0 & \vdots & & \ddots & 0 & \cdots & \vdots & \ddots & 0 \\ 0 & \cdots & 0 & \zeta_{(K-1)0} & 0 & \cdots & 0 & \zeta_{(K-1)1} & 0 & \cdots & 0 & \zeta_{(K-1)(K-1)} \end{pmatrix} \quad \cdots (E.4.6)$$

$$\mathbf{G} = \begin{pmatrix} \Gamma & & & \\ & \Gamma & & \\ & & \ddots & \\ & & & \Gamma \end{pmatrix} \quad \cdots (E.4.7)$$

with $\zeta_{k'k''}$ denoting the $k'k''$'th element of $\mathbf{U}\mathbf{\Lambda}^{1/2}$ and Γ being given by:

$$\Gamma = [\gamma_0 \; \gamma_1 \cdots\cdots \gamma_{K-1}]^H \quad \cdots (E.4.8)$$

$$\gamma_k = [1 \; e^{-j\phi_k} \; e^{-j2\phi_k} \cdots\cdots e^{-j(M'-M'')\phi_k}]^T \quad , \quad 0 \le k \le K-1 \quad \cdots (E.4.9)$$

The $K^2 \times (M'-M''+1)K$ matrix $\mathbf{G}$ has a block Vandermonde structure and is therefore of full rank K^2 provided it has more columns than rows, or, in other words, as long as

$$M'-M'' \ge K \quad \cdots (E.4.10)$$

The K rows of $\mathbf{Z}$ are clearly linearly independent (none of the rows can have all its elements equal to zero, or else the corresponding signal variance would also be zero), so that rank$\mathbf{Z} = K$. By the Sylvester's law of nullity[3] we therefore have:

$$\left.\begin{aligned} &\text{rank}\mathbf{D} \le \min(\text{rank}\mathbf{Z}, \text{rank}\,\mathbf{G}) = K \\ &\text{rank}\mathbf{D} \ge \text{rank}\mathbf{Z} + \text{rank}\mathbf{G} - K^2 = K \end{aligned}\right\} \Rightarrow \text{rank}\mathbf{D} = K$$

The rank of $\mathbf{D}$ and therefore of the smoothed covariance matrix $\bar{\mathbf{R}}_S$ is thus equal to K subject to condition *(E.4.10)*.

---

[3] Sylvester's law of nullity [MIR 55], [WYL 75] states that if $\mathbf{A}$ is an $L_A \times L_{AB}$ matrix of rank ρ_A and $\mathbf{B}$ is an $L_{AB} \times L_B$ matrix of rank ρ_B, then:

$$\rho_A + \rho_B - L_{AB} \le \text{rank}(\mathbf{AB}) \le \min(\rho_A, \rho_B)$$

E.5 SINGULARITY OF SIGNAL CROSS-SPECTRAL DENSITY MATRIX FOR FULLY CORRELATED SIGNALS

Consider the tempo-spatial covariance matrix $\mathbf{R}_{\mathbf{s}}(\tau) = \mathcal{E}\mathbf{s}(t)\mathbf{s}^H(t-\tau)$ and its Fourier transform $\mathbf{P}_{\mathbf{s}}(\omega)$ for the wideband signal vector

$$\mathbf{s}(t) = [s_0(t)\ s_1(t)\ s_2(t) \cdots\cdots\ s_{K-1}(t)]^T$$

where two of the signals, say $s_0(t)$ and $s_1(t)$, are coherent, so that for some time delay t_0 and a complex constant ξ:

$$s_0(t) = \xi\, s_1(t-t_0) \qquad \cdots (E5.1)$$

Denoting

$$r_{k'k''}(\tau) = \mathcal{E}s_{k'}(t)s^*_{k''}(t-\tau)$$
$$p_{k'k''}(\omega) = \int_{-\infty}^{\infty} d\tau r_{k'k''}(\tau)e^{-j\omega\tau} \quad , \quad 0 \le k', k'' \le K-1 \qquad \cdots (E5.2)$$

we have:

$$\mathbf{R}_{\mathbf{s}}(\tau) = \begin{pmatrix} |\xi|^2 r_{11}(\tau) & \xi\, r_{11}(\tau-t_0) & \xi\, r_{12}(\tau-t_0) & \cdots & \xi\, r_{1(K-1)}(\tau-t_0) \\ \xi^* r_{11}(\tau+t_0) & r_{11}(\tau) & r_{12}(\tau) & \cdots & r_{1(K-1)}(\tau) \\ \xi^* r_{21}(\tau+t_0) & r_{21}(\tau) & r_{22}(\tau) & \cdots & r_{2(K-1)}(\tau) \\ \vdots & \vdots & \vdots & \ddots & \vdots \\ \xi^* r_{(K-1)1}(\tau+t_0) & r_{(K-1)1}(\tau) & r_{(K-1)2}(\tau) & \cdots & r_{(K-1)(K-1)}(\tau) \end{pmatrix} \qquad \cdots (E5.3)$$

and

$$\mathbf{P}_{\mathbf{s}}(\omega) = \begin{pmatrix} |\xi|^2 p_{11}(\omega) & \xi\, p_{11}(\omega)e^{-j\omega t_0} & \xi\, p_{12}(\omega)e^{-j\omega t_0} & \cdots & \xi\, p_{1(K-1)}(\omega)e^{-j\omega t_0} \\ \xi^* p_{11}(\omega)e^{j\omega t_0} & p_{11}(\omega) & p_{12}(\omega) & \cdots & p_{1(K-1)}(\omega) \\ \xi^* p_{21}(\omega)e^{j\omega t_0} & p_{21}(\omega) & p_{22}(\omega) & \cdots & p_{2(K-1)}(\omega) \\ \vdots & \vdots & \vdots & \ddots & \vdots \\ \xi^* p_{(K-1)1}(\omega)e^{j\omega t_0} & p_{(K-1)1}(\omega) & p_{(K-1)2}(\omega) & \cdots & p_{(K-1)(K-1)}(\omega) \end{pmatrix} \qquad \cdots (E5.4)$$

Notice that the first two columns (and also the first two rows) of $\mathbf{P_s}(\omega)$ are linearly dependent, rendering the cross-spectral density matrix singular at all frequencies. The signal covariance matrix $\mathbf{R_s}(0)$ is given by,

$$\mathbf{R_s}(0) = \begin{pmatrix} |\xi|^2 r_{11}(0) & \xi r_{11}^*(t_0) & \xi r_{12}^*(t_0) & \cdots & \xi r_{1(K-1)}^*(t_0) \\ \xi^* r_{11}(t_0) & r_{11}(0) & r_{12}(0) & \cdots & r_{1(K-1)}(0) \\ \xi^* r_{21}(t_0) & r_{21}(0) & r_{22}(0) & \cdots & r_{2(K-1)}(0) \\ \vdots & \vdots & \vdots & \ddots & \vdots \\ \xi^* r_{(K-1)1}(t_0) & r_{(K-1)1}(0) & r_{(K-1)2}(0) & \cdots & r_{(K-1)(K-1)}(0) \end{pmatrix} \quad \cdots (E.5.5)$$

and if:

$$\begin{matrix} r_{k1}(t_0) \neq r_{k1}(0) \\ r_{1k}^*(t_0) \neq r_{1k}(0) \end{matrix} \quad , \quad 1 \leq k \leq K\text{-}1$$

then the first two columns (or first two rows) of $\mathbf{R_s}(0)$ will be linearly-independent and $\mathbf{R_s}(0)$ will generally be full-rank. For flat-spectrum signals in the (angular) frequency band from ω_{LO} to ω_{HI}:

$$r_{k1}(t_0) = 2\cos\left(\frac{\omega_{HI}+\omega_{LO}}{2} t_0\right) \frac{\sin\left(\frac{\omega_{HI}-\omega_{LO}}{2} t_0\right)}{\frac{\omega_{HI}-\omega_{LO}}{2} t_0} p_{k1} \quad , \quad 1 \leq k \leq K\text{-}1$$

and beyond a correlation time of

$$\frac{\omega_{HI}-\omega_{LO}}{2} t_0 \geq \pi \Rightarrow t_0 \geq 2\pi/(\omega_{HI}-\omega_{LO})$$

$|r_{k1}(t_0)|$ is indeed much smaller than $r_{k1}(0)$.

F. BEAMFORMING SIMULATION PROGRAM

F.1 GENERAL OVERVIEW

RING is a user-friendly personal-computer program, written in QuickBasic, for the analysis of a ring array of discrete radiating elements. It may be used to assess the effectiveness of pre-DFT and post-DFT alignment in arrays of user-specified elements, analyse, under various configurations and error models, the beamwidth and sidelobe performance of directional beams formed in either element space or mode space, display the amplitude and phase characteristics of omnidirectional phase modes, and simulate phase-comparison DF based on either omnidirectional or sectoral phase modes patterns. The compiled RING package (final update: 12th March 1993), running on a DOS platform, comprises four executable files: RING.EXE, RINGOPT.EXE, RINGDSP.EXE and RINGHLP.EXE which must all reside in the same directory (default: `C:\RING` or else the user will be prompted for the exact directory path), as well as the QuickBasic-4.5 run-time module BRUN45.EXE. The program is started by invoking the first executable file name: `RING`. The corresponding QuickBasic source code comprises four chained program files: RING.BAS, RINGOPT.BAS, RINGDSP.BAS and RINGHLP.BAS, each of which consists of one or more modules of functions and subprograms. For the complete list of modules with their respective sub-modules see Table F.1.1

Input to the program is entered either manually or loaded from pre-saved data files, and includes the array geometry, parametrically synthesised or measured element patterns, pseudo-random aperture excitation errors, element position and element pattern errors, complex element-space and mode-space weighting input, compensation algorithms and ranges of relevant parameters for computation. Output may be graphically displayed in a default or customised form, listed in a scrollable table or saved as an ASCII data file in one of three formats. The first two file formats allow the saved file to be imported and displayed by external charting packages whereas the third is the input/output file format of program RING itself, consisting of all the entered or loaded input data together with the evaluated output.

Modules	*Submodules*		
RING.BAS	SUB ArrowLine	SUB AspectRatio	SUB ClearText
	SUB ExitProgram	SUB ExitText	SUB LoadInOut
	SUB LoadInText	SUB LoadRNG	SUB MainDiagram
	SUB MainMenu	SUB MainText	SUB MatLet
	SUB MatSca	SUB SaveData	SUB Welcome
	SUB SaveInput	SUB SaveInText	FUNCTION ATAN2!
	FUNCTION LOG10!	FUNCTION MAX%	FUNCTION MIN%
RINGH.BAS	SUB HelpMain	SUB HelpRandom	SUB HelpSet
RINGI.BAS	SUB InputDiagram	SUB InputMenu	SUB InputText
	SUB LoadEPT	SUB LoadPatt	SUB LoadPattText
	SUB RandomDiagram	SUB RandomMenu	SUB RandomText
	SUB SetDiagram	SUB SetMenu	SUB SetText
	SUB ViewPattData		
RINGHLP.BAS	SUB AspectRatio	SUB ClearText	SUB HelpCorrections
	SUB HelpInput	SUB HelpLoadIn	SUB HelpLoadPatt
	SUB HelpOptions	SUB HelpOutputD	SUB HelpOutputM
	SUB HelpOutputP	SUB HelpOutputR	SUB HelpSaveIn
RINGOPT.BAS	SUB ArrowLine	SUB AspectRatio	SUB ClearText
	SUB CorrectionsDiagram	SUB CorrectionsMenu	SUB CorrectionsText
	SUB MatLet	SUB MatSca	SUB OptionsDiagram
	SUB OptionsMenu	SUB OptionsText	FUNCTION ATAN2!
	FUNCTION LOG10!	FUNCTION MAX%	FUNCTION MIN%
RINGD.BAS	SUB HelpWeightingD	SUB OutDiagramD	SUB OutputMenuD
	SUB OutTextD	SUB WeightingDiagramD	SUB WeightingMenuD
	SUB WeightingTextD		
RINGM.BAS	SUB HelpWeightingM	SUB OutDiagramM	SUB OutputMenuM
	SUB OutTextM	SUB WeightingDiagramM	SUB WeightingMenuM
	SUB WeightingTextM		
RINGP.BAS	SUB OutDiagramP	SUB OutputMenuP	SUB OutTextP
RINGR.BAS	SUB OutDiagramR	SUB OutputMenuR	SUB OutTextR
RINGDSP.BAS	SUB ArrayMul	SUB ArrowLine	SUB AspectRatio
	SUB ClearText	SUB HelpDisplay	SUB HelpSaveOut
	SUB MatAdd	SUB MatAss	SUB MatCnjg
	SUB MatInv	SUB MatLet	SUB MatMul
	SUB MatSca	SUB MatTra	SUB ScaMul
	SUB SetArrays	SUB SetEvector	SUB SetPsiVector
	FUNCTION ATAN2!	FUNCTION ImDiv!	FUNCTION ImInv!
	FUNCTION ImMul!	FUNCTION IntRndPatt!	FUNCTION LOG10!
	FUNCTION MAX%	FUNCTION MIN%	FUNCTION Pulse%
	FUNCTION ReDiv!	FUNCTION ReInv!	FUNCTION ReMul!
RINGC.BAS	SUB ComputeD	SUB ComputeM	SUB ComputeP
	SUB ComputeR	SUB Element45	SUB PostCorrect
	SUB PreCorrSet	SUB PreCorrSingle	SUB PostFilter
	SUB SetElements	SUB SetGmatrix	SUB SetModes
	SUB SetModes2	SUB Sinc	FUNCTION Element!
RINGU.BAS	SUB ArrayMinMax	SUB AutoScale	SUB CustomiseDisp
	SUB CustomiseText	SUB DisplayDiagram	SUB DisplayMenu
	SUB DisplayText	SUB DrawGrid	SUB LabelsMenu
	SUB ListData	SUB ListOutput	SUB PlotOutput
	SUB SaveData	SUB SaveFile	SUB SaveOutput
	SUB SaveOutText	SUB SaveRNG	SUB XscaleMenu
	SUB YscaleMenu	FUNCTION Amplitude	

Table F.1.1 Program structure

RING is fully menu-driven with a 'local' flow chart and a ?help option available at almost every menu levels. There are, however, a few limitations to the current version of the program:

i element patterns may be randomised in amplitude but not in phase
ii only narrowband (single-frequency) pre-DFT correction may be simulated
iii the program does not evaluate the directivity, beamwidth or peak sidelobe level
iv the program cannot generate statistical patterns (minimum and maximum envelope, mean, mean ± standard deviation etc.) from a set of Monte-Carlo runs

A general flow chart of the program is displayed in *Fig. F.1.1*, with the rest of this appendix devoted to a detailed account of all menu screens.

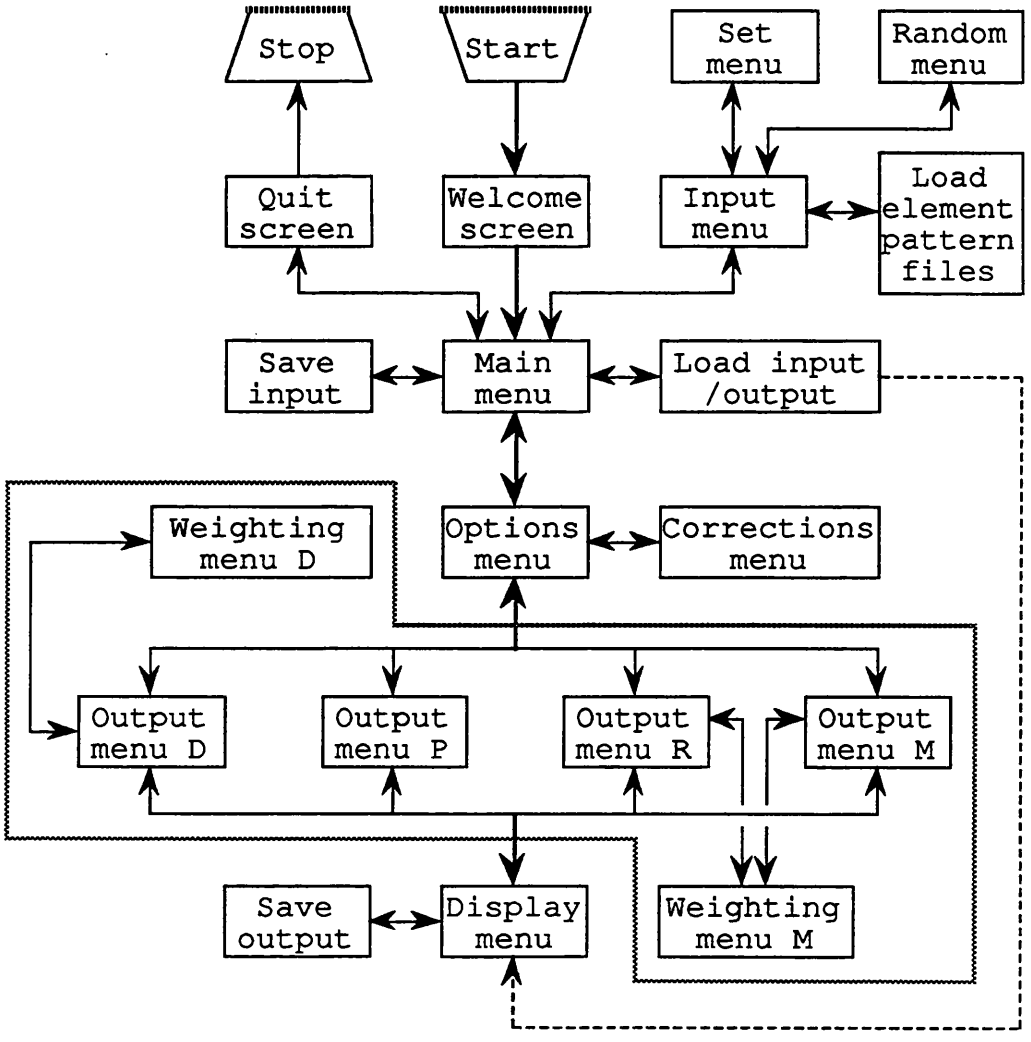

Fig. F.1.1 General flow chart

F.2 WELCOME AND QUIT MENUS

When started, the program displays a 'Welcome screen' which prompts the user to proceed by pressing one of two keyboard letters – see *Fig. F.2.1.* Under the **R** option all inputs to the program are reset to their default values. If the **P** key is pressed, the program loads the inputs and various settings of its previous session from a file called RINGPRF.RNG. This data file is automatically created in the root directory whenever the program quits. In both cases, the program proceeds to the Main menu which is described in section F.3.

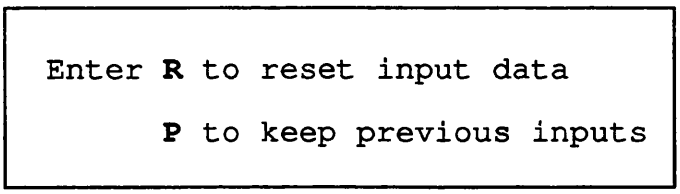

Fig. F.2.1 Welcome menu

The last menu screen before quitting is shown in *Fig. F.2.2.* It is accessible from the Main menu under the **Q**uit program option, prompting the user either to confirm his wish to quit or to return to the Main menu without quitting. Each option may be selected either by hitting the appropriate highlighted letter (**C** or **Q**), or by using the up or down arrow keys ↑ and ↓ to move a red triangular pointer to the desired choice and pressing the **Enter** key. The **C**ancel option is also be selected if the **Esc** key is pressed.

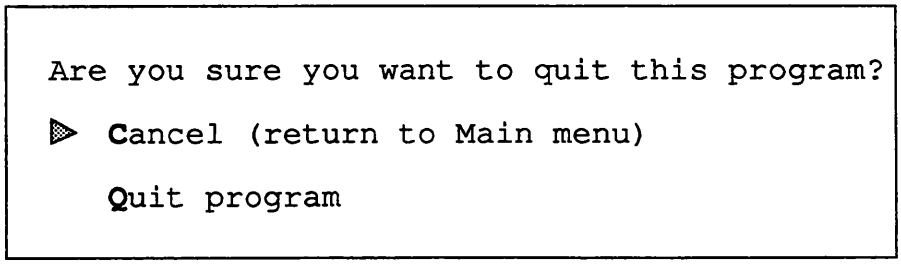

Fig. F.2.2 Quit menu

F.3 MAIN MENU

The Main menu screen which is shown in *Fig. F.3.1* prompts the user for one of six menu options which may be invoked by either using the ↑ and ↓ keys to move a red pointer to the desired choice and then pressing **Enter**, or by hitting the relevant highlighted letter.

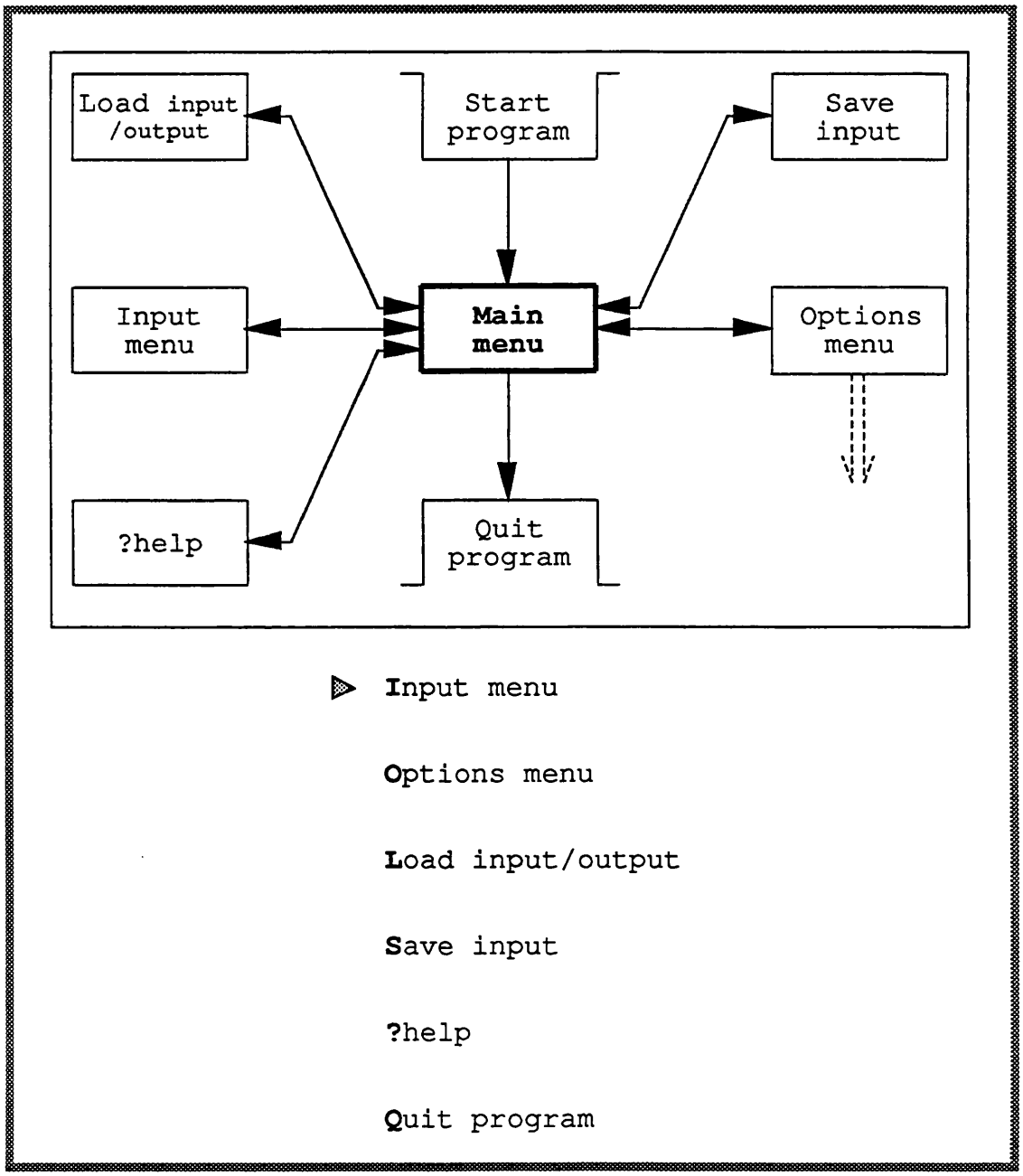

Fig. F.3.1 Main menu screen

F.4 SAVE INPUT MENU

This menu screen which is displayed in *Fig. F.4.1* is accessible from the Main menu, enabling the user to save all of the previously entered input data and settings in the session as a sequential file of ASCII characters, with a user-defined file name + the extension RNG. The file is saved on the storage device selected under the `Select default Drive` option (by using the → or ← key to point a yellow arrow at drive A, B, C or D) and in the directory specified (without the drive letter) under the `Directory Path` option. In addition, this menu may be used to perform the DOS command `DIR` for the selected drive and directory by moving the red pointer (using the ↑ and ↓ keys) to **List** `files (DIR)` and pressing **Enter** (for `DIR/P`) or by pressing **L** (for `DIR/W`).

The saved input file may be read and used as an optional input to the program at a later session through the 'Load input/output' menu which is described in the next section.

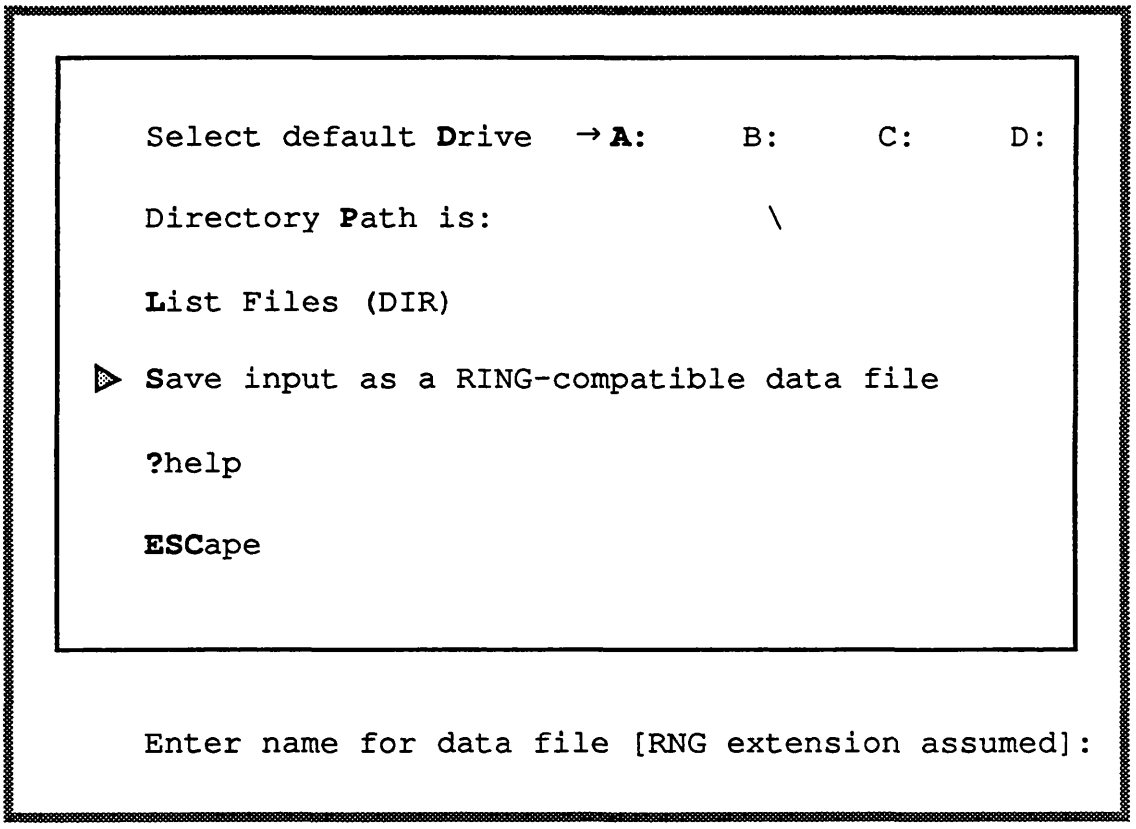

Fig. F.4.1 Save input menu screen

F.5 LOAD INPUT/OUTPUT MENU

This menu, shown in *Fig. F.5.1*, enables the user to read input data which has previously been stored via the 'Save input' menu described in section F.4, or via the 'Save output' menu which is outlined in section F.17. The file, with an assumed RNG extension, is loaded from the storage device and directory specified by the `Select default Drive` and the `Directory Path` options respectively, which also serve to define the `List files (DIR)` option.

If an *input* data file (one that has been stored via the 'Save input' menu) is loaded, pressing the **Esc** key will return the program to the Main menu. If, on the other hand, an *output* data file (stored via the 'Save output' menu) is loaded then both input and previously computed output data will be read by the program and **Esc** will 'short-cut' the program to the Display menu (described and illustrated in section F.15) without further processing, to which it would ordinarily arrive at the end of computations.

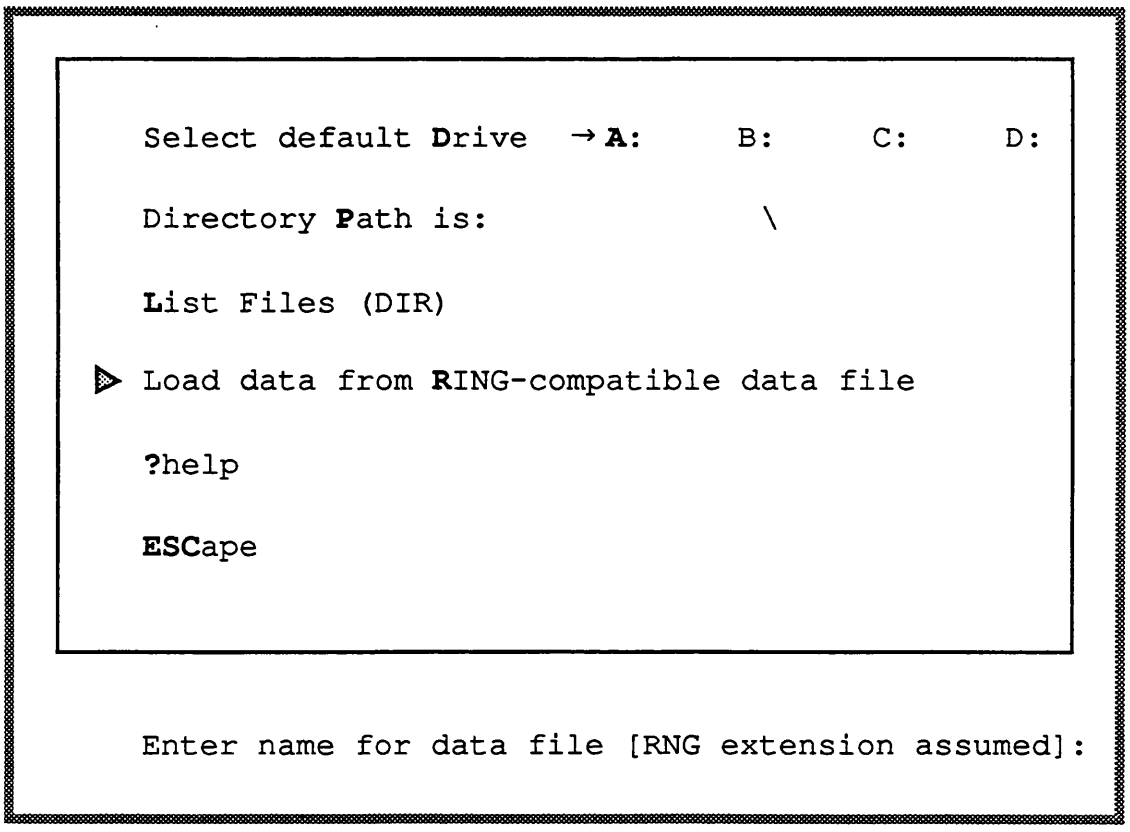

Fig. F.5.1 Load input/output menu screen

F.6 INPUT MENU

The Input menu shown in *Fig. F.6.1* together with its sub-menus are used for defining the geometric and electrical parameters of the array.

The first four options from the top enable the user to define:

i operating frequency f normalised to an arbitrary 'reference frequency' f_0 (default value: 1). f is also equal the first frequency in the **Frequency range** option under the four Output menus described in section F.12 and may therefore be entered or modified from these menus instead.

ii pulse width T multiplied by the above reference frequency f_0. For cw operation (i.e. infinite pulse width), enter: 0 (default value).

iii total number of elements M on the ring (default: $M = 8$)

iv nominal array radius normalised to the wavelength at the reference frequency f_0 (default: $M/4\pi$)

To enter new input (to replace the default or previously entered data) the red pointer is brought next to the required option by either using the ↑ and ↓ keys or by hitting the relevant highlighted letter, and then pressing **Enter** or the → key; the new data may then be entered in the usual way.

Note whenever M is modified, so are the array radius and the number of sampled angles L (see Corrections menu, section F.11). The updated radius is for $\lambda/2$ inter-element spacing at f_0 and L is changed to $2M$. The radius and L may then be modified without affecting M.

The next five options are 'switches', set by first selecting the option as before and then using the → or ← key to point the yellow arrow at any of the optional positions:

i The Element pattern switch sets the element patterns to
- omni-directional
- omni-directional + a random amplitude fluctuation which is defined under the Random menu (section F.8)
- a sum of Fourier (cosine) coefficients + an optional exponential term defined under the Set menu (section F.7)
- the above definition + a random amplitude fluctuation as defined under the Random menu.

- patterns loaded from measured data files via the 'Load element files' menu
- the above data + a random amplitude fluctuation as defined under the Random menu.

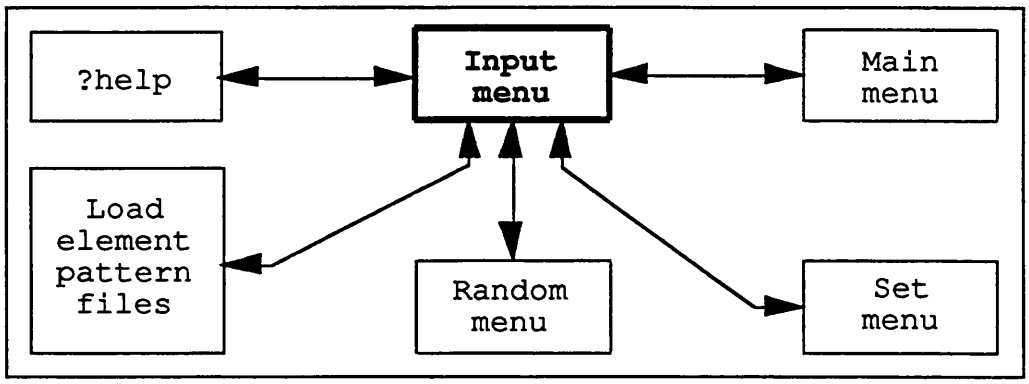


```
▶ Normalised Frequency        → Old    New f/fo = 1.000
  Nmsed Pulse Width (0: cw)   → Old    New  Tfo = 0.0
  Number of eleMents          → Old    New   M  =   8
  Normalised array rAdius     → Old    New a/λo = 0.6366
  Element patterns            →Omni    Rand  Set  Set+Rand
                                       Files Files+Rand
  Phase centre Displacement   →None    Rand  Set  Set+Rand
  Pattern roTation            →Nomin   Rand  Set  Set+Rand
  Element Gains               →Unif    Rand  Set  Set+Rand
  Element Phases              →Unif    Rand  Set  Set+Rand
  Set menu
  Random menu
  Load element pattern files
  ?help
  Back to main menu
```

Fig. F.6.1 Input menu screen

ii The Phase centre displacement switch keeps the elements in their nominal positions (default) or displaces them deterministically, at random or both as defined under the Set and Random menus.

iii The Pattern rotation switch may set each element pattern to be nominally rotated according to the nominal position of the element in the array (default) or to undergo a deterministic or random pattern roll as defined (beyond the nominal values) under the Set and Random menus.

iv The Element gains and Element phases switches set the gain and insertion phase of each channel to 0 dB and 0° respectively (default), or uses the random and/or set definitions entered via the Set and Random menus.

The last five options are invoked by moving the red pointer as before and pressing **Enter** or simply by hitting the highlighted letter. Pressing **B** or the **Esc** key returns the program to the Main menu. The **S**`et menu`, **R**`andom menu` and **L**`oad element pattern files` options are described in sections F.7, F.8 and F.9 respectively.

F.7 SET MENU

Under this menu, which is displayed in *Fig. F.7.1*, the element patterns, the angular and radial displacement and the rotation of each element (beyond its nominal value) as well as the gain and insertion phase of each array channel may be deterministically set and viewed. Options are selected by moving the red pointer with the ↑ and ↓ keys or by pressing the highlighted letter.

Element patterns may be parametrically defined either globally or at two frequencies (typically chosen as the lower and upper operating frequencies) with interpolated values taken in between. In the first case, `Pattern response` **F**`requency` must be set (using the → or ← key) to `All`, whereas in the second case it is set to `Freq1` or to `Freq2` before data is entered. The actual values of the two frequencies are entered by selecting the **I**`nterpolation frequencies` option, pressing **Enter** or the → key and entering the values of the lower (`Freq1`) and upper (`Freq2`) frequencies (normalised to f_0), each followed by **Enter**. Note that there is *no* extrapolation, so that the element pattern remains unchanged below `Freq1` or above `Freq2`.

New values are given to sets of Fourier (cosine) coefficients (in the case of the third option from the top) or to sets of elements or channels (in the case of the next five options) by pressing **Enter** or the → key, entering the new value, the 'From'

number and the 'To' number each followed by **Enter**. In the case of element pattern, coefficient no 7 is ρ in an additional term of the form $\rho^{(1-\cos\varphi)}$.

Each parameter set may be viewed by pressing **L** while the relevant option is selected (including the relevant Pattern response **F**requency option). If necessary the **PageUp** and **PageDown** keys may be used to scroll the list on the screen. The program is returned to the Input menu by pressing **B** or the **Esc** key.

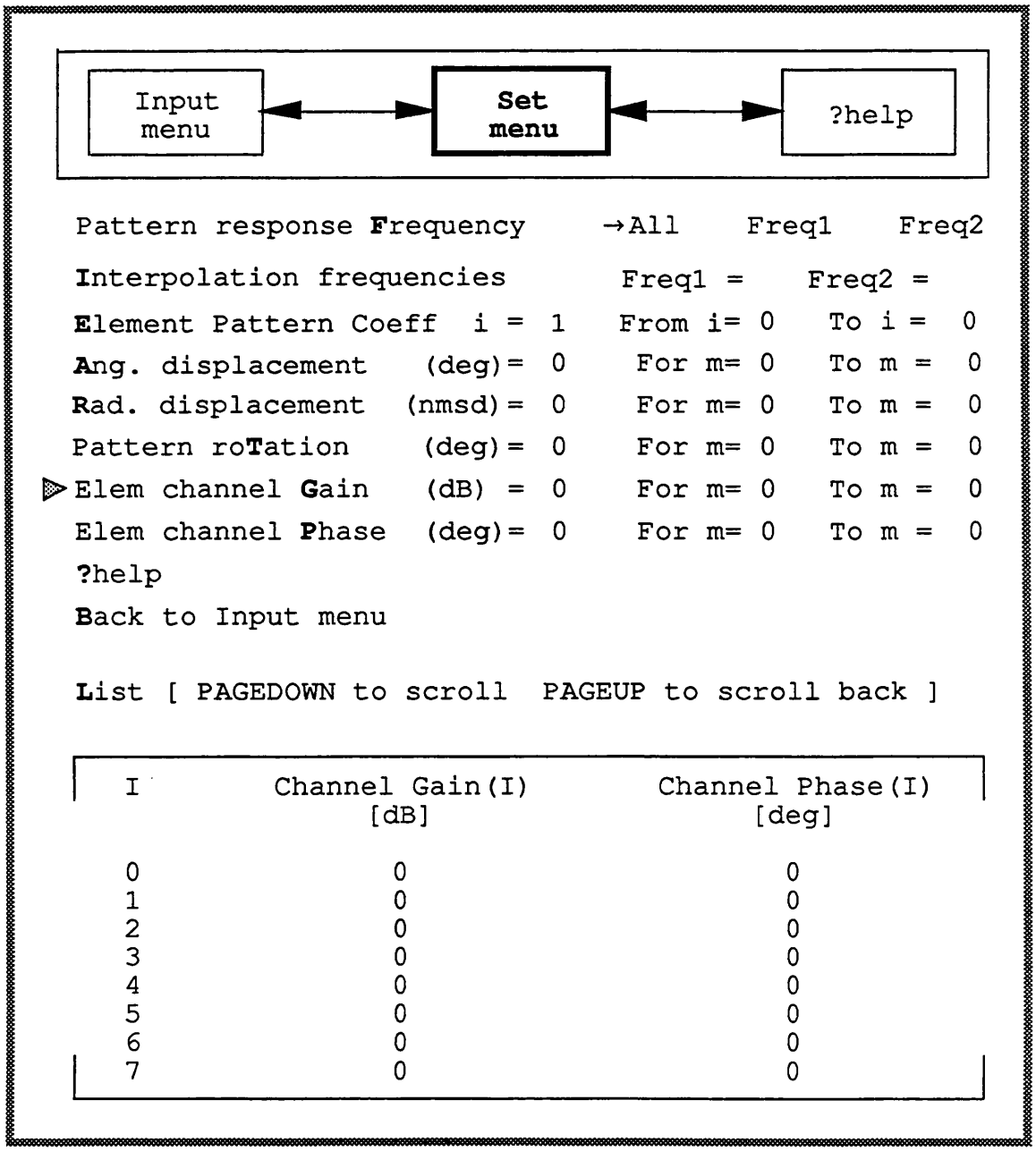

Fig. F.7.1 Set menu screen

F.8 RANDOM MENU

This menu is used to enter uniformly distributed random errors to the array parameters. As shown in *Fig. F.8.1*, the amplitude fluctuation of the element patterns and the random component of the channel gains are expressed in ±dB, the random angular displacement and rotation of each element as well as the electrical insertion phases are expressed in ±degrees and the random radial displacement of the array elements is normalised to the wavelength at the reference frequency f_0. The amplitude fluctuation of the element patterns is randomly generated for each element pattern at L angular directions (the number of sample angles L is entered under the Corrections menu - see section F.11) and interpolated for other angles according to the desired display resolution. The `Random Initialisation integer` option may be used to obtain different ensembles of the pseudo-random generator, but note that new ensembles are always obtained whenever one (or more) of the Input menu switches (see section F.6) is set to `Rand`, `Set+Rand` or `Files+Rand` during the same session. As before pressing **B** or the **Esc** key returns the program to the Input menu.

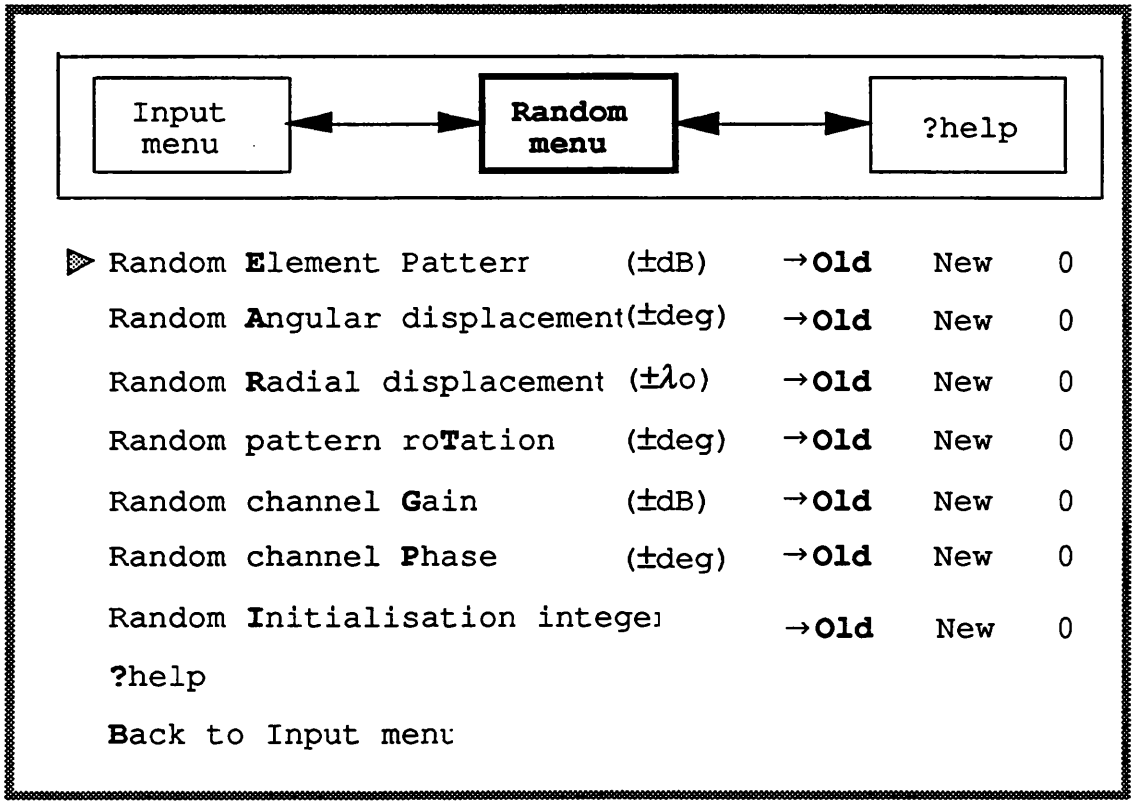

Fig. F.8.1 Random menu screen

F.9 LOAD ELEMENT PATTERN FILE MENU

This menu whose screen is displayed in *Fig. F.9.1* allows the user to read in a measured element pattern file at a single frequency. The file, with an assumed EPT extension, is loaded from the storage device and directory specified by the `Select default Drive` and the `Directory Path` options respectively, which also serve to define the `List files (DIR)` option. The loaded pattern data may be viewed using the `View loaded pattern data` option with the **PageUp** and **PageDown** keys used for scrolling the screen. The program supports the automatic loading of a set of data files whose names are suffixed with appropriate indices (that could, say, denote the frequency as in `PREFIX12.EPT`). To specify the frequencies and corresponding indices to the program, select the `Frequency samples` options, press **Enter** or the → key and type in the first (`From`) and last (`To`) normalised frequencies as well as the frequency step (`Step`), each followed by **Enter**. Then select the `Used file indices` option and enter the first index (`From`) and index step (`Step`) using the **Enter** or the → key, pressing **Enter** after each entry. The set

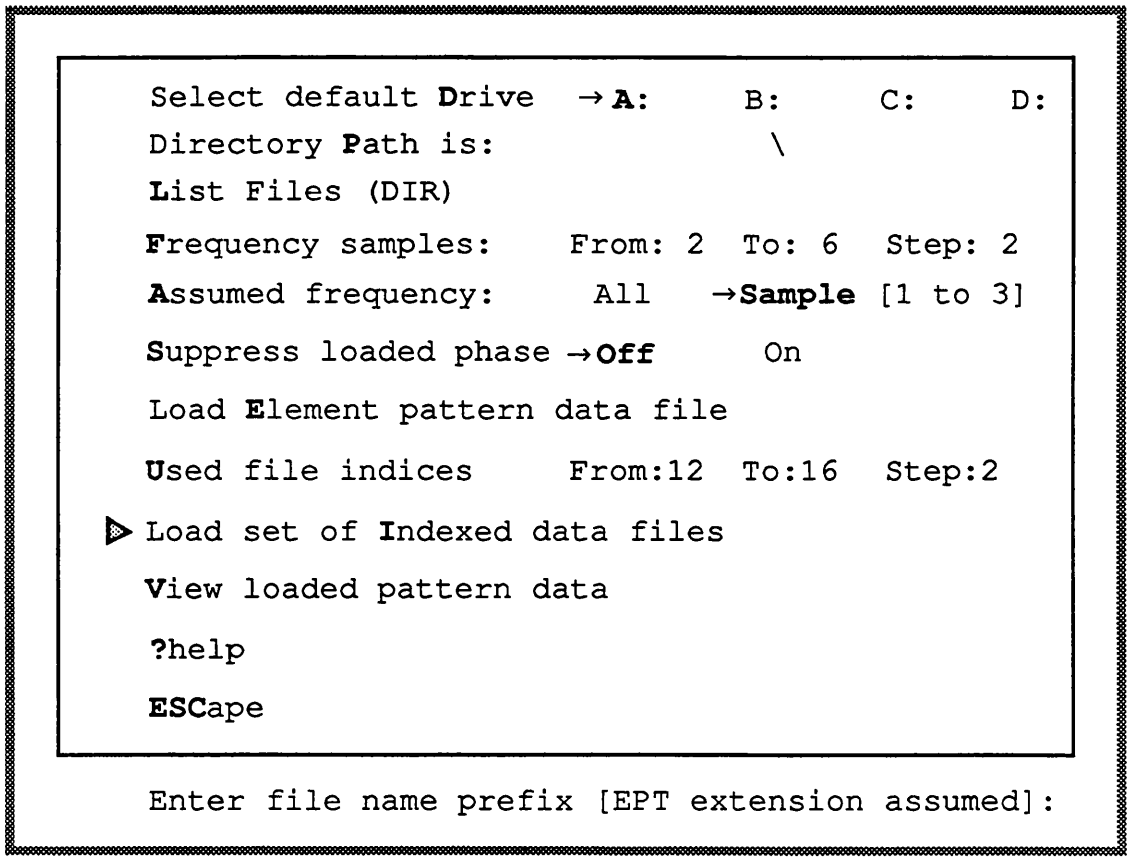

Fig. F.9.1 Load element pattern file menu screen

of files may then be loaded through the `Load a set of Indexed data files` option. For a single file to be loaded, select the **A**`ssumed frequency` option, and use the → or ← keys to switch between `All` (data file to be loaded will be assumed to apply to all frequencies) and `Sample`. In the latter case type in a single frequency sample number and press **Enter**. Then load the file using the `Load` **E**`lement pattern data file` option.
Note the frequency sample number typed in under the **A**`ssumed frequency` option also determines which frequency (i.e. loaded file) is viewed when **V**`iew loaded pattern data` is invoked. If the **A**`ssumed frequency` option is set to `All`, then frequency sample no. 1 is viewed.

Each loaded element pattern file must be a sequential ASCII file that has been filled in the following (QuickBasic) format:

```
OPEN Filename$ + ".EPT" FOR OUTPUT AS #1

WRITE #1, Np%, Ne%, Nr%, AdbRef0!, PhdegRef0!

FOR Elem% = 0 TO Ne% - 1
  FOR Point% = 0 TO Np% - 1
    WRITE #1, Adb!(Point%, Elem%), Phdeg!(Point%, Elem%)
  NEXT Point%
NEXT Elem%

FOR Elem% = 0 TO Ne% - 1
  FOR Point% = 0 TO Np% - 1
    WRITE #1, AdbRef!(Point%, Elem%), PhdegRef!(Point%, Elem%)
  NEXT Point%
NEXT Elem%

CLOSE #1
```

where,

`Np%` - number of samples over a full 360° sector. This integer defines the angular resolution of the measured data

`Ne%` - number of element patterns measured. If this integer is different from the total number of elements in the array then the program assumes that `Ne%=1`, the pattern data is assumed to start at $\varphi = 0°$ for element $m = 0$ and the same data is also entered (after adequate angular rotations) for each of the other array elements. If `Ne%` equals the number of array elements then the program assumes that direction $\varphi = 0°$ always refers to the location of element $m = 0$.

`Nr%` - number of reference patterns measured. Set:

`Nr%=0` when no reference data is available

`Nr%=1` when all patterns are to share the same reference (relevant when array channels are simultaneously measured)

`Nr%=Ne%` when `Ne%` reference patterns are included in the file

`Adb!(Point%, Elem%)` refers to the amplitude in dB of the measured radiation pattern of element no. `Elem%` at an observation angle of `(Point%/Np%) 360°`.

`Phdeg!(Point%, Elem%)` refers to the electrical phase in degrees of the measured radiation pattern of element no. `Elem%` at an observation angle of `(Point%/Np%) 360°`.

`AdbRef!(Point%, Elem%)` measured reference amplitude in dB of element no. `Elem%` at an observation angle of `(Point%/Np%) 360°`.

`PhdegRef!(Point%, Elem%)` measured reference phase in degrees of element no. `Elem%` at an observation angle of `(Point%/Np%) 360°`.

`AdbRef0!` - additional constant amplitude (dB) reference

`PhdegRef0!` - additional constant phase (deg) reference

The loaded element pattern phases may be suppressed and replaced by the usual synthesised geometry-dependent phases by setting the `Suppress loaded phases` option to `On` using the → or ← keys.
The program is returned to the Input menu by pressing the **Esc** key.

F.10 OPTIONS MENU

As shown in *Fig. F.10.1*, the Options menu directs the user to a number of menus which define various options of the program:

- Specifying the type of correction and alignment implemented
- Plotting one or more phase mode patterns
- Plotting one or more directly-formed (element-space) array patterns
- Plotting one or more modally-formed (mode-space) radiation patterns
- Plotting the comparative pattern of two (SPM-) beams identically formed by the same number of equally excited but different phase modes.

These are all described in detail in sections F.11 and F.11.

The program is returned to the Main menu by pressing `B` or the **Esc** key.

F.11 CORRECTIONS MENU

This menu shown in *Fig. F.11.1* allows the user to enable or disable narrowband pattern correction ('PrE-DFT correction') at frequency f (defined via the Input menu or output menus – see the respective sections F.6 and F.12) and two options of either narrowband (at frequency f) or broadband mode alignment ('Post DFT correction'). `No of sampled angLes` refers to the number of (equally spaced) sampled direction angles which enter the correction algorithms (the display resolution is separately defined in the Output menus of section F.12) – the default value is $L=2M$. The next two options from the top refer to wideband mode alignment. `No of sampled frequencies` is the number N of frequency samples used to define digital IIR or FIR mode-alignment filters. The sampled band is from the mix-down

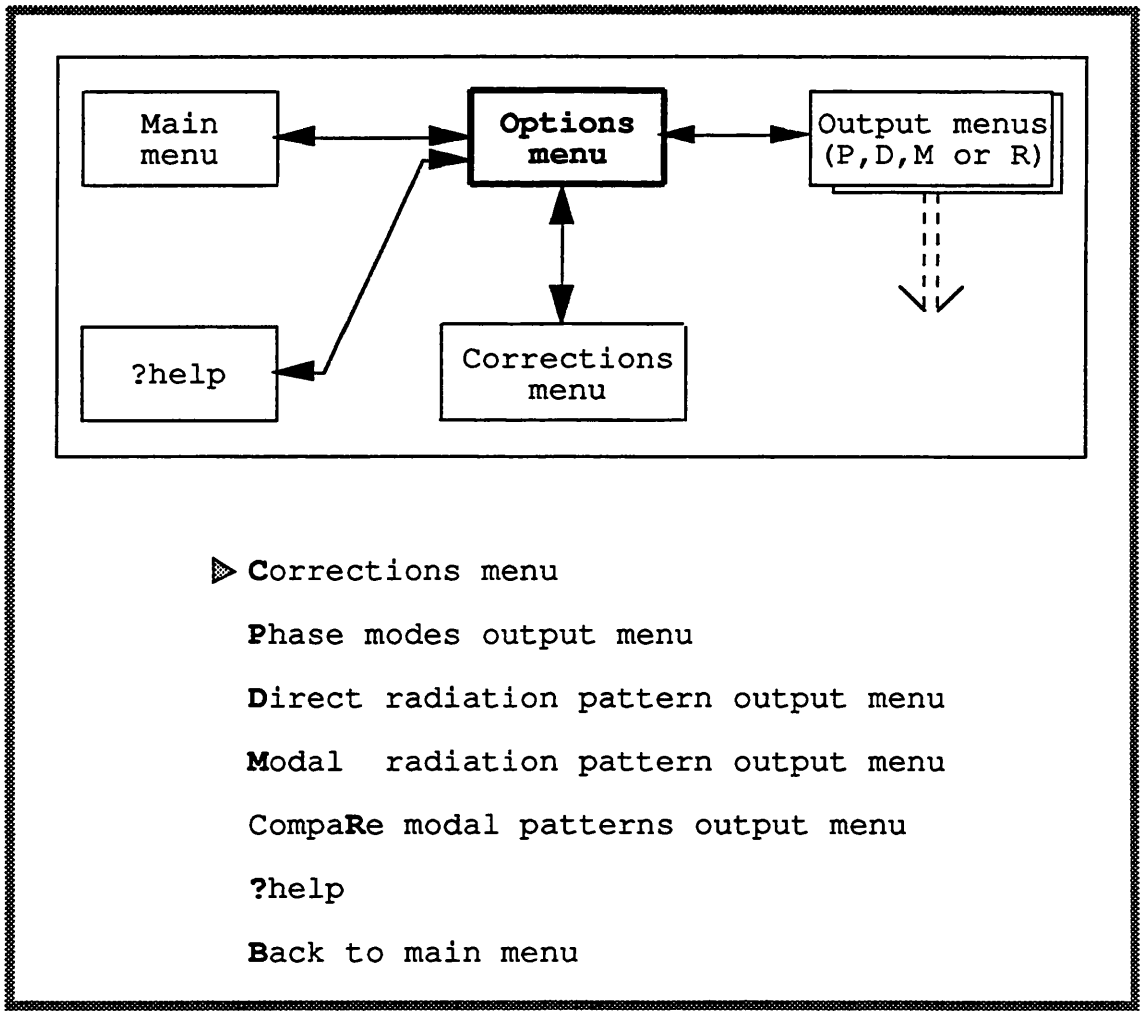

Fig.F.10.1 Options menu screen

frequency shift (entered, normalised to f_0, under the **Mix** down to baseband option, 0 if Off) to the sampling frequency. The latter is specified (normalised to f_0) under the **S**ampling frequency option. The first $(N+1)/2$ samples are taken from measurements or synthesised data, with the last two samples (3 for even N) weighted down. A complex conjugate version of these samples is then added in reverse order about the $(N/2)$'th position in the sequence. **C**orrected modes lets the user define the range of modes which will be affected by the correction schemes. The IIR and FIR settings of the **P**ost-DFT correction option refer to the filters discussed in chapter 3, section 3.6 where the order of the FIR filter (or filter block in the IIR implementation) is $N-1$. Note though that modes $\pm M/2$ undergo amplitude rather than phase mode alignment.

Return to the Options menu is via keys **B** or **Esc**.

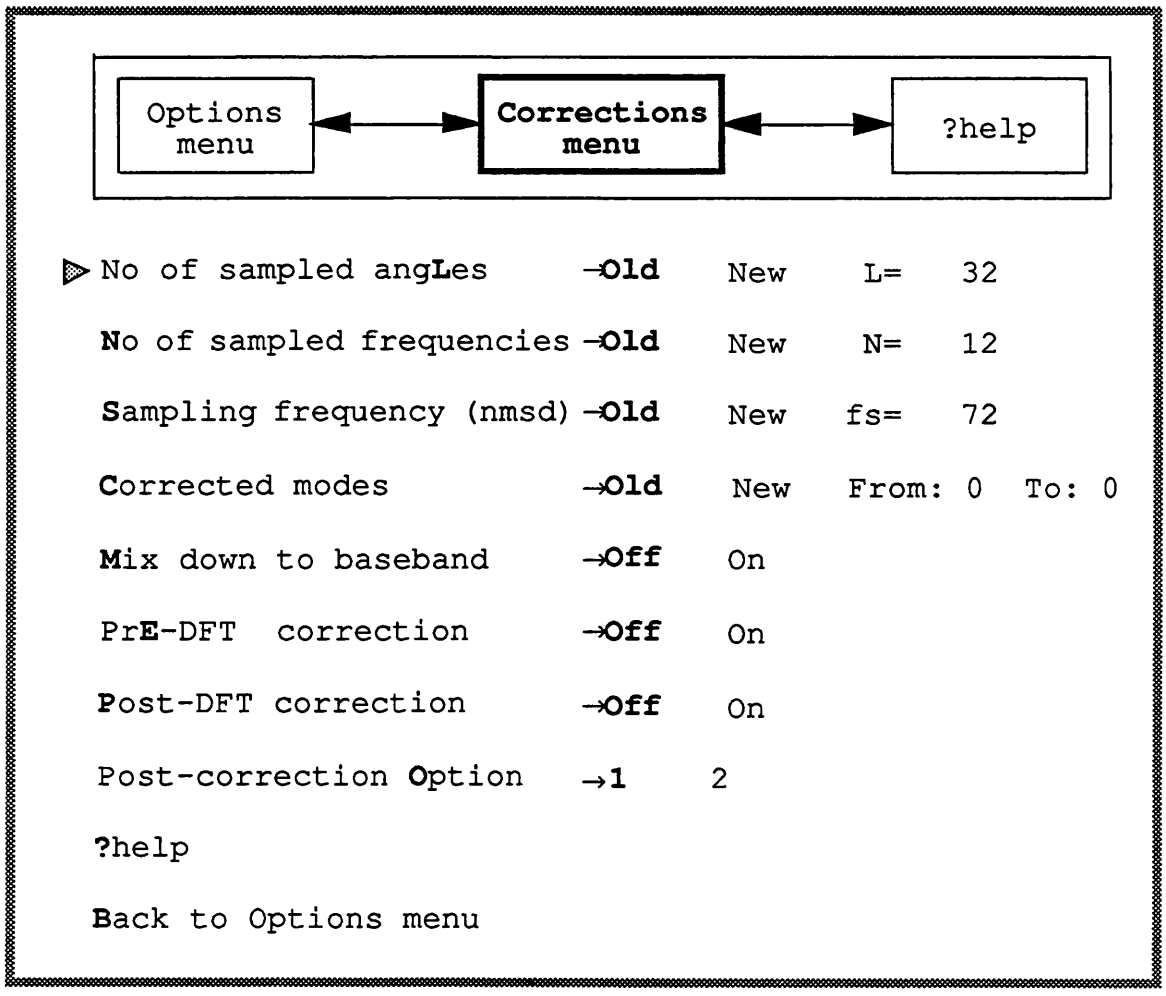

Fig. F.11.1 Corrections menu screen

F.12 OUTPUT MENUS

The four Output menus described in this section are accessible via the Options menu. They allow the user to define the abscissa as angle, frequency or time and set the range and resolution for each of these parameters. The **D**isplay computed output option starts off the computation process and sends the program to the Display menu when it is completed. To go back to the Options menu one may press **B** or the **Esc** key or move the red pointer to the last option and press **Enter**.

The Direct (element-space) radiation pattern output menu shown in *Fig. F.12.1*, is intended for the synthesis of element-space radiation beams. In that menu, aperture excitation may be set to co-phased or co-delayed in the direction specified by **S**can (co-excitation) angle option as well as arbitrarily weighted in amplitude and phase through the Set **W**eighting taper option which invokes the Direct weighting menu described in section F.13.

The Phase modes output menu shown in *Fig. F.12.2* is the program branch leading to the formation of one or more omnidirectional phase modes. The range of mode numbers is entered via the **M**ode range option (lower mode number, upper mode number and step size).

The Modal (mode-space) radiation pattern output menu shown in *Fig. F.12.3* controls the synthesis of mode-space beams. Here the **M**ode range option refers to the set of phase modes used to form the modal radiation pattern. The phase modes may be 'scan phased' in any direction and arbitrarily weighted in amplitude and phase through the **S**can angle [by IDFT] and Set **W**eighting taper options respectively, the latter invoking the Modal weighting menu which is described in section F.14.

The 'Compare modal patterns' output menu shown in *Fig. F.12.4* controls the evaluation and display of a comparative pattern formed by subtracting the amplitudes (in dB) and phases of two beams (e.g. sectoral phase modes) which are formed by summing different but equal-size sets of adjacent phase modes. Each set of modes is equally tapered in amplitude and in phase through the Set **W**eighting taper option and scan phased via the **S**can angle [by IDFT] option. The Set **W**eighting taper option invokes, as in the Modal radiation pattern output menu, the Modal weighting menu described and illustrated in section F.14, and in fact the same modal taper is shared between these two output menus (provided that the mode ranges are set to the same number of phase modes).

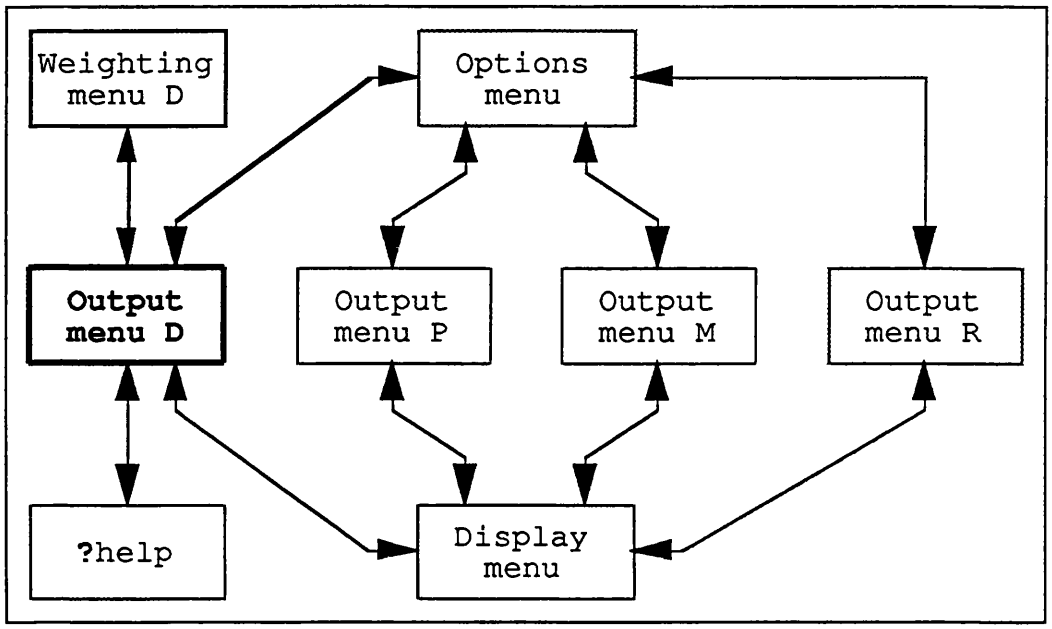

▶ **C**o-excite →**Off** Co-phase Co-delay

Versus →**Angle** Frequency Time

Frequency range f/fo = From: 1.000 To: 1.000 step: 0.

Time range fot = From: 0. To: 0. step: 0

Angle range (deg) phi = From: -180 To: 180 step: 1

Scan (co-excitation) angle (deg) Phi0 = 0.

Set **W**eighting taper

Display computed output

?help

Back to Options menu

Fig. F.12.1 Output menu D screen

The two sets of excited phase modes are selected via the `1st beam's mode range` and `2nd beam's mode range` options (for the second beam, only the `From` mode number is entered by the user).

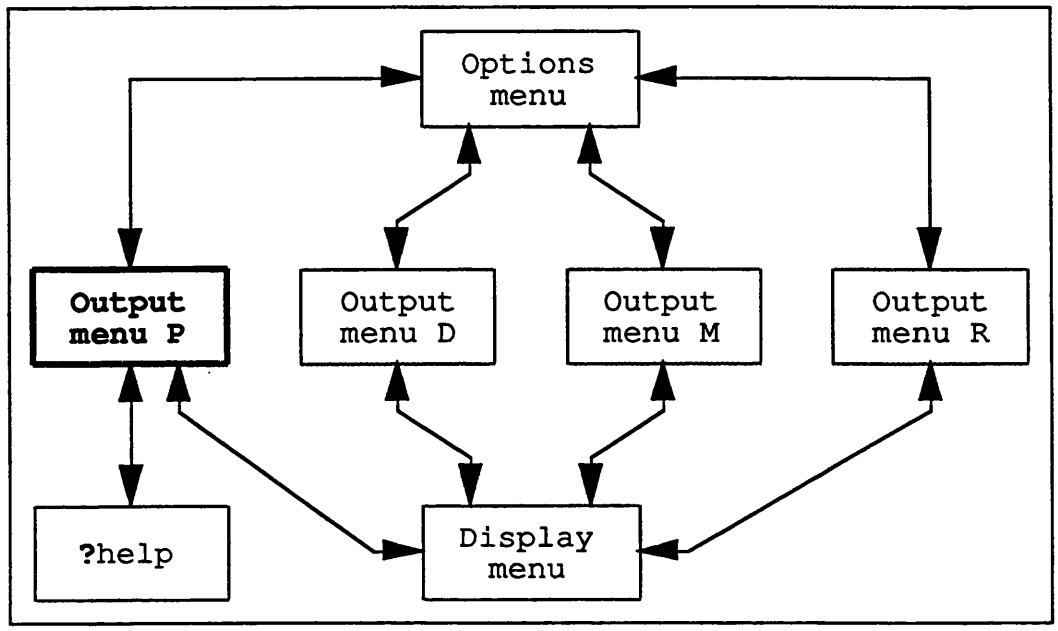


```
►Versus                    →Angle      Frequency      Time
 Frequency range f/fo =   From: 1.000   To: 1.000   Step: 0.
 Time range       fot =   From: 0.      To: 0.      Step: 0
 Angle range (deg) phi =  From: -180.   To: 180.    Step: 1.
 Mode range        mu =   From: 0       To: 0       Step: 1

 Display computed output

 ?help

 Back to Options menu
```

Fig. F.12.2 Output menu P screen

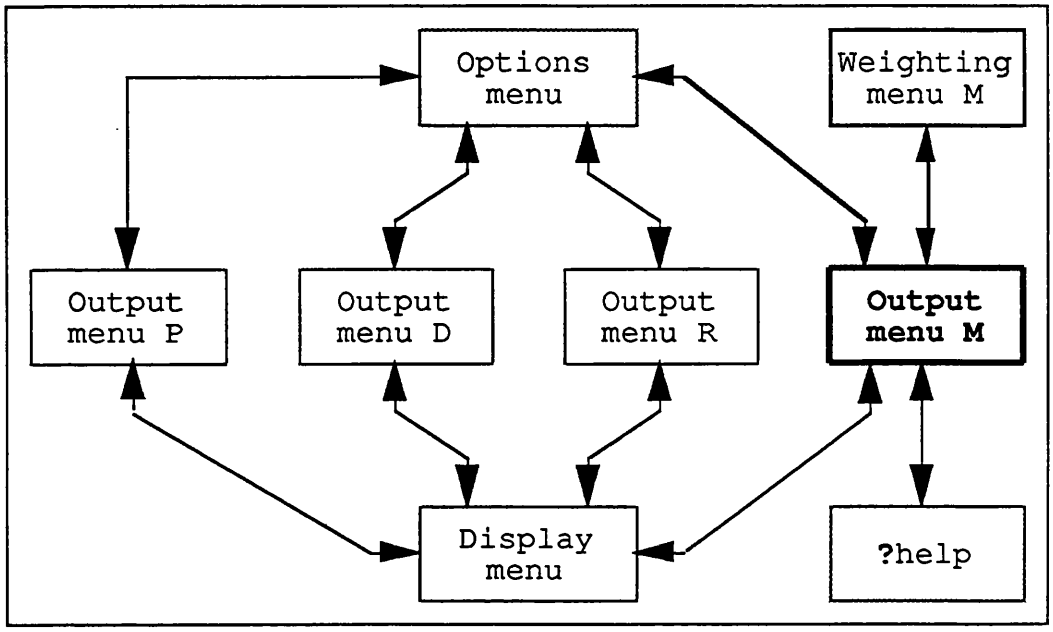

▷ **V**ersus → **Angle** Frequency Time

Frequency range f/fo = From: 1.000 To: 1.000 Step: 0

Time range fot = From: 0. To: 0. Step: 0

Angle range (deg) phi = From: -180. To: 180. Step: 1.

Mode range mu = From: 0 To: 0

Scan angle [by IDFT] (deg) Phi0 = 0.

Set **W**eighting taper

Display computed output

?help

Back to Options menu

Fig. F.12.3 Output menu M screen

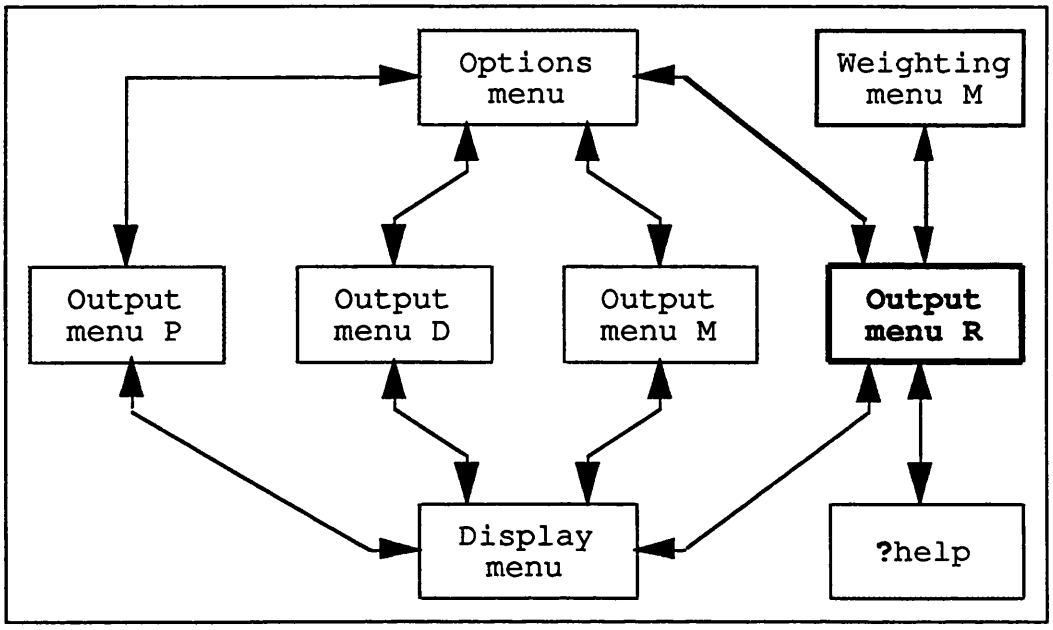

▶ **V**ersus →**Angle** Frequency Time

Frequency range f/fo = From: 1.000 To: 1.000 Step: 0

Time range fot = From: 0. To: 0. Step: 0

Angle range (deg) phi = From: -180 To: 180 Step: 1

1st beam's mode range From: 0 To: 0

2nd beam's mode range From: 0 To: 0

Scan angle [by IDFT] (deg) Phi0 = 0

Set **W**eighting taper

Display computed output

?help

Back to Options menu

Fig. F.12.4 Output menu R screen

F.13 DIRECT WEIGHTING MENU

This menu, shown in *Fig. F.13.1*, allows the user to set and view an amplitude and phase excitation taper at the array aperture for element-space radiation beams. Amplitude (dB) or phase (deg) values are entered to a range of elements by first selecting the desired option and pressing **Enter** or the → key, then typing in the new value, and the first (`For m =`) and last (`To m =`) element numbers in the group of elements to which it is to be applied, each followed by **Enter**. The taper may be listed at any time by pressing **L** and scrolling if necessary with the aid of the **PageDown** or **PageUp** keys.

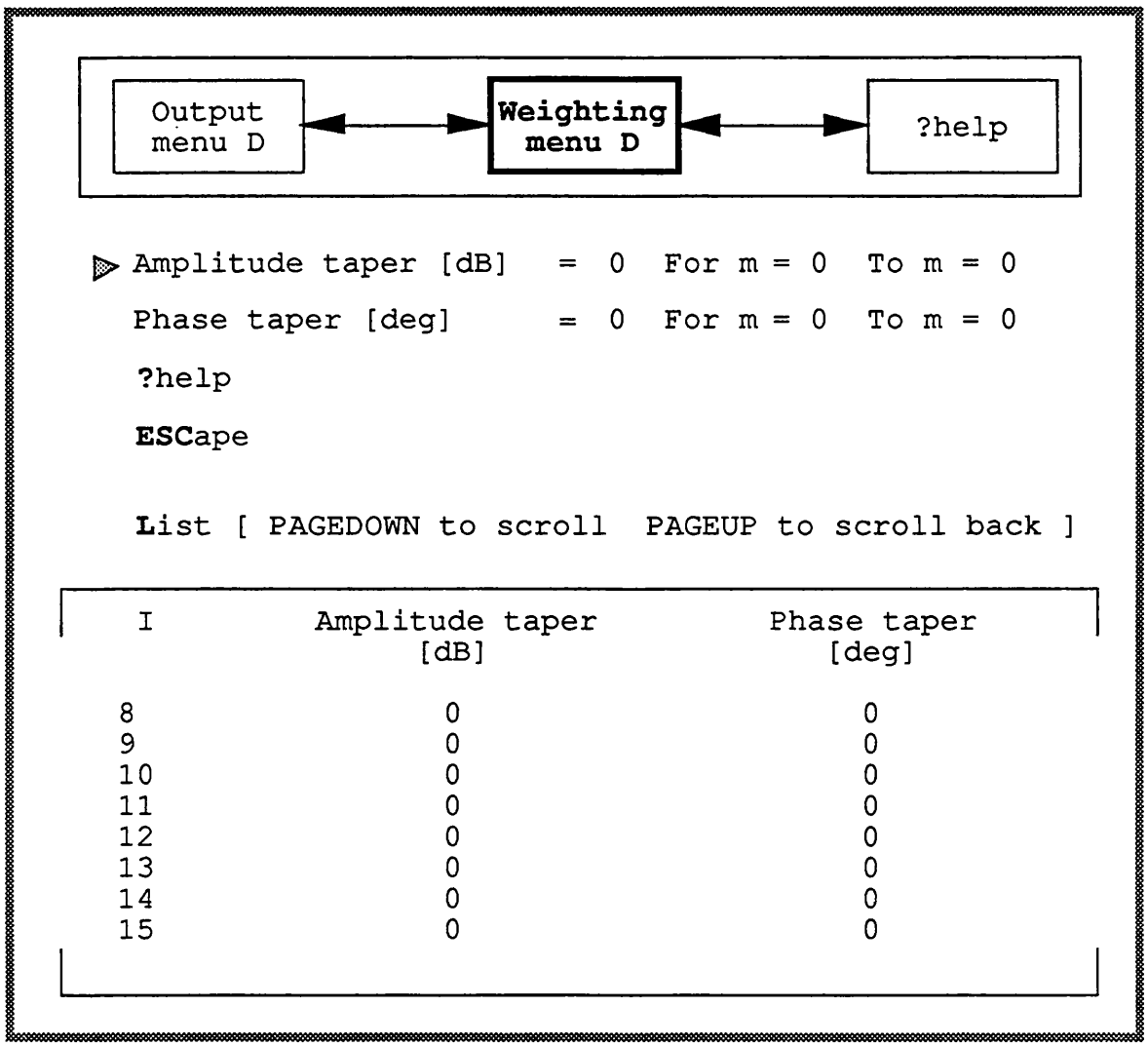

Fig. F.13.1 Direct weighting menu screen

F.14 MODAL WEIGHTING MENU

The 'Modal weighting menu' shown in *Fig. F.14.1*, allows the user to set and view an amplitude and phase excitation taper at the phase mode outputs, for the synthesis of a mode-space radiation beam. It may be invoked either from the Modal radiation pattern output menu or from the 'Compare modal patterns' output menu described in section F.12. Amplitude (dB) or phase (deg) values are entered and listed as in the Direct weighting menu of section F.13.

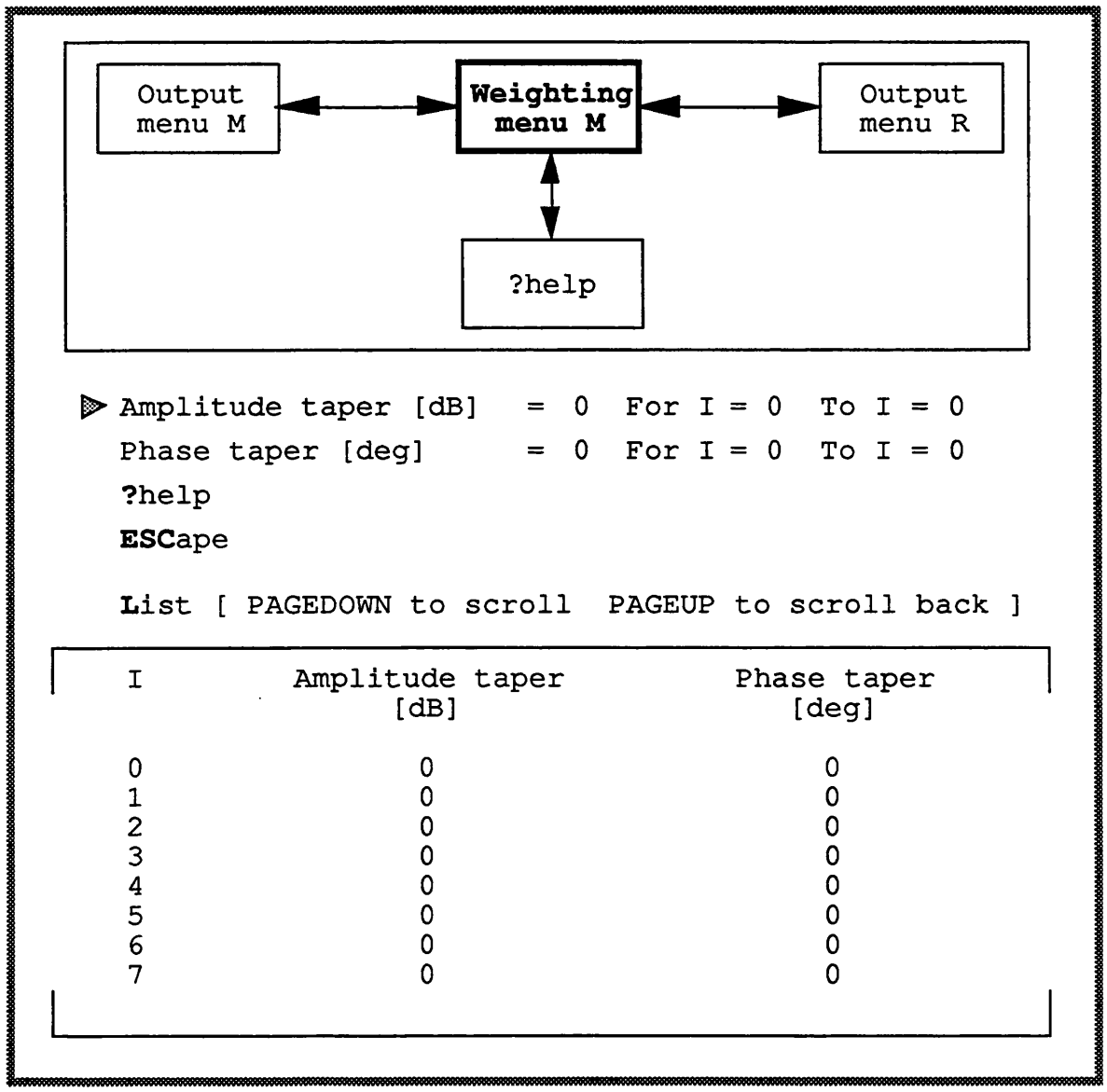

Fig. F.14.1 Modal weighting menu screen

F.15 DISPLAY MENU

The display menu shown in *Fig. F.15.1* appears as soon as the radiation pattern computations have been completed. It allows the user to:

- display, list or save the output amplitude and phase data
- add an optional amplitude (dB) and phase (degree) offset to the displayed, listed and saved outputs
- show or hide the xy grid and graph labels
- set the x-axis grid and label to automatic or customised
- set the y-axis grid + all other labels to automatic or customised

All the above switches are set by using the → or ← keys to point the yellow arrow at the selected position. Invoking the `Customise scale + labels` option will direct the program to the Customise menu which is described in section F.16.

The output data may be:

- plotted by selecting the `Amplitude plot` or `Phase plot` options. Initially all computed graphs will be plotted; to re-plot the whole set, press 0, to re-plot a single graph press the corresponding graph number (1 to 9). Pressing any other key will return program to the Display menu.
- listed by invoking the `List output` option. Initially the first 24 lines are displayed; to scroll use the **PageDown** or **PageUp** keys and press the **Esc** key to return to the Display menu.
- saved by invoking the `Save output` option. This sends the program to the Save output menu which is described in section F.17.

Pressing **B** or the **Esc** key returns the program back to one of the four output menus described in section F.12.

F.16 CUSTOMISE MENU

This menu shown in *Fig. F.16.1* allows the user to add labels and modify the displayed scale limits, grid and tick (subdivision) marks. `Customise Labels`, `Customise X scale` or `Customise Y scale` are first selected in the usual way and then activated by pressing **Enter** or the → key. This turns the red pointer into a static yellow arrow and activates a new movable red pointer within the selected frame. New data is then entered for the selected option by pressing **Enter** or the → key, typing in the new entry and pressing **Enter** again.

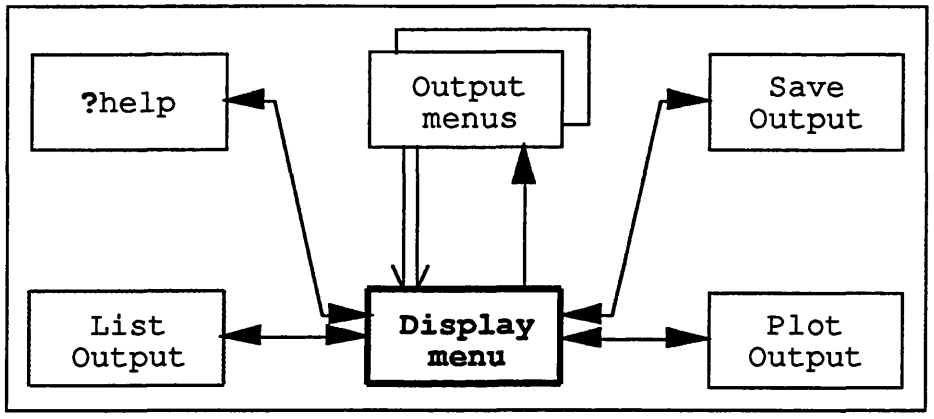

▶ **G**rid + labels → On Off

Xscale → Auto Custom

Yscale → Auto Custom

Offset output by 0 dB + 0 deg

Customise scale + labels

Amplitude plot

Phase plot

List output

Save output

?help

Back to Output menu

Fig. F.15.1 Display menu screen

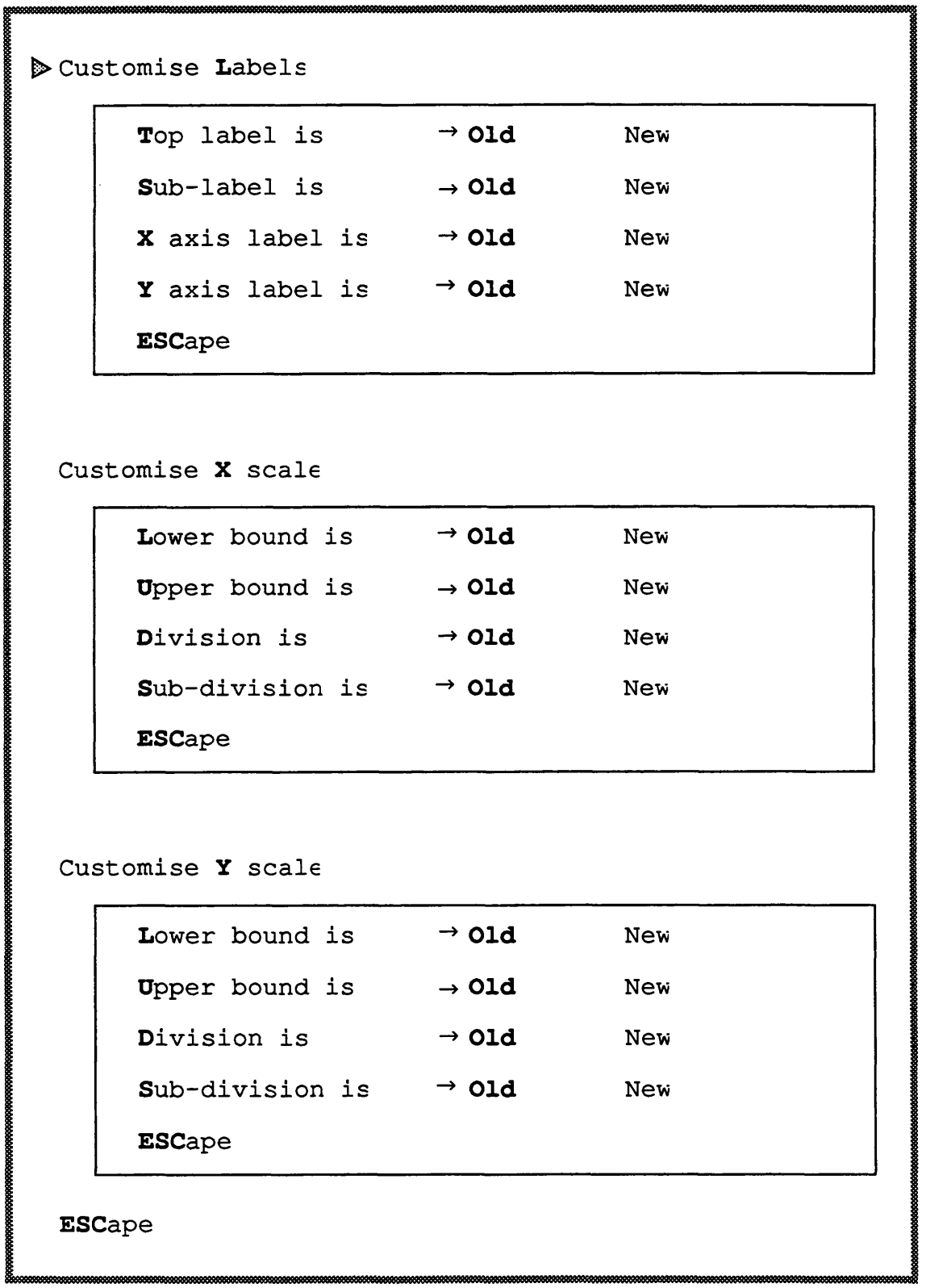

Fig. F.16.1 Customise menu screen

By pressing the **Esc** key the red pointer will vanish from within the selected frame and will replace the static yellow arrow on the outside. It may now be moved in the usual way to select a new option. Pressing the **Esc** key again will return the program to the Display menu.

The entered parameters are defined as follows:

i **Top label** - the label printed on the top line above the plot frame. It defaults to 'Amplitude plot' or 'Phase plot' when the **Yscale** option in the Display menu is set to Auto.

ii Top **Sub-label** - the label printed underneath the top label.

iii **X-axis label** - the label printed underneath the X-axis. It defaults to 'Phi (degs)', 'Normalised Frequency f/fo' or 'Normalised Time fot' when the **Xscale** option in the Display menu is set to Auto.

iv **Y axis label** - the label printed to the left of the Y-axis. It defaults to '[dB]' or '[deg]' when the **Yscale** option in the Display menu is set to Auto.

v **Lower bound** - refers to the the lowest point on the X or Y axis. This is automatically set if the corresponding **Xscale** or **Yscale** option in the Display menu is set to Auto.

vi **Upper bound** - refers to the highest point on the X or Y axis. This is automatically set if the corresponding **Xscale** or **Yscale** option in the Display menu is set to Auto.

vii **Division** - the grid step on the X or Y axis. This is automatically set if the corresponding **Xscale** or **Yscale** option in the Display menu is set to Auto.

viii **Sub-division** - the step size between minor ticks on the X or Y axis. It defaults to the grid step (i.e. no minor ticks) if the corresponding **Xscale** or **Yscale** option in the Display menu is set to Auto.

F.17 SAVE OUTPUT MENU

The 'Save output menu' shown in *Fig. F.17.1* enables the user to save on the selected storage device and the specified directory:

- all the previously entered input data and settings + the computed output data on a sequential ASCII file with a user-defined file name + the extension RNG. The output file may be used as an optional input to the program at a later session through the 'Load input/output menu' - see section F.5.
- the computed output data only (optionally offset through the `Offset output` option of the Display menu – see section F.16) in a sequential ASCII file with a user-defined file name + the extension TDA (for tab-delimited data) or CDA (for comma-delimited data), which may be imported by an external charting package.

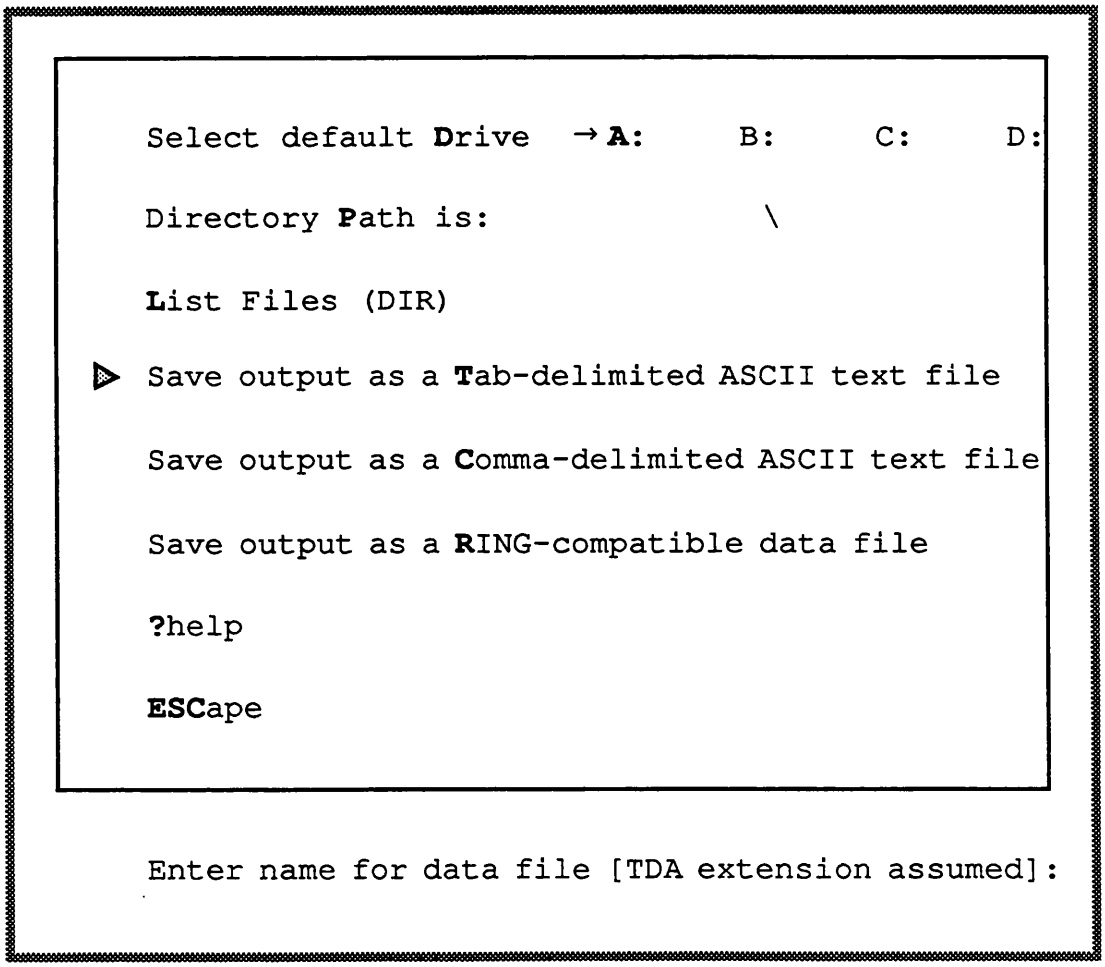

Fig. F.17.1 Save output screen


Printed by Central Services, University College London